Design, Synthesis, and Characterisation of Metal–Organic Framework Crystal–Glass Composites (MOF CGCs)

Christopher W. Ashling

Submitted for the degree of
Doctor of Philosophy
at the University of Cambridge

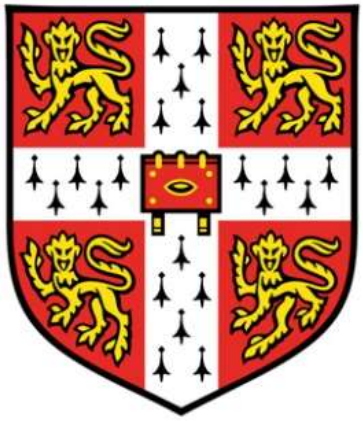

Girton College, Cambridge, UK

Supervisor: Dr Thomas D. Bennett

October 2021

Declaration

This thesis is the result of my own work and includes nothing which is the outcome of work done in collaboration except as declared in the Preface and specified in the text. It is not substantially the same as any that I have submitted or is being concurrently submitted for a degree or diploma or other qualification at the University of Cambridge or any other University or similar institution except as declared in the Preface and specified in the text. I further state that no substantial part of my thesis has already been submitted or is being concurrently submitted for any such degree, diploma or other qualification at the University of Cambridge or any other University or similar institution except as declared in the Preface and specified in the text. It does not exceed the prescribed word limit for the relevant Degree Committee.

Christopher W. Ashling

Acknowledgements

I would like first to thank the research councils that funded this PhD: the Royal Society and the Commonwealth Scientific and Industrial Research Organisation (CSIRO).

Next, I would like to thank my supervisor Dr Thomas D. Bennett, for both the opportunity to undertake this PhD and his unerring support, belief, and guidance throughout my time at the University of Cambridge. This research and my academic progress have only been possible through the countless opportunities presented to me throughout this project. I would also like to thank each and every member of the Hybrid Materials group, both past and present, for their contributions to this work. It is difficult to precisely define the positive influence of colleagues that takes place during beamline visits, group presentations, office discussions and lunchtime chats. However, each has added considerable value to this project and my ability to carry out rigorous science. Among such influences, I would like to thank, in particular, Louis Longley, Dr Jingwei Hou, and Thomas Southern for their invaluable scientific conversations, company whilst working late into the night, and their camaraderie, especially during low points of my time at Cambridge.

Members of the Materials Science and Metallurgy department I would like to thank are Dr Rachel Evans, Dr Sean Collins (now at the University of Leeds), and Dr Duncan Johnstone for their collaboration and helpful suggestions in the preparation of manuscripts detailed herein. Further afield, I would like to thank Prof Shane Telfer (and Dr Thomas Bennett) for providing a fantastic collaborative opportunity to work in New Zealand for a second time to collect dozens of informative gas sorption isotherms with Dr Lauren Macreadie using equipment unavailable at my host institution. Another special thanks I would like to extend is to my former supervisor Dr Timothy Easun at Cardiff University, whom I had the great pleasure to meet again at various conferences and who generously continued to offer sound career advice throughout my PhD.

On a personal note, I feel this PhD would not have been possible without the love and support of my parents, Carolyn and Richard Ashling, who were, and always have been, paragons of support during tough times and have never stopped believing in me.

One of the greatest and personally meaningful opportunities this PhD afforded me was the chance to meet my partner, Bryony, and the opportunity to step into the role of being a father. Thank you for the countless things you've done to support me, and the experiences we've shared in this time; I'm excited to meet what the future brings.

I extend the last of these acknowledgements to the Cambridge University American football team, The Pythons; I have always felt welcome and valued by the team from my first year here. Aside from the indispensable social aspects of the

team, this sport also gave me purpose to strive for physical strength and discipline. In particular, I would like to thank my brothers in arms: Nathan Butler, Jonathan Williams, Nicholas Timmons, and Colton Runyan, for the years of brotherhood we shared in the trenches. I wish you all the best of luck in the future.

Finally, I would like to add that it is unfortunate that a considerable portion of this project was spent under lockdown measures in response to the global COVID-19 pandemic caused by SARS-CoV-2. However, neither hell nor high water could abate the progress of science. In this vein, I am reminded of a particularly Stoic philosophy relayed by J. R. R. Tolkien:

> "I wish it need not have happened in my time," said Frodo.
>
> "So do I," said Gandalf, "and so do all who live to see such times. But that is not for them to decide. All we have to decide is what to do with the time that is given us."
>
> — **J. R. R. Tolkien, *The Fellowship of the Ring*.**

Abstract

Metal–organic frameworks (MOFs) are a highly topical class of three-dimensional porous materials proposed for applications such as gas storage, separations, and catalysis. Typically, MOFs are synthesised as microcrystalline powders of nanometer- to millimetre-sized particles ill-suited to industrial settings without prior processing. However, recent research has revealed solid-liquid transitions within the family, which is used here to create a class of functional, stable and porous composite materials. Described herein is the design, synthesis and characterisation of MOF crystal–glass composites formed by dispersing crystalline MOFs within a MOF glass matrix.

The first of these novel materials incorporates MIL-53 within a ZIF-62 glass matrix where the crystalline phase's coordinative bonding and chemical structure are preserved. Whilst the phases are separated, the interfacial interactions between the proximate microdomains improve the mechanical properties of the glass composite. More significantly, the high-temperature, open-pore phase of MIL-53, which spontaneously transforms to a narrow pore phase upon cooling in the presence of water, is stabilised at room temperature in the crystal–glass composite. This leads to a significant improvement in CO_2 adsorption capacity. This enhancement is further explored and maximised by synthesising a compositional series of composites. The distribution and integrity of the crystalline component in this series were determined, and these findings were used to identify the maximum crystalline loading and maximum CO_2 adsorption capacity.

In addition to the study of MIL-53, other MOF crystal-glass composite (MOF CGC) systems were explored, and the thermal stability considerations in the formation of MOF CGCs are highlighted. Resultantly, two separate MOFs were identified, MIL-118 and UL-MOF-1, with which MOF CGCs were successfully synthesised. These new materials, alongside the prototypical MOF CGC, formed using MIL-53, were studied using scanning electron microscopy, powder X-ray diffraction, and gas sorption techniques to reveal an approximate kinetic diameter limitation of gases that may permeate through the glass matrix. Furthermore, the thermal expansion behaviour of these three MOF CGCs was investigated. Specifically, variable-temperature powder X-ray diffraction data and thermomechanical analysis show the suppression of thermal expansivity in each of these three crystalline MOFs when suspended within a ZIF-62 glass matrix. In particular, for the two flexible frameworks, the average volumetric thermal expansion (α_V) was found to be near-zero in the crystal–glass composite.

Contents

List of Abbreviations

Abbreviation	Meaning
°C	Degrees Celsius
1-MCP	1-methylcyclopropene
2,6-ndc	2,6-naphthalenedicarboxylate
***a*MOF**	Amorphous metal–organic framework
API	Active pharmaceutical ingredient
BABA	Back-to-back recoupling sequence
BDC	1,4-benzenedicarboxylate
BET	Brunauer-Emmett-Teller
bIm	Benzimidazolate
CGC	Crystal–glass composite
CLH	Constant load and hold
COF	Covalent organic framework
COSY	Correlation spectroscopy
CRN	Continuous random network
CSM	Continuous stiffness measurement
CTE	Coefficient of thermal expansion
DMF	*N,N*-dimethylformamide
DoE	Department of energy
DQ-SQ	Double-quantum single-quantum
DSC	Differential scanning calorimetry
EDS	Energy-dispersive X-ray spectroscopy
EELS	Electron energy-loss spectroscopy
FPMD	First-principles molecular dynamics
fs	Femtosecond
FSDP	First sharp diffraction peak
FT-IR	Fourier-transform infrared
GFA	Glass-forming ability
HDA	High-density amorphous
ICTAC	International confederation for thermal analysis and calorimetry
ILAG	Ionic liquid assisted grinding
Im	Imidazolate
iPDF	Interface pair distribution function
IUPAC	International union of pure and applied chemistry

K	Kelvin
LAG	Liquid assisted grinding
LDA	Low-density amorphous
LVDT	Linear variable displacement transducer
MAS	Magic angle spinning
MMM	Mixed matrix membrane
MOF	Metal–organic framework
MOF CGC	Metal–organic framework crystal–glass composite
MOP	Metal–organic polyhedra
MPa	Mega Pascal
MQG	Melt-quenched glass
MS	Mesoporous silica
NASA	National aeronautics and space administration, U.S.A.
nm	Nanometer
NMF	Non-negative matrix factorisation
NMR	Nuclear magnetic resonance
NTE	Negative thermal expansion
PALS	Positron annihilation lifetime spectroscopy
PDF	Pair distribution function
PEL	Potential energy landscape
PEO-PA	Polyether oxide-polyamide
PMMA	Polymethylmethacrylate
PSD	Proton spin-diffusion
PSDF	Pore size distribution function
PXRD	Powder X-ray diffraction
RF	Radiofrequency
RMC	Reverse Monte Carlo
RMS	Royal mail ship
SAXS	Small-angle X-ray scattering
SBU	Secondary building unit
SDT	Scanning DSC and TGA
SED	Scanning electron diffraction
SEM	Scanning electron microscopy
SRJ	Strain-rate jump
SRO	Short-range order
STEM	Scanning transmission electron microscopy

STP	Standard temperature and pressure
T_g	Glass transition temperature
TGA	Thermogravimetric analysis
T_m	Melting temperature
TMA	Thermomechanical analysis
TPPM	Two-pulse phase-modulated
VT-PXRD	Variable temperature powder X-ray diffraction
XANES	X-ray absorption near-edge spectroscopy
XRD	X-ray diffraction
ZIF	Zeolitic imidazolate framework

List of Figures

List of Tables

Chapter 1 Introduction

1.1 Porous Materials

Simply speaking, porous materials comprise materials that possess empty space. Porous materials have been the backbone (quite literally) for much of life on Earth, including a variety of rocks, soil, wood, bone, and even biological tissue. The "holes" in these materials, often referred to as the void spaces, can range in size from visible holes, such as those in sponges, to angstrom-sized ($\times 10^{-10}$ m) channels wherein gases pass through spaces as narrow as the molecules of the gases themselves. Since many of these void spaces are accessible, these materials' effective surface area extends much farther than the outside surface, reaching values above 7000 m^2/g.[1] For perspective, a single gram of material with this surface area would be equivalent to 1.3 full-sized American football fields, and just over 45 kg would have an equivalent surface area to the entire island of Malta (316 km^2).

1.1.1 Nomenclature

Technically, a porous solid is a solid material with cavities or channels deeper than they are wide, *i.e.* in practice, the cavities must extend significantly into the material.[2] This definition excludes solids such as those patterned with hemispherical voids, such as the dimples on golf balls or the craters, basins, and maria that decorate the moon's surface. Whilst the pores can vary in size by several orders of magnitude, the ones discussed most heavily here are those with pore sizes under 0.1 μm. Several families of porous materials exist below this threshold and are remarkable for their exceptional surface areas. The materials studied herein contain pores narrower than 100 nm and are termed nanoporous materials, which itself is separated into three general categories: macro- (>50 nm), meso- (2–50 nm), and micro- (<2 nm) porous materials whose delineation serve as conversational aids.

It is important to note that not all porous samples are *intrinsically* porous. The exceptional surface areas of some materials can be induced *via* the templating or scaffolding of individual molecules through which the imperfect solid-state packing of these materials induces an *extrinsic* porosity.[3] It is in the difference between intrinsic and extrinsic porosity that the difference between voids and pores is established. Voids are defined as the space *between* particles, whereas pores are the spaces or cavities *within* a particle.[2] The resolution of voids and pores within a sample is often non-trivial since the magnitude of each type of cavity may overlap.

***Table 1: Nomenclature of Porous Solids**. Adapted from reference 2.*

Term	Definition
Porosity	Ratio of total *pore* volume to apparent volume of particle or powder
Total Porosity	Ratio of volume of voids and pores (open and closed) to volume occupied by solid
Open Porosity	Ratio of volume of voids and open pores to volume occupied by solid
Porous Solid	Solid with cavities or channels which are deeper than wide
Void	Space between particles
Open Pore	Cavity or channel with access to the surface
Interconnected Pore	Pore which communicates with other pores
Blind Pore (or dead-end pore)	Pore with a single connection to the surface
Closed Pore	Cavity not connected to the surface
Pore Size	Pore width (diameter of cylindrical pore or distance between opposite walls of a slit)
Nanopore	Pore of internal width less than ~100 nm
Micropore	Pore of internal width <2 nm
Mesopore	Pore of internal width between 2 and 50 nm
Macropore	Pore of internal width >50 nm
Pore Volume	Volume of pores determined by stated method
Surface Area	Extent of surface assessed by a given method (experimental or theoretical) under stated conditions
External Surface Area	(1) Area of surface outside all pores (2) Area outside micropores
Internal Surface Area	(1) Area of all pore walls (2) Area of micropore walls
True Density	Density of solid, excluding pores and voids
Apparent Density	Density including closed and inaccessible pores, as determined by stated method

For intrinsically porous materials, it is also important to understand how the pores extend through the material since this may influence whether the increased surface area in the material is accessible to the probe molecules. Some pores, for example in many hierarchically structured polymers, exhibit pores in their structures which are enclosed and cannot be accessed: these are called closed pores. These pockets affect measured values since they are indistinguishable from a non-porous area using typical porosimetric measurements. Resultantly, the reported values which rely on access to all surfaces do not reflect the true values of the system. For example, using gas sorption (see **Section 3.1.9**) the reported surface area will not reflect the true surface area since the probe will not be able to adsorb to the internal surfaces of the closed pores.

1.1.2 Naturally Occurring Porous Materials

There are numerous types and sources of naturally occurring porous materials, found in a vast span of biomes which may exhibit both intrinsic and extrinsic porosity (**Figure 1**). Functionally, the porosity observed for many living systems is necessary for their survival; most sea sponges rely on constant water flow through their bodies to obtain food and oxygen. Their porosity increases their surface area, enhancing the rate of uptake in both of these systems. Transitioning to a much smaller scale, the inner regions of bones are also porous (**Figure 1c**) but require a scanning electron microscope (SEM) to

observe. The porosity of bones allows for the improved storage of minerals and bone marrow to produce red and white blood cells.

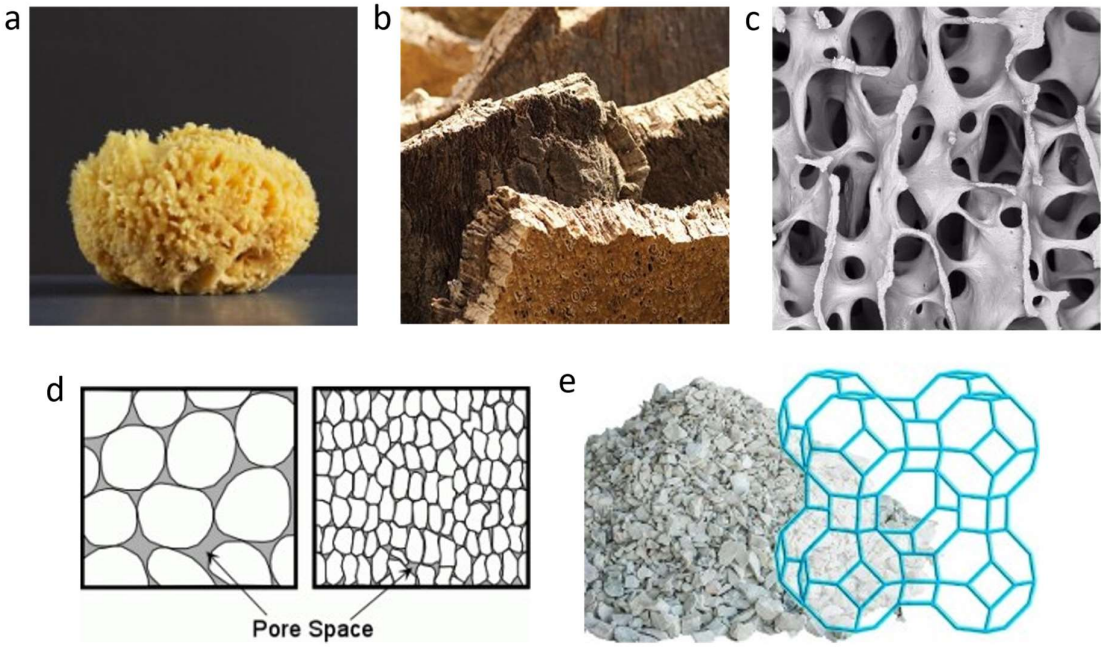

***Figure 1**: **Naturally occurring porous materials** a. sea sponge, b. cork, c. bone under a scanning electron microscope, d. diagram of soil particles, e. zeolite stones overlayed with a representative structural diagram of molecular connectivity with RHO topology; in this illustration, each corner represents the position of a Si or Al atom connected by bridging oxygen. Reproduced from references 4–8.*

A class of rock-like structures known as zeolites are naturally occurring materials that exhibit intrinsic microporosity.[9] The name "zeolite" is derived from Greek ζέω (zéō), meaning "to boil", and λίθος (líthos), meaning "stone" as a result of the observed evaporation of water under rapid heating. This behaviour is a result of the exceptional surface areas of zeolites, to which a large volume of water adsorbs.[10] Structurally, zeolites consist of single metal cations (typically aluminium or silicon) tetrahedrally coordinated by bridging oxo-anions at ~150° metal-oxygen-metal dihedral angles.[11] Zeolites may exist in greater than 40 naturally occurring, topologically distinct forms, with indefinitely extending channels intrinsic to the crystalline framework.[9] As a result of these extending accessible open pores, zeolites have been heavily researched for a variety of applications such as molecular sieving,[12] and catalysis.[13]

1.1.3 Synthetic Porous Materials

Whilst zeolites exhibit exceptional surface areas, extensive research has allowed for the development of various synthetic porous materials with improved physical properties, including synthetic zeolites. The benefit of synthetically producing these materials is that specific properties such as particle size, specific surface area, density, permeability, and pore diameters may be targeted. An example of the importance of such research is the particulate shape and size. Nanoscale materials have so far demonstrated promising results for both cell specificity and transfer through cellular membranes.[14]

Controlling both the porosity and size of the material has led to the development of nanoscale porous materials studied for cancer treatments due to their release of active pharmaceutical ingredients in targeted cells.[15,16]

Only nanoporous synthetic materials are discussed further here and are separated into three categories: inorganic, organic, and hybrid materials. The definitions of these terms are somewhat loosely used in the literature but obey general principles. Organic structures are primarily hydrocarbon-based materials with the allowance of some heteroatomic species such as oxygen (*e.g.* alcohols, ketones, carboxylic acids, aldehydes, esters, ethers) or nitrogen (*e.g.* amines, amides, nitriles, cyanides). Inorganic materials are those which do not comprise any organic materials as necessary components to the structure. Hybrid materials are thus defined by the requirement of both inorganic and organic materials as necessary to construct the material.

1.1.3.1 Inorganic Porous Materials

Inorganic synthetic porous materials comprise a small number of the total number of developed materials. However, similar to zeolites, a class of silica (silicon dioxide) materials known as mesoporous silica (MS), which comprise honeycomb-like silica structures, have been fabricated.[17] These structures are typically produced by the packing of colloids—three-dimensional macrostructures formed by the assimilation of amphiphilic surfactant molecules such that the hydrophilic "heads" and hydrophobic "tails" are all oriented towards their preferred solution forming emulsions in oil/water mixtures—which templates the self-assembly of silica around the micellar structures.[18] Upon completion of the dihydroxylation reactions required to form the Si–O bonds, the templating micelles are removed, typically by heating, producing nanometer-sized channels extending through the hardened, templated silica. Such materials offer high surface areas using low-cost materials.

1.1.3.2 Organic Porous Materials

Another method to produce both economically and environmentally friendly porous materials is through the carefully controlled carbonisation of organic precursors to form an amorphous (irregularly ordered, *i.e.* lacking long-range order) porous solid, known as activated carbons. The exhibited structural irregularity in the product often generates complex nanoporous structures as evidenced by the nature of their physisorption isotherms (see **Section 3.1.9.1**), which present composite, hysteretic isotherms with calculated surface areas surpassing 1000 m^2/g.[19] Such solids, sourced from easily processed and renewable organic matter, are desirable for low-cost porous materials. However, this cost-effectiveness and ease of fabrication come at the cost of atomic control of the end material since the precise atomic configuration of the material is unknown.

An example of a crystalline organic system arises from the self-assembling polymerisation of organic precursors. These materials, known as covalent organic frameworks (COFs), are connected entirely through covalent bonds by reversible cross-linking of rigid organic species.[20] The precursors to these materials are most frequently affixed with boronate ester,[21–24] imine,[25–28] and hydrazone[29,30] functional groups that require few steps to cross-link. There exists an extensive selection of rigid organic species which may be used as "building blocks" in the assembly of a COF; the length, width, connectivity—and even the addition of functional groups—can all be selected for in the COF precursors. Such versatility provides tunability of pore sizes, specific surface areas, and the introduction of accessible functional groups.

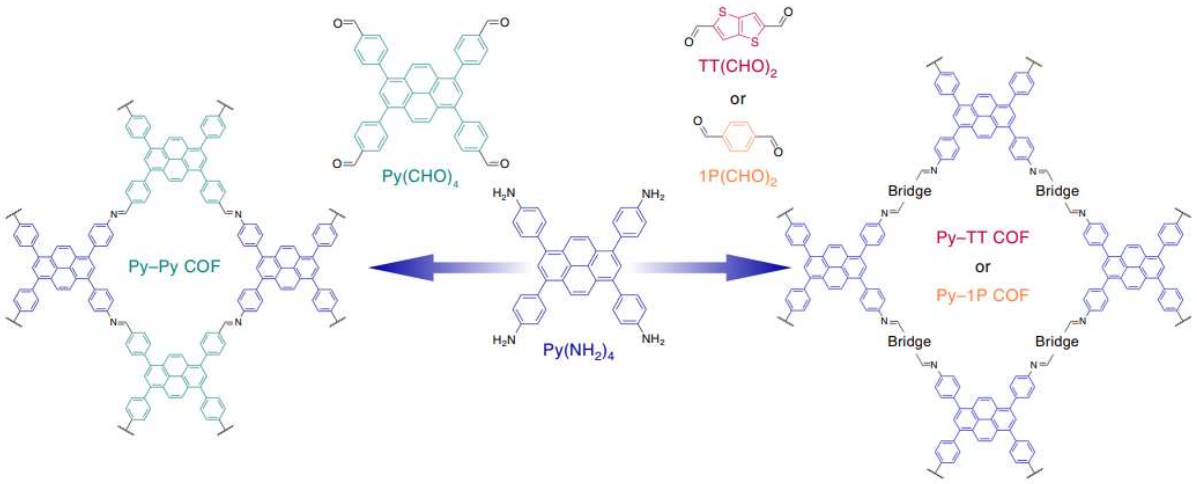

Figure 2: Schematics for the synthesis of two covalent organic frameworks (COFs)*; Py-Py COF, and Py-TT/Py-1P from the starting $Py(NH_2)_4$ precursor. Reproduced from reference 31.*

An example of this is shown in **Figure 2**, where tetradentate $Py(NH_2)_4$ species (centre) may be integrated into two distinct COFs through reaction with two linkers of different denticity. The reaction of $Py(NH_2)_4$ with a similarly structured tetradentate linker $Py(CHO)_4$ results in a COF (Py-Py COF) with small rhombus-shaped pores as each molecule is connected at each corner by a molecule of the opposing structure. Such is not the case when reacting $Py(NH_3)_4$ with the bidentate ligands of $TT(CHO)_2$ or $tP(CHO)_2$. In these cases, a COF with a larger pore diameter (with pore diagonals increasing to 2.4 nm from 2.0 nm) than Py-Py COF is achieved by bridging $Py(NH_2)_4$ molecules together, extending the length of the sides.[31]

The term COF is a blanket term for a variety of materials that may be constructed by the reaction of organic precursors to form porous materials. Illustrated in **Figure 2** are two-dimensional covalent organic frameworks, but by altering the connectivity of the linkers, both one-, two- and three-dimensional COFs may be synthesised.[32] Furthermore, zero-dimensional, discrete, nanometer-sized cages may be similarly synthesised, named porous organic cages (POCs), or covalent organic cages (COCs) (**Figure 3**) which are covalently bonded polyhedra with open centres.[33]

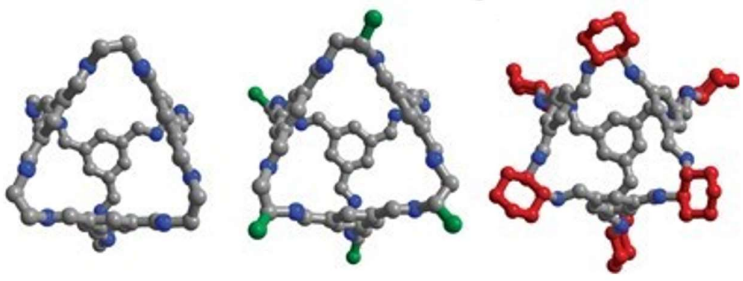

Figure 3*: **A selection of three desolvated tetrahedral porous organic cages** synthesised by the condensation reaction of 1,3,5-triformylbenzene with (left) 1,2-ethylenediamine, (middle) 1,2-propylenediamine, and (right) (*R,R*)-1,2-diaminocyclohexane. Reproduced from reference 33.*

Individual porous organic cages are often isolated as crystalline solids comprising cages stacked together in a long-range repetitive manner, which makes them a fascinating subject for porous materials. Since the cages themselves are porous, crystalline POCs exhibit both intrinsic *and* extrinsic porosity, *i.e.* porosity from both within and without the cages. POCs exhibit large apparent surface areas of 835 m^2/g and may be used for hydrocarbon or noble gas separations.[3,34,35]

1.1.3.3 Hybrid Porous Materials

Utilising both inorganic and organic components and borrowing properties from both families, hybrid materials comprise inorganic metal clusters coordinatively bonded to organic linkers. These materials may take on a variety of forms from nanometer-sized cages to one-, two-, and three-dimensional frameworks, analogous to many of the previous covalent organic frameworks. Metal–organic polyhedra, or MOPs, much like POCs, are "zero-dimensional", discrete, nanometer-sized polyhedra. Unlike POCs, however, the organic linkers in this material are connected through coordination bonds to a metal centre (metal node) which may be a single metal ion or a small cluster of connected metal ions.

From these metal nodes, a MOP may be post-synthetically modified to append molecules to the outer surface of the framework. By doing so, further functionality may be induced. One such example is illustrated in **Figure 4**, where MOP-18 is surface functionalised with aliphatic chains. This modification enables the MOP to be suspended in a lipid bilayer, into which the aliphatic chains of the MOP extend, mixing with the phospholipid hydrophobic tails.[36] Of the variety of hybrid materials, this functionality is unique to MOP due to their small and defined sizes. However, the most extensive body of research regarding porous, hybrid materials studies the three-dimensional hybrid porous materials, metal–organic frameworks, MOFs. This research focuses specifically on the development and application of MOF materials.

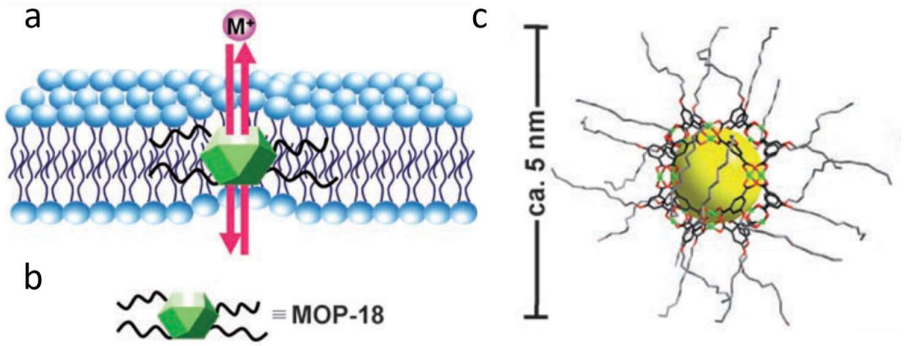

Figure 4: Schematic of a surface functionalised MOP penetrating into a lipid bilayer. *a. Induced ion channel formed by the insertion of a MOP into a lipid bilayer, b. schematic illustration of a surface functionalised MOP (MOP-18), and c. a detailed illustration of MOP-18 with a yellow sphere representing the void space within the MOP. Adapted from reference 36.*

1.2 Metal–Organic Frameworks

Metal–organic frameworks (MOFs) have been the focus of an increasing portion of the scientific community since the 1990s due to their versatility and tunability. Like previous examples, these hybrid materials comprise inorganic metal nodes (also known as secondary building units, SBUs) and organic linkers (also referred to as organic struts or ligands)

bonded together *via* coordination bonds extending indefinitely in one, two, or three dimensions.[37] Due to the separation of framework components on a highly ordered scale, MOFs are typically highly porous materials that exhibit nanoscale channels extending through the material (**Figure 5**). Members of these materials hold the current record for the largest surface areas (> 7000 m^2/g) and are promising for an array of potential applications, ranging from gas storage to molecular separations, sensing, and catalysis.[1,37]

The metal node of a MOF may be either a single metal ion or a cluster of metal atoms (typically connected by the organic ligands, bridging hydroxy, or oxo-anion species) which controls the connectivity, *i.e.* the number and directionality of emerging ligands, of the resulting framework. Selection of these building blocks and their connectivity is essential to controlling the resultant framework's dimensionality and structure.[38] Described by Tranchemontagne *et al.*, there are over 125 unique metal node motifs,[38] which, combined with a vast scope of applicable metals and organic linkers, gives a colossal scope of possible MOFs. Perhaps the archetypal example of the >99,000 reported MOFs[39] in the literature is MOF-5, $Zn_4O(BDC)_3$ (BDC: benzenedicarboxylate, $C_8H_4O_4^{2-}$), which adopts an octahedral ReO_3 bonding topology, connected by organic linkers of *para*-benzenedicarboxylate (**Figure 5**).[40]

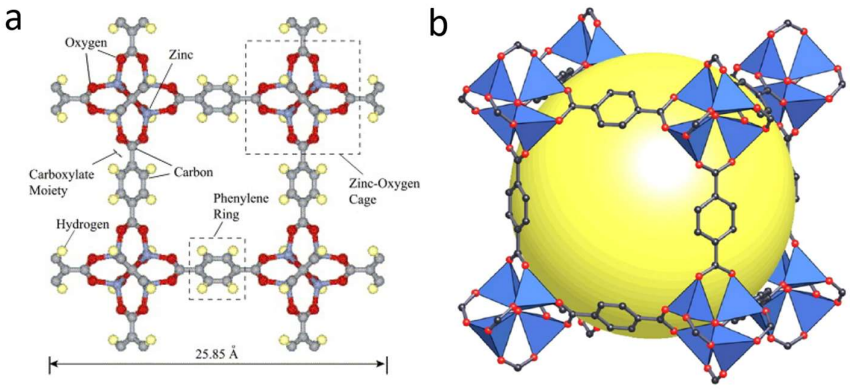

Figure 5: Schematic of the bonding and free volume of a metal–organic framework, MOF-5. *a. Local bonding in MOF-5, and b. a three-dimensional structure of MOF-5 with internal pore volume shown using yellow spheres, C – Black, O – Red, Zn represented by blue tetrahedra, H – Omitted. Adapted from references 41 and 42, respectively.*

1.2.1 MOF Composite Materials

The combination of MOFs as part of a composite material has enabled the production of unique materials with a large scope of applications. Research into MOF composites may be split into two categories: 1) those which utilise MOFs to stabilise other structures, and 2) those which aggregate small MOF particles into larger contiguous samples.[43] Examples of the former include the deposition of catalytically active metal nanoparticles (NPs) to the internal surfaces of a MOF (**Figure 6a**). The predictability of pore size within a crystalline framework permits selection of a material with pores small enough to effectively inhibit the aggregation of NPs whilst supporting them on an accessible internal surface.

MOFs may also support large proteins, such as in **Figure 6b,** where an enzyme is trapped within a MOP, or **Figure 6c** where a MOF is grown around an enzyme. In both cases, the enzyme remains catalytically active and is stabilised by

physically prohibiting the morphological change associated with denaturation.[44] Compositing a MOF with another MOF has also been achieved in core-shell structures such as in **Figure 6d** where crystalline particles of Co-MOF-74 are coated with layers of ZIF-67 of controllable thickness. Such a modification may introduce further functionality or improve the stability of the encapsulated MOF. Notably, in the case of Co-MOF-74@ZIF-67 a significant improvement in photocatalytic ability was observed.[45]

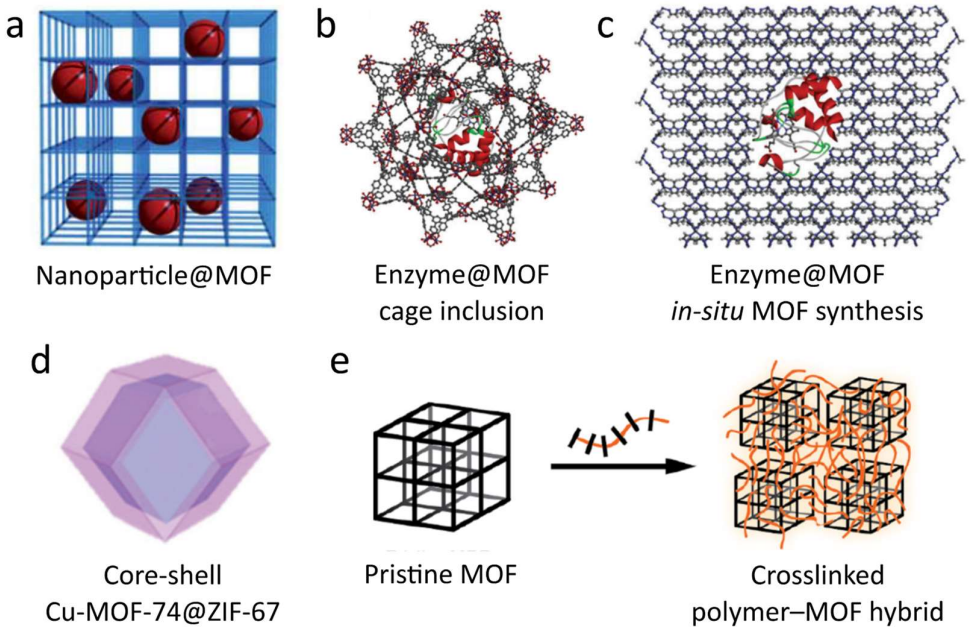

***Figure 6**: **Illustrations of a variety of MOF composite materials.** Illustrations of a. nanoparticles@MOF, b. polymer@MOF cage inclusion, c. polymer@MOF in-situ MOF synthesis, d. core-shell Co-MOF-74@ZIF-67, and e. reaction depicting the crosslinking of MOF particles using a polymer. Adapted from references 44, 45, 47, and 48.*

In each of the above examples, MOFs have been employed to enhance the properties of other materials; however, the microcrystalline nature of MOFs is typically industrially incompatible as the powders may block machinery. Accordingly, many studies have aimed to address this issue through the aggregation of MOF powders into more applicable bulk samples. In one study, MOF particles are bound together by the replacement of MOF linkers with polymers that mimic the linker bonding forming crosslinked hybrid composites (**Figure 6e**). A variety of materials such as activated carbons and polymers have been investigated for their compatibility with MOFs *via* growth or deposition of MOFs onto rigid bodies such as honeycomb cordierite structures (**Figure 7**).[48]

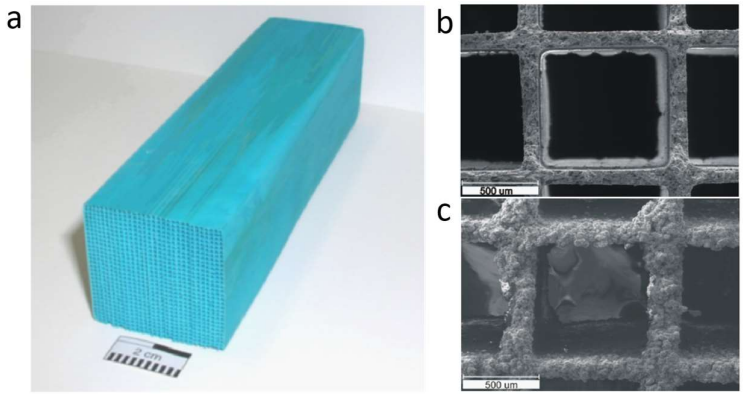

***Figure 7*: *Images of HKUST-1 grown on the surface of a material with uniaxially extending channels*.** *a. an optical image of $Cu_3(btc)_2$ on cordierite, b. scanning electron microscope image before growth, and c. after MOF growth. Adapted from reference 48.*

1.2.2 Industrial Applications of MOFs

While research has demonstrated the potential for MOF use in a diverse selection of applications, few have been successfully implemented in industrial settings, despite their prevalence in the literature. Below are listed a selection of commercialised MOFs:

TruPick® by *MOF Technologies Ltd.™* is a product developed to enhance the shelf-life of fruits such as bananas, pears, and apples. These fruits naturally ripen by an auto-catalytic process where ethylene is released during the ripening process and binds to ethylene receptors causing an acceleration of fruit ripening. TruPick® is a MOF, loaded with the cycloalkene 1-methylcyclopropene (1-MCP), and when exposed to moisture, releases the adsorbed 1-MCP. This 1-MCP then binds to the fruit's ethylene receptors, suppressing the auto-catalytic ripening and extending the shelf-life of the product.[49]

ION-X® by *NuMat Technologies, Inc.™* is the product name of a gas delivery cylinder for use in the microelectronics industry. Many microelectronics use toxic gases, such as phosphine (PH_3), boron trifluoride (BF_3), and arsine (AsH_3), as dopants which require safe delivery mechanisms. ION-X® uses MOFs to store these gases in a canister at sub-atmospheric pressures requiring vacuum-suction to release these gases. This system's advantage is that any piercing damage to the container will cause air suction into the cylinder rather than the release of pressurised toxic gases.[49,50]

MOFgen Ltd™ is another company that works to commercialise MOFs for biomedical applications. By loading the MOF with biologically active gases or therapeutic agents, active products may be developed for the moisture-induced release of medicinal compounds. Whilst products and suppliers are currently undisclosed, an example product was revealed in an interview: "For example, we can deliver a burst of nitric oxide gas that kills the area of infection to start with, and then a slow-release of an antimicrobial agent to help keep the infection away".[49]

Each of these companies has found an application for MOFs in its isolated, microcrystalline form. The development of MOF composites may impel the commercialisation of further MOF-based materials. However, the application of MOFs is not necessarily limited to those in the crystalline state.

1.3 Non-Crystalline MOFs

1.3.1 Structural Disorder

Order and disorder are properties that describe the presence or absence of symmetry or correlation in a system. There are four recognised categories of disorder that a framework may observe: topological, static, dynamic, and low-dimensional.[51] However, the order described herein will focus primarily on topological order. In this context, order describes the atomic arrangement within a structure in a long-range, repetitive manner. By contrast, disordered or "amorphous" frameworks maintain defined local geometries but without long-range periodicity.

Because this structural regularity occurs at an atomic scale, powders may also be crystalline. In a perfect crystalline material, the atoms or molecules are arranged in a regular, periodic manner. However, defects often appear in crystalline materials as vacancies, impurities, and dislocations within the solid.

1.3.2 Disordered Frameworks

MOF research has primarily focused on crystalline MOFs due to the ease of characterisation by X-ray diffraction methods, such as powder X-ray diffraction (PXRD). However, some MOFs also exist in an amorphous state, either synthesised directly or through the diminution of crystallinity upon heating, pressurisation, or ball milling.[52–55] Whilst some amorphous MOFs (*a*MOFs) may be synthesised directly with no crystalline counterpart,[56] some MOFs which may exist in either phase have been shown to be stoichiometrically identical to their crystalline counterparts. However, the two phases differ in their physical and physicochemical properties.[57–59]

Computational models fitted to experimental data of these amorphous MOFs fit a continuous random network model that describes randomisation of the connectivity between units of metal-ligand-metal bonding between metal nodes. This distance is known as the short-range order or local order (as discussed in **Section 1.3.3**) of *a*MOFs. This randomisation precludes any long-range order within the structure and introduces "defects" into the solid, such as an abundance of unsaturated metal sites and a distribution of micropore-scale void spaces.[52,60]

The breakdown of the long-range order in amorphous materials eradicates the defined lattice planes in the crystalline material that give rise to the peaks in the diffraction pattern. As such, the comparatively featureless diffraction pattern of an amorphous solid is often mistaken for a failed synthesis product and promptly disregarded. These amorphous products may, however, be utilised in ways that crystalline MOFs cannot. For example, amorphous UiO-66 has been used to trap calcein (an active pharmaceutical ingredient (API) equivalent) inside the framework (**Figure 8**) and increase the drug delivery timeframe from a typical 2 days to 30 days. This material is fabricated by loading the API into the crystalline framework and collapsing the framework to trap the API within the resultant amorphous network.[61] *a*MOFs also offer considerable industrial utility since processing and handling of the materials may be done without consideration of diminishing crystallinity.

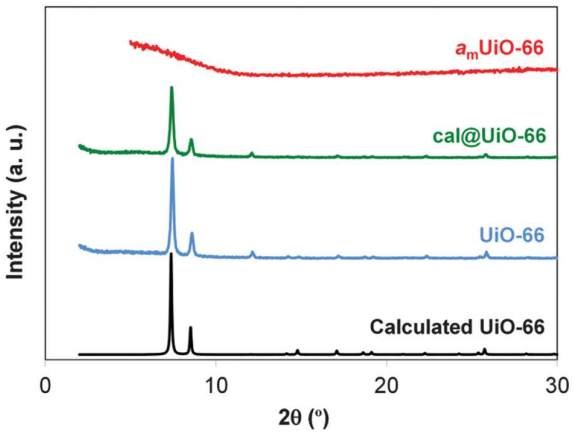

***Figure 8*: Amorphous and crystalline diffraction patterns.** *The difference in diffraction pattern features is shown here for a MOF (blue) then loaded with an API-equivalent (green) and the same sample upon amorphisation (red) displaying the elimination of Bragg diffraction peaks. Adapted from reference 61.*

1.3.3 Glasses

To be classified as a glass, a material must be amorphous and undergo a glass transition when heated towards the liquid state. **Figure 9** illustrates the specific volume change of a crystalline solid upon melting and cooling to form a glass; the reverse of this graph, therefore, illustrates the glass transition and recrystallisation. The ordinate of these graphs equally represents the entropy, *S*, or enthalpy, *H*, changes. On melting a crystalline material, the subject is heated at a constant rate to the melting temperature, T_m. From there, the solid stops heating whilst the input energy expands the material and undergoes a first-order transition in forming a liquid. Since the heat capacities of the liquid and the crystal are different, the gradient $\frac{dH}{dT}$, $\frac{dS}{dT}$, or $\frac{dV}{dT}$ reflects this, inducing a gradient change between the heating regions in the different phases.

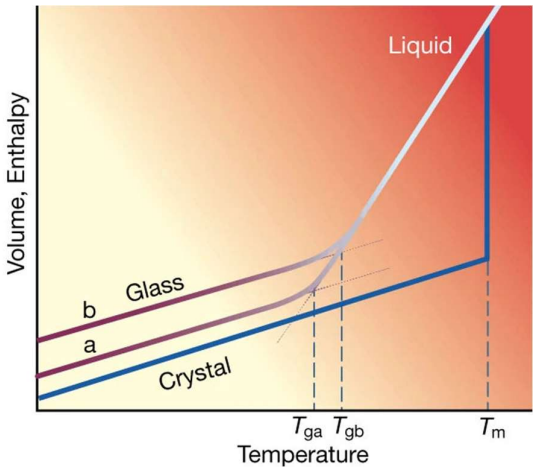

***Figure 9*: Illustration of the enthalpies concerning the crystalline, liquid, and glass states.** *Line a demonstrates the enthalpy change for a slow-cooled glass at lower values than for rapid cooling of the melt shown in b. Reproduced from reference 62.*

Unlike melting, the glass transition, T_g, is a second-order transition that adds curvature between the differing gradients (heat capacities) of the glass and the liquid. The temperature of this transition, T_g, is calculated from the convergence of the extrapolated gradients. Upon cooling from the liquid, a weak glass-forming material requires rapid cooling to undergo vitrification as slow cooling of a weak glass-former gives rise to the enthalpic/entropically-driven recrystallisation of the material. However, strong glass-formers are more stable in their liquid state and allow for slower cooling rates in forming a glass. The glass-forming ability—GFA, measured as the slowest cooling rate that produces a glass from the liquid state—is commonly regarded as a measure of the resistance to crystallisation from the melt. Another measure of the GFA is the ratio of the glass transition temperature to the melting temperature, T_g/T_m, which is inversely proportional to the material's glass-forming ability; typically, a strong glass-former is a material with a T_g/T_m above two-thirds.[57]

The glass transition temperature of a solid depends on the quenching rate from the liquid state. Slow cooling allows the liquid time to arrange into more stable conformations resulting in a lower glass transition temperature (**Figure 9**, glass a). Conversely, supercooling from the molten state disallows the material to relax into more stable conformations, leaving the glass in a state of greater entropy/enthalpy/volume, resulting in a higher T_g (**Figure 9**, glass b).

The structural rearrangements may be thought of in an energy landscape, as in **Figure 10**, where fast cooling from a high temperature causes the material to set in a shallow, high-energy basin. In contrast, slow cooling allows the material to traverse the various transition states moving to lower energy states. In theory, a glass produced by cooling at an infinitely slow pace would produce an "ideal glass", which is the lowest possible potential energy state of that glass.[63]

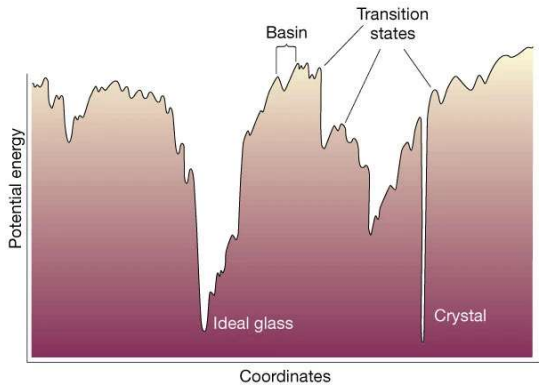

Figure 10: Illustration of a hypothetical glass potential energy landscape. *The x-axis represents all configurational coordinates displaying multiple energy wells a glass may be trapped within in this diagram. Reproduced from reference 62.*

Whilst no long-range order is present in the resultant material, where contiguous bonding exists in the structure, some short-range order (SRO) remains. For example, in silica glass, the silicon-oxygen long-range connectivity is disrupted, but some local, short-range order is maintained. Si–O–Si bonds in this structure retain the same bond lengths and bond angles but do not possess the periodicity of the crystalline sample. This SRO is evident in models of SiO_2 by the retention of four-coordinate silicon atoms connected by two-coordinate oxygen atoms. Though the random connectivity past this local bonding causes the long-range order loss, this mode of connectivity induces ring-like structures reminiscent of the crystalline structure.

Silica-based materials (SiO_2, **Figure 11**) are perhaps one of the most common examples of glass-forming materials and have been used extensively throughout human history as both a tool and a means of artistic expression. Resultantly, SiO_2 research comprises the vast majority of research regarding glasses. While this provides an informative model of the nature of atomic arrangements in amorphous materials and of glass behaviour, larger structural components result in greater system complexity. Glasses may be classified into four groups by their constituent materials; inorganic glasses, metallic glasses (amorphous metals), organic glasses, and in recent studies, hybrid glasses. This work will focus on the development of hybrid glasses.

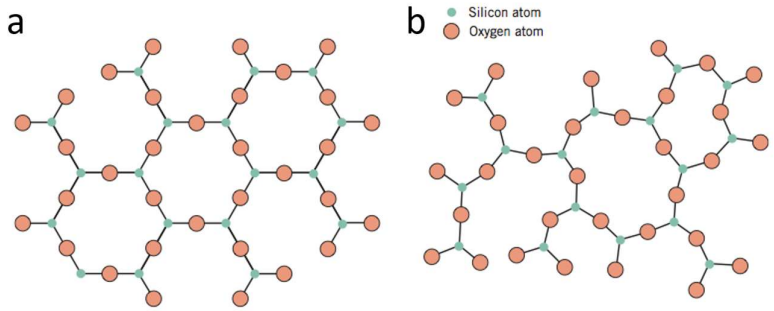

Figure 11: Crystalline and amorphous polymorphs of SiO_2. *Illustrations of a.* crystalline *polymorph of crystalline SiO_2 showing bridging oxygen atoms connecting silicon atoms forming hexagonal channels, and b. a disordered model of a SiO_2 glass. Reproduced from reference 64.*

1.3.4 Liquid MOFs and Melt-Quenched MOF Glasses

MOF glasses are part of the hybrid glass category and were the most recently discovered of the four glass families.[65] It is unclear how many of the >99,000 metal–organic frameworks[66] melt; however, progress has been made in the identification of further melting MOFs, including ZIF-62 $[Zn(Im)_{1.75}(bIm)_{0.25}]$ and TIF-4 $[Zn(Im)_{1.8}(mbIm)_{0.2}]$ with melting temperatures, T_ms, of 437 and 440 ˚C respectively.[65,67] Thus far, the common denominator between the known melting MOFs is that they all contain imidazolate linkers; evidence would also suggest that the crystalline framework's topology/density may influence its melting ability through the stabilisation of the cationic species in the melting mechanism.[67,68] Discovery of novel MOF glasses and the relationship between the known glass-formers is a burgeoning topic but is still in its infancy. As such, the thermal behaviour of only a small proportion of the total known MOF structures has been thoroughly investigated, and fewer have demonstrated the capability to form melt-quenched glasses.[69]

Differential scanning calorimetry (DSC) is a common thermal characterisation technique across material science, yet is seldom used to characterise MOFs (**Figure 12a**). The standard method of analysing thermal behaviour in these compounds remains thermogravimetric analysis (TGA), which monitors mass loss with temperature. However, this technique does not detect physical changes that occur without mass loss, such as recrystallisation. In one of the rare cases of the use of DSC, the first evidence of melting was reported for ZIF-4 at *ca.* 577 °C.[70] After cooling from the liquid state, a melt-quenched glass was obtained, which demonstrated ultra-high glass-forming ability.[65]

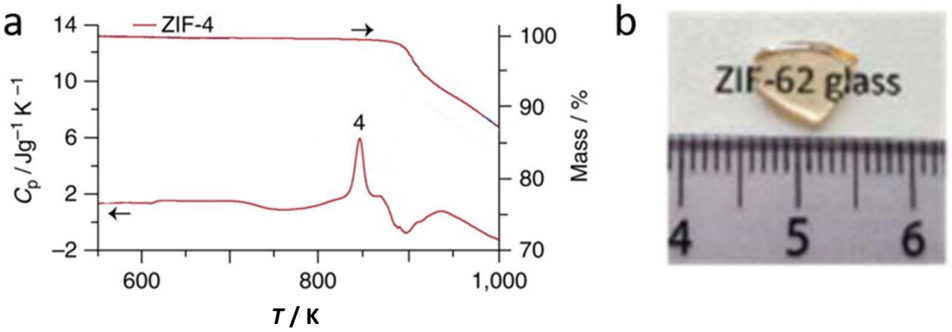

Figure 12: Discovery of the melting of MOFs. *a. DSC and TGA of ZIF-4 showing an apparent melting transition, T_m at point 4. Adapted from reference 70, and b. an optical image of a a_gZIF-62 sample, reproduced from reference 71.*

Given the number of atoms in the unit cell, and possible polymorphism, and metastability, crystalline MOFs are regarded as somewhat challenging to characterise. However, liquid and glass MOFs represent an increased challenge due to the lack of long-range structure. One method of extracting information about the structure of the glass is through modelling experimental data. Interestingly, as shown from the modelling of amorphous ZIF-4 (**Figure 13**), the imperfect packing caused by the SRO units' randomisation induces void spaces throughout the material. The void spaces, apparent in the reverse Monte Carlo (RMC) model, are consistent with gas sorption data, demonstrating that the MOF glasses may be porous to small gases (**Figure 13c**).[72,73] In a study using ZIF-76-mbIm, $Zn(Im)_{1.0}(5\text{-mbIm})_{1.0}$, the pore volume of the glass was observed to be 0.062 cm^3g^{-1} from 0.185 cm^3g^{-1} in the crystalline state.[73]

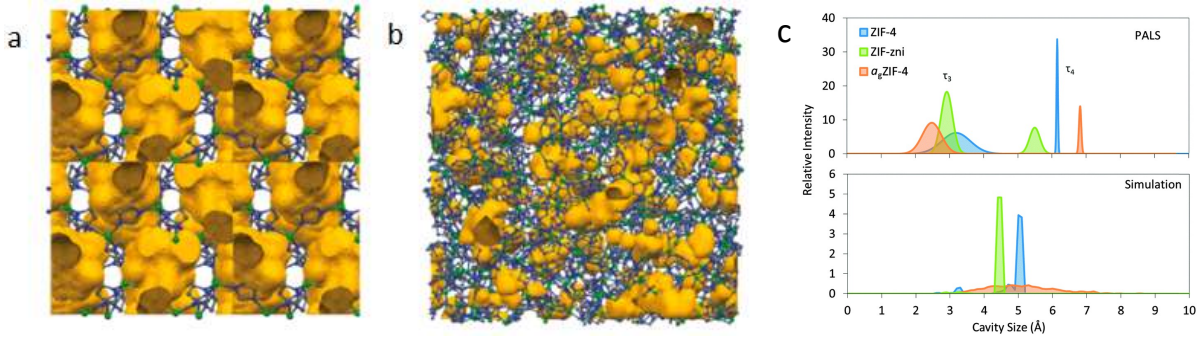

Figure 13: Simulated structures of crystalline and amorphous ZIF-4. *a. Crystalline ZIF-4 where the orange space represents free volume, b. Atomic configuration of a_gZIF-4 obtained by reverse Monte Carlo (RMC) modelling of synchrotron and neutron total scattering data where C – Grey, N – Blue, Zn – Green. Reproduced from reference 68. c. Cavity sizes of three ZIF-4 morphologies obtained through positron annihilation lifetime spectroscopy and simulation, reproduced from reference 74.*

MOF glasses also demonstrate a range of other properties, making them an excellent candidate for use as supporting material for other crystalline MOFs. Specifically, (i) a_gZIF-62 (ZIF-62 glass, **Figure 12b**) displays high optical transmittance in the visible and near infra-red regions (~90% from 400–1600 nm),[71] (ii) the refractive indices (1.56 at 589 nm) and Abbe number, *v*, (*ca*. 31) of the ZIF glass places the optical properties of a_gZIF-62 in a comparable region of the refractive index-Abbe number diagram to the upper range of polymers,[71] and (iii) the mechanical properties of ZIF glasses have been shown to demonstrate characteristics of both inorganics and organics and exhibit resistance to ductile fracture.[75,76] The

transparency of the material may provide a unique opportunity to view macrostructural defects such as bubbles or dislocations within the solid, which may impact performance. Such properties make a_gZIF-62 a promising host matrix for a crystalline MOF component, which would allow for the fusion of the optical and mechanical properties of the glass phase with the porous properties of the crystalline phase to form industrially suitable, contiguous solids.

1.4 Vision and Objectives

The overall aim of this work is to investigate the synthesis, structure and properties of a new class of metal–organic framework-based materials formed by combining the crystalline states of MOFs with newly discovered melt-quenched MOF glasses. The formation of functional, mechanically stable, monolithic materials would expand MOF science at a fundamental level and provide engineering solutions to the low mechanical processability of the microcrystalline MOF state by facilitating bulk material formation. The utilisation of porous glass may provide the necessary properties required to suspend a MOF into a stable bulk solid without impairing the properties of the crystalline component. To achieve this, specific aims and objectives for work detailed herein are as follows:

1. To select suitable crystalline MOFs and MOF glasses from the libraries available and fabricate a prototypical material that preserves the crystalline component within a supporting MOF glass matrix. This will involve careful consideration of the balance between the decomposition temperatures of crystalline MOFs and the liquid-phase temperature regions of glass-forming MOFs. It will also involve finding a suitable processing methodology to embed a crystalline MOF component within the glass state; adequate melting times and temperatures must be studied to identify a system that allows for adequate flow of the viscous, liquid MOF.
2. To investigate the suitability of the resultant materials for use with a variety of gases by contrasting the gas uptake properties of the pure crystalline materials against the resultant composites. Ideally, the supporting matrix should be permeable to the guest species, allowing diffusion of the gases to the crystalline component.
3. Investigate the composites' thermomechanical properties through nanoindentation and measure the response of both the isolated crystalline components and bulk composite materials to temperature.

Contrasting the crystalline MOF response between the isolated and the composited samples may aid in identifying potential effects on the crystalline MOF upon encapsulation. The determination of any leading effects such as intra-composite interactions—*e.g.* linker penetration—and understanding how the MOF is supported within the matrix helps determine their potential applications. This information would also serve to guide the development of further MOF composites. Before this work, **Chapter 2** presents an in-depth literature review focused on the literature's current state concerning the above aims and objectives.

Chapter 2 Literature Review

2.1 Crystalline Metal–Organic Frameworks

The majority of research on metal–organic frameworks (MOFs) studies their crystalline phases. This is due to several reasons; (i) The common misconception in the MOF field that MOFs are exclusively crystalline solids, (ii) amorphous materials are much more challenging to characterise, and (iii) crystalline frameworks generally exhibit lower densities and greater surface areas than their amorphous counterparts, which enables many of their potential applications.

2.1.1 Synthesis and Structure of Metal–Organic Frameworks

2.1.1.1 Solvothermal/Hydrothermal Synthesis

MOFs are supramolecular compounds formed *via* a process of self-assembly. They are synthesised using various methods, but most typically by heating the component reagents in a sealed container with a liquid. These methods are known as hydrothermal or solvothermal synthesis when using water or organic solvent, respectively. The assembly process is driven by coordination bonds with competing and templating interactions such as hydrogen bonding and π–π interactions.[77]

In a process known as isoreticular synthesis, alteration of MOF properties, such as pore diameter, is achievable by the careful selection of synthesis reagents. For example, a series of MOFs developed by Yaghi *et al.* named Isoreticular MOFs, or IRMOFs, were systematically synthesised to increase the distance between opposing corners of the hexagonal channels in the IRMOF-74 series up to a staggering 98 Å (**Figure 14**). This framework engineering feat was accomplished by constraining the topology-defining properties of the material, such as the connectivity of the metal nodes and the linearity and denticity of the organic linker, whilst increasing the linker length.[78]

This modular nature of MOFs has led to nearly 100,000 unique structures[39] and effectively enables the tunability of certain physical properties. This strategy is not applicable in all cases since the metal node may change to favour another configuration under the altered conditions. A further obstacle is that the framework may become unstable upon solvent removal and collapse.[79]

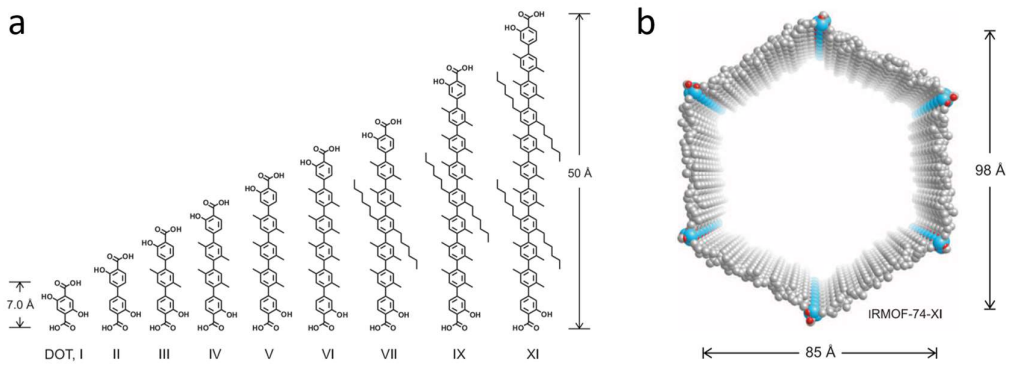

***Figure 14**: **Isoreticular synthesis and sequential pore-size increase of MOFs.** a. the systematic increase in linker length which retain crystalline topology, and b. representation of IRMOF-74-XI using the XI linker from a. C – Grey, Zn – Red, O – Blue. Adapted from reference 78.*

2.1.1.2 Alternate Synthetic Pathways

An environmentally-, economically-, and energetically friendly alternative to the synthesis of MOFs is the mechanosynthetic pathway. This technique employs the mechanical milling of the MOF precursors at room temperature, often without solvent—or in some cases using µL volumes, to produce MOFs in a matter of minutes rather than days.[80,81] Whilst it is possible to use a mortar and pestle, mechanical mills are preferred for their reproducibility and systematic studies.[82] The solventless aspect of mechanosynthesis is vital for industries that deal directly with foods or medicinal products since toxic solvents such as *N,N*-dimethylformamide (DMF), or methanol, are required for the preparation of many MOFs.[83]

The first study to monitor the *in-situ* mechanochemical milling reactions took place in 2013, where custom equipment was designed by Friščić *et al.* to allow reaction jars to be placed in the path of high-energy synchrotron X-ray beams whilst the reaction was taking place.[84] Quantitative X-ray diffraction analysis of the reaction products using Pawley and Rietveld refinements allowed for the real-time observation of product crystallinity, crystal phase, and average particle size. The first experiments to be performed in this setup were the reactions of ZnO with 2-methylimidazole (HmIm) to form ZIF-8, $Zn(mIm)_2$, by means of liquid-assisted grinding (LAG), and ionic liquid-assisted grinding (ILAG). Interestingly, the use of 3 mol% NH_4NO_3 was shown to dramatically improve the rate of reaction in the formation of ZIF-8 (**Figure 15**).

Another notably environmentally friendly synthetic pathway is the use of microwave irradiation to synthesise MOFs.[85] This route also does not require the application of high temperatures as with hydro/solvothermal reactions but instead generates heat through dipole rotation and ionic conduction mechanisms. The best solvents for use in microwave synthesis are, therefore, water or ionic liquids with high dipole moments as these molecules attempt to align themselves with the magnetic component of the oscillating waves, translating to physical heating. This technique provides multiple advantages such as (i) short reaction times, (ii) fast crystal nucleation, (iii) fast crystal growth, and (iv) high product yields.[86,87]

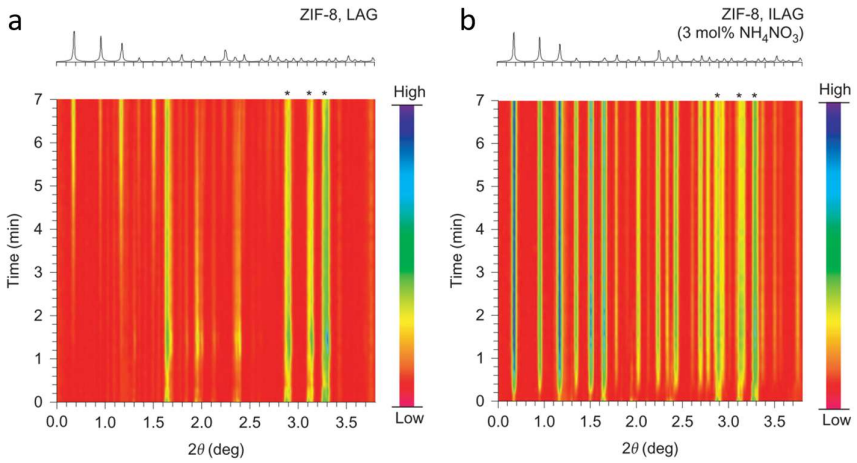

***Figure 15**: **X-ray diffraction tracked synthesis of ZIF-8 by ball-milling.** Time-resolved diffractogram for the a. liquid assisted grinding (LAG), and b. ionic liquid-assisted grinding (ILAG) of ZIF-8. Reproduced from reference 88.*

2.1.1.3 Synthetic Challenges

2.1.1.3.1 Interpenetration

One of the limits of isoreticular synthesis is apparent when preparing MOFs with extremely large pore volumes, and particularly those with cubic topologies. A process known by many names: catenation, interpenetration, intrapenetration, or polyknotted coordination,[89] is where two or more frameworks are built around each other, intertwined and locked together.[90] The entangled frameworks are formed such that breaking bonds would be required to separate them. The cubic IRMOF-1 to IRMOF-16 series designed by Yaghi *et al.* (**Figure 16**) to improve methane storage capabilities clearly demonstrates this phenomenon. Interpenetration can be seen for samples of IRMOF-9 and above, where the pore volume is large enough to accommodate the synthesis of another framework within its pores.

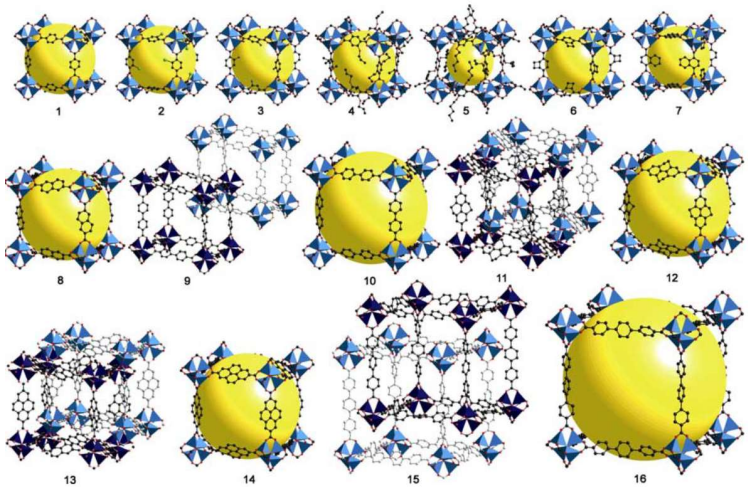

***Figure 16**: **Induction of interpenetration through increasing pore size.** A series of IRMOFs where the topology of the framework has been kept constant but the functionalities (IRMOF-1 to IRMOF-7) and the distances between carboxylate groups (IRMOF-8 to IRMOF-16) have been altered. Pore volume represented by yellow spheres. C- Black, O- Red, Zn represented by blue pyramids, H – Omitted. Adapted from reference 91.*

Interpenetration is a process that is often actively avoided due to an inherent decrease in the pore volume of the material.[92] In MOF synthesis, materials are typically completely interpenetrated or entirely non-interpenetrated, and thus, care must be taken concerning the synthesis conditions.[93] However, examples do exist of partial interpenetration, which is a strategy employed to confer new physical properties of MOF materials.[94] For example, Ferguson *et al.* demonstrated controllable dependence of partial interpenetration in MUF-9, ZnO_4(*rac*-1)$_3$ (*rac*-1 = biphenyl-4-4'-dicarboxylic acid with a phenyl-substituted diazocine bridge), on the quantity of DMF in the reaction medium.[94]

2.1.1.3.2 MOF Activation

It is commonly observed that after synthesis, the pores of the framework are occupied by solvent and unreacted linker, together with other impurities. The removal of such species *via* heating or vacuum treatments is called framework "activation". There are various methods designed to remove guest molecules from the pores of permanently porous MOFs whilst retaining their structural integrity, which is comprehensively described by Mondloch *et al.*.[95] The conventional method remains the use of a vacuum with heating,[96] however, this technique is not applicable to all MOFs—especially those with larger pore volumes—due to a balance of capillary force strength and surface tension against the coordination bond strength.

An alternative method to remove guest molecules from MOFs that collapse under vacuum heating is through a method known as solvent exchange. Here, the MOF is submerged in a solvent with a lower boiling point than the synthesis solvent and allowed time to dissolve pore occupying species into the solvent. This diluent solvent is periodically replaced to extract as much excess material from the MOF as possible. The lower boiling point of the solvent is indicative of weaker intermolecular interactions which require lower temperatures to evaporate. This allows the framework to be activated at much lower temperatures.[95] This is a common technique to activate MOFs, as the process of exchanging solvents often removes any other unwanted impurities such as excess ligand that may be strongly adsorbed to the internal surfaces of the MOF. Activation of a material is typically confirmed using thermogravimetric analysis (TGA), which measures the mass of the sample over a temperature range (See **Section 3.1.7**).

2.1.2 Zeolitic-Imidazolate Frameworks

Zeolitic imidazolate frameworks (ZIFs) are a subset of MOFs which include imidazolate (Im, $C_3H_3N_2^-$) or imidazolate-based linkers within the framework. The tetrahedral metal nodes of these materials are connected by organic ligands with bond angles similar to the M–O–M bond in inorganic zeolites (**Figure 17a,b**). Resultantly, many of these frameworks are isostructural with zeolites, replacing the bridging oxygen with organic ligands (**Figure 17c**).[97] ZIFs are highly porous MOFs,[97] and have been investigated for their gas separation potential, membrane potential, application in catalysis as a support for nanoparticles, sensing capabilities, and drug delivery applications.[98]

The prototypical example of a ZIF is ZIF-8 [Zn(mIm)$_2$; mIm: 2-methylimidazolate, $C_4H_5N_2^-$] (commercially known as Basolite Z1200) which is a homoleptic MOF that adopts a sodalite topology as shown in **Figure 17**. Due to its ease of synthesis and exceptional porosity, ZIF-8 has been investigated for all of the aforementioned applications.[99–103] Many members of the ZIF family have been empirically shown to exhibit relatively exceptional chemical and thermal stabilities among MOFs.[104]

They are thus more able to be employed at higher temperatures than what would be expected, on average, for the wider MOF family.

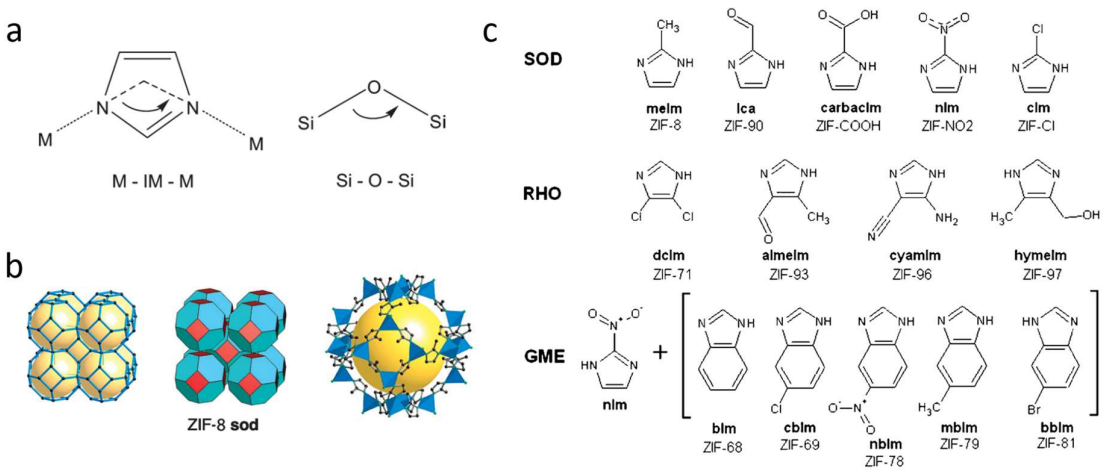

***Figure 17**: **Similarities in the bonding and resultant structures of ZIFs and zeolites.** a. An illustration of the similar 145° angle of M–Im–M to Si–O–Si, b. atomic configuration of ZIF-8 shown as i) stick diagram ii) tiled diagram iii) largest cage in the ZIF with ZnN_4 tetrahedra in blue and the internal pore volume represented by a yellow sphere. Adapted from reference* 104*. c. List of various imidazole based linkers and their resulting topologies. Adapted from reference 105.*

2.2 Physical Properties of MOFs

2.2.1 Gas Adsorption Properties

As one of their most heavily researched applications, MOFs are highly regarded for their ability to store gases. Gas storage techniques are highly sought after to improve the space efficiency of gas transport at safe working temperatures and pressures. The current view to achieving this is through the adsorption of gases to the surfaces of highly porous materials. The development of containers that efficiently densify gases to manageable volumes is crucial in the green future of hydrogen fuels.[106] Since MOF materials are the current record holders for recorded specific surface areas (*i.e.* surface area per gram), there has been much interest in the use of MOFs for such a purpose. The ability to tune the properties of MOFs enables the development of materials with greater porosity by altering the topology, pore diameter, and functionality of the linker. Furthermore, structural defects such as missing linkers or clusters are well-known to exist in MOFs and may be controlled to tune porosity.[107] Disorder may also be introduced into the structure in a top-down approach, such that the porosity may be controllably reduced to meet specific porosity requirements.[108]

Perhaps one of the most outstanding records of the progress in this area is a benchmark computational study on a range of MOFs delineating the relationship between pore volume, Brunauer-Emmett-Teller (BET, see **Section 3.1.9**) surface area, and gravimetric deliverable hydrogen gas capacity in MOFs.[109] This study revealed that the copper-based hexacarboxylate NU-125 MOF[110] achieves an exceptional 8.5 wt% gravimetric hydrogen storage, surpassing the ultimate

U.S. department of energy target (6.5 wt%) under temperature and pressure swings of 77 to 160 K and 100 to 5 bar, respectively.

In addition to the ability to store gases, the controllable pore diameter of MOFs allows for the separation of gas mixtures through both molecular sieving and chemical affinity. Molecular sieving is an exclusionary process whereby molecules that cannot diffuse through the material pores are filtered from a mixture.[111] The tunable pore size of MOFs may allow for the controllable molecular separation of materials based on their physical size. The separation of materials *via* their chemical affinity to a structure relies not on the gated external permeability but through the physisorption interactions formed whilst the components diffuse through the material. A material may unequally retard the diffusion of components within a mixture based on differing sorbent-adsorbate affinities, separating mixtures based on their diffusion rates.

Commercially important gas separations include CO_2/N_2 (flue gas separation), CO_2/CH_4 (natural gas purification), H_2/N_2 (hydrogen separation), O_2/N_2 (air separation) and N_2/CH_4 (natural gas purification) separations.[112] These separations are typically performed using cryogenic distillation[113] adsorbents, or polymer membranes—over 90% of which are made from only six different types of polymers.[114] However, these polymers display selectivity-to-permeabilities orders of magnitude lower than those of MOFs (**Figure 18**). Replacing current distillation technology—which accounts for roughly a quarter of U.S. industrial energy consumption—with membranes would reduce their energy consumption by 90%.[115] However, the scalability of MOF synthesis and unknown long-term stability within industrial settings—especially in the presence of water vapour—are key limiting factors to their application.[112]

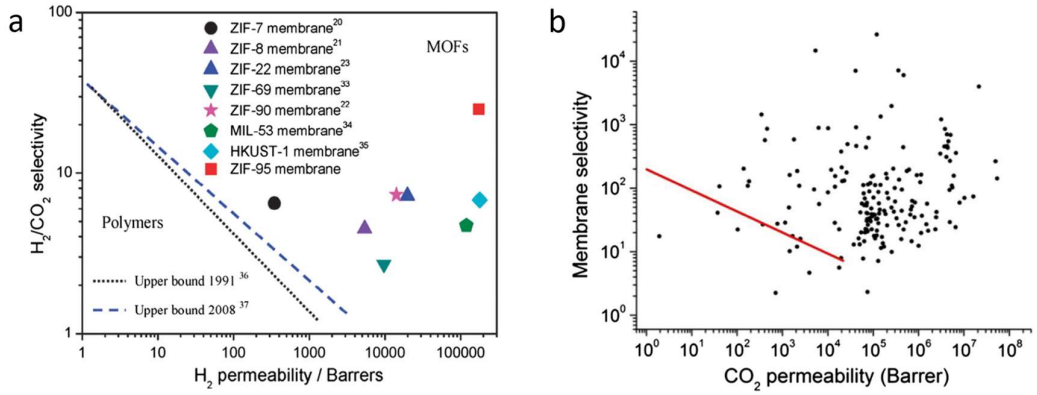

***Figure 18*: Comparison between the selectivities and permeabilities of MOFs and polymers.** *a. Exceptional selectivity and permeability of a range of MOF membranes, surpassing the upper bounds of polymer membranes. b. Calculated CO_2/N_2 membrane selectivity vs. CO_2 permeability for 179 MOFs at 303 K. The solid red line indicating the upper bound for polymeric membranes. Reproduced from reference 112.*

2.2.2 Thermal Stability

Metal–organic frameworks are also known as 'soft porous crystals' due to their reportedly relatively weak thermal and mechanical stabilities.[116] However, the variability in the makeup of MOFs allows for a wide range of exhibited properties complicating their generalisation. The thermal stability of MOFs is composition- and structure-dependent, with MOF

families showing various ranges stabilities in the range of *ca.* 150–600 °C (**Figure 19**). However, the exact thermal stability is a result of the interplay between the ligand and node stabilities.

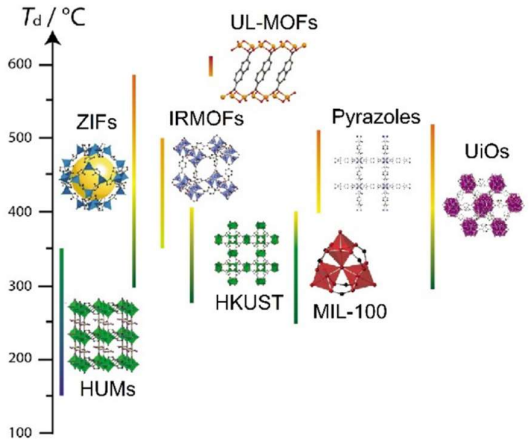

***Figure 19**: **The relative thermal stabilities of a range of distinct MOF families**. Data collated from the reported decomposition temperature values as measured by TGA. Reproduced from reference 117.*

A recent study presented two categories of MOF thermal decomposition pathways: ligand-centred and node-centred decomposition, noting that such processes are not strictly independent and governed by the relative stability of the MOF components.[117] The ligand-centred decomposition mechanism, common in carboxylate MOFs such as MOF-5, and UiO-66, involves fragmentation of the metal–oxygen, oxygen–carbon, and carbon–carbon bonds. This process results in the release of CO_2 and fragments of the organic linker, occurring at *ca*. 500 °C. In contrast, node-centred decomposition, exhibited by both HKUST-1, Cu(btc) [btc – 1,3,5-benzenetricarboxylate], and MIL-100, $Fe_3O(H_2O)_2OH(btc)_2$, involves decoordination of solvent molecules coordinatively bound to the metal nodes preceding the formal decomposition. This may distort the framework, weakening intra-ligand bonding and resulting in ligand fragmentation. The temperature stability of a MOF is not the only interesting thermal property of MOFs, but also *how* the material behaves upon heating.[117]

2.2.3 Thermal Expansion

Understanding the exact thermal expansivity profile of a system is a crucial property that may govern its applicability. In one prominent example, it is believed that the unaccounted-for volumetric thermal dependency of a single O-ring was responsible for the catastrophic failure of a 1986 NASA rocket, 73 seconds after liftoff, in an event dubbed the Space Shuttle Challenger Disaster.[118]

For metals and many densely packed materials, thermal expansion is governed by the extension of interatomic bonds. This is illustrated in the Morse potential energy curve, which accounts for attractive and repulsive forces affecting the average internuclear separation of two bonded atoms (**Figure 20**). These forces cause divergence from a standard harmonic system. The resultant asymmetric curve details a change in the average internuclear separation of the bonded pair as a function of temperature.

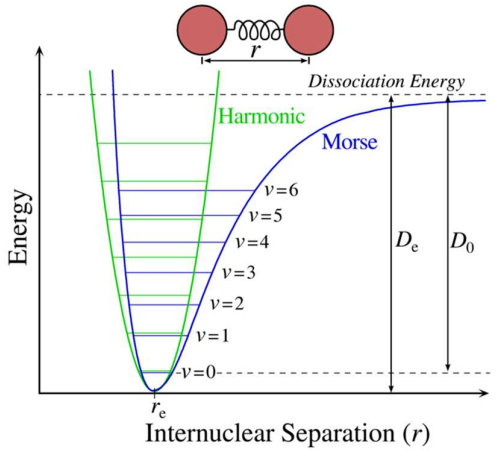

***Figure 20*: Morse potential curve illustrating the anharmonicity of atomic bond vibrations.** *In this diagram the Morse potential (blue) behaves like a realistic diatomic system and asymptotes to a dissociation energy D_e. This energy is slightly larger than the energy required for dissociation, D_0, due to the zero-point energy at the lowest vibrational state. Reproduced from reference 119.*

The degree to which the real system diverges from the harmonic model is inversely proportional to the atomic pair's bond strength, such that covalent bonds typically expand less than ionic or metallic bonds. Measurement of expansion using a bulk material is complicated by the connectivity/topology of the structure. Thermally induced chemical interactions within the material and higher-order movements within the structure may impact the volume/expansivity of the material. A typical example of a higher-order structural rearrangement within a framework is the ”breathing” behaviour of MIL-53, Al(OH)(BDC). MIL-53 is a well-characterised MOF that exhibits both thermal and pressure-induced reversible volumetric expansion and contraction.[120]

This framework undergoes a reversible structural adjustment upon solvent removal or heating, in a process is known as “breathing”. MIL-53 has three structural arrangements (**Figure 21**).[121] MIL-53 crystallises in a “winerack” structure with large internal pores held open by excess solvent and unreacted ligand in the as-synthesised state (MIL-53-as, *Pnma*). When the pore-occupying species are expelled, typically by heating, an open-pore structure (MIL-53-lp, *Imma*) is formed which is stable at high temperatures. The spontaneous uptake of water into the MIL-53-lp phase, typically upon cooling, causes the pores to contract to produce a narrow-pore structure (MIL-53-np, *Cc*). MIL-53-np may reversibly transition to the MIL-53-lp phase in a process known as “breathing”. This transition induces colossal changes in the structural volume, which would not be possible through bond stretching alone.

***Figure 21: Diagram of the activation process of MIL-53 and the transition between different states**. The as-synthesised MIL-53 material, MIL-53-as, may be activated through the MIL-53-lp state and cooled to the MIL-53-np state via the uptake of water. C, grey; O, red; Al, pink; H, omitted for clarity; solvent, purple. Reproduced from reference 122.*

In principle, the Morse potential diagram will always detail an increase in bond length with temperature; however, complex structural rearrangements within a material—especially in porous materials—may be thermally induced, leading to material contraction on heating. In contrast to the large positive thermal expansions observed in MIL-53, colossal contractions, called negative thermal expansion (NTE), are also observed in a selection of MOFs (**Figure 22a**). Notably, the introduction of defects into UiO-66(Hf), $Hf_6O_4(OH)_4(O_2C\text{-}C_6H_4\text{-}CO_2)_6$, through the use of formic acid modulator, has been shown to lead to the colossal NTE behaviour of the structure upon elimination of the formate ligands as a result of distortions to the Hf_6 metal node octahedra (**Figure 22b**).

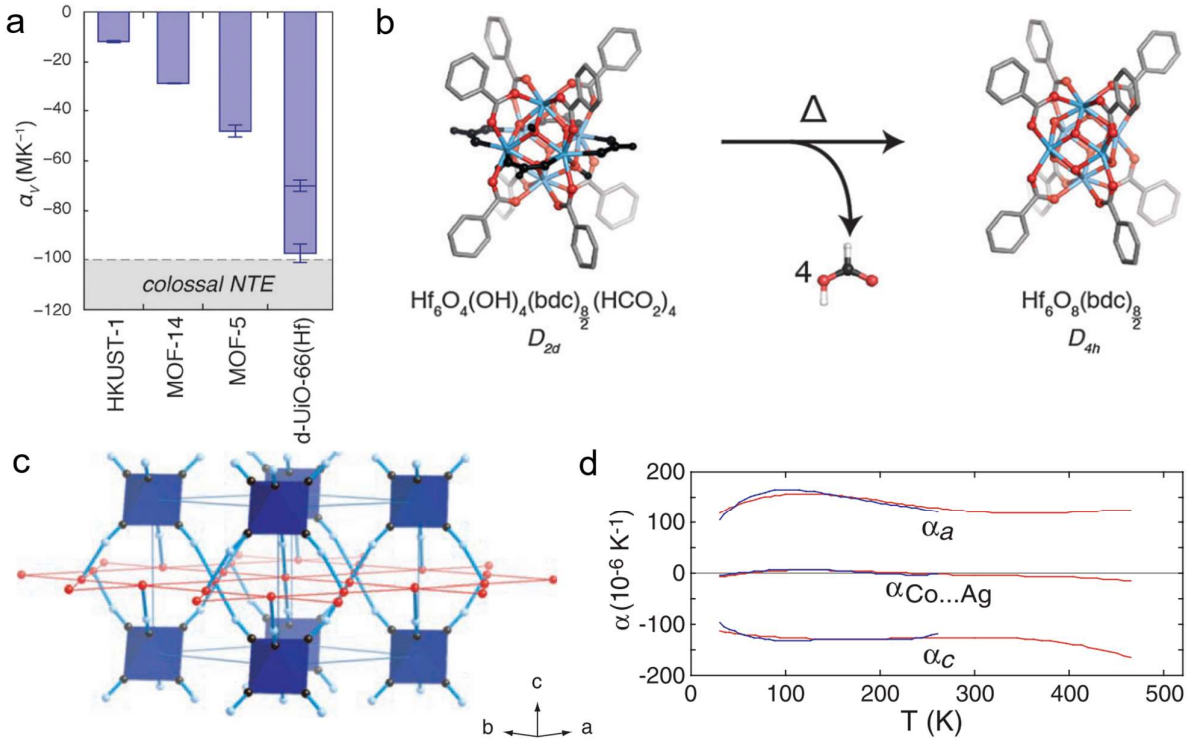

***Figure 22*: The thermal expansion values and mechanisms for a selection of framework materials.** *a. Coefficients of thermal expansion for a selection of known isotropic negative thermal expansion MOFs. The two values given for densified-UiO-66(Hf) correspond to upper and lower defect concentrations. b. Elimination of formic acid modulator (black) from the UiO-66(Hf) metal node. Hf, blue; O, red; and C, grey. Reproduced from reference 123. c. Trigonal lattice of $Ag_3[Co(CN)_6]$, CoC_6 octahedra, blue; Ag^+ cations, red. d. The linear coefficients of thermal expansion for the lattice parameters of $Ag_3[Co(CN)_6]$ together with a polynomial (n=5) fit of experimental data. Reproduced from reference 124.*

The value by which the measured expansivity is compared is the coefficient of thermal expansion, α_v, which can be expressed in **Equation 1**, where *V* is the cell volume.[125] The mean value of dV/dT may be determined by extracting the gradient from a linear region of a volume-temperature plot or differentiating a second-order polynomial fit. Similarly, the linear coefficient of thermal expansion of each unit cell parameter, *e.g.* α_a may be determined from the *a* parameter as in **Equation 2**.

$$\alpha_v = \frac{1}{V}\left(\frac{\delta V}{\delta T}\right)_P \qquad \textit{Equation 1.}$$

$$\alpha_a = \frac{1}{a}\left(\frac{\delta a}{\delta T}\right)_P \qquad \textit{Equation 2.}$$

Values of thermal expansion in **Figure 22a** represent isotropic values of volumetric change, which only describe the effective volumetric change arising from change over the three spatial dimensions. It is often helpful to study the uniaxial expansion over the crystallographic axes, as in **Figure 22c,** which displays simultaneous colossal positive and negative thermal expansion over two orthogonal axes (**Figure 22d**).

This type of analysis is performed using variable temperature powder X-ray diffraction (VT-PXRD, see **Section 3.1.2**) and provides detailed structural information about the mode of expansion of known crystalline systems. However, for systems that lack long-range order, this analysis must take place on a bulk scale using techniques such as thermomechanical analysis (TMA, see **Section 3.1.12**); TMA is a bulk measurement that records the net macroscale movements that occur within a sample as a representation of the expansivity. This technique is instrumental in studying the expansion of disordered crystalline, amorphous, or glass systems.

2.2.4 Mechanical Properties

Other material properties of concern relate to the material's mechanical stability and response to physical stimuli on a bulk scale. For the application of bulk samples, it is critical to understand how a material behaves under operating conditions to avoid catastrophic failures. One notable example of this is the RMS Titanic which, during its 1912 maiden voyage through the North Atlantic Ocean from Southampton to New York City, struck an iceberg. Later analysis of the hull steel quality would reveal that the material used, although likely the best available at the time, had a high ductile-brittle transition temperature, making it unsuitable for use at low temperatures. Among other issues, the steel brittleness at the freezing –2 °C ocean temperature would be partially responsible for this disaster.[126]

Typical methods to investigate mechanical properties are tensile and compression tests that involve applying uniaxial stress to a length of material to extract stress-strain relations that describe a range of material characteristics. There are typically two regimes of material deformation in a stress-strain graph: elastic and plastic deformation; the presence, gradient, area, and transition of these two regimes define specific material characteristics. The typical initial region of material response to applied stress is through *elastic deformation* (**Table 2**). This region is where macrostructural movements occur without breaking atomic bonds to accommodate the induced stress. This is a reversible process, and on the release of the applied stress, the material will return to its original shape following Hooke's law. The relationship between stress and strain in this region is known as Young's modulus, *E*, which is an important parameter that may be used to determine how much a material may shorten or lengthen under respective compressive or tensile loads (**Figure 23a,b**). Materials with greater values of *E* are said to be *stiffer*, describing a greater resistance to deformation.

On applying greater stresses, a material may begin to deform inelastically in a region known as *plastic deformation*. In this region, bonds are broken, and the material is irreversibly deformed. The point at which the material begins to deform

plastically is called the yield strength and is useful to determine the maximum load a material may withstand without permanent deformation. However, not all materials undergo plastic deformation, instead fracturing at much lower strains; these are called *brittle* materials and exhibit low resistance to crack propagation, such as SiO_2 glasses. For materials that exhibit greater resistance to crack propagation and undergo considerable plastic deformation, such as steel (**Figure 23**), fracture occurs at much larger stresses and are called *ductile* materials. Many other critical mechanical properties, such as creep, fatigue, and fracture toughness, may be determined using a range of other techniques and equipment but are out of the scope of this research (**Table 2**).

Table 2: A list of relevant material properties.

Characteristics	Symbol	Definition	Units
Stress	σ	A physical property measuring the internal forces of neighbouring particles in resistance to applied loads	N/m^2 (Pa)
Strain	ε	The total deformation in relation to the initial dimension of the material, parallel to the applied force	
Young's Modulus	E	A measure of material stiffness, quantified by the change in strain upon application of stress during elastic deformation	N/m^2 (Pa)
Bulk Modulus	K	The materials' ability to resist compression, calculated as the inverse of the gradient on a pressure-volume graph multiplied by the negative of the volume	N/m^2 (Pa)
Poisson Ratio	ν	The materials' expansion or contraction perpendicular to expansion or contraction in the direction of the applied load	N/m^2 (Pa)
Elastic Deformation		Deformation of a material that is reversed when the load is removed	
Plastic Deformation		Deformation of a material that is not reversed when the load is removed	
Hardness	H	The materials' ability to resist plastic deformation	N/m^2 (Pa)
Stiffness	k	The materials' resistance to deformation calculated as the force per unit of axial extension under tensile load, or contraction on compressive load	N/m
Compliance		The inverse of stiffness	m/N
Yield Strength	σ_{ys}	The point in a stress-strain curve that indicates the end of elastic behaviour	N/m^2 (Pa)
Ultimate Strength	σ_{uts}	The greatest stress observed during a tensile test	N/m^2 (Pa)
Toughness	U_t	The materials' ability to absorb energy up to fracture, calculated as the area under the stress-strain curve	N/m^3
Resilience	U_r	The materials' ability to absorb energy during the elastic region of deformation	N/m^3
Brittleness		A measure of the materials' lack of ability to deform plastically before fracture. Brittle materials display much greater compressive than tensile strengths and fracture at small strains	
Ductility		A measure of the materials' ability to deform plastically before fracture. Ductile materials display similar compressive and tensile strengths and fracture at large strains	

Whilst tensile and compression tests are standard practice for the characterisation of bulk materials, the microcrystalline nature of MOF materials has, so far, precluded such analysis using this technique. A technique developed for such analysis is nanoindentation which, briefly, indents a diamond tip of known dimensions into the surface of a sample, measuring the indentation depth with respect to the applied force (see **Section 3.1.5**). Additionally, high-pressure X-ray experiments using a diamond anvil cell have been utilised to extract properties such as the bulk moduli.[55,127,128]

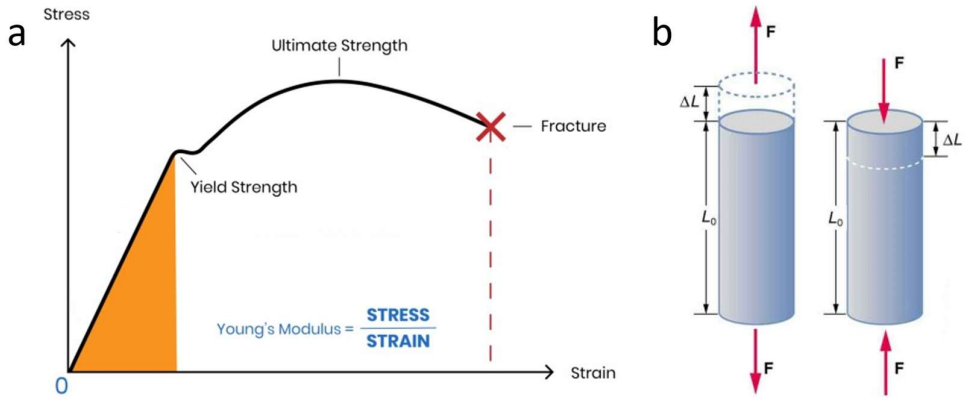

***Figure 23*: A typical stress-strain graph for steel.** *a. This diagram demonstrates how to measure fundamental material properties such as the Young's modulus and yield strength. This material undergoes regimes of both elastic and plastic deformation. Adapted from reference 129. b. Diagram of the extension and compression, ΔL, of a rod under respective tensile (left) and compressive (right) loads, F, applied to a length of material, L_0. The Young's modulus gives the relation between the force and change in length. Reproduced from reference 130.*

Due to the requirement of specialised equipment, the study of mechanical properties is not routine in the MOF field. Nevertheless, studies of these properties on a variety of MOF materials provide sufficient information regarding their general mechanical properties. Though average measurements from nanoindentation studies reveal valuable data, the anisotropic nature of MOF systems effects orientation-dependent property values, as demonstrated through molecular dynamic simulations.[131] Furthermore, the diverse selection of component materials combined with the numerous topological configurations with various symmetries imparts unique orientation-property profiles. However, of the compiled MOF bulk moduli detailed in reference [132], crystalline MOF samples were observed to occupy overlapping regions of bulk moduli, in relation to their density, with regions of foams, polymers, and zeolites as well as occupying their own region of material space (**Figure 24a**).

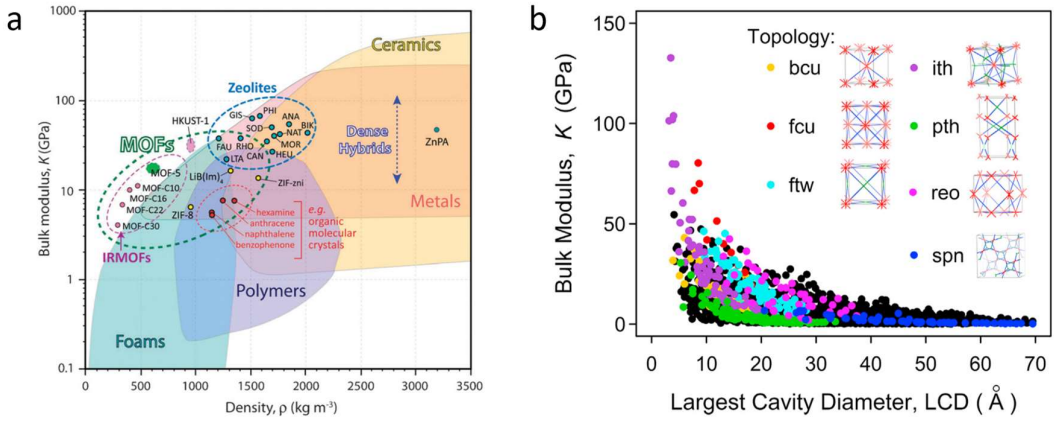

***Figure 24*: Comparison between the bulk modulus of MOFs and other materials in a similar area of material space related to how this property correlates with its largest cavity diameter.** *a. Ashby-style plot of bulk modulus-density profile of MOFs in relation to a variety of other materials, reproduced from reference 132. b. Machine learning calculations of MOF bulk moduli with respect to their largest cavity diameter, reproduced from reference 133.*

To address the void of unknown mechanical properties within the vast number of known MOF structures, it would require enormous quantities of time and resources to synthesise and measure each material individually. Instead, one group applied machine learning in combination with molecular dynamics simulations to extract bulk moduli of a variety of MOF systems with common topologies (**Figure 24b**).[133] This work provides key data to extract structure-property relations within MOF systems, such as an apparent inverse correlation between the bulk modulus and the diameter of its largest cavity.

On application of pressure, the specific mode of elastic deformation in these materials is unique to the framework but typically arises from intermolecular bond stretching or rotation. As described previously, in the case of MIL-53, the application of pressure along defined orientations causes macrostructural pore-size dynamics, driving the opening or closing of the pores. Further applied pressures to the yield strength of a MOF typically indicates an irreversible pore collapse and further rupture of intermolecular bonding upon plastic deformation of the sample. If crystallinity is desired in the product, analysis and consideration of the material strength should be taken to avoid unwanted structural deformation.

2.3 Amorphous Metal–Organic Frameworks

It was widely believed that MOFs were exclusively crystalline materials despite no mention of crystallinity in the International Union of Pure and Applied Chemistry (IUPAC) definition of a MOF, reported in 2013—"A metal–organic framework, abbreviated to MOF, is a coordination network with organic ligands containing potential voids".[134]

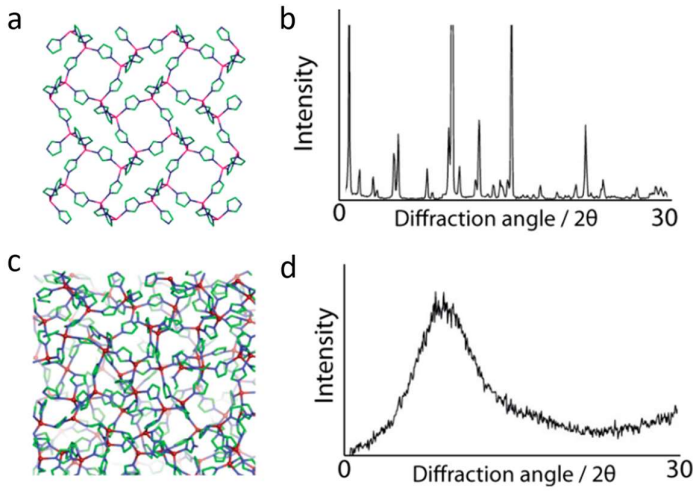

***Figure 25**: **Powder diffraction difference between crystalline and amorphous samples.** Atomic configuration and corresponding PXRD patterns of a–b. ZIF-1 [$Zn(Im)_2$], and c–d. aZIF-1 (of comparable size). C – Green, N – Blue, Zn – Red. Adapted from reference 52.*

Nevertheless, the synthesis of crystalline structures is deemed to be highly desirable, and with the absence of assignable diffraction peaks in amorphous structures, these systems may have been erroneously discarded as failed synthesis products. The PXRD profile of the amorphous state is often the first indicator of amorphisation in a structure. The loss of

Bragg peaks and the production of a broad hump called a first sharp diffraction peak (FSDP) indicates the loss of a periodic arrangement of atoms within the structure as shown for ZIF-1, $Zn(Im)_2$ (**Figure 25**).[*1]

Amorphisation is often an irreversible process for MOF systems such as ZIF-8, $Zn(mIm)_2$,[135] and MOF-5, $Zn_4O(BDC)_3$.[136] In the process of thermal amorphisation, some imidazolate complexes undergo partial decomposition to form the amorphous $M^{II}(Im)_2$ product.[137,138] However, the loss of structural components is not a pre-requisite for amorphisation, as demonstrated by a family of zinc tris(4-pyridyl)triazine frameworks, and zeolitic imidazolate frameworks.[54,139]

2.3.1 *a*MOF Nomenclature

MOFs may be amorphised by a variety of means, and the distinction between materials derived by such methods are detailed in **Table 3**. The introduction of this material nomenclature is often useful when discussing the difference between amorphous materials prepared by various means. However, this is not an exhaustive list, and other novel methods such as X-ray exposure may also induce amorphisation in MOFs.[140]

***Table 3**: **Nomenclature of amorphous MOFs.** Adapted from reference 141.*

Method of amorphisation	Product terminology
Pressure	a_PMOF
Ball-milling	a_mMOF
Heating[a]	a_TMOF
Melt-quenching	a_gMOF
Hot-pressing	a_{gp}MOF
Re-melting	a_{gr}MOF

[a] Thermally amorphised and melt quenched glass MOFs are distinguished by the presence or absence of a liquid state before glass formation. The latter is formed by quenching a liquid state, whilst the former does not involve the formation of a liquid state. The use of a_T to describe (amorphous solid) MOFs by heating was introduced several years before the discovery of the melt-quenched state.

2.3.2 Pressure-Induced Amorphisation

The application of pressure to amorphise a structure provides a mechanical stimulus that stresses the framework beyond its elastic limit, plastically deforming the structure by breaking bonds. In some cases, the structural damage may induce atomic reconfigurations leading to the production of amorphous MOFs. Though research has pointed to interesting phenomena in the application of hydrostatic pressure, where behaviour is largely dependent on the molecular size of the pressure-transmitting fluid,[127] this section will only concern the application of uniaxial pressure.

[*1] *Care must be taken not to confuse the amorphous profile for nanometre-sized crystalline particle—known as nanocrystalline—samples that display similar X-ray profiles with no clear Bragg peaks.*[298] *The deconvolution of the two can be performed using total-scattering pair distribution function (PDF) analysis (see **Section 3.1.4**).*

Shaping MOF materials by compression is a common technique for the compaction of MOF powders into usable pellets. However, this can cause amorphisation or loss of crystallinity even at low pressures. Compaction was found to prohibitively affect the catalytic performance of HKUST-1 at only 0.4 GPa, with notable reductions for ZIF-8 and SIM-1 at similar pressures.[142] The pressure required to totally amorphise ZIF-8 through compaction was studied by Chapman *et al.* where complete loss of Bragg peaks was induced at less than 1.2 GPa pressure.[135] This is, however, an order of magnitude greater than the pressure required to amorphise a sample of MOF-5, which does so at an extremely low pressure of 3.5 MPa.[136]

Ball-milling is another method used to amorphise structures; this technique is a distinct form of pressure-induced amorphisation due to the unique pressure application method. In contrast to the uniaxial pressures exerted in the previously discussed examples, ball-milling adds an element of shear force to the applied mechanical stresses. While this mechanosynthetic technique may assemble crystalline MOF structures from building blocks, the applied kinetic energies can also displace atomic bonds within the structure. One example of this is the ball-milling of ZIF-8, which induces amorphisation (**Figure 26**). Another example of such a system is ZIF-4, $Zn(Im)_2$, which may be both synthesised, amorphised, and recrystallised through mechanical force (**Figure 26**). As demonstrated by Bennett *et al.*, the energy input method can directly influence the navigation between physical states in this system.[54] It is clear that mechanically milling the structure provides a unique method of energy transfer that cannot be achieved by temperature alone.

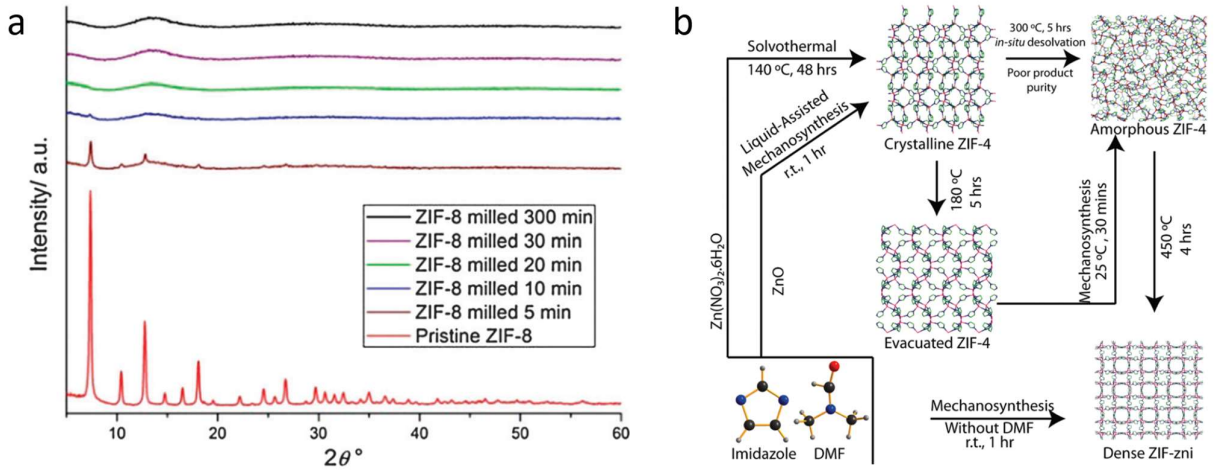

***Figure 26**: **The mechanosynthetic amorphisation of ZIF-4 and ZIF-8.** a. Amorphisation of ZIF-8 through ball-milling for 5–300 minutes, reproduced from reference 143. b. The synthetic pathways in the formation of ZIF-4, a-ZIF-4, and ZIF-zni structures through thermally- and mechanically-induced transitions, reproduced from reference 54.*

The amorphisation of ZIF-8 by ball-milling was further studied by Friščić *et al.* through *in situ* diffraction studies which revealed that the rate of amorphisation can be controlled by modulating both the concentration and quantity of the added liquid medium.[84,88,144] Additionally, further ball-milling of the ZIF-8 structure induced recrystallisation through a dense *kat* phase to a more dense *dia* phase (**Figure 27**). The order of structural transformations observed in this study reveals that stepwise transitions are driven by the formation of increasingly stable solid phases, following Ostwald's rule of stages. This rule, reported in 1897, states that during crystallisation, the system moves through minimal changes in

free energy, implying the first isolated product in crystallisation is the least thermodynamically stable polymorph.[145,146] What this suggests is that for both ZIF-4 and ZIF-8 polymorphs, the amorphous phase is not the lowest thermodynamically stable polymorph despite holding the greatest structural entropy.

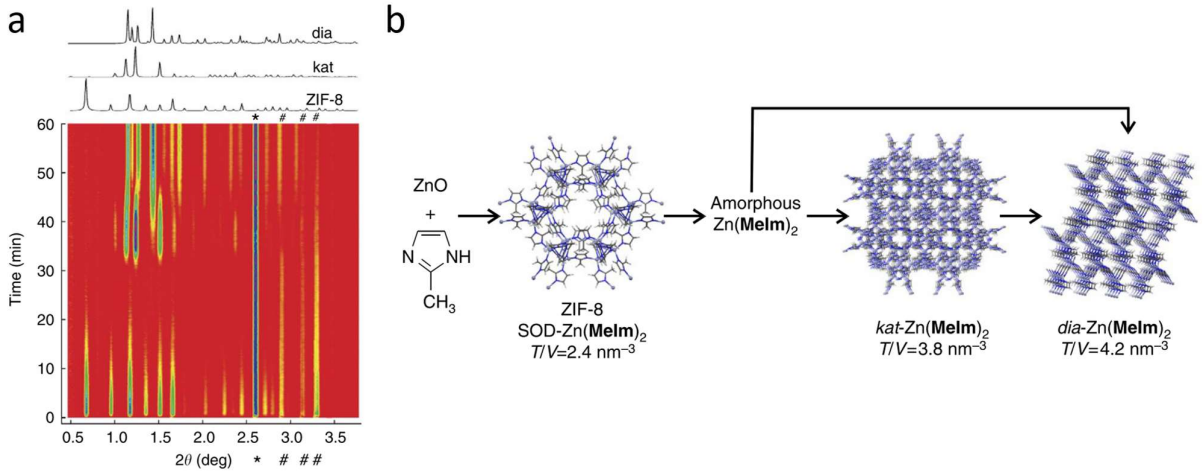

***Figure 27**: **The structural transformations of ZIF-8 via ball-milling**. a. time-resolved diffractogram, and b. structural transformations of the liquid assisted grinding of ZnO with 2-methylimidazolate with the corresponding crystal structures. Calculated tetrahedra (T) per volume (V) for each framework below. Reproduced from reference 144.*

Whilst ZIF-8 undergoes no thermal amorphisation, it does undergo pressure-amorphisation at low pressures. A constant-stress molecular dynamics study revealed that pressure decreases the shear modulus of the framework and that temperature changes do not induce instability in the framework. Furthermore, the presence of guest molecules within the framework greatly increases the shear resistance.[147] One application of such pressure-induced amorphised materials is the permanent storage of species within the pores of the collapsing framework. This concept has been shown using ZIF-8, ZIF-69, and ZIF-mnIm where harmful I_2 molecules were successfully sequestered within the inaccessible pores of the amorphous frameworks.[148]

2.3.3 Thermal Amorphisation

Thermal energy in a system induces both atomic and molecular vibrations and—in interacting particle systems such as MOFs—phonons. Often, other than the average displacement from the equilibrium position, the only structural change occurs at the decomposition of the framework. However, some members of the ZIF family undergo structural rearrangement to an amorphous configuration before framework decomposition.[149] The mechanism of this thermal amorphisation was studied in ZIF-4 using far-IR spectroscopy to reveal that the flexibility of the Zn–N tetrahedra may be a critical factor in the structural rearrangements that give rise to amorphisation.[150] These amorphous solids retain their particle morphology, displaying no evidence of flow (**Figure 28**).[55] A thermodynamic study into ZIF-4 revealed the amorphisation process from ZIF-4 to a_TZIF-4 to be an *exothermic* (4.1 kJ mol^{-1}) process indicating stability over the crystalline ZIF-4.[151] However, samples of $Zn(Im)_2$ are observed to undergo recrystallisation from the amorphous state to a more thermodynamically stable, dense, non-porous ZIF-zni phase.[52]

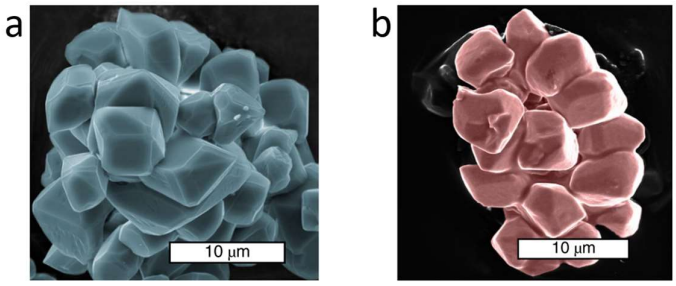

***Figure 28*: Colourised SEM images of ZIF-62 displaying no evidence of flow after thermal amorphisation**. *a. crystalline ZIF-62, and b. thermally amorphised, a_TZIF-62. Reproduced from reference 55.*

2.3.4 The Structure of Amorphous MOFs

It is observed for three polymorphs of the $Zn(Im)_2$ MOF—ZIF-1, ZIF-3, and ZIF-4—that the amorphous structure is considerably denser than the crystalline MOF; ZIF-3 undergoes a 34% increase in apparent pycnometric density upon amorphisation, seemingly independent of amorphisation technique.[54] Accordingly, the increase in structural density affects the structure's gas uptake, drastically reducing the measured surface areas and altering the framework's porosity and permeability. For example, the permeability of nitrogen gas (N_2) through ZIF-8, $Zn(mIm)_2$ (mIm = 2-methyl-imidazolate), is lost as a result of amorphisation.[52,54]

The gas sorption isotherms of the *a*MOFs also indicate two critical aspects of their structure; (i) the loss of immediate low-pressure gas uptake indicates a loss of *accessible* microporosity within the structure, and (ii) the induction of hysteresis (imperfect retracing of adsorption data upon desorption) upon amorphisation indicates slower gas diffusion kinetics in the *a*MOF (**Figure 29**). The presence of hysteresis, in turn, shows that pathways still exist within the amorphous structure but indicate a loss of periodic channels.

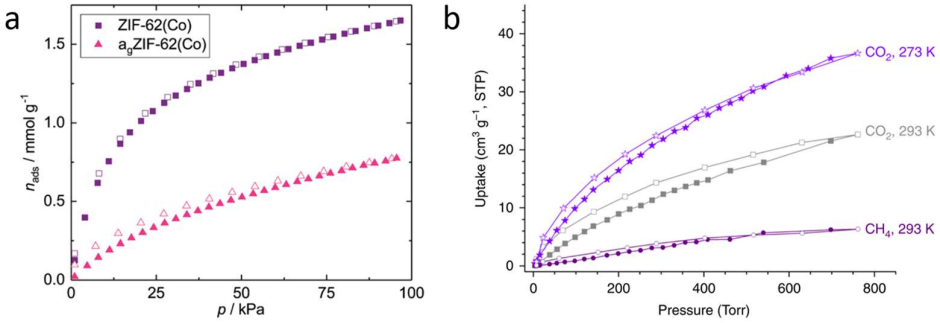

***Figure 29*: Gas sorption isotherms of porous ZIF glasses.** *a. CO_2 gas sorption isotherms for crystalline and amorphous ZIF-62. b. hysteresis observed for a sample of amorphous ZIF-76-mbIm. Reproduced from references 72 and 73.*

To investigate the dense atomistic connectivity within *a*MOFs, the diffuse scattering that gives rise to the FSDP in the PXRD pattern may be utilised since it contains useful two-atom pair data. Recorded total-scattering diffraction data may be processed to produce pair distribution function (PDF) data (**Figure 30**); peaks in the resultant graph indicate atomic distances within the sample as a histogram of total atomic contributions. PDF data for a sample of a_TZIF-4 indicate bond

distances up to *ca*. 7 Å, which align with C–C, Zn–N, Zn–C, and Zn–Zn distances, corresponding to the bonding between Zn–Zn nearest neighbour pairs. Up to the Zn–Zn bond pair at 6 Å, the crystalline and amorphous samples of ZIF-4 are identical, confirming component integrity within the *a*MOF, but also detailing the range at which the disorder within the system occurs.[52] The short-range similarity of these patterns confirm the tetrahedral Zn coordination environment, and the imidazolate bridging between Zn nodes is common to both phases.[59]

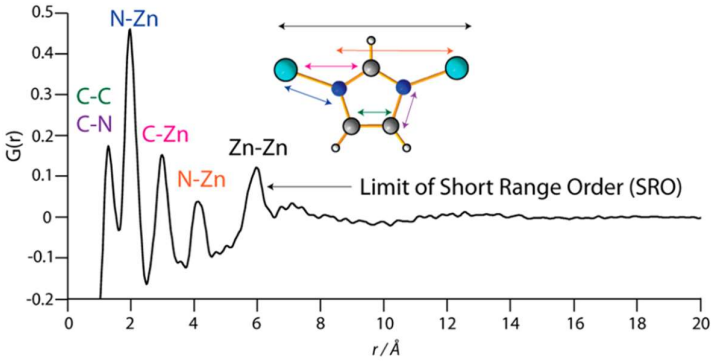

***Figure 30**: **Assigned PDF data of a_TZIF-4, Zn(Im)$_2$**. Each peak in this graph represents atom pair distances within the material. The font is coloured to match the atom pair distance arrow marked in the short-range order unit of ZIF-4. Zn, turquoise; N, blue; C, grey; H, white. Reproduced from reference 52.*

Attempts have been made to model the structure of the amorphous MOFs through Reverse Monte Carlo (RMC) simulations. This modelling method is a random walk algorithm designed to model the experimental data by altering and simulating the input structure. RMC modelling of the crystalline-amorphous transitions in zeolites has shown that the framework connectivity is preserved during amorphisation: the short-range order of ZIF-4 should therefore be constrained in the refinement.[59,152] Whilst models using the crystalline ZIF-4 and ZIF-zni structures were input to simulate the data, the best fit to experimental data was found using a model based on an established continuous random network (CRN) topology of *a*-SiO_2. This model was modified by replacing the Si with Zn atoms and replacing the O atoms with imidazolate ligands, which provided an excellent fit to the recorded short, and medium-range order atom-pair distributions of ZIF-4 (**Figure 31**).[59]

The resultant structure of *a*ZIF-4 using the *a*-SiO_2 model is consistent with the previous experimental data displaying a greater atomic density than its crystalline counterpart, and a loss of periodic channels. The tortuous pathways observed in the amorphous model pore space (**Figure 31f**) would also give rise to the observed hysteresis in the gas sorption isotherms. Whilst the determination of absolute atomic positions of all atoms within amorphous systems is not currently possible—and neither would it be precisely repeatable, even if it were—this model provides clear evidence that the non-crystalline samples are not highly-disordered crystalline solids, but "truly" amorphous systems.[59]

The structure of amorphous MOFs should not be considered a single state since structural studies of amorphous zeolites reveal entire potential energy landscapes (PELs) of unique structural arrangements within the solid.[153,154] The structures corresponding to the local minima within these landscapes are correlated to their atomic density, such that the low-density amorphous (LDA) systems are located deep in the PEL. ZIF systems have shown similar behaviour, and the

resultant density—and by extension, position in the PEL—has been shown to be dependent on the method of amorphisation.[70]

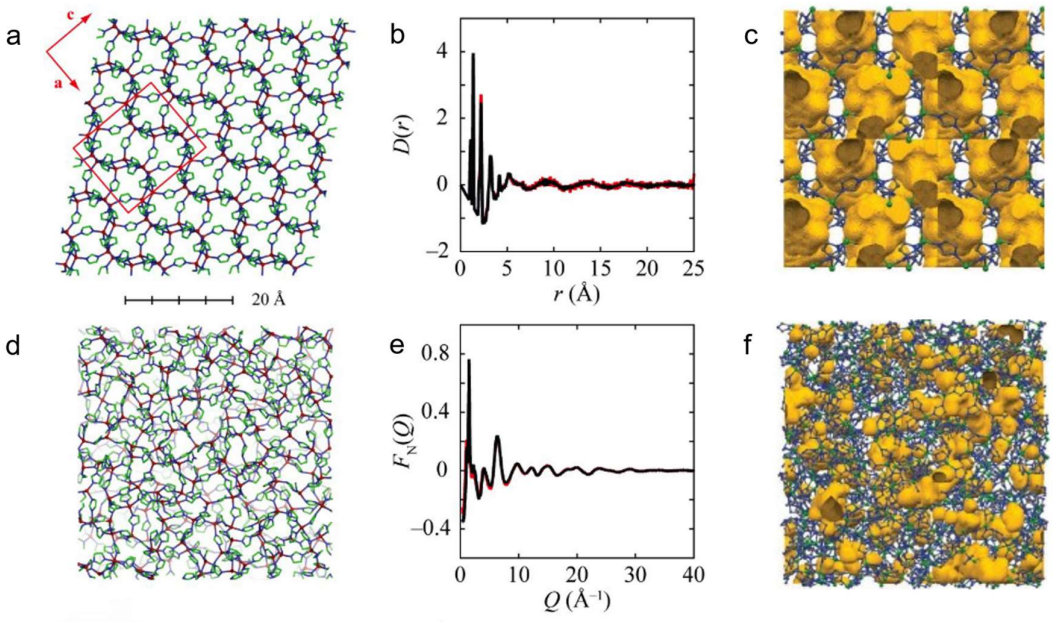

***Figure 31**: **Atomic configurations of ZIF-4 from the refinement of total scattering data.** a. A region of crystalline ZIF-4 showing the unit cell in red, b. the corresponding RMC fit to the total scattering data of aZIF-4, and c. the corresponding pore volume of the crystalline system. d. A region of the ZIF-4 structure based on the CRN topology of SiO_2, of roughly equal volume, e. the corresponding RMC fit, and f. the pore volume of an amorphous ZIF-4 gained from modelling synchrotron and neutron total scattering data. C, green; N, blue; Zn, red; H/D omitted for clarity. Experimental data in black and refinement in red. Pore volume in yellow. Reproduced from references 59 and 68.*

2.3.5 Melting

Shortly after the discovery of thermally amorphised ZIFs, some of the very same members of the ZIF family were observed to undergo a phase transition from crystalline solids to liquids (**Figure 32**). These liquids were subsequently cooled to form melt-quenched glasses.[65] Melt-quenched glasses are distinguished by the presence of a liquid state; this is an essential factor due to the particulate fusion that imparts a change in physical properties. In each case, the liquid state is preceded by the formation of a solid amorphous phase (**Figure 32e**).

The working hypothesis was that the reconstructive processes involved in amorphisation are caused by the breaking and reforming of Zn–N bonds within the structure. However, this did not explain the trend in the melting temperatures observed across these materials. The lowest temperature melting transition was for ZIF-62, $Zn(Im)_{1.75}(bIm)_{0.25}$, at 437 °C, with ZIF-4 being the most resistant to melting (590 °C). If the strength of the Zn-N bonds determined the activation energy of the melting transition, stronger Zn-N bonds would have higher T_ms. However, the observed melting temperatures trend showed that the reverse was true.

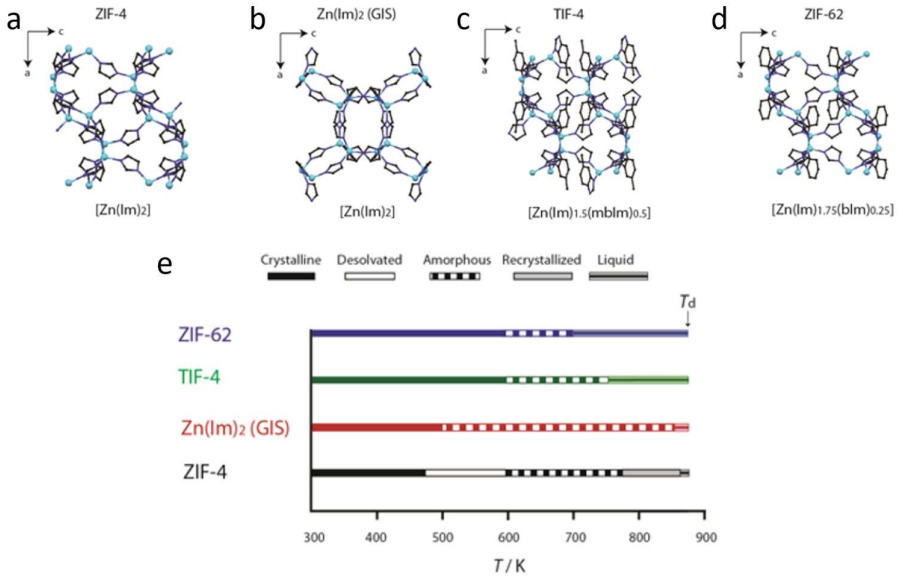

Figure 32: Known melting MOFs and their thermal reconstruction temperatures. *Structural representations of four glass-forming ZIFs, a. ZIF-4, b. GIS, c. TIF-4, and d. ZIF-62, and e. the temperatures of their reconstructive transitions measured at atmospheric pressure. Reproduced from reference 65.*

In these materials, the Zn–N bond strength changes with the functional groups around the imidazolate ring through differences in the electron-donating ability of the nitrogen.[65] The electron-donating capacity of these ligands roughly correlates with the pK_a of their conjugate acids; Im = 6.8, mbIm = 12.46, and bIm = 12.8. Of the ligands within these frameworks, imidazole has the weakest electron-donating capability but has the highest T_m.

The mechanism was further studied using first-principles molecular dynamics (FPMD) to model Zn–N and Zn–Zn bond distances within the structure and relate them to the Lindemann parameter—the root mean square fluctuation in atomic position about the equilibrium lattice position. The Lindemann criterion for melting specifies that the departure from linearity in the behaviour of the global atomic spacing within a system signifies a solid-to-liquid transition.[155] Despite the relatively low accuracy of this method, a threshold value of 0.15 Δ_L (the dimensionless Lindemann parameter) is taken as a critical value to determine melting. However, this value may vary between 5–20%.[156] In these simulations, neighbouring zinc atoms deviate from the initial linear behaviour at around 1,200 K, which corresponds to a sudden increase in heat capacity of the simulated system.[68] After 1,200 K, this model predicts the rapid increase in the concentration of undercoordinated zinc ions (**Figure 33**).

This data, combined with the rapid dissociation and reassociation of imidazolate ligands within the model, supports a proposed melting mechanism. Snapshots of the picosecond reactions that occur provide defined reaction steps that occur during the melting process (**Figure 34**). Melting of ZIF-4 was shown to be a rapid ~400 fs association-dissociation of imidazolate between zinc nodes. In this time, the zinc coordination sphere fluctuates from a tetrahedral geometry to trigonal monopyramidal where an imidazolate ligand decoordinates from the zinc centre, forming an unsaturated trigonal planar complex. The unsaturated complex relaxes to a trigonal pyramidal geometry and is approached by another imidazolate linker which coordinatively bonds to the unsaturated zinc site, regenerating the original tetrahedral

geometry. This recoordination randomises the directionality of the resultant ligands removing the long-range order of the material. This mechanism is analogous to the single rate-determine step nucleophilic substitution, S_N1, reactions that occur in organic molecules.

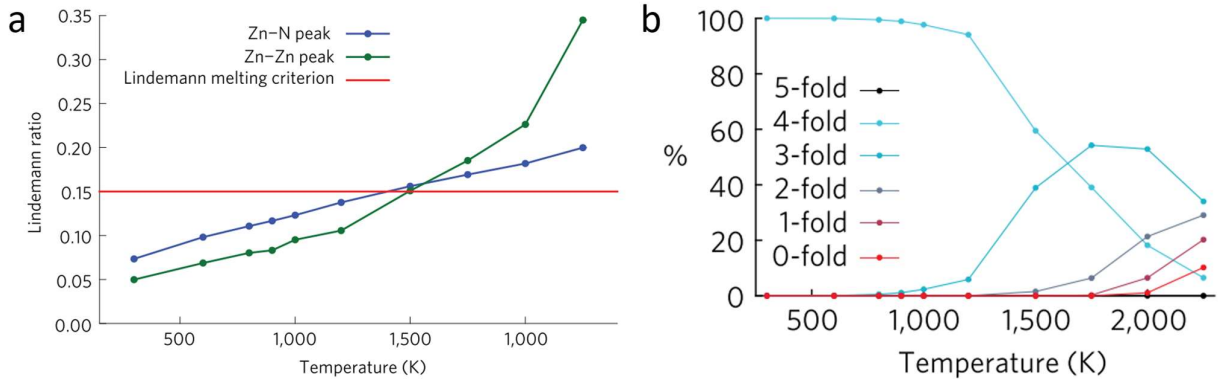

***Figure 33**: **The thermal dependence of the bond vibrations and Zn coordination environment of ZIF-4.** a. Lindemann ratios of the Zn–N and Zn–Zn atomic vibrations in ZIF-4, and b. predicted concentration of coordination around the zinc metal sites on heating. Reproduced from reference 68.*

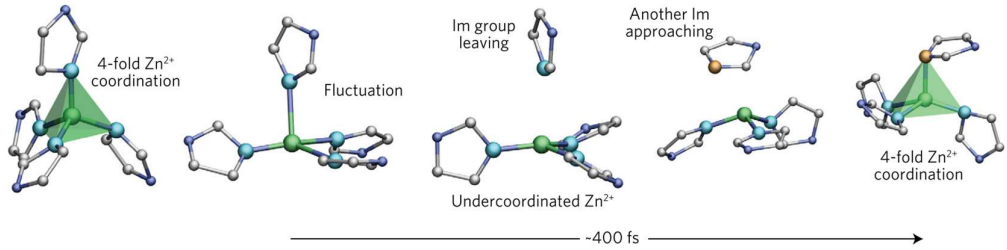

***Figure 34**: **The melting mechanism of ZIF-4 as determined by Bennett et al.** The displayed mechanism represents critical events occurring in a molecular dynamic simulation occurring over a ~400 fs timeframe. Zn, green; C, White; N, Blue (initial); Orange (incoming). Reproduced from reference 68.*

The computational and experimentally derived mechanism provides some guidance for the investigation of other potentially melting MOF candidates: (i) the metal node cannot be sterically over-encumbered for the approaching ligand; (ii) the coordination bond strength must be strong enough for the framework to withstand high temperatures, and not too strong such that the activation energy for the ligand to decoordinate becomes too high; (iii) the structure must have enough pore volume to accommodate the free movement of an approaching ligand; (iv) the metal node coordination geometry must be flexible, and non-covalent interactions must stabilise the undercoordinated ion pair.

2.3.6 Thermodynamics of Melting

As suggested by Bennett *et al.*, the melting of MOFs may not be dependent on the stability of the node or ligand individually but on a careful balance of low node stability in combination with high ligand thermal stability. This

arrangement results in unstable coordination environments of the node whilst preventing the decomposition of the ligands at higher temperatures.[117]

Given the dependence of the Zn–N bond breakage as necessary for the melting of a ZIF, the activation free energy required to break this bond ($\Delta F^{\ddagger}$) in ZIF-4 was calculated from partial radial distribution function analysis. By determining the Zn-N distance in each PDF, the potential of mean force (PMF, $F(r)$) was calculated through the relationship of the Boltzmann constant (K_B) and the calculated Zn–N distance ($g(r)$) over a range of temperatures through **Equation 3**, allowing for the calculation of $\Delta F^{\ddagger}$. This was fitted using linear regression to determine the enthalpy change ($\Delta H^{\ddagger} \approx 121$ KJmol^{-1}) and entropy change ($\Delta S^{\ddagger} \approx 34$ Jmol^{-1}K^{-1}) according to the Van 't Hoff equation (**Equation 4**).[68]

$$F(r) = -K_B\, T \ln g(r) \qquad \textit{Equation 3.}$$

$$\Delta F^{\ddagger}(T) = \Delta H^{\ddagger} - T\Delta S^{\ddagger} \qquad \textit{Equation 4.}$$

Applying these thermodynamic principles to the synthesis of melting MOFs, three-dimensional MOFs with low-temperature melting were revealed in a 2021 study.[157] At its core, melting—which is referred to as *fusion*—is a thermodynamic event that has enthalpic and entropic components. This can be expressed as follows where: T_m, melting temperature; ΔH_{fus}, enthalpy of fusion; ΔS_{fus}, entropy of fusion.

$$T_m = \frac{\Delta H_{fus}}{\Delta S_{fus}} \qquad \textit{Equation 5.}$$

Through this relationship, by minimising ΔH_{fus}, and maximising ΔS_{fus}, the melting temperature can be effectively reduced. Accordingly, ΔH_{fus} minimisation requires a balancing of the net interatomic force strengths between the solid and liquid phases. Since the melting of a species entails the dissociation and reassociation of bonds, this thermodynamic contribution is addressed by lowering the coordination bond strength, thereby reducing the net enthalpic change.[157] The maximisation of ΔS_{fus} is somewhat more complex since the various entropic contributions in the liquid and solid states of metal–organic frameworks are less well understood. The system enthalpy regards the total strength of the atomic interactions in the structure. However, constraining molecules in the solid phase—thus restricting their configurational, vibrational, or rotational degrees of freedom—can be performed to increase ΔS_{fus}. In the case of the metal-bis(acetamide) frameworks, specifically $Co(bba)_3[CoCl_4]$ (bba = *N*,*N*'-1,4-butylenebis(acetamide)), low-symmetry, high-flexibility ligands were implemented such that the long, saturated alkyl chains are constrained to a linear configuration in the solid phase.[157]

Due to the lack of thorough DSC performed in the MOF field, it is unknown how many of the tens of thousands of known MOF structures undergo melting. However, the melting of five separate groups of glass-forming hybrid crystalline systems is known, which produce glasses on cooling from the melt.

2.4 Hybrid Glasses

Fundamentally, hybrid materials comprise two or more of the organic, inorganic, and metallic families of materials as necessary for their structure. MOFs are an example of hybrid materials since they comprise both organic and inorganic

components; however, these three-dimensional structures are only one of the six known families of hybrid glass-forming families (**Figure 35**). Perhaps the earliest reported examples of melting and glass formation in hybrid materials, before ZIFs (**Figure 35a**), were of one-dimensional zinc phosphonate coordination polymers, *e.g.* $[Zn(HPO_4)(H_2PO_4)_2](ImH_2)_2$ (**Figure 35b**).[158] In this system, recrystallisation from the glass state in this structure permits the reversible amorphisation to the initial crystalline configuration, a property unobserved for ZIFs.[158,159] For members of this family, and for the thiocyanate based glasses (**Figure 35c**),[160] their ionic interactions combined with melting temperatures below an arbitrary 100 °C threshold, *technically* permit the classification of these materials as ionic liquids.

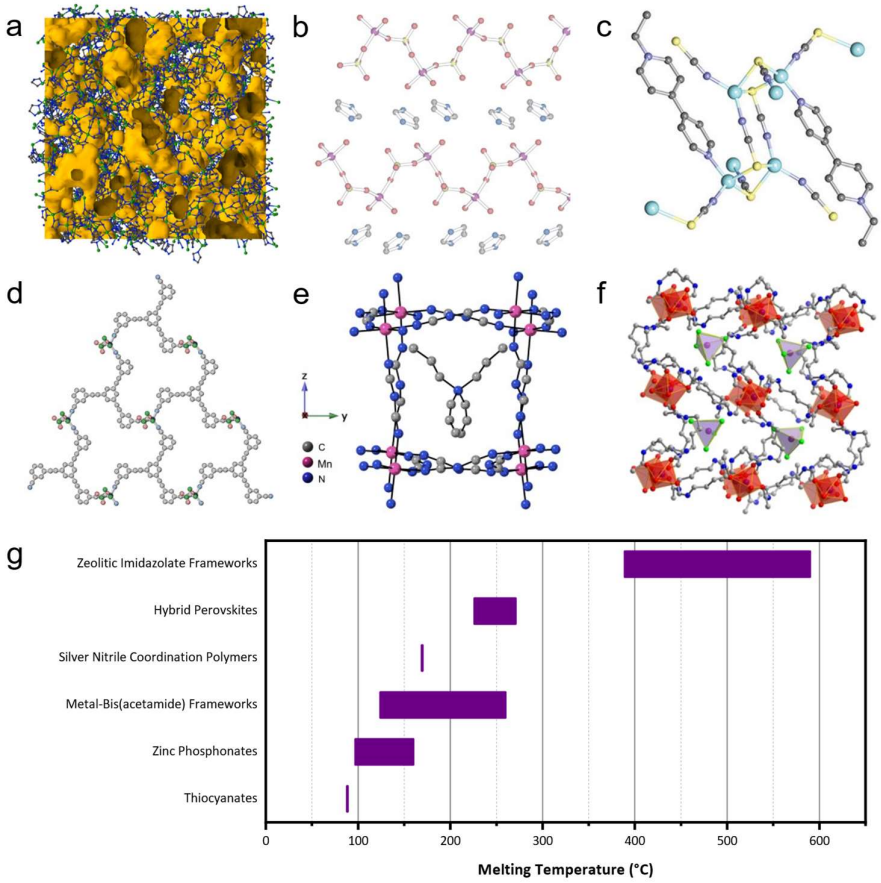

***Figure 35**: **Configurations of the currently known glass-forming hybrid material structures and their reported melting ranges.** a. zeolitic imidazolate frameworks, b. zinc phosphonates, c. thiocyanates, d. silver nitrile coordination polymers, e. hybrid perovskites, f. metal-bis(acetamide) frameworks, and g. melting temperature ranges of each material. Data extracted from and reproduced from references 68, and 155–159.*

In recent studies, two further examples of melting MOFs were introduced, a 2-dimensional silver nitrile-based coordination polymer (**Figure 35d**) and hybrid organic–inorganic perovskites (**Figure 35e**). The latter is based on the well-known inorganic perovskite structures, which comprise corner-sharing, octahedral, halide-coordinated metal ions with large organic (or Cs^+) cations occupying the cubic pores. The hybrid organic–inorganic perovskite structures replace the halide ligands with longer, bidentate organic species that bridge the anionic metal sites. The most recent family of melting

hybrid materials, metal-bis(acetamide) frameworks (**Figure 35f**), were borne of a study aimed at synthesising low-temperature melting 3-dimensional frameworks.[157]

2.4.1 Pair Distribution Function (PDF) Analysis on Hybrid Glasses

The amorphous nature of glasses means that the atomic arrangement within these systems is identical in nature to previously discussed amorphous structures (see **Section 2.3.4**). One key difference is that by moving through a liquid state to form a glass, the fusion of the particulate provides larger samples. As for all amorphous materials, the atomic configuration cannot be extracted as precisely as for a crystalline system using current methodologies due to the aperiodicity in amorphous systems. However, the local- and intermediate-range structural features contained within the total scattering data may provide key structural information such as the atomic distances, coordination numbers, and particle sizes.[164] PDF analysis is a complementary technique that, in combination with composition-determining techniques such as NMR and mass spectrometry, is crucial for determining local order structure in amorphous materials. One of the main advantages of this technique, in the characterisation of hybrid glasses, is its ability to provide evidence of cross-linker node distances.

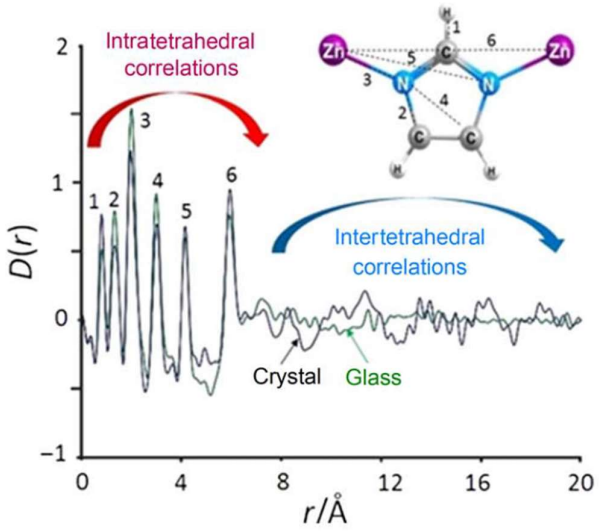

Figure 36: The difference between the PDF of crystalline and amorphous ZIF-62. *a. PDF comparison of crystalline ZIF-62 (black) and a$_g$ZIF-62 (dark green). Intratetrahedral distances in the structure labelled 1–6 and are shown inset. Reproduced from reference 57.*

A common method to accurately identify the observed interactions in amorphous materials is to measure a crystalline sample of the same composition first—typically before a crystalline-amorphous transition, for the greatest accuracy. By beginning with a crystalline sample of known atomic arrangement, the atom pair distances can be calculated and assigned to the PDF of the crystalline material. The distances of these atom pair interactions may then be compared and contrasted to the observed peaks in the PDF of the glass (**Figure 36**). In hybrid materials, where long organic linkers are present, the structural integrity of these materials can be confirmed in the short range of this technique. However, the critical information from this technique is to characterise the contiguous bonding within the sample. In the sample of ZIF-62,

$Zn(Im)_{2-x}(bIm)_x$, the presence of peak 6 in the PDF provide evidence of connected nodes over the linker distance.[165] These inter-node atom-atom correlations evidence continuation of bonding throughout the structure. However, the marked reduction in peak intensity past this short-range order, in comparison to the crystalline sample, indicate the elimination of structural periodicity.

Notably, any change in peak position or intensity is a direct result of physical changes within the system. Accordingly, changes in peak position may be a result of moving or missing atom-atom distances, and the introduction of new peaks can be used to identify the successful incorporation of material.[165,166]

2.4.2 ZIF-62 Glass (a_gZIF-62)

Of the known zeolitic imidazolate frameworks, ZIF-62 is amongst the lowest melting temperature members—with a T_m of 437 °C—but perhaps has the largest body of research amongst such members. ZIF-62 comprises M^{2+} nodes tetrahedrally coordinated to bidentate, bridging ligands of both imidazolate and benzimidazolate. This system crystallises in an orthorhombic (P*bca*) space group with a *cag* net topology (**Figure 37a,b**).[97] ZIF-62 has been synthesised from both cobalt, zinc, and mixtures of the two metals.[57,72,167] Interestingly, the cobalt variant, ZIF-62(Co), melts at a slightly lower temperature of 432 °C,[72] and a mixture of the two systems induces non-linear optical properties not observed in either single-metal species.[167] Furthermore, broad mid-IR luminescence has been observed for cobalt-containing a_gZIF-62 arising from cobalt *d-d* transitions and can be enhanced by increasing cobalt concentration.[168]

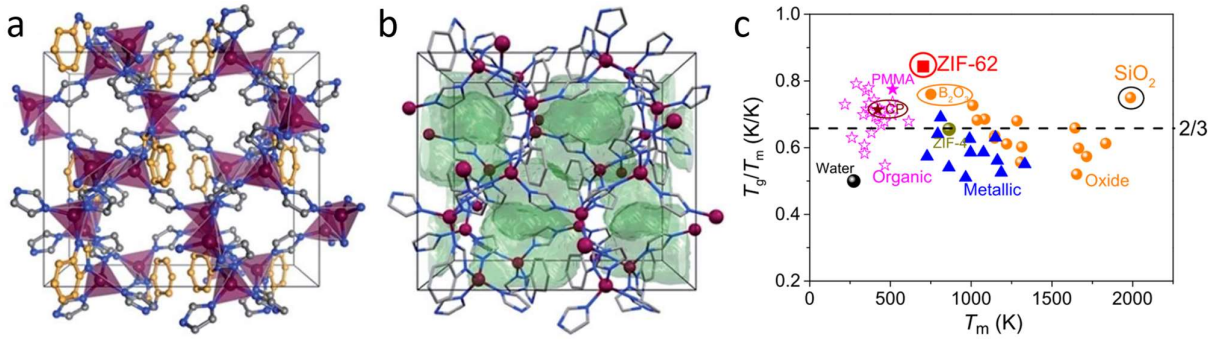

***Figure 37**: **Configurations of ZIF-62 and its glass-forming ability relative to other families of glasses.** a. Schematic illustrations of ZIF-62 depicting equal occupation of Im and bIm linkers. representation of the crystal structure viewed along the* b *axis. The metal coordination environment is represented by purple tetrahedra, and bIm carbons are coloured orange. b. identical view of the structure with solvent accessible volume depicted in green. Metal, purple; C, grey; N, blue. Reproduced from reference 72, and c. A comparison of T_g/T_m ratios between ZIF-62 and other glass-forming systems. Reproduced from reference 57.*

A 2018 paper describing the melting and glass-formation of ZIF-62(Zn) revealed that this system exhibits an unparalleled glass-forming ability with a T_g/T_m ratio of 0.84 (**Figure 37c**). The T_m and T_g are dependent on the linker ratio and, interestingly, inversely proportional to the bIm concentration in the x = 0.12–0.22 range of $Zn(Im)_{2-x}(bIm)_x$. Furthermore, ZIF-62 was compared to silica with respect to their crystal growth kinetics, measured by heating close to T_m over 24 hours. Silica also displays a high glass-forming ability and exhibits low rates of crystal growth on annealing. However, whilst

micrometre crystallites are observable in silica glass after 24 hours, no detectable crystallisation was observed for a_gZIF-62, indicating even lower crystal growth kinetics.[57]

The phase stability of ZIF-62 was studied using DSC and a pressure-controlled diamond anvil cell with cell-penetrating synchrotron source X-ray data. By quenching to observe sample morphology, the distinction between liquid and high temperature, or pressure, amorphisation could be made; particulate fusion is not observed for samples which have not passed through a liquid phase. This study revealed the distinct stability fields of crystalline, high temperature amorphous, high pressure amorphous, and liquid states of ZIF-62. Interestingly, pressure may be applied to promote low-temperature melting of ZIF-62, significantly reducing the melting point to *ca*. 360 °C at just over 2 GPa pressure.[55] This information is helpful to understand the range of operating conditions for the application of ZIF-62 (**Figure 38**).

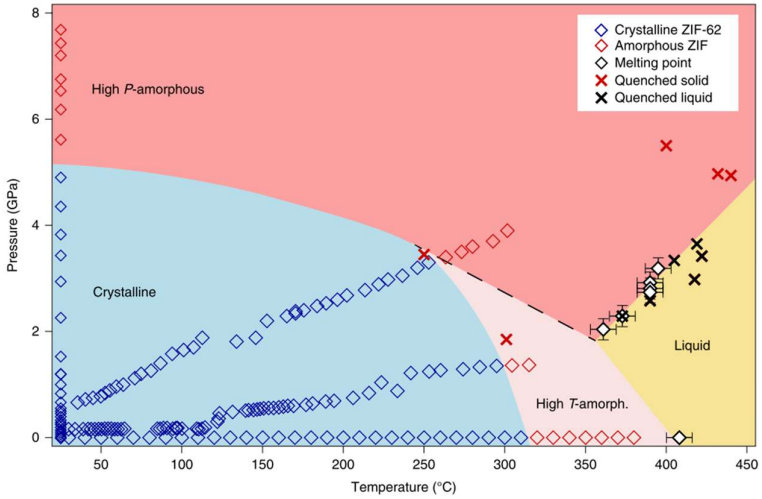

Figure 38: Temperature-pressure stability fields of ZIF-62. *By recording the PXRD patterns and observing macrostructural changes, areas of pressure and temperature-induced transitions have been delineated. Reproduced from reference 55.*

Of particular interest regarding ZIF-62 is its ability to retain porosity in the glass. Whilst a_gZIF-62 is slightly denser than crystalline ZIF-62,[65] a 6% internal pore volume was recorded for the glass—down from 27% in the crystalline material—as determined by positron annihilation lifetime spectroscopy (PALS).[57] This retention of pore void space is supported by gas sorption studies of a_gZIF-62 which demonstrate permeation of CO_2 (**Figure 29**) to gases as large as propene (**Figure 39a**) within the pores of the glass.[58,72] The gas uptake in the glass is non-linearly dependent on the bIm:Im ratio where a_gZn(Im)$_{1.83}$(bIm)$_{0.17}$ displayed greater uptake than either a_gZn(Im)$_{1.95}$(bIm)$_{0.05}$ or a_gZn(Im)$_{1.65}$(bIm)$_{0.35}$ for both propane and propene (**Figure 39a**). Furthermore, a_gZIF-62 is selective between propane and propene in both theoretical calculations and apparent in the uptake-time profiles for each gas (**Figure 39b**), where equilibration to 90% uptake takes over six times longer for propane than propene for a sample of a_gZnIm$_{1.83}$bIm$_{0.17}$.[58] The uptake rate difference between the two species can be utilised in membrane-based technologies.

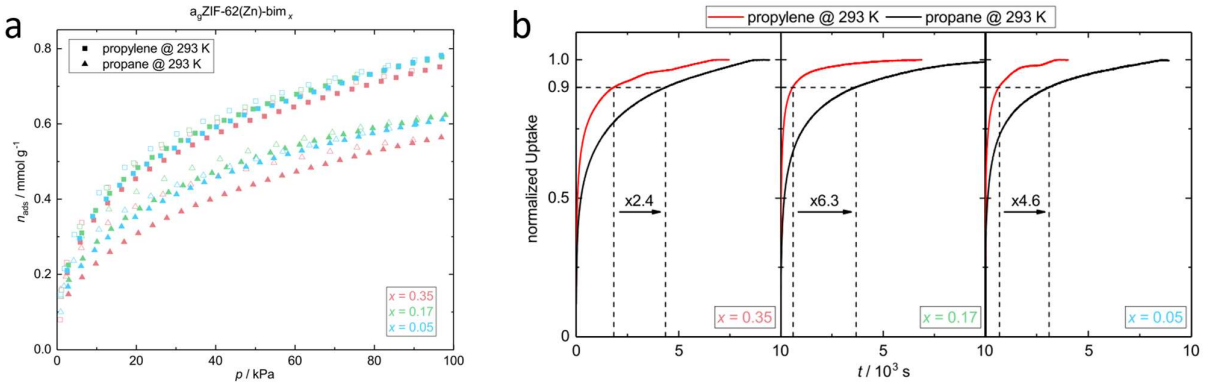

Figure 39: C_3 selectivity of a$_g$ZIF-62(Zn) shown via the kinetic sorption profiles of gas sorption isotherms*. a. Propane and propylene (propene) gas sorption isotherms of* a$_g$*ZIF-62(Zn) (293 K) glasses varying the concentration of bIm linker. b. Kinetic sorption profiles of propane and propene recorded with an equilibrium pressure of ~54 kPa. The adsorption and desorption branches are respectively shown with solid and open symbols. Reproduced from reference 58.*

On a macrostructural level, a_gZIF-62 forms a transparent bulk glass[*2] with a 90% transmittance in the visible and near-infrared frequencies (*i.e.* 400–1600 nm). This is corroborated by the determined high homogeneity of the glass and low spatial fluctuations in the optical transparency.[76] The refractive index (1.56 at 589 nm) and Abbe number, v (*ca.* 31), of ZIF glasses place the optical properties of a_gZIF-62 in a comparable region of the refractive index-Abbe number diagram to the upper range of polymers, but like many of the other properties, can be tuned to a small degree by altering the linker ratio.[71] This high optical transparency is considerable in conjunction with the system's physical properties.

Whilst there is some disagreement in values of physical properties of a_gZIF-62, with recorded Young's moduli, E, of 4.1 GPa (from molecular dynamics),[169] 5.2 GPa,[169] 6.1 GPa,[170] 6.58 GPa,[75] 7.15 GPa,[171] 8.7 GPa,[55] and 8.8 GPa,[65] this material, and MOF glasses in general, display a Young's modulus-density profile distinct from both inorganic and metallic glasses. This profile of MOF glasses aligns with the upper region of elastic polymers (**Figure 40a**)—also known as elastomers or rubbers—establishing a truly unique material space for these materials, with uncharted application potential.

Extensive nanoindentation studies have also been carried out to extract complex physical characteristics such as the strain-rate sensitivity of indentation hardness, m, a characteristic describing the time dependence of deformation.[75] In this study, m was measured through two methods, constant load and hold (CLH) and strain-rate jump (SRJ) tests (**Figure 40b**) extracting respective values of 0.0822 and 0.0717, similar to that of polycarbonate, polysulfide, and PMMA polymers (m = 0.05–0.10).[75,172] In this study, a_gZIF-62 and a_gZIF-4 are shown to behave as Newtonian viscous solids, where a_gZIF-76 and a_gZIF-76-mbIm behave as rigid, plastic solids. This behaviour of a_gZIF-62 and a_gZIF-4 is ascribed to their greater density compared to the more porous a_gZIF-76 systems. Furthermore, this study details investigation into the fracture properties, revealing that, unlike inorganic and metallic glasses, a_gZIF-62 does not undergo ductile fracture within the limits of

[*2] It is noted that, in one study, annealing the glass for 24 hrs is required to achieve this result.[57]

spherical scratch testing. Therefore, it is concluded that the effect of superstructural parameters on the network rigidity determines the mechanical response of MOF glasses.[75]

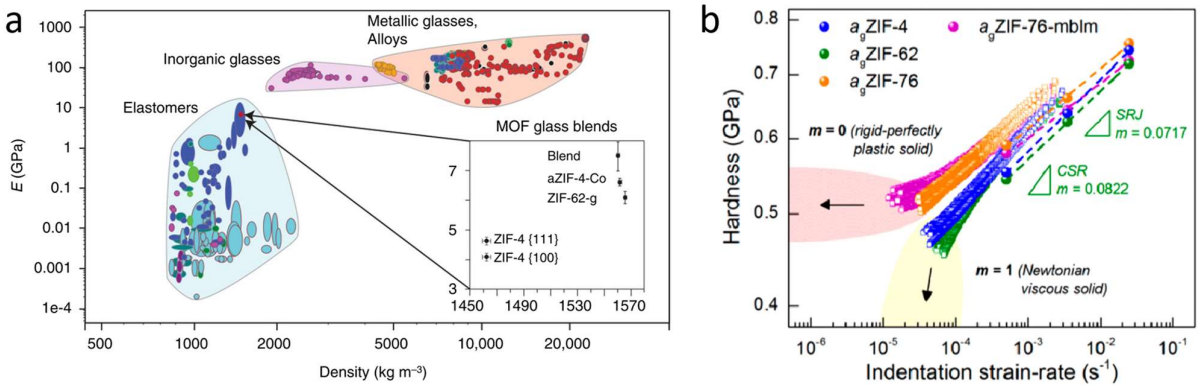

Figure 40: The mechanical properties of ZIF glasses compared to other glassformers. *a. Ashby style plot of a selection of MOF glasses (blends) placed in context with known inorganic glasses, metallic glasses, alloys, and elastomers. Reproduced from reference 170. b. Relationship between the hardness, H, and the indentation strain-rate of four MOF glass systems. Reproduced from reference 75.*

In corroboration of the absence of ductile fracture, a_gZIF-62 shows no evidence of macro-ductility either, displaying brittle behaviour in fracture toughness testing, with a brittleness index, B_{index}, of 0.7, similar to disordered calcium-silicate-hydrate gel (0.62), but significantly lower than *a*-SiO_2 glass (0.9).[169] This study revealed that a_gZIF-62 displays exceptionally low fracture toughness behaviour between the ranges of foams and elastomers. Molecular dynamic simulations were employed to understand the origin of this behaviour. Simulations were initiated with pre-cracked a_gZIF-62, and the strain was gradually increased (**Figure 41**); cracks were observed to propagate *via* the rupture of Zn–N bonds.[169] Each of these macrostructural feature investigations of MOF glasses serves to clarify a broader perspective of these materials, highlighting their advantages to elucidate their potential applications. An important feature of MOF glasses is their ability to form bulk structures, overcoming key problems related to the application of MOF powders.

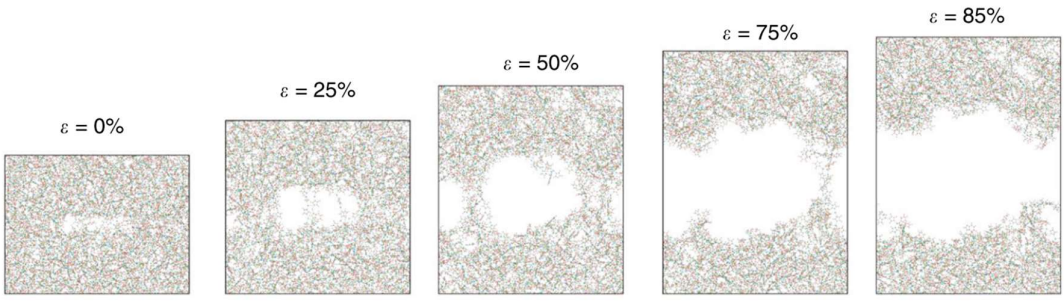

Figure 41: Structural representation of crack propagation in pre-cracked a_gZIF-62 upon increasing strain, ε*. These images are generated by molecular dynamic simulations of a pre-cracked sample, displaying structure deformation processes and limiting bond strengths. Zn, blue; C, red; N, green; H, grey. Reproduced from reference 169.*

2.5 Macroscale MOF Structures

Whilst crystalline MOFs have shown exceptional properties, several industrial practicability issues remain. One barrier is the inherent difficulties in processing and shaping MOF microcrystalline powders into mechanically robust macroscale morphologies.[173,174] Conventionally, high-pressure pelletisation or binders are used in the shaping of MOF powders, but these treatments have been shown to decrease material efficacy significantly.[175] However, a few separate studies have produced bulk samples with promising results. In one, a 2 cm diameter, 0.5 cm thick monolithic sample of ZIF-4 was prepared using a spark plasma sintering press, displaying near-identical properties to the original material (**Figure 42a**); this technique is, however, limited to melting MOFs.[176] For non-melting frameworks, monoliths of HKUST-1 have been fabricated using sol-gel syntheses with reflective surfaces, where the constituent particles could no longer be observed (**Figure 42b,c**).[173,177]

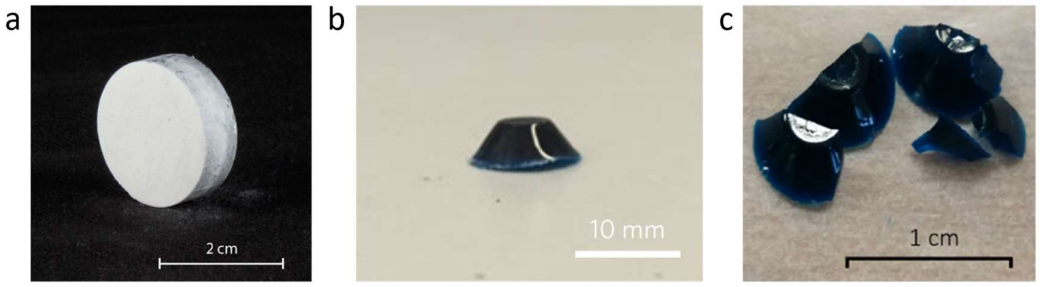

Figure 42: Optical images of a range of MOF monolith samples. *a. ZIF-4 pellet using spark plasma sintering press, reproduced from reference 176, b. monolith of HKUST-1 using sol-gel synthesis, reproduced from reference 173, and c. monolith of HKUST-1 using another sol-gel synthesis method. Reproduced from reference 177.*

The formation of composites by combining MOFs with more processable materials such as polymers offers solutions to the aforementioned problems in manufacturing robust bulk structures. These macroscale architectures, membranes, and thin films are particularly important given the requirements for continuous, defect-free coverage and flexibility under pressure.[178] Mixed matrix membranes (MMMs) are a prototypical case of such materials.[179] Here, a crystalline MOF filler is typically dispersed in an organic polymer; a typical synthesis involves the suspension of the desired MOF, polymer, and solvent into a homogeneous, viscous 'ink' before shaping and curing/drying to yield a MMM (**Figure 43**).[180,179]

The disordered nature of the polymeric organic component within MMMs provides both structural stability and facilitates shaping. However, significant penalties are incurred, including pore blocking by the matrix, aggregation of the filler and poor adhesion between the two components, which prevents high loading capacities.[181] To improve the compatibility between the two species, there have been attempts to functionalise the surface of the MOF with species that have a higher affinity to the surface of the polymer. For example, in a recent study, the interfacial compatibility of UiO-66 [$Zr_6O_4(OH)_4(BDC)_6$] with polyether oxide-polyamide (PEO-PA) blocks (Pebax-1657) was improved by synthesising an analogue of UiO-66 with additional functional groups extending from the benzene ring. The introduced $–NH_2$ and $–CO_2H$ functional groups permit stronger physisorption bonding to the surface of the polymer.[182]

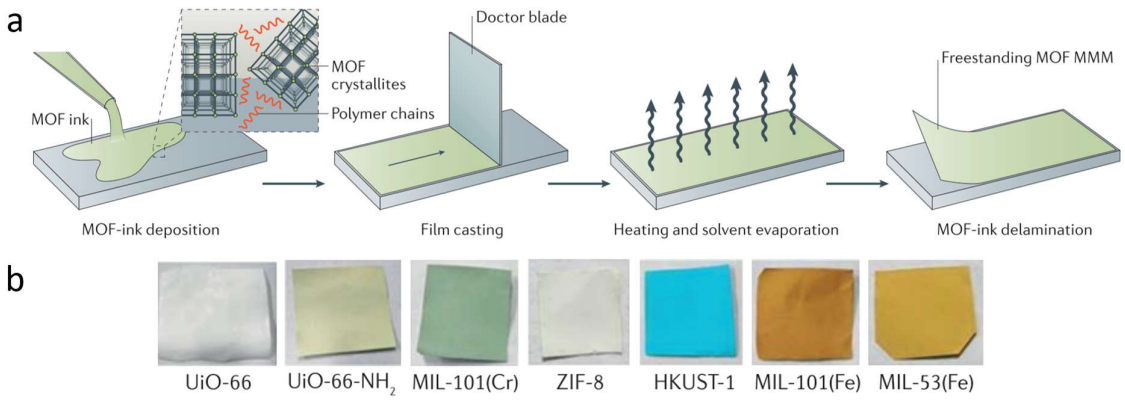

Figure 43: Illustration of a typical mixed-matrix membrane (MMM) synthesis. *a. A typical synthesis of a MMM by creating a depositing a MOF-ink, film casting, and evaporating off the solvent, and b. optical images of successfully synthesised MMMs using typical MOFs. Adapted from reference 179.*

In contrast to such techniques, MOF glasses provide their own bulk MOF material through the *fusion* of MOF particulate. Utilising the ability of the ZIF-62 particulate to fuse together, coupled with the inherent porosity and demonstrated separation potential of a_gZIF-62, research has been conducted to investigate the potential to form thin-layer MOF glass membranes. Since fusion of the particulate generates contiguous bonding throughout the structure, MOF glasses are uninterrupted by voids left by the sintering process—which are likely to weaken the structure. Furthermore, the contiguous bonding of MOF glasses imparts an advantage over polymer-supported MOF materials both in stiffness and interfacial compatibility. MOF-on-polymer membranes are known to exhibit void spaces between MOF particulate, polymer strands, and at MOF-polymer interfaces. Such incompatibility leads to unwanted channels through the material, detracting from potential separation ability. Therefore, the synthesis and characterisation of composite materials without these disadvantages is of great importance to bridge the divide between advanced MOF material synthesis and practical device fabrication.

2.6 Potential Applications for Amorphous MOFs

One immediate benefit to the application of amorphous over crystalline MOFs is that there are inherently fewer considerations with regard to structure-dependency on temperature and pressure. However, due to the nascency of *a*MOF research, the full extent of their potential application has not been exhaustively explored.

One of the fundamental applications of these materials is the ability to take advantage of the crystalline-amorphous transition. In one study, a selection of crystalline ZIFs were loaded with iodine gas and ball-milled to the amorphise the structure.[148] This structural collapse prevents the iodine from escaping the structure, irreversibly trapping the gas. In principle, this process should be applicable to any species that may permeate into the crystalline MOF, but not exit the amorphous material. This would enable amorphous MOFs to act as permanent storage for a broad range of materials, from air-sensitive catalysts to harmful gases.[148]

Another interesting application of *a*MOFs is in the controlled slow release of molecules for drug delivery. In a 2015 study, calcein, a structural analogue to an API, was loaded within the pores of a UiO-66, and the structure was collapsed to trap the guest molecules. The difference between the rates of release from the crystalline and amorphised frameworks show an order of magnitude difference, where the guest is reported to release the adsorbed calcein over 30 days in the amorphous sample, compared to 2 days for the crystalline material.[61] This increased delivery time was unprecedented for nanoparticulate drug delivery systems.[61] Utilising property changes upon amorphisation has also been demonstrated through the conversion of an insulating copper-based MOF to a semiconducting amorphous MOF.[183]

On a morphological level, the ability to form macroscale MOF structures through liquid state fusion improves the suitability of MOFs in systems otherwise ill-suited to the fine powder nature typical of crystalline MOFs. Porous MOF glasses have already demonstrated hydrocarbon separation abilty[58] leading to the production of thin-film membranes exhibiting high separation performance for H_2/CH_4, CO_2/N_2, and CO_2/CH_4 gas mixtures.[184] The unique physical properties of MOF glasses, located in a previously unoccupied area of material space, may also be utilised. One suggested application is in the production of scratch-resistant, non-brittle glass surfaces;[75] such materials would be well-suited for optoelectronic applications. Accordingly, amorphous MOFs hold keys to accessing unique physicochemical properties and functionality unobtainable by crystalline MOFs alone. In this work, new materials are sought which utilise the porosity and particulate fusion of MOF glasses.

Chapter 3 Experimental Methods and Materials

3.1 Characterisation Techniques

3.1.1 X-ray Diffraction

3.1.1.1 Theory

X-ray diffraction (XRD) analysis is a routine technique typically employed to analyse crystalline materials. The measurement of a diffraction pattern involves irradiating the sample with X-rays and measuring the intensity of the diffracted X-rays over a range of angles. X-ray diffraction (XRD) experiments may be divided into two categories: single-crystal and powder XRD. The former is generally used for *ab initio* structural investigations of materials with unknown structure; this method uses a single, large crystalline sample and records the diffraction of an incoming beam using a 2-dimensional, fixed detector. This is repeated over a number of crystalline orientations until sufficient data is recorded. These data are then consolidated and analysed to extract the crystal system, unit cell size, symmetry, and space group to refine a plausible distribution of atoms most accurately describing the atomic arrangement. This technique provides a detailed view of the structure but is labour-intensive, costly and highly technical. There are also strict material requirements for the experiment, such as that it requires a uniform, single 10–100 µm size crystal sample, which are often difficult to obtain with MOF materials.

In contrast, powder X-ray diffraction (PXRD) is a quick and simple method that is typically used for structural confirmation or small changes to a known system. This method has fewer sample criteria, requiring only a level powder, regardless of crystalline orientation. The apparatus then irradiates the sample and scans a range of 2θ values whilst optionally rotating the sample (**Figure 44a**). The angular position of the diffracted waves is governed by the Bragg equation shown in **Equation 6**.[185]

$$n\lambda = 2d\,sin(\Theta) \qquad \textbf{Equation 6.}$$

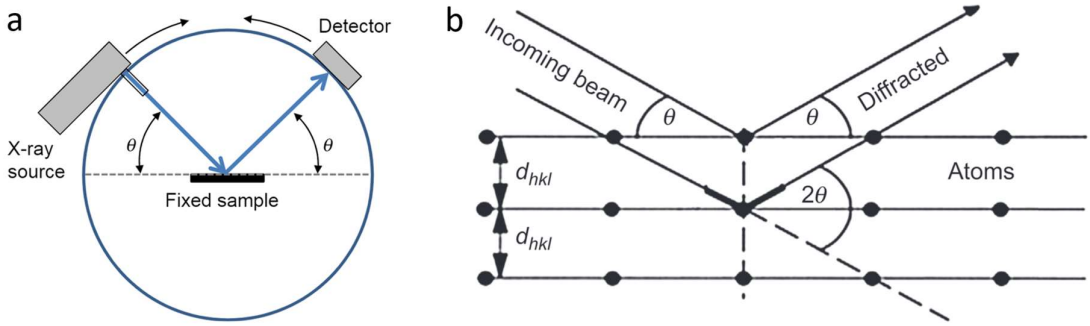

Figure 44: Typical powder X-ray diffraction setup and constructive interference conditions. *a. Setup of a Bragg-Brentano powder X-ray diffractometer displaying the how measurements at different 2θ are taken. And b. Illustration of the elastic scattering of an X-ray from atoms in a periodic solid. Reproduced from reference 186.*

The Bragg equation describes the criteria for constructive interference to occur, involving the wavelength of the incident X-ray, λ, lattice spacing, d, and the angle of incidence, θ. This can be visualised in **Figure 44b** where lattice planes of the sample are represented by points. In this diagram, the lower in-phase photon must travel an extra distance to and from the lower plane, compared to the upper photon. If the total extra distance, given by 2dsin(θ), is equal to an integer number of wavelengths of the incoming X-ray, then the two diffracted photons will be in-phase and coherent. These photons constructively interfere, and high-intensity diffraction is recorded at this angle. Due to the relationship between the diffraction angle and the material d-spacing, the measured peaks, therefore, provide information regarding the atomic periodicity. In the experiment, peaks in recorded intensity correspond to reflections relating to crystal planes within the sample.

3.1.1.2 Powder X-ray Diffraction Experimental

Room temperature data were collected on ground samples of the composite materials with a Bruker-AXS D8 Advance powder diffractometer using Cu K_α radiation (λ = 1.5418 Å) and a LynxEye position-sensitive detector in Bragg-Brentano (θ–θ) parafocussing geometry. Diffraction patterns were typically recorded at 2θ values of 5–40° with a time/step of 0.75 seconds over 1724 steps through a 0.012 mm Ni filter.

3.1.2 Variable Temperature PXRD (VT-PXRD)

X-ray diffraction techniques may also be performed at a range of temperatures and refined to provide information about how the sample reacts to temperature. In this experiment, the sample is typically placed under a vacuum, and the sample stage is heated. This experiment may be performed continuously or incrementally. In a continuous experiment, a sample is heated at a set rate and continuously irradiated to determine precise thermal dependencies of diffraction peaks, especially for those relatively unstable to the experimental conditions. In contrast, incremental experiments heat and equilibrate at set temperatures and isothermally hold whilst a full PXRD scan is recorded before elevating the temperature to record the following pattern. Among many other informative data that may be extracted using this technique, the rate of thermal expansion may be calculated and compared to other systems *via* the coefficient of thermal

expansion. For each axis, this value is defined by **Equation 7** where α_a is the linear coefficient of thermal expansion (CTE), and *a* is the length of the unit cell parameter.[125]

$$\alpha_a = \frac{1}{a_0}\left(\frac{da}{dT}\right)_P \qquad \textit{Equation 7.}$$

The replacement of $\frac{\mathrm{da}}{\mathrm{dT}}$ with $\frac{\Delta \mathrm{a}}{\Delta \mathrm{T}}$ for determination by VT-PXRD can be shown using *via* a Taylor expansion. Assuming α_a is constant with temperature allows integration of **Equation 7** to give **Equation 8.** Which has a Taylor expansion of **Equation 9.**

$$\Delta a = a_0\left(e^{\alpha_a \Delta T} - 1\right) \qquad \textit{Equation 8.}$$

$$\Delta a = a_0\left(\left(1 + \alpha_a \Delta T + \frac{\alpha_a^2 \Delta T^2}{2} + \cdots\right) - 1\right) \qquad \textit{Equation 9.}$$

If the value of $\frac{a_0 \alpha_a^2 \Delta T^2}{2}$ is comparable to the error in the lattice parameter measurement for all samples, then the Taylor expansion can be truncated after the second term, giving **Equation 10.**

$$\alpha_a = \frac{1}{a_0}\left(\frac{\Delta a}{\Delta T}\right)_P \qquad \textit{Equation 10.}$$

This equation is valid for materials that (i) exhibit small changes in the CTE over the measured temperature range and (ii) undergo small expansion values relative to the initial volume of the material. The temperature dependant, volumetric expansion values of refined unit cells calculated from variable temperature PXRD data, may be calculated with **Equation 11**. The mean value of $\Delta V/\Delta T$ may be determined by extracting the gradient from a linear region of a volume-temperature plot or differentiating a second-order polynomial fit. The assumptions in this relationship are justified as above.

$$\alpha_v = \frac{1}{V_0}\left(\frac{\Delta V}{\Delta T}\right)_P \qquad \textit{Equation 11.}$$

3.1.2.1.1 VT-PXRD Experimental

Data were collected on ground samples of each material, which were mixed with ~10% by volume of silicon powder (Si), using a Bruker D8 Advance equipped with an MRI high-temperature chamber and a Vantec detector, using Cu K_α radiation (λ = 1.5418 Å) under vacuum (8.5×10^{-3} mbar). Prior to running the experiments, height adjustments were performed to optimise the full-width at half-maximum (FWHM) value of the (111) silicon standard reflection at *ca.* 28.45° 2θ. Samples were heated in 20 °C increments from 30 °C to an appropriate end temperature. Diffraction patterns at 2θ values of 5–40° were recorded at each increment with a time/step of 0.6s over 0.04° steps.

In situ synchrotron data were collected at the small-angle X-ray scattering (SAXS) beamline of the Australian Synchrotron facility. Dried crystal powder samples were loaded into 1.0 mm quartz capillaries under Ar protection in a glove box. The in-situ synchrotron powder diffraction was investigated with beamline SAXS radiation at 16 keV, 2675 mm camera length using a Pilatus 1M detector in transmission mode. For each analysis, a line scan of 3 mm at 0.3 mm s^{-1} was conducted.

The background of the empty capillary was subtracted. The data were processed using in-house developed Scatterbrain software for averaging and background subtraction.

3.1.3 PXRD Refinements

The recorded PXRD pattern may provide a variety of information regarding the structure of the crystalline material. PXRD data may be refined in software, such as TOPAS, to accurately predict many of the structural properties of the recorded sample using a crystallographic information file taken of the same material. Two of the main refinement strategies, and ones used herein, are Pawley and Rietveld refinements.

A Pawley refinement uses only the space group and lattice parameters from the provided crystallographic information and attempts to match the recorded data. Each space group is defined by a set of symmetry operations; symmetry allowed reflections are defined for each system. The *d*-spacing of the calculated peaks is then determined by the lattice parameters of the unit cell. Accordingly, a Pawley refinement predicts the possible *hkl* indices of the structure and relates them to the peak positions in 2θ by the given X-ray wavelength. The input parameters, such as the unit cell, background, crystal size, and preferred orientation, are subsequently refined to match the positions of the calculated peaks to the recorded pattern.

A Rietveld refinement is a more complex strategy that utilises all the information contained in the crystallographic information file. Each atom, its position, shape, and its X-ray scattering contributions may be treated as separate variables to refine the PXRD data. Certain techniques may be employed to simplify the data; one such method is to use a rigid body assumption which is a set of atoms defined by cartesian coordinates. This may be used where known structures are present in the system, such as rigid organic linkers in MOFs with defined structure; this reduces the number of variables in the refinement. Unlike a Pawley refinement, a Rietveld refinement refines the peak intensity of the recorded pattern to obtain greater structural information, such as precise preferred crystalline orientation and exact atomic positions. The benefit of refining data in this way is that the refined data generates a visualisable geometric explanation of the data.

Further information that can be gleaned from PXRD data is crystal sizes (defined by the Scherrer equation[187] which relates peak width to grain size) and crystal strain. Furthermore, by use of a well-defined standard (such as silicon powder), accurate temperature and pressure calculations, contributions to crystallinity, and sample displacement calculations can be made. For many, mixing standards with the sample is standard practice since experimental and sample contributions to the pattern can be separated using calculations made using the standard.

3.1.3.1 Experimental

Chapter 5 Sequential Refinements

PXRD patterns were analyzed by Rietveld refinements using TOPAS academic (V6) software.[188] Pseudo-Voigt peak shapes were globally refined as a single set of parameters for all scan files. A 9th-order Chebychev polynomial background, a Gaussian background peak accounting for the amorphous background from the ZIF-62 glass, scale factors, unit cell parameters of the MIL-53 structure, as well as 8th-order spherical harmonics preferred orientation corrections were

refined individually for all scans. In the analysis of these materials, preferred orientation was included, despite no apparent preferred dimensional growth in the SEM images, for two reasons: i) the ball-milling step in the production of the composite induces stresses that may shear apart the frameworks along weak crystal planes, thus introducing a level of dimensional preference not present in the pure MOF materials, and ii) the application of pressure is well-known to induce preferred orientation in a system to allow for optimum packing under pressure. The refinements were thus permitted to allow for a preference in crystalline orientation to account for these factors.

Chapter 7 Sequential Refinements

VT-PXRD data were analyzed with TOPAS academic (V6) software.[188,189] Reported thermal expansion data for Si provided an accurate calculation of unit cell parameters for the Si standard.[190] Using these values, peak position was corrected for sample displacement across sample series. XRD data were refined sequentially using the reported crystallographic information files of MIL-118B, MIL-53-lp, or UL-MOF-1; atomic positions were included but were constrained in the refinements.[121,191,192] To account for the diffuse scattering from α_gZIF-62 in the MOF CGCs, a broad Gaussian peak was added and permitted to refine sequentially. Subsequent refinements in the series were performed using the final values for the previous pattern as initial values. A Pearson VII function and an 8th-order Chebychev polynomial background were used to model the peak shape and the background, respectively. Scale factors, unit cell parameters, 8th-order spherical harmonics and preferred orientation corrections were refined individually for all scans. Preferred orientation was included for the reasons listed in the previous refinements.

3.1.4 Pair Distribution Function (PDF)

Pair distribution function is an advanced technique involving the Fourier transform of X-ray total scattering data to determine the probability of finding an atom relative to an average atom at the origin. The wavelength of the incident beam determines the resolution of the data; the maximum resolution of two peaks corresponds to the radius of the resultant Ewald sphere, given by λ/2. Therefore, the use of synchrotron X-rays provides the greatest resolution of real-space data (**Figure 45**). The improvement of *Q* space resolution—through the sacrifice of real space resolution—makes this technique invaluable for studying materials on an atomistic scale, and therefore indispensable for the study of amorphous materials.[193,194] Initially, PDF was used to study inorganic specimens;[195,196] however, applying this technique to nanocrystalline powders and molecular solids such as MOFs has rewarded indispensable utility for probing atomic distances.[164] In the calculation of this data, the scattering coordinate and magnitude of the scattering momentum, *Q*, is defined by the incident wavelength, λ, and the scattering angle, θ:

$$Q = \frac{4\pi \sin(\theta)}{\lambda} \qquad \textbf{Equation 12}.$$

In the derivation of the pair distribution function from the total scattering data, the measured scattered amplitude is equated to the sum of the scattering of each atom and self-scattering components are then isolated. A factor known as the Laue monotonic diffuse scattering is then incorporated to account for the imperfect cancellation of intensities at

destructive interference conditions originating from unequal X-ray scattering strengths. The data are then normalised by the total number of scatterers, *N*, and the average scattering factor, <*f*>, to subtract the self-scattering term.[197]

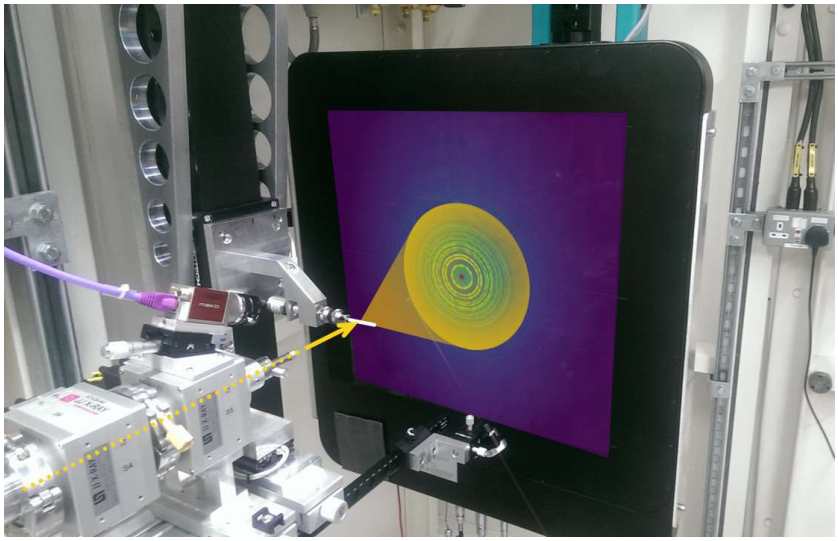

***Figure 45**: **Experimental setup at Diamond Light Source, U.K., I15-1**. This apparatus is used for the recording of total scattering X-ray data for pair distribution function analysis. The yellow arrow indicates the synchroton-source X-ray path, scattering within the projected yellow cone. Recorded intensity is overlayed on the detector. Reproduced from reference 198.*

Isotropy must be assumed such that all crystalline orientations are present to apply this theory to amorphous and non-crystalline solids. The scattering coordinate dependent interatomic distance, Qr_{ij}, is therefore assumed to be equal to $Qr_{ij}\cos\theta$. In doing so, θ takes all values with equal probability, giving the total scattering structure factor, *S*(*Q*) as:

$$S(Q) - 1 = \left[\frac{1}{N\langle f\rangle^2}\right]\sum_{i\neq j} f_j^*(Q) f_i(Q)\left[\frac{\sin(Qr_{ij})}{Qr_{ij}}\right] \qquad \textbf{Equation 13.}$$

Where f_i and f_j^* are the form factors for atoms *i* and *j*, which, due to the diffuse shape of the electron cloud makes them a function of *Q*.[199] The reduced total scattering function, *F*(*Q*), used to calculate the PDF, is related to *S*(*Q*) as follows:

$$F(Q) = Q[S(Q) - 1] \qquad \textbf{Equation 14.}$$

The experimental PDF, *G*(*r*), can finally be expressed as a function of the reduced total scattering structure function, *F*(*Q*), and integrated over the measured values of *Q*, as follows:

$$G(r) = \frac{2}{\pi}\int_{Q_{min}}^{Q_{max}} F(Q)\sin(Qr)\,dQ \qquad \textbf{Equation 15.}$$

Where the 2/π prefactor to the Fourier transform is introduced to ensure that the sine transformation begins at 1—since the zero-point lies at the centre of an atom.[197,199] The limits of the scattering momentum are experimentally determined

parameters, where Q_{max} may be calculated by the wavelength of the incident beam as per **Equation 12**. The PDF has also been expressed by accentuating the correlations at higher atomic distances factoring in the atomic number density, ρ_0, as follows:

$$D(r) = 4\pi p_0 r G(r) \quad \textbf{Equation 16}.$$

Such calculations would provide accurate atom-pair distances for a perfect, isolated sample in a vacuum. However, the experiment is typically performed in air, and the sample is packed into a silicate glass capillary. To account for this, atmospheric scattering and scattering from an empty container are subtracted from the data.

The data are then processed by the user in GudrunX in an iterative process by tuning data correction parameters to ensure that the data are meaningful. Examples of such processes are the subtraction of inelastic scattering effects from charged particles (Compton scattering), adjusting the minimum radius for Fourier transform, and removal of truncation oscillations due to a slowly varying *Q*-dependent background through the introduction of a top-hat function.[197]

3.1.4.1 Calculating *G*(*r*) from a model

For a known structural model, the *G*(*r*) can be calculated using PDFGUI software[200] from the atomic number density, ρ_0, and the atomic pair density, $\rho(r)$ as follows:

$$G(r) = 4\pi r[\rho(r) - \rho_0] \quad \textbf{Equation 17.}$$

Where the atomic pair density can be expressed as the average weighted probability of finding an atom at a distance *r* from any atom within the system.[199] This can be calculated by the summation of atom pair distances from a reference point, weighted by the scattering factor of the pair as follows:

$$\rho(r) = \frac{1}{4\pi r^2 N} \sum_i \sum_{j \neq i} \frac{b_i b_j}{\langle b \rangle^2} \delta(r - r_{ij}) \quad \textbf{\textit{Equation 18.}}$$

Where b_i and b_j are the scattering factors of atoms *i* and *j*, $\langle b \rangle$ is the average scattering factor, and r_{ij} is the distance between atoms *i* and *j*.[199] δ here is not a variable, but a Dirac delta function that distributes the density of a point mass and is applied to account for diffusivity of the electron cloud. This equation may also be separated into individual scattering components to model the PDF of specified atom pairs within a system.[197] This is known as the partial PDF, $G_{ij}(r)$, and is particularly useful in assigning atom pairs in the total PDF.

3.1.4.2 Experimental

Data were obtained at the I15-1 beamline, Diamond Light Source, UK (λ = 0.161669 Å, 72 KeV). All samples were finely ground, packed into 1 mm diameter SiO_2 capillaries or into 1.17 mm (inner) diameter borosilicate capillaries before analysis. Data were taken of the background, empty capillary, and of all samples to a Q_{max} of 26 $Å^{-1}$. Normalised total scattering data were corrected individually through Breit-Dirac factors, Compton scattering, tweak factors, top-hat widths, minimum radii for Fourier transforms, width of broadening in *r*-space, broadening powers, and refined to a Q_{max}

of 24 Å^{-1} using the open-source GudrunX software.[197,201] Predicted patterns were generated using the respective reported crystallographic information files available online and the PDFGUI software.[200]

3.1.5 Nanoindentation

3.1.5.1 Theory

Nanoindentation is a common technique in the quantitative analysis of small-scale mechanical behaviour. This technique involves the impression of a metallic tip of a known shape into the surface of a material, measuring the load required as a function of displacement. The precision of the indenter position accentuates errors from external vibrations; therefore, vibration isolation is essential for accurate data. In **Figure 46a** a triangle-based pyramid-shaped indenter tip, known as a Berkovich indenter, is illustrated; these and spherical indenters are two commonly used tip shapes due to their symmetry.

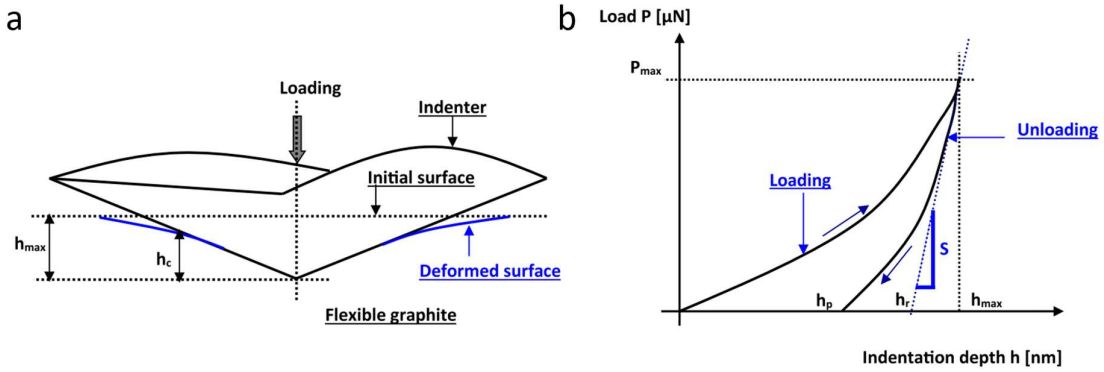

Figure 46: Illustration of a typical indenter and load-displacement profile from Nanoindentation. *a. Diagram of the indenter tip penetrating into a sample. b. A typical Load-indentation graph during nanoindentation. Reproduced from reference 202.*

The most widely adopted method for indentation is the Oliver and Pharr method. In a typical experiment, the surface is located by lowering the indenter until a small pre-set load is achieved, which is defined as the surface. The load and displacement into the surface are both continuously measured as the indenter penetrates to a set depth into the sample. As the tip is lowered, two processes occur, deformation of the sample plastically around the tip and elastic deformation as the specimen resists the load.[203]

To measure the physical properties of the sample, the sample-indenter contact area must be calculated. Importantly, the surface of the sample deforms under the applied load by a sink-in depth, h_s; the penetration depth of the indenter, h_c, is, therefore, less than the depth of the intender top from the surface, h_{max} (**Figure 46a**). The contact height can therefore be expressed as:

$$h_c = h_{max} - h_s \qquad \textit{Equation 19.}$$

However, this does not account for pile-up, where indented material is displaced around the periphery of the indenter, increasing the contact area. Further calculations are made assuming negligible pile-up.[203] Therefore, h_s can be approximated as:

$$h_s = \epsilon \frac{P_{max}}{S}$$ ***Equation 20.***

Where P_{max} is the maximum load, S is the stiffness (**Figure 46b**). The geometry of the tip is accounted for with a constant, ϵ, where, for example, ϵ can be approximated to 0.72 and 1.00 for a conical indenter and a flat punch, respectively.[204] A Berkovich indenter can be modelled by a conical indenter with an identical depth-to-area relationship, which is valid for a conical indenter with a half-included angle of 70.3°.[203,205] The calculated value of h_s can be inserted into **Equation 19**. The contact area, A, of the indenter can therefore be measured as a function of h to account for indenter shape.

$$A = F(h_c)$$ ***Equation 21.***

Usage of the indenter leads to the grinding of the tip which induces tip curvature. This may be modelled using constants determined by curve-fitting procedures, $C_0 \ldots C_8$, in **Equation 23**, accounting for curvature over a wide range of depths.

$$A = \sum_{n=0}^{8} C_n (h_c)^{2-n}$$ ***Equation 22.***

$$A = C_0 h^2 + C_1 h + C_2 h^{1/2} + C_3 h^{1/4} + \cdots + C_8 h^{1/128}$$ ***Equation 23.***

Upon determination of A, the hardness, H, may therefore be measured as the load per area unit. This is typically measured from the initial unloading region of the experiment. This definition of hardness works when there is negligible elastic recovery during unloading.[203]

$$H = \frac{P_{max}}{A}$$ ***Equation 24.***

The unloading stiffness, S, and contact area, A, may also be used to calculate Young's modulus, E, through the calculation of an *effective* elastic modulus, E_{eff}, as follows:

$$S = \beta \frac{2}{\sqrt{\pi}} E_{eff} \sqrt{A}$$ ***Equation 25.***

Where β is a constant accounting for deviations in the calculated stiffness, and whilst traditionally taken as unity, may vary significantly.[206] Finally, E_{eff} is related to the Young's modulus, E, through the Poisson's ratio, ν, and indenter elastic constants ν_i and E_i.[203]

$$\frac{1}{E_{eff}} = \frac{1-\nu^2}{E} + \frac{1-\nu_i^2}{E_i}$$ ***Equation 26.***

3.1.5.2 Continuous Stiffness Measurement

An improvement to current methods of measuring the stiffness of a material may be performed by using a continuous stiffness measurement. In this method, oscillations are introduced to the force signal, and the corresponding displacement signal is measured. In this technique, values of H and E are measured as a function of depth rather than

calculating a single overall measurement. The calibration and testing procedures are shorter in this method, and furthermore, the method evades issues surrounding time-dependent plasticity and thermal drift.[203]

3.1.5.3 Experimental

Samples for nanoindentation were mounted on a steel plate using Loctite Super Glue to weight the sample and encased in hardened epoxy resin. The steel plate was carefully ground by using coarse sandpaper on a water irrigated rotary disc, gradually reducing the sandpaper grit until revealing the sample. The sample surface was then carefully smoothed to a 0.25 µm finish using diamond paste on fabric rotary disks.

The Young's modulus and hardness were determined using an Agilent MTS Nanoindenter XP, fitted with a Continuous Stiffness Measurement (CSM) module. Nanoindentation was carried out using a triangular pyramidal Berkovich diamond tip at room temperature. All samples were repeatedly indented to a specified depth ≤2000 nm at a frequency of 45 Hz and at a constant strain rate of 0.05 s^{-1} before taking an average of the results. The load-displacement data collected were analysed using the Oliver & Pharr method.[203] A Poisson's ratio of 0.4 was used, similar to reported values of a_gZIF-62.[57,169]

The Berkovich indenter was calibrated against fused silica (E = 71.2–74.8 GPa). Between each test, the tip head was cleaned by indenting 5 times into a sample of aluminium. Microscope to indenter calibration was performed between each sample.

3.1.6 Nuclear Magnetic Resonance (NMR) Spectroscopy

3.1.6.1 Theory

Nuclear magnetic resonance (NMR) spectroscopy is a non-destructive technique that requires very little sample (*ca*. 10 mg) and both ^{1}H and ^{13}C NMR are routinely used to determine the structure of a compound. This technique is typically performed on a dissolved sample using a deuterated solvent such as $CDCl_3$. Since MOFs are typically insoluble, the disintegration of the framework for dissolution using a deuterated acid is typical; doing so allows for the structural confirmation, and determination of the relative concentration, of organic ligands within a MOF system.

NMR relies on the presence of nuclear "spin" momentum direction, *I,* and spin angular momentum, *S*, specific to isotopes with specific combinations of protons and neutrons. NMR applies an intense magnetic field in which nuclei with non-zero values of *I* may be excited and measured (**Table 4**). Spin states are degenerate in the absence of a magnetic field and split in accordance with their alignment with the magnetic field, such that spins that oppose the magnetic field are destabilised and higher in energy. The number of accessible states in each isotope is governed by the angular momentum. The energy of the transition is governed by the nuclide specific, gyromagnetic constant, γ and the magnetic field strength, B_0. The gyromagnetic constant itself is a measure of how strongly a nucleus is affected by a magnetic field and is intrinsic to the nucleus, where, for example $^{14}N < {}^{15}N < {}^{2}H < {}^{13}C < {}^{31}P < {}^{19}F < {}^{1}H$.[207]

Since ^{1}H is often present in organic molecules and possesses a nonzero spin angular momentum, proton NMR is often employed for structural determination. However, the presence of an NMR active atom does not translate directly to a

clear NMR signal. For example, recording ^{13}C NMR spectra for the same time as ^{1}H NMR spectra will yield poorer quality results because of the relative abundances of the two isotopes in the sample. Hydrogen is observed to be 99.98% abundant in the ^{1}H isotope, with 0.02% abundance from ^{2}H and trace amounts of ^{3}H, whereas carbon is observed to be 98.9% abundant in the ^{12}C isotope and only 1.1% ^{13}C (and trace amounts of ^{14}C). Since ^{1}H is almost 91 times as abundant in hydrogen as ^{13}C is in carbon, the signal received in ^{1}H NMR spectrum is clearer and requires fewer pulse sequences, and by extension, less time to acquire spectra with acceptable signal to noise ratios.[207]

***Table 4**: **Angular momentum of a range of nuclides**. Reproduced from reference 207.*

Nuclide	***I***
^{12}C, ^{16}O, ^{18}O, ^{28}Si, ^{32}S	0
^{1}H, ^{13}C, ^{15}N, ^{19}F, ^{31}P, ^{29}Si	1/2
^{2}H, ^{6}Li, ^{14}N	1
^{7}Li, ^{11}B, ^{23}Na, ^{35}Cl, ^{37}Cl, ^{33}S	3/2
^{58}Co	2
^{17}O, ^{27}Al, ^{55}Mn, ^{127}I	5/2
^{10}B	3
^{45}Sc, ^{51}V, ^{59}Co, ^{133}Cs	7/2

To acquire the signal, highly precise radiofrequency (RF) emitters slowly vary an emitted frequency and when the resonance conditions are met, the nucleus absorbs the RF energy and is excited to a higher energy state; this absorption is then detected, and the decay of the signal is recorded. The precise chemical shift of a species is dependent on a phenomenon known as *shielding*. The electron cloud surrounding the nucleus shields the nucleus from the applied magnetic field *proportional to* the applied magnetic field and may be distorted and reshaped by the bonded and neighbouring atoms. For example, bonding to atoms with higher electronegativity will draw electron density away from the nucleus, reducing the shielding effects of the electron cloud and increasing the chemical shift of the signal; this is known as a *downfield* shift.[207]

There are typical chemical shift ranges for various types of nuclear environments, such as alkanes, alkenes, carboxylic acids, and benzene rings, but to assign the recorded spectrum correctly, knowledge of chemical composition and likely configurations may be required. To further distinguish between nuclei in this experiment, surrounding atoms with a non-zero spin angular momentum up to *ca*. 5 bonds away may couple with the nucleus and predictably split the chemical shift. This unique information regarding the manner of this splitting details the type, number, and relative angle of neighbouring nuclei. Importantly, in NMR the signal obtained for each nucleus is directly proportional to the number of atoms producing the signal. Therefore, the integration of different signals will give relative quantities of each chemically equivalent nucleus.[207]

By centring the experiment on a single frequency and sequentially varying the relaxation times in the experiment, a two-dimensional experiment may be obtained in an experiment known as correlation spectroscopy (COSY). During this

experiment, the magnetisation of coupled protons is mixed, and the resultant spectra indicate which protons are coupled by showing a change in the recorded intensity at the cross-section of the proton chemical shifts on a contour plot.[207]

3.1.6.2 Magic Angle Spinning

The recorded chemical shift depends on the spin's alignment with the applied magnetic field (chemical shift anisotropy) and dipole-dipole interactions. In the liquid state, the free movement of molecules averages these two variables to zero, providing a single clear environment. In contrast, specimens in the solid-state are constrained in their orientation, presenting a wide range of chemical shifts, often too obscured to characterise. It is for this reason that the liquid state is often the preferred method of characterisation.

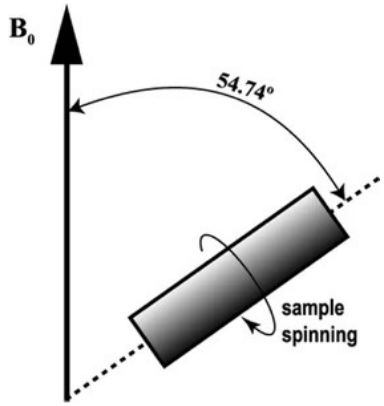

Figure 47: Diagram of the magic angle spinning (MAS) setup. *Reproduced from reference 208.*

However, by spinning the sample at incredibly high frequencies (reaching 150 kHz)[209] at an angle where the angular dependence of the dipole moment to the applied magnetic field, B_0, is zero ($3\text{Cos}^2\theta_m - 1 = 0$; *ca.* 54.74°), this produces much higher resolution spectra for solid-state materials (**Figure 47**).[207] This process is called magic angle spinning (MAS) and allows for the characterisation of insoluble solids and larger specimens such as proteins and MOFs without the need for acid digestion.

3.1.6.3 Experimental

Chapter 4 Solid-state NMR

The solid-state nuclear magnetic resonance (NMR) experiments were performed on a 600 MHz Varian NMR system equipped with a 1.6 mm HXY MAS probe. All samples were spun at magic-angle spinning (MAS) rate of 40 kHz. Larmour frequencies for ^{1}H and ^{13}C were 599.47 and 150.74 MHz, respectively. The frequency axes of the recorded spectra were calibrated against the resonance frequencies of tetramethylsilane. ^{1}H MAS NMR spectra were collected using a Hahn-echo pulse sequence with the 90° pulse width of 1.5 µs and echo delay of a single rotation period. 16 scans were accumulated with the repetition delay of 5 s. ^{1}H-^{13}C cross-polarisation (CP) MAS NMR spectra were recorded by first exciting protons and transferring polarisation to carbon nuclei using the amplitude-ramped CP block with a duration of 4 ms. During the acquisition, a high-power two-pulse phase-modulated (TPPM) heteronuclear decoupling was applied.[210,211]

2D ^{1}H-^{1}H double-quantum single-quantum (DQ-SQ) homonuclear-correlation NMR spectrum was obtained by employing the back-to-back recoupling sequence (BABA).[212] One BABA cycle was used for double-quantum coherence excitation and one for reconversion. A delay of 25 μs was added prior to the 90° read-out pulse of 1.65 μs. The spectral width in the indirect dimension was 40 kHz, and 150 slices were accumulated along the indirect dimension with 32 transients each. ^{1}H-detected 2D proton spin-diffusion (PSD) spectra were measured for spin-diffusion mixing times ranging between 1 and 1000 ms. Each measurement consisted of 160 increments along T_1 with 128 scans per increment and a repetition delay of 0.5 s. T_2 filter was added at the end of the PSD pulse sequence to suppress broad peaks in the direct dimension. Delays before and after the 180°-pulse both lasted 2 ms. ^{13}C-detected 2D PSD spectra were measured for spin-diffusion mixing times of 0 and 10 ms. Before the ^{13}C acquisition, the polarisation was transferred between protons and carbons by utilising 1 ms CP block.[213] In this experiment, 10 increments were taken with 4096 transients each and a repetition delay of 0.5 s.

In 1D ^{27}Al-^{1}H PSD experiment, only the protons in close vicinity of aluminium nuclei (*e.g.*, the protons of MIL-53) were polarised using ^{27}Al-^{1}H CP block of 1 ms after the selective ^{27}Al excitation pulse of 20 μs; 100,000 scans were recorded with a recycling delay of 0.1 s. Spin-diffusion mixing times ranged between 0 and 500 ms.

Chapter 5 Liquid-state NMR

Measurements were carried out by the NMR Service in The Department of Chemistry, University of Cambridge. Data were recorded on a Bruker 500 MHz DCH Cryoprobe Spectrometer. Samples were prepared for NMR by digesting *ca.* 50 mg of each sample in 0.7 mL of a premixed solution of d^{6}-dimethyl sulfoxide (3.5 mL) and deuterium chloride (1.4 mL), sonicating for 5 minutes and allowing 24 hours for the MOFs to dissolve.

3.1.7 Thermogravimetric Analysis (TGA)

Thermogravimetric analysis (TGA) is a thermal characterisation technique used to analyse mass-loss events such as sample decomposition. In this technique, a sample is accurately weighed on a stage before being transferred to a furnace. In this furnace, the sample may be exposed to air or protecting gases such as N_2 or Ar at a known flow rate. The sample is then heated, and the weight of the sample monitored as a function of temperature.

TGA is a routine characterisation method for MOFs, as analysis of a full TGA scan provides information regarding the relative masses of the MOF and its potential impurities (**Figure 48**). Such impurities may be excess synthesis material, such as solvent and unreacted linker, which decompose or evaporate from the MOF during TGA. The absence of any mass-loss events that are not assignable to the pure MOF typically indicates successful framework activation. This technique may also be used to calculate the framework composition to determine the metal-linker ratio.[215] However, this analysis does not provide information about thermal events that occur without mass loss.

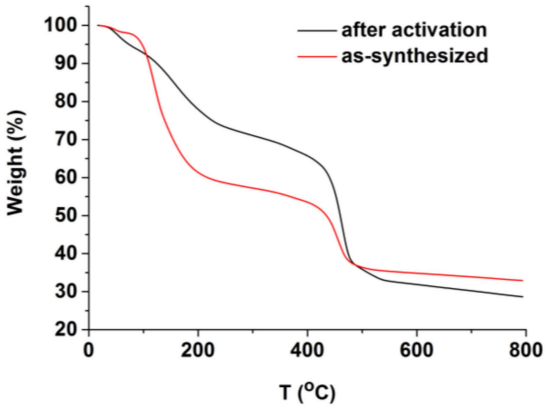

***Figure 48**: **Thermogravimetric analysis of a metal–organic framework before and after activation.** Unreacted linker in the as-synthesised sample accounts for ~40 wt% of the structure, expelled from 100–200 °C. Upon activation, this is reduced to ~ 30 wt%. Reproduced from reference 214.*

3.1.7.1 Experimental

Chapter 4 TGA Measurements

Thermogravimetric analysis and DSC analysis were conducted using a TA instrument SDT Q600. The MOF powder samples were placed in a ceramic crucible situated on a sample holder and then heated at 10 °C min^{-1} to above the melting temperature of ZIF-62 under an Ar environment. For the two-cycle TGA/DSC scans, after the first upscan, the sample was cooled back to 30 °C at 10 °C min^{-1} under an Ar environment, and then ramped up to the targeted temperature at the rate of 10 °C min^{-1} for the second upscan.

Chapter 6 TGA Measurements

Thermogravimetric analysis was performed using a TA Q500 TGA. All scans were heated at 10 °C min^{-1} with a nitrogen protective gas and allowed to cool to RT in air.

3.1.8 Differential Scanning Calorimetry (DSC)

3.1.8.1 Theory

DSC is a programmable technique that measures the heat flow in to and out of a sample in relation to a reference sample; this reference is typically an empty crucible. In this experiment, the sample and reference are placed onto thermoelectric disks surrounded by a furnace and heated at a linear heating rate. Temperature differences between the sample and reference crucibles, ΔT, are a product of the different heat capacities (C_p). The attached thermocouples measure this difference to determine the heat flow, q, by accounting for the resistance of the thermoelectric disks, R as **Equation 27**.[216]

$$q = \frac{\Delta T}{R} \qquad \textit{Equation 27.}$$

Typically, the temperatures of the sample and reference cells are raised identically over time (**Figure 49a**). The difference in the energy required to heat the sample with respect to the reference represents the heat absorbed and released from

the sample during respective endothermic and exothermic processes. Calibrations of the standard eliminate effects from the sample container. The area under the peak corresponds to the energy absorbed or released from the material to undergo that transition (**Figure 49b**). This technique is critical for determining exothermic and endothermic processes which occur without mass loss, such as melting or recrystallisation.[216]

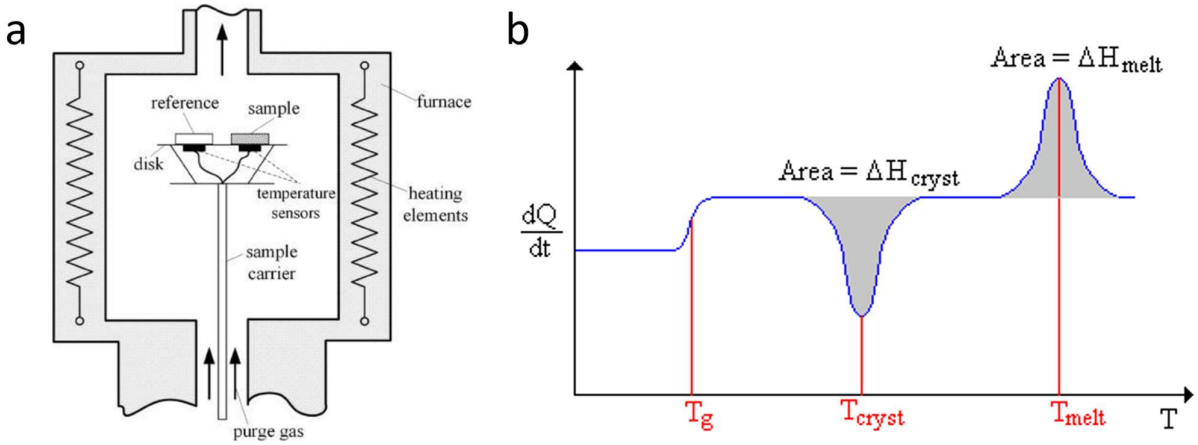

Figure 49: Differential scanning calorimetry analysis. *a. a typical setup of a differential scanning calorimeter. Reproduced from reference 217. b. An example thermogram where transition labels indicate the centre of the peak in this diagram. Reproduced from reference 218.*

3.1.8.2 Experimental

Chapter 4 DSC Measurements

DSC analysis was performed simultaneously with TGA analysis using a TA instrument STD Q600, see **Section 3.1.7.1**.

3.1.9 Porosimetry

3.1.9.1 Gas Sorption

Gas adsorption is a widely used technique measuring material properties such as specific surface area, pore sizes, effective gas storage volumes, adsorption enthalpy, and selectivity between gases.[2,219,220] The experiment measures the physisorption of gaseous molecules to the surface of a material by dosing the container with a known volume of gas and measuring the pressure difference. A standard isotherm is measured as a graph of adsorbed volume, V_a, as the ordinate against an abscissa of P/P_0. The shape of the resulting isotherm may be indicative of structural characteristics.

There are 6 identified and designated isotherm types, denoted in Roman numerals (**Figure 50**); Type I - microporous materials; Type II – non-porous/macroporous (> 500 Å) materials; Type III & V – porous materials where adsorbent interaction is greater than adhesive adsorbate – adsorbent forces; Type IV– Mesoporous (> 20 Å) materials; Type VI – staged multilayer adsorption of typically non-porous materials.[221,222] Type IV isotherms are particularly common in MOFs due to their mesoporous nature; a type IV isotherm shape can be explained in three steps, (i) Initial fast uptake of

adsorbate filling the micropores of the structure in decreasing pore volume order, (ii) flattening off of uptake due to surface saturation, (iii) bulk condensation of adsorbate gas forming a liquid on the surface of the material.

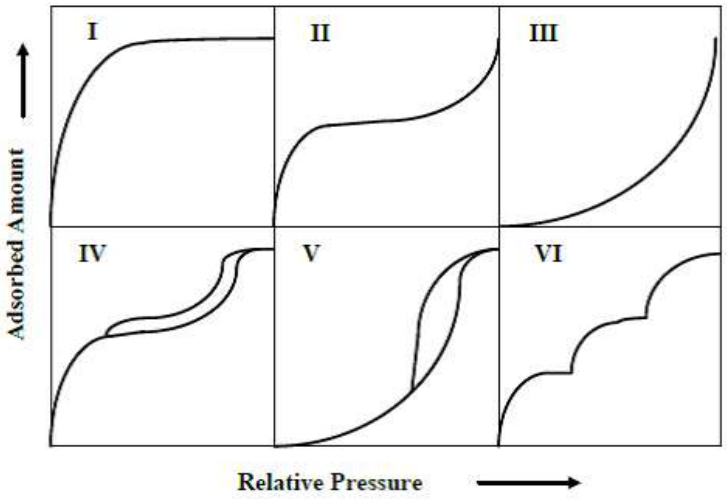

Figure 50: Diagrams of the six isotherms typical of a range of materials. *The shape of a recorded isotherm may be compared to these isotherm types to indicate the type of porous material and the adsorbant-adsorbate interactions present. Reproduced from reference 223.*

Computational approaches to calculate the ideal geometrical surface area of microporous MOFs displayed close agreement to the experimental values.[224] Furthermore, N_2 (77 K) has long been the standard analyte gas employed to determine the BET surface area; however, for porous materials that exhibit polar heterogenous surfaces, Ar (87 K)—whilst expensive—is recommended for its absence of a quadrupolar moment.[225]

The Brunauer-Emmett-Teller (BET) method is a theory published in 1938, as an extension of the monolayer adsorption work presented by I. Langmuir, which takes into consideration multilayer adsorption.[226] Calculation of the BET specific surface area is a routine measurement that yields an accurate *approximation* of the specific surface area. The resultant value should not be considered the true value, but as an *apparent surface area*, since several approximations are made:

1. A material has a set, finite number of vacant adsorption sites, filled uniformly;
2. Layers adsorbed beyond the initial layer behave as liquids;
3. The number of adsorbed layers is arbitrary, and the multilayer has infinite thickness at saturation;
4. The surface of the sample is energetically homogenous; all sites have identical heats of adsorption;
5. Adsorbed layers do not interact and
6. The heat of adsorption and condensation are identical for layers above the first.

Analysis of the surface area of a material is performed as a function of vapour pressure and can be expressed in **Equation 28.** where, P is the partial vapour pressure of adsorbate at analysis temperature (Pa); P_0 is the saturated pressure of adsorbate gas (Pa); V_a is the volume of gas adsorbed at pressure, P (ml); V_m is the volume of gas required to produce a monolayer at STP (ml); and C is a constant related to enthalpy of adsorption of the adsorbate gas on the sample.

$$\frac{1}{\left[V_a\left(\frac{P_0}{P}-1\right)\right]} = \frac{C-1}{V_m C} \times \frac{P}{P_0} + \frac{1}{V_m C}$$ ***Equation 28.***

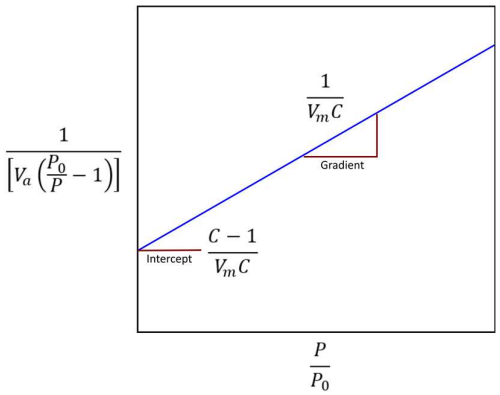

Figure 51: Determination of BET surface area. *Regression analysis of $1/[V_a((P_0/P) - 1)]$ against P/P_0 and extrapolation to determine the intercept yields information on both variables V_m and C.*

Plotting $1/[V_a((P_0/P) - 1)]$ against P/P_0, yields a graph with a slope of $C - 1/V_mC$ and an intercept of $1/V_mC$ where the values of V_m and C may be determined by a regression plot. Using the calculated V_m value, and assuming close packing physisorption, the surface area can be calculated by using the area occupied by a single molecule of the analyte gas.[227,228] Using this information the total surface area, S_{total}, and resultant specific surface area, S_{BET}, can be expressed in **Equation 30**.

$$S_{total} = \frac{V_m N_A s}{V}$$ ***Equation 29.***

$$S_{BET} = \frac{S_{total}}{a}$$ ***Equation 30.***

Where N_A is Avogadro's constant, s is the adsorption cross-section (specific to the gas molecule), V is the molar volume of the gas, and a is the sample mass. Rouquerol *et al.*[2,229] recommend that in processing these values, the porosimetry data must fulfil four criteria, the last two known as the "consistency criteria", and are laid out below to apply this theory to microporous solids such as MOFs:

1. The quantity C should be positive (*i.e.* any negative intercept on the ordinate of the BET plot is an indication that one is outside the valid range of the BET equation);
2. The application of the BET equation should be limited to the pressure range where the term $V_a(P_0 - P)$ or alternatively $V_a(P/P_0 - 1)$ continuously increases with P/P_0; all data points above the maximum in the plot should be discarded;
3. The pressure range corresponding to V_m should be within the pressure range selected for the calculation and
4. The calculated value of $V_a(P/P_0)$, *i.e.* $1/(\sqrt{C}+1)$, should not differ, say, by more than 10%, from the value of P/P_0 corresponding to the BET V_m value obtained by application of **Equation 28.** Otherwise, it is necessary to change the chosen range of relative pressures.

In doing so, resultant BET values are both standardised and physically meaningful, providing the best comparison of reported values.

The gas sorption isotherms can be further processed to extract predicted pore size distribution function (PSDF) through a number of theoretical models. One of the most prominent classical models is the 1951 Barrett-Joyner-Halenda (BJH) method. The "classical" models of PSDF calculations rely on the Kelvin equation, which relates the pressure to the radius of curvature of a liquid meniscus. The Kelvin equation is valid for materials in the mesopore range but begins to break down when applied to microporous materials such as MOFs.[230]

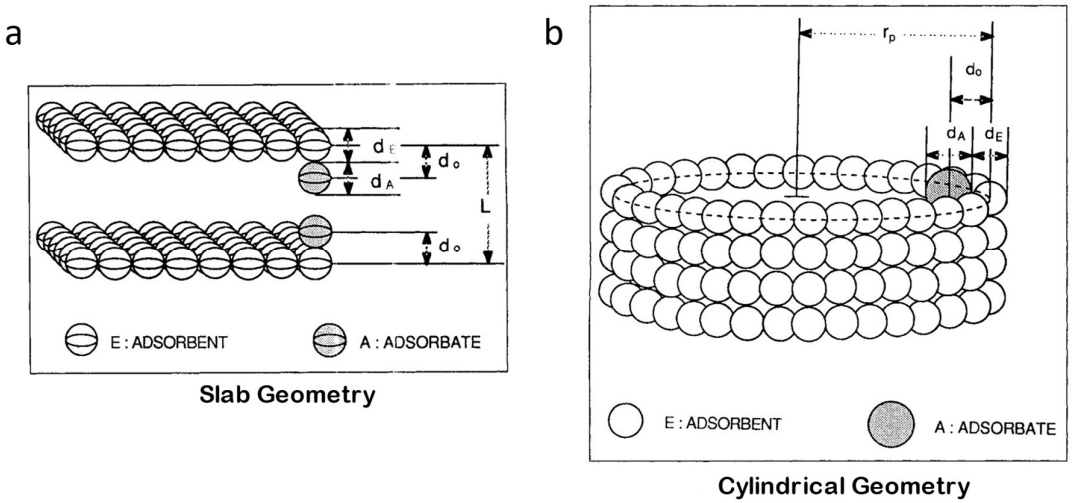

Figure 52: Slab and cylindrical geometries *used to model the pore size distribution of porous materials. Adapted from reference 231.*

In response, G. Horváth and K. Kawazoe introduced a model in 1983 based on density functional theory (DFT), which considers factors such as the direct interaction of adsorbate with the adsorbent surface and the micropore filling process. In this model, samples are treated as slabs with infinitely extending graphitic planes separated by a fixed distance (**Figure 52a**).[232] This model was further developed by A. Saito and H. C. Foley in 1991 to incorporate a cylindrical geometry to represent microporous systems such as zeolites better (**Figure 52b**).[231] In this model, it was assumed that:

1. The pore is a perfect cylinder of infinite length but finite radius, r_p;

2. The inside wall of the cylinder is a single layer of atoms, oxide ions in the case of a zeolite, which is taken as a continuum of potential interaction. The interaction with the pore wall is taken to be due only to the dispersion forces;

3. Adsorption occurs only on the inside wall of a cylinder in the micropore region, and

4. The interaction of adsorption is taken to be due only to that between the adsorbate and the adsorbent, with the latter considered to be the oxide ion of the zeolite.

Comparison of the theoretical models using gas sorption data of a zeolite with known aperture size indicated that the cylindrical model provided the best fit, accurate to ±0.005 nm in this sample. This model is expressed in **Equation 31** where N_{AV} is Avogadro's number, R is the molar gas constant, N_A is the specific density of adsorbant, N_E is the specific density of adsorbent, $A_{A\text{-}A}$ and $A_{E\text{-}A}$ are dispersion constants, d_o is the arithmetic mean of diameters of adsorbate and

adsorbent, *K* is the coefficient (**Equation 32.**), *n* is the order of the dispersion term, *m* is the order of the repulsion term, r_p is the radius of micropore cylinder, α_k and β_k are constants (**Equation 33.** and **Equation 34.**), and *Γ* is the gamma function.[231]

$$ln\left(\frac{P}{P_0}\right) = \frac{3}{4}\frac{\pi N_{AV}}{RT}\frac{(N_A A_{A-A} + N_E A_{E-A})}{d_o^4} \times \sum_{k=0}^{\infty}\left[\frac{1}{2K+1}\left(1-\frac{d_o}{r_p}\right)^{2k} \times \left\{\frac{21}{32}\alpha_k\left(\frac{d_o}{r_p}\right)^{10} - \beta_k\left(\frac{d_o}{r_p}\right)^{4}\right\}\right]$$

Equation 31.

$$K = \left(\frac{n}{n-m}\right)\left(\frac{n}{m}\right)^{\frac{m}{(n-m)}}$$

Equation 32.

$$\sqrt{\alpha_k} = \frac{\Gamma(-4.5)}{\Gamma(-4.5-k)\Gamma(k+1)}$$

Equation 33.

$$\sqrt{\beta_k} = \frac{\Gamma(-1.5)}{\Gamma(-1.5-k)\Gamma(k+1)}$$

Equation 34.

3.1.9.2 Experimental

All pycnometric measurements were conducted with a Micromeritics Accupyc 1340 helium pycnometer. The typical mass used for each test was around 100 mg, and the reported value was the mean and standard deviation from a cycle of 10 measurements.

Chapter 4 Gas Sorption Measurement

CO_2 (273 K, ice water bath) and N_2 (77K, liquid N_2) adsorption measurements were performed using a Micromeritics ASAP 2020 instrument with around 50 mg for N_2 measurements. All samples were degassed at 200 °C overnight before transferring to the analysis port. Sample masses were remeasured post-degas activation.

The argon physisorption experiments were carried out at 87 K on a BEL max apparatus (Microtrac BEL) coupled with a helium cryostat. After weighing (approx. 100 mg), the samples were outgassed to 200 °C for 10 h prior to temperature equilibration for the experiments at 87 K. A stepwise introduction of gas (argon purity 99.9999%) was employed. Helium was used for dead space calibration after the argon adsorption measurement. The micropore size distribution was calculated using the Horwath-Kawazoe method[232] *via* the Saito-Foley approach.[231]

High-pressure CO_2 adsorption at 303 K was carried out on a Rubotherm electromagnetic balance set-up (Rubotherm gmbh). After weighing (approx. 200 mg), the samples were outgassed to 200 °C for 16 h prior to temperature equilibration for the experiments at 303 K. A stepwise introduction of gas (CO_2 purity 99.998%) was employed. Helium was used to correct for buoyancy effects prior to the CO_2 adsorption measurements.

Water adsorption was carried out on a Hiden balance set-up (Hiden) at 298 K. After weighing (approx. 30 mg), the samples were outgassed to 200 °C for 16 h prior to equilibration at the set temperature of the experiments at 298 K. A carrier gas of nitrogen was used in which the relative water humidity was controlled between 2 and 98% in stepwise increments.

Chapter 5 Gas Sorption Measurements

Measurements here were performed using a Micromeritics ASAP 2020 instrument with no less than 20 mg of sample in an identical manner to those performed in Chapter 4**.**

Chapter 6 Gas Sorption Measurements

Samples were degassed overnight at the specified temperature for 12 hrs on before transferring to the analysis port of a Quantachrome iQ2 instrument. Sample weight was measured post-degas activation. Sample temperature was accurately equilibrated at 273 K and 293 K with a temperature-controlled water bath and at 77 K with liquid N_2. Gas adsorption measurements were performed using ultra-high purity (99.99%) gases.

3.1.10 Scanning Electron Microscopy (SEM)

Scanning electron microscopy (SEM) is a technique that can be used to image samples at a much greater magnification than capable with optical microscopes. SEM uses an electron gun that emits a concentrated electron beam down a column under high vacuum. The high-energy electron beam is then manipulated through a series of condenser lenses and apertures to achieve a desired irradiation spot size before reaching the mounted sample. SEM produces images by rastering the sample with this electron beam and recording spatially resolved data, the resolution of which is determined by the spot size, down to an approximate limit of *ca*. 1 nm.[233]

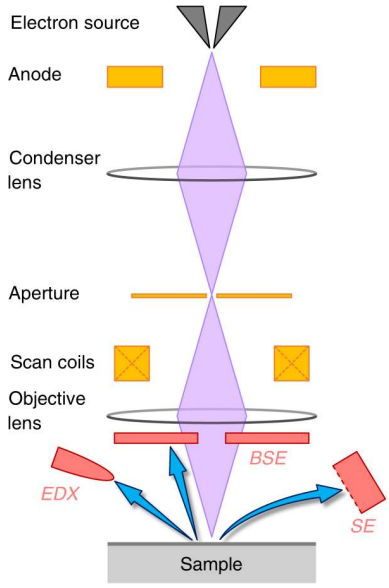

Figure 53: An illustration of a typical scanning electron microscope apparatus. *Adjustment of each component provides a different form of control of the irradiating electron beam. Reproduced from reference 234.*

The multitude of different interactions of electrons with matter gives rise to several possible analytical techniques, such as the analysis of—in order of their surface penetration depth—cathodoluminescence, Auger electrons, secondary electrons, elastically and inelastically backscattered electrons, characteristic X-rays, continuum X-rays, and fluorescent X-rays. However, typical SEM apparatus is limited to the recording of backscattered and secondary particles/photons. A significant issue with using this technique on non-conductive samples is sample charging; when no path exists for irradiating electrons to flow to earth, the sample becomes charged and repels incoming electrons; this typically results in image distortion. To avoid this, samples are typically finely coated in a highly conductive material such as chromium, gold, or palladium using a sputter coater.

3.1.10.1 Experimental

Chapter 4 SEM Measurements

The surface morphologies of the glass composite samples were investigated using a high-resolution scanning electron microscope, FEI Nova Nano SEM 450. All samples were dried at 30 °C followed by chromium coating prior to imaging.

Chapter 6 SEM Measurements

SEM was performed using a Thermo ScientificTM Phenom ProX scanning electron microscope. Powder and monolithic samples were prepared for SEM by securing to aluminium SEM pin stubs using carbon tape. Samples were coated in gold using an Emtech K575 sputter coater.

3.1.11 Scanning Transmission Electron Microscopy (STEM)

Scanning transmission electron microscopy (STEM) is distinct from SEM due to the transmission of the electron beam through the sample and the detector located underneath. To facilitate this, samples are spread over a grid to maximise signal detection whilst minimising sample exposure. Modern instruments may typically form a probe with a size in the range 0.1–10 nm, enabling nanoscale variations to be mapped. The analytical signal may be recorded at each probe position to reveal local variations in, for example, atomic structure and composition. The simultaneous detection of multiple signals, including annular dark-field imaging, scanning electron diffraction (SED), energy-dispersive X-ray spectroscopy (EDS), and electron energy-loss spectroscopy (EELS), provides the multivariant characterisation of chemical composition and crystallinity mapping of nm-sized crystals.[235]

3.1.11.1 Scanning Electron Diffraction (SED)

SED involves the acquisition of a two-dimensional electron diffraction pattern at every position as a narrow electron probe is scanned across the specimen. When the electron probe is positioned on a crystalline region of material, strong diffraction to Bragg reflections will typically be observed, whereas when the electron probe is positioned on non-crystalline material, no sharp Bragg reflections will be measured. Determining probe positions at which sharp diffraction peaks are recorded provides a way to observe crystalline and non-crystalline regions directly.[236] This was achieved by finding diffraction peaks in every measured diffraction pattern using a difference of Gaussians method, which involves

subtracting a blurred version of the diffraction pattern from a less blurred version of the diffraction pattern, as implemented in the pyXem library.

3.1.11.2 Energy-Dispersive X-ray Spectroscopy (EDS) Imaging

One such specialised technique is energy-dispersive X-ray spectroscopy (EDS) which detects the emission of characteristic X-rays for fingerprint elemental analysis (**Figure 54a**). In this method, a focused electron beam ionises the sample, generating unstable electron vacancies. Electrons from higher energy states relax to fill this hole, and as a result, the difference in energies of the two states is released from the sample in the form of an X-ray photon. The energy of the emitted X-ray is dependent on the electronic and vibrational energy states that the electron was knocked from, and those states from which the relaxing electron originated.[237]

EDS uses the Siegbahn notation[238] of the Lyman, Balmer, Paschen, Brackett *etc.* spectral series of the hydrogen atom (**Figure 54b**). Here, the lowest energy shell is denoted as *K*, followed sequentially by the *L, M, N etc*. shells, the transitions from the closest higher energy shell is denoted as the α transition, followed by the β transition from the second closest higher energy shell, such that all transitions to the *K* shell are named K_α, K_β, K_γ *etc.* and those to the L shell are named L_α, L_β, L_γ *etc.* Since the K shell is located closest to the nucleus, it does not experience the shielding of higher state shells. As such, it has the highest ionisation energy, causing the *K* series to display the highest energy signals. The probe is scanned across a selected area of the sample generating an EDS pattern for each image pixel. This EDS pattern measures the intensity against the energy of the detected X-rays wherein the assignment of known, strong, and non-overlapping element-specific transitions may be performed. This shows local changes in element presence and abundances directly proportional to the number of atoms per unit volume of the elements.[239]

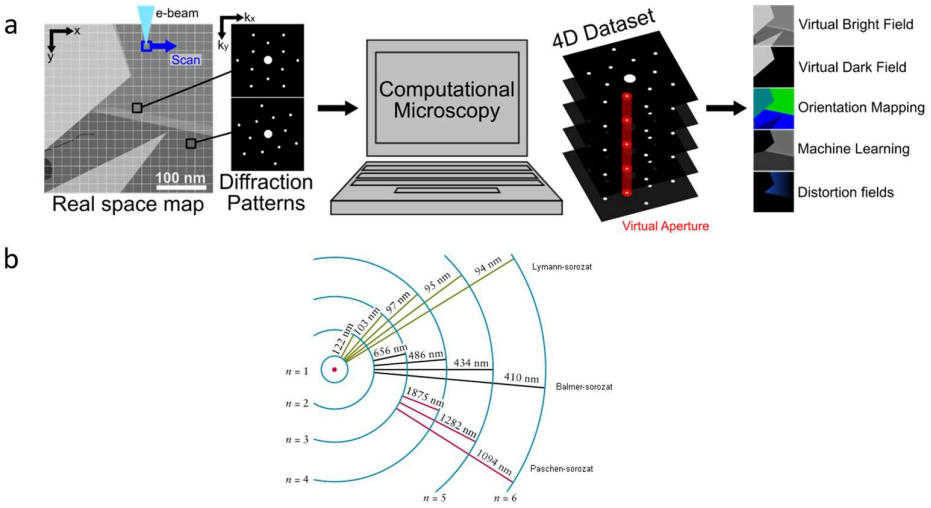

Figure 54: Schematic of STEM processing and spectral series. *a. Schematic of the SED data acquisition and processing, reproduced from reference 240, and b. illustration of the hydrogen spectral series, reproduced from reference 241.*

3.1.11.3 Electron Energy-Loss Spectroscopy (EELS)

Electron energy-loss spectrometry (EELS) is a technique that measures the kinetic energy of the transmitted scattered electrons. There may be several modes of electron-energy loss within a system, such as Bragg scattering, radiation damage, phonon excitation (macroscale molecular motions), plasmon excitation (oscillatory sample electron displacement caused by the Coloumb repulsion of sample electrons by the fast-moving electron radiation forming a *plasmon wake*), and core-electron excitation, each of which display measurable, characteristic electron energy losses. Analysis of the energy loss profile may be performed to determine properties such as elemental composition, elemental oxidation state, core-loss/near-edge fine structure, material thickness and electronic properties of semiconductors and insulators.[242]

3.1.11.4 Experimental

Chapter 4 STEM Analysis

Scanning electron diffraction (SED) was performed using a JEOL ARM300F at the Diamond Light Source, U.K., fitted with a high-resolution pole piece, cold field emitter, and JEOL spherical aberration correctors in both the probe forming and image forming optics. The instrument was operated at 200 kV and aligned in a nanobeam configuration using the corrector transfer lenses and a 10 µm condenser aperture to obtain a convergence semi-angle of ~1.6 mrad and a diffraction-limited probe diameter ~1.6 nm. Data were acquired with a scan step size of ~4 nm and a camera length of 15 cm. The probe current was ~14 pA. A Merlin-medipix direct electron detector,[243,244] which is a counting type detector, was used to record the electron diffraction pattern at each probe position with an exposure time of 0.5 ms per probe position leading to a total electron fluence of ~200 $eÅ^{-2}$ based on the probe current, exposure time, and assuming a disk-like probe of the diameter above. SED was acquired over a raster pattern comprising 256 × 256 probe positions, and each diffraction pattern comprised 256 × 256 pixels. X-ray EDS maps were acquired from the same regions, following SED acquisition, using a larger probe current, obtained using a 150 µm condenser aperture in order to generate sufficient X-ray counts. SED experiments were later performed with the following parameters: a convergence semi-angle of ~0.3 mrad; a diffraction-limited probe size of diameter ~5 nm; a probe current of ~6 pA, and an exposure time of 1 ms per probe position.

STEM, EDS, EELS and tomography were performed using an FEI Osiris microscope (Thermo Fisher Scientific) equipped with a high-brightness X-FEG electron source and operated at 80 kV. The beam convergence semi-angle was set to 11.0 mrad. For EELS, the collection semi-angle was estimated as 40.8 mrad. EDS was acquired using a Super-X EDS detector system with four detectors mounted symmetrically about the optic axis of the microscope. For STEM-EDS tomography, EDS spectrum images were acquired over a tilt-series from −65° to 75° in 10° increments using a Fischione tomography holder, with a probe current estimated at <450 pA. Pixel dwell times were increased at high tilt due to a large number of copper counts at increasing tilt-angle.

Chapter 5 STEM Analysis

Analysis was performed in an identical manner to those in Chapter 4 with slight adjustments of: convergence semi-angle of ~0.8 mrad and a diffraction-limited probe diameter <5 nm. Data were acquired with a scan step size of ~5.2 nm and a

camera length of 20 cm. The probe current was ~2 pA. each probe position was exposed for 1 ms per probe position, leading to a total electron fluence of ~ 5 eÅ^{-2}.

Data Processing

SED data were processed using the open-source pyXem Python library to find diffraction peaks in every measured diffraction pattern using a difference of Gaussians method, which involves subtracting a blurred version of the diffraction pattern from a less blurred version of the diffraction pattern.

Data were processed using Hyperspy[245], an open-source software coded in Python. Maps of each X-ray emission line of interest (Zr L_α, Al K_α, Zn K_α) were first extracted by integrating in an energy window, background-subtracted by linear interpolation from adjacent regions of the spectrum without other X-ray peaks present. Map intensities were then re-normalised such that the total intensity of each element was constant throughout the tilt-series, a valid assumption for particles where the mass of the element in the field of view is constant throughout the tilt-series. The re-normalised maps were then aligned by centre-of-mass, and the tilt-axis was adjusted using Scikit-Image, an open-source image processing software coded in Python, by applying shifts and rotations to minimise artefacts in back-projection reconstructions. A compressed sensing reconstruction algorithm coded in MATLAB (Mathworks) was used to perform independent reconstructions of the metal-centre spatial distributions. This compressed sensing tomography implementation used three-dimensional total generalised variation[246] regularisation in conjunction with a real-space projector from the Astra toolbox[247] and using the primal-dual hybrid gradient method[248] to solve the reconstruction problem. Reconstructions were visualised in Avizo (Thermo Fisher Scientific) software without any further image processing. Visualisations are presented as volume renderings where each volume element is assigned a colour and relative solid appearance based on the intensity at the corresponding volume elements of the reconstruction. Visualisations for each independent element reconstruction were superimposed in the final visualisations, and a selection of cuts through the volume were used to examine sub-surface features.

3.1.12 Thermomechanical Analysis (TMA)

Thermomechanical analysis (TMA) is a one-dimensional measurement, defined by the International Confederation for Thermal Analysis and Calorimetry (ICTAC) as "*A technique where the deformation of the sample is measured under constant load*".[249] In a typical experiment, a sample is placed on a stage, and a rod is placed atom the sample. A specified load is then applied to the rod, providing a known force to the sample. A furnace is lowered over the sample with a proximal thermocouple for accurate temperature readings (**Figure 55a**). Programmable heating and cooling sequences are then specified, controlling such parameters as the heating rate, end temperatures, isothermal regions. During the experiment, any change in the height of the rod as a result of the material expansion is measured through a highly precise linear variable displacement transducer (LVDT).[250] By changing the tip shape of the push rod, different thermomechanical properties may be probed; a flat end is typically used for expansion or compression properties, where finer tips may be used to study penetration or flexure properties (**Figure 55b**).

Characteristic features of the material, such as the glass transition temperature, T_g, melting temperature T_m, and the softening temperature, T_s, may be extracted from the recorded change in the specimen length (**Figure 55c**). The softening point is the temperature at which the material passes an arbitrary softness, defined as the intersection of the extrapolated regions either side of the transition.[250] From a region of linear expansion, the coefficient of thermal expansion, α, may be extracted from the initial length, L_0, and the gradient of the expansion.

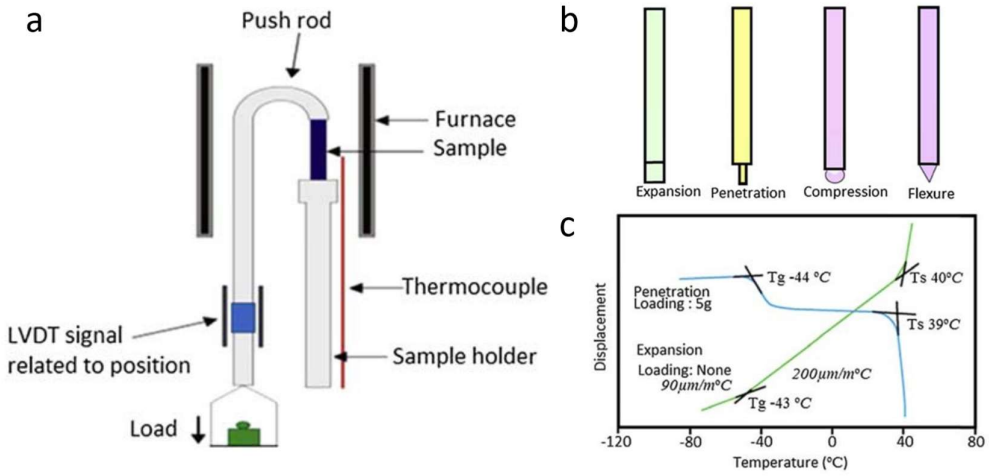

Figure 55: The typical setup, rod tips, and data from thermogravimetric analysis. *a. Schematic of a typical setup for thermomechanical analysis displaying a push rod atop a sample specimen within a furnace. b. A selection of push rod tip shapes and their uses, and c. typical data from a polymer sample detailing the glass transition and softening temperatures. Reproduced from reference 250.*

$$\alpha = \frac{1}{L_0}\left(\frac{\Delta L}{\Delta T}\right)_P$$ ***Equation 35.***

3.1.12.1 Experimental

Data were taken on a small portion (*ca*. 1 mm × 1 mm) of each of the as-synthesised composite monolith materials on a TA Instruments Q400 thermomechanical materials analyzer (TMA). The experiment was performed with a force of 0.05 N and protected by N_2 gas.

3.2 Material Preparation

3.2.1 Synthesis of Metal–Organic Frameworks

IRMOF-8 A sample of IRMOF-8 [$Zn_4O(ndc)_3$; ndc = 2,6-naphthalenedicarboxylate, $C_{12}H_6O_4^{2-}$] was obtained from Mark Allendorf (Sandia National Laboratories, United States) which displayed thermal stability under Ar to 450 °C and matched the predicted pattern generated from the .cif file in the literature confirming structural properties.

MIL-53 Aluminium nitrate nonahydrate (26 g, 69.3 mmol) and terephthalic acid (5.76 g, 49.6 mmol) were dissolved in water (100 ml) and placed into a Teflon-lined autoclave and placed in an oven at 220 °C for 72 hours. The resulting powder was washed with deionised water (3 x 30 ml) and dried in a vacuum oven at 150 °C for 24 hours.

MOF-5 Terephthalic acid (5.065 g, 30.5 mmol) and trimethylamine (8.5 mL) were dissolved in DMF (400mL). Zinc acetate dihydrate (16.99 g, 77.4 mmol) was dissolved in DMF (500 mL). The zinc salt solution was added to the organic solution with stirring over 15 minutes, forming a white precipitate and the mixture was stirred for a further 2.5 hrs. The precipitate was filtered and immersed in *N,N*-dimethylformamide (DMF, 250 mL) overnight. It was then filtered again and immersed in chloroform (350 mL). The solvent was exchanged 3 times over 7 days (after the second, third and seventh day). The bulk of the solvent was decanted and the product was evacuated overnight under vacuum and then heated under vacuum for 6 hrs.

ZIF-4 Zinc nitrate hexahydrate (1.2 g, 4.03 mmol) and imidazole (0.9 g, 13.2 mmol) were dissolved in DMF (DMF, 90 mL) and transferred to a 100 mL screw-top jar and heated to 100 °C for 72 hrs. Product was allowed to cool to room temperature and crystals were separated by vacuum-assisted filtration and washed with DMF (3 x 30 mL). Crystals were activated by washing with dichloromethane (DCM, 3 x 30 mL) and dried under vacuum at 130 °C for 16 hrs using a vacuum oven.

ZIF-62 Zinc nitrate hexahydrate (1.65 g, 5.54 mmol) and imidazole (8.91 g, 130 mmol) were added to a 200mL screw-top jar, dissolved in DMF (75 mL) and stirred for 1 hr. Once complete dissolution was achieved, benzimidazole (1.55 g, 13.1 mmol) was added heated to 130 °C for 48 hrs. Product was allowed to cool to room temperature and crystals were separated by vacuum assisted filtration and washed with DMF (40 mL) and DCM (40 mL) before being dried in the oven at 60 °C overnight.

MIL-120 Aluminium nitrate nonahydrate (1.44 g, 6.76 mmol), 1,2,4,5-benzenetetracarboxylic acid (0.225 g, 0.885 mmol), sodium hydroxide (4 M, 1.53 mL), and water (9 mL) were added to a Teflon lined autoclave and placed in a 210 °C preheated oven and held for 24 hrs. The resulting white powder was filtered and washed with water (40 mL) before being transferred to a 100 ml round-bottom flask with water (60 mL) and refluxed at 100 °C for 10 hrs. The product was centrifuged (2500 rpm, 15 mins) and dried in the over at 70 °C overnight.

MIL-126 Scandium nitrate hydrate (85 mg, 0.368 mmol), biphenyl-4,4'-dicarboxylic acid (68 mg, 0.281 mmol), DMF (6.25 mL), conc. hydrochloric acid (37%, 25 µL) were added to a 25 mL screw-top jar and sonicated until dissolution (~15 mins). The clear solution was placed into a 120 °C preheated oven for 24 hrs. The product was transferred to a centrifuge tube and centrifuged (2500 rpm, 15 mins) to collect a white powder. This powder was stood in DMF (10 mL) overnight and centrifuged again (2500 rpm, 10 mins) and acetone exchanged three times over three days before collecting the product by centrifuging (2500 rpm, 5 mins), decanting the liquid and drying in a 60 °C preheated oven overnight.

CUMOF-9 Ytterbium(III) chloride hexahydrate (1.08 g, 2.79 mmol) and water (6.13 mL) was added to a Teflon lines autoclave and stirred for 2 mins. 2,6-naphthalenedicarxylic acid (0.103 g, 0.476 mmol) and trimethylamine (0.111 mL) were added to to the solution and the mixture was stirred for a further 5 mins. The suspension was then sealed and

placed in 145 °C preheated oven and held for 4 hrs. The reaction vessel was allowed to cool to room temperature and was isolated by filtration under vacuum and washed with ethanol (30 mL) before drying ain the over at 70 °C overnight.

MIL-118 Aluminium nitrate nonahydrate (150 mg, 0.704 mmol) and 1,2,4,5-benzenetetracarboxylic acid (50 mg, 0.197 mmol) were added to a Teflon lined autoclave before adding water (5 mL). The autoclave was sealed and placed into a 210 °C preheated oven for 24 hrs. The product of this was isolated by replacing the liquid with water (20 mL) and centrifuging (2500 rpm, 10 mins) twice. The resultant white powder was placed in a 70 °C preheated oven overnight.

ULMOF-1 Lithium nitrate (0.345 g, 5.00 mmol), 2,6-naphthalenedicarboxylic acid (0.565 g, 2.61 mmol), ammonium fluoride (38 mg), and DMF (15 mL) were added to a Teflon lined autoclave and placed in a 180 °C preheated oven and held for 5 days. Upon cooling, the reaction mixture was transferred to a centrifuge tube and the liquid was replaced with ethanol (20 mL). The sample was stirred for 5 mins before centrifuging (3000 rpm, 5 mins) to collect a white powder which was dried in an oven at 60 °C overnight.

3.2.2 Synthesis of Metal–Organic Framework Crystal–Glass Composites

Chapter 4 MOF CGC Synthesis

A fabrication process was developed for the composites in which powders of the crystalline glass former (ZIF-62) and crystalline MOF filler were ball-milled together for varying lengths of time. After amorphisation of the glass former through ball-milling for various times and frequencies, 100 mg of the mixture was compressed into a 13 mm diameter circular pellet under 10 tonnes of force (0.739 GPa pressure) for 1 minute. The pellet was placed between glass slides (**Figure 56**) and heated in a furnace for 10 minutes at 450 °C at a heating rate of 10 °C min^{-1} under an argon atmosphere. The resulting composite was then allowed to cool to room temperature in air.

Chapter 5–**Chapter 7** MOF CGC Synthesis

MOF CGCs were prepared in an identical manner to those in Chapter 4 with the adjustment of heating at 20 °C min^{-1} to 450 °C and holding isothermally for 15 minutes before cooling.

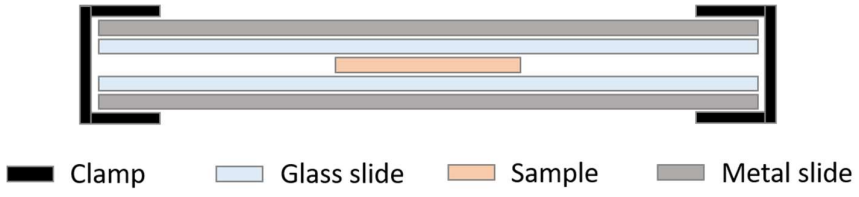

Figure 56: MOF CGC sample preparation. *The pelletised sample is placed between glass slides and held together using metal slides and clips before placing into the furnace.*

3.2.2.1 Ball-Milling

Samples were ball-milled by placing *ca*. 100 mg of sample into a steel jar with a 7 mm stainless steel ball and shaken at specified frequency. General settings used are 25 Hz for 10 minutes to retain crystallinity, but specific times and frequencies used are stated where applicable.[52]

Chapter 4 Synthesis of a Prototypical MOF Crystal–Glass Composite (MOF CGC)

In this chapter, a variety of MOFs are studied to determine suitable candidates for both the crystalline phase and glass matrix for MOF CGC synthesis. The first example of a metal–organic framework crystal–glass composite is synthesised, and various analytical techniques are employed to study features of the composite, such as crystal integrity and domain proximity. A system comprising a flexible MOF, MIL-53, within an a_gZIF-62 matrix is found to retain crystallinity. Notably, the room temperature unstable, large-pore phase of MIL-53 is suspended in the MOF glass at room temperature. Due to this metastable state stabilisation, a 25% MIL-53 by weight (referred to as wt% herein) is observed to uptake a greater quantity of CO_2 than the combination of its parent materials. This work is published in the following manuscripts:

[1] Hou J., Ashling C. W., Collins S. M., Krajnc A., Zhou C., Longley L., Johnstone D. N., Chater P. A., Li S., Coulet M.-V., Llewellyn P. L., Coudert F.-X., Keen D. A., Midgley P. A., Mali G., Chen V., and Bennett T. D., **Metal–organic framework crystal–glass composites**, *Nature Communications* 2019, **10**, 2580.

Towards this publication, my contributions included the recording and processing of the total scattering data at Diamond Light Source, UK, to generate the pair distribution functions (PDF) and in the recording of the nanoindentation data. Furthermore, I aided in analysing the PDF, gas sorption, and NMR data before helping to write the manuscript.

[2] Tuffnell T. M., Ashling C. W., Hou J., Li S., Longley L., Ríos Gómez M. L., and Bennett T. D., **Novel metal–organic framework materials: blends, liquids, glasses and crystal–glass composites**, *Chem. Comm*. 2019, **55**, 8705.

In this review, I contributed a section on MOF CGCs regarding the work carried out in the previous publication.[251]

4.1 Material Selection

In the synthesis of a suspended MOF material, the primary consideration in material selection is component compatibility. In this work, the aim is to develop a material with a crystalline MOF embedded within a solid matrix where the selected application of the crystalline component is achievable whilst supported within the host matrix. In such a material, the practicality of the active MOF material is improved for systems ill-suited to microcrystalline powders, especially in, for example, gas storage systems. Therefore, component compatibility, preventing decomposition, is paramount to the synthesis of a workable product.

4.1.1 Selection of a Host Matrix

Current methods to fabricate bulk MOF materials using a host matrix have utilised polymers, silica, and porous carbons.[251] Mixed-matrix membranes have been sucessful in utilising the liquid state of polymers to encapsulate the crystalline MOF material through the use of a liquid "ink" state. The ability to flow permits the encapsulation of a MOF *within* a material and not be dependent on surface interactions to maintain structural integrity. Similar to these materials, the liquid state of a porous glass would likely permit the formation of a porous composite with greater stiffness than a MMM. A few selection criteria for the glass phase must be implemented to form a composite using a glass matrix:

1. The glass-forming component must melt at a temperature at which the crystalline material remains intact.
2. The viscosity of the melt liquid must be low enough to undergo appreciable flow to fully suffuse the crystalline material.
3. The glass transition temperature of the resultant MOF CGC must be high enough for elevated composite working temperatures, and
4. The host glass must be permeable to the analyte materials, unless a percolation threshold (the minimum permeable material required at which a substance may pass through an otherwise impermeable material *via* a network of connected permeable components) has been achieved.

Criterion 1 precludes the use of silica-based glasses since the required temperatures far exceed the decomposition temperatures of even the most thermally stable of MOFs. Therefore, the glasses formed from hybrid materials are considered in **Table 5**.

Whilst MOF glass (a_gMOF) research is a burgeoning topic in the field of hybrid glasses, the selection of available a_gMOFs is minimal in its nascency. Furthermore, the first known MOF glass former was discovered to melt at 593 °C (ZIF-4), which far exceeds the decomposition temperature of a vast majority of MOFs. However, the melting of several further MOFs has since been revealed, which exhibit significantly lower melting temperatures (**Table 5**).

Another class of hybrid materials referred to as inorganic coordination polymers (*i*-CPs) (though the definition is widely disputed) display significantly lower melting temperatures than ZIFs. However, whilst the ability to encapsulate an expanded selection of MOFs is undoubtedly beneficial, this reduction in T_m is accompanied by an associated decrease in T_g. As such, the working temperatures at which the resultant MOF CGC may be applied is significantly reduced (**Table 5**).

Table 5: A list of known melting hybrid materials. *Adapted from reference 69.*

Entry	T_m [°C]	T_g [°C]	Glass Applications	Ref
***o*-CPs (organic coordination polymers)**				
$[M(1,2,4\text{-triazole})_2(H_2PO_4)_2]$ ($M = Zn^{2+}$, Cd^{2+}, Cr^{2+}, Mn^{2+})	184	Zn^{2+} = 32 Cd^{2+} = 79–90 Cr^{2+} = 62 Mn^{2+} = 90	Anhydrous conductivity	156, 249–251
ZIF-4, $Zn(Im)_2$	593	LDA = 316 HDA = 292		70
ZIF-62(Zn): $Zn(Im)_{2-x}(bIm)_x$ $Zn(Im)_{1.75}(bIm)_{0.25}$	437	318	Kinetic separation of propylene/propane	58, 65
ZIF-62(Co): $Co(Im)_{2-x}(bIm)_x$ $Co(Im)_{1.75}(bIm)_{0.25}$	432	290		58, 72
ZIF-76, $Zn(Im)_{1.62}(5\text{-ClbIm})_{0.38}$	451	310	Gas uptake of CO_2 and N_2	73
ZIF-76-mbim, $Zn(Im)_{1.33}(5\text{-mbIm})_{0.67}$	471	317		73
Cu(isopropylimidazolate)	185	NA		255
***i*-CPs (inorganic coordination polymers)**				
$[Zn(HPO_4)(H_2PO_4)_2](ImH_2)_2$	160	30	Anhydrous H^+ conductivity	159
$[Zn_3(H_2PO_4)_6(H_2O)_3\cdot bimH$	164	NA		159
$[Zn_3(H_2PO_4)_6(H_2O)_3]\cdot H(2MebIm)$	97	NA		159
$[Zn_2(HPO_4)_2(H_2PO_4)(5ClbImH)_2](H_2PO_4)(MeOH)$	148	72	Gas uptake (H_2O and methanol vapour) and anhydrous H^+ conductivity	256
$[Cd_3(SCN)_2Br_6(C_2H_9N_2)_2]$	142	NA		257
$[Cu_2(SCN)_3(C_2bpy)]$	187	68		161
$[Cu_2(SCN)_3(C_4bpy)]$	138	59		
$[Cu_2(SCN)_{12}(Phbpy)_4]$	217	71		
$[Cu_2(SCN)_3(3\text{-Pybpy})]$	203	72		
(1-butyl-4-methylpyridinium)$[Cu(SCN)_2]$	80	NA		160

[a] Im=imidazolate, bIm=benzimidazolate, 5-ClbIm=5-chlorobenzimidazolate, 2MebIm=2-methylbenzimidazolate, C_2bpy=1-ethyl[4,4'-bipyridin]-1-ium, C_4bpy=1-butyl[4,4'-bipyridin]-1-ium, Phbpy=1-phenyl[4,4'-bipyridin]-1-ium, 3-Pybpy=[3,1':4',4''-terpyridin]-1'-ium, NA=not available. [b] Tg depends on the time of the ball milling processes. [c] Gas uptake is reported for glasses with $[Zn(Im)_{2-x}(bIm)_x]$, where x=0.05, 0.17, and 0.35. [d] Gas uptake is observed for $[Zn(Im)_{1.0}(5\text{-ClbIm})_{1.0}]$ and $[Zn(Im)_{0.93}(5\text{-mbIm})_{1.07}]$.

Were it not for the relatively high temperatures required to process MOF glasses, these materials would be ideal candidates for several reasons: firstly, MOFs exhibit relatively high glass transition temperatures, permitting thermal stability to a broader range of temperatures; secondly, selected a_gMOFs have demonstrated permanent porosity, ideal for the fabrication of a porous composite; and lastly, a_gMOFs encompass similar chemical identities to the supported

crystalline MOF due to their inherent chemical similarity. The concession to the use of these materials is that the available selection of crystalline MOFs is significantly reduced.

Despite their high melting temperatures, α_gMOFs are selected here due to their numerous material advantages. In response, the glass-forming MOF with the lowest T_m is selected to allow for the most extensive range of available crystalline MOF materials. At the time of experimentation, the lowest known melting temperature of a ZIF was ZIF-62(Co), with a melting temperature, T_m, of 432 °C (**Table 5**). However, ZIF-62(Zn) was selected for experimentation since (i) there is only a slight difference in the melting temperatures between the two analogues (5 °C), (ii) zinc salts are cheaper, and (iii) cobalt species are significantly more toxic and carry avoidable associated risks.

4.1.2 Selection of a Crystalline Component

The primary concern in selecting a crystalline MOF component whilst using a MOF glass matrix is thermal stability. Despite the tens of thousands of reported MOF structures, few are thermally stable above 437 °C (T_m of ZIF-62(Zn) – hereon denoted as ZIF-62) as shown in **Section 2.2.2**. The exact decomposition temperature of MOFs is a result of the delicate interplay between the metal–linker bond strengths, linker decomposition, and node stability. ZIFs are amongst the most stable of MOF materials due to the lack of low-temperature carboxylate functional group decomposition and strong metal–linker bonds.

For the liquid MOF to suffuse the crystalline MOF, they must be both subject to the same thermal treatment, and thus the T_m of the selected MOF glass former is the minimum requirement to melt the MOF glass. Decomposition of the crystalline component would result in a non-functional composite—or in the case of partial degradation, the introduction of carbonised product, discolouration, and possible macroscale crack formation in the end composite.

Thermogravimetric analysis is, to some degree, a standardised measurement in the MOF field, especially in the discovery of *new* MOFs. However, at the time of writing, no single body of research detailing the decomposition temperatures of any substantial range of MOFs exists; therefore, a targeted search would not be possible. Determination of thermal stability from TGA is also complicated by the inconsistent use of an inert atmosphere on heating (such as nitrogen or argon) which suppresses oxidative decomposition, giving different thermal stabilities in each case. Furthermore, thermal stability during an isothermal regime is difficult to predict from a TGA carried out at a constant heating rate to decomposition. In this case, isothermal heating is required as sufficient time must be given to the mixture at a temperature above the melting point, T_m, of the glass-forming material for the glass component to flow appropriately. Additionally, the combination of crystalline and glass MOFs must be such that no flux melting occurs–a phenomenon known for ZIF materials.[258] With this in mind, several relatively thermally stable frameworks have been listed in **Table 6**.

MIL-53 appears to be an ideal study case due to its thermal stability, inexpensive reagents, simple solvothermal synthesis, and considerable porosity.[121,259] Additionally, the breadth of research regarding the crystalline structure and phase transitions of MIL-53 may be beneficial to the characterisation of the structure. MOF decomposition has subsequently been explored in more detail.[117] This review delineates the exact method of decomposition for a variety of frameworks

and establishes the relationship between the decomposition temperature and node and ligand stability in MOFs. This review supports ideas expressed in this section regarding the consistency of reporting MOF stabilities using TGA.

Table 6: Potential MOFs compatible with a$_g$ZIF-62. *Potential metal–organic framework materials (where rough decomposition temperatures have been extracted from the onset of decomposition) to outline candidates which display thermal stability to above 437 °C.*

MOF	Composition	T_d / °C *	Function	*Ref*
IRMOF-8	$[Zn_4O(ndc)_3]$	450	Friedel-Crafts Acylation	260
MIL-53	[Al(OH)(BDC)]	500	Gas Sorption	259
MIL-68	$[V^{III}(OH)(BDC)]$	~550		261
MIL-118	$[Al_2(OH)_2(C_{10}O_8H_2)]$	495		191
MIL-120	$[Al_4(OH)_8(C_{10}H_8H_2)]$	560		262
MIL-126 (Sc)	$[Sc_3O(H_2O)_2(bpdc)_3X]$ (where X = OH^- or Cl^-)	~500		263
MOF-5	$[Zn_4O(BDC)_3]$	440	Friedel-Kraft Alkylation	264
NOTT-300	$[Al_2(OH)_2(C_{16}O_8H_6)]$	400	Selective Gas Capture	265
NU-1000	$[Zr_6(\mu_3\text{-}OH)_8(OH)_8(TBAPy)_2]$	450	Catalyst Support	264, 265
UIO-66	$[Zr_6O_4(OH)_4(BDC)_6]$	375	Membranes	266, 267
UL-MOF-1	$[Li_2(2,6\text{-ndc})]$	610		192
ZIF-8	$[Zn(mIm)_2]$	500	Membranes	268, 269

*Conditions specified in the reference

4.2 MIL-53 Metal–Organic Framework Crystal–Glass Composites

With the chosen material components of MIL-53 and ZIF-62(Zn) as the first candidates for use in a composite of this variety, the synthesis of a composite prototype is detailed herein. The composites formed through the suspension of a crystalline MOF within a MOF glass matrix will be called metal–organic framework crystal–glass composites, or MOF CGCs for short.

4.2.1 Material Synthesis and Characterisation

MIL-53 and ZIF-62 were respectively hydrothermally and solvothermally synthesised according to their published procedures (see **Section 3.2.1**) and powder X-ray diffraction data were recorded of the resulting white crystalline powders (**Figure 57**). A small sample holder was used in these experiments, and an imperfect instrumental beam setup can be seen here in the elevated baseline at low angles. ZIF-62 matched well with the simulated crystalline pattern, and the MIL-53 powder pattern matched with the large-pore as-synthesised MIL-53 structure (MIL-53-as). However, extra peaks are present in both PXRD profiles, at *ca*. 8° and 12° 2θ in **Figure 57a** and again at *ca*. 14° and 22° 2θ **Figure 57b**. Le Bail or Rietveld refinement of these patterns may indicate whether these inconsistencies are impurities; however, the magnitude of the difference is small enough that no further investigation is carried out. MIL-53 is typically synthesised in this MIL-53-as phase which contains excess synthesis material within the pores of the framework, holding it in a large-pore configuration. The crystalline size of the MOF powders was further studied using

scanning electron microscopy (SEM) where representative crystalline sizes of each powder are shown in **Figure 58**. The size of the MIL-53 crystals was smaller than those of ZIF-62, at less than 5 µm. The small size of MIL-53 is ideal for the formation of a composite since it will be easier to suffuse than larger particulate.

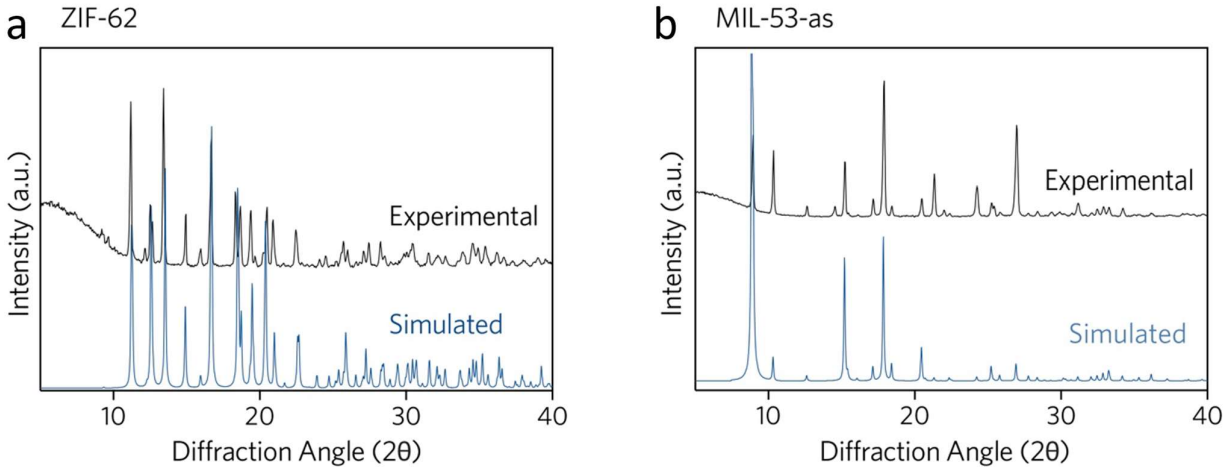

Figure 57: Confirmation of ZIF-62 and MIL-53-as synthesis. *Powder X-ray diffraction data of a. ZIF-62, and b. MIL-53-as.*

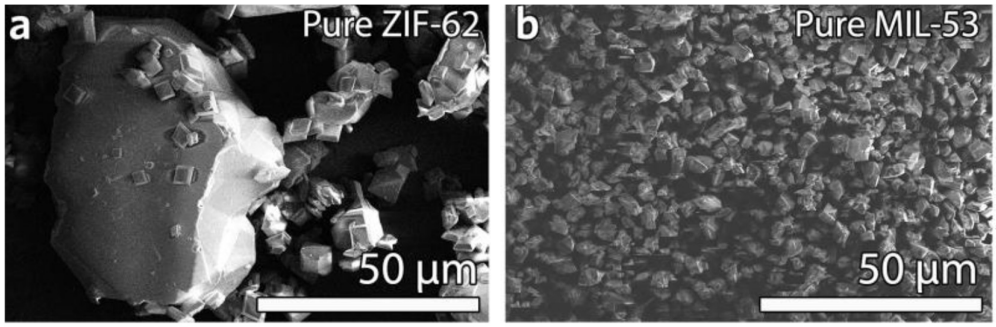

Figure 58: Particle size analysis of ZIF-62 and MIL-53. *Scanning electron microscopy images of a. Pure ZIF-62, and b. Pure MIL-53-np.*

For further confirmation, simultaneous Scanning DSC and TGA (SDT) data were recorded of each sample under an inert Ar atmosphere to confirm the expected thermal behaviour (**Figure 59**). In an initial scan, MIL-53 was heated to 800 °C and displayed three mass-loss events (**Figure 59a**) attributable to two-step desorption of surface-adsorbed and encapsulated BDC at *ca*. 380 °C and 430 °C, and the decomposition of the framework at *ca*. 580 °C, sequentially. This two-step desorption of BDC is also observed by Férey *et al.*, confirmed through observation of protonated linker bands in IR analysis; these species may be removed through calcination at 330 °C for 3 days in air.[121,272] In this scan, MIL-53 demonstrated stability above the melting temperature of ZIF-62, following reported thermal stabilities. A second scan using another sample of MIL-53 (**Figure 59b**) was heated to 450 °C, allowed to cool to room temperature, and reheated to 400 °C, showing no further BDC desorption in the second heating regime, confirming full BDC desorption when heated to 450 °C. The slight curvature in the DSC baseline is likely an instrumental artefact.

The TGA trace of ZIF-62 was featureless between the initial desolvation at *ca*. 250 °C and decomposition at *ca*. 600 °C (**Figure 59c**). ZIF-62 was synthesised here similarly to the method published by Yue *et al*. who also observed a mass-loss

event shortly before 200 °C. This event, whilst slightly above the boiling point of DMF (153 °C), was attributed, by Yue *et al*., to a loss of DMF from the material since DMF was observed in the NMR spectrum of the crystalline ZIF-62.[57] The simultaneous DSC measurement showed an endothermic response attributed to a solid-liquid transition (melting) at 435 °C, in agreement with previously reported data.[65] A second DSC scan using a second portion of ZIF-62, heating to 450 °C, cooling to room temperature, and reheating to 450 °C (**Figure 59d**) displayed a melting event at 435 °C again on initial heating, and a change in heat capacity at *ca*. 315 °C corresponding to the reported glass transition temperature of the species.[65] The T_g is taken here as the onset of the thermal event, finishing at *ca*. 350 °C, calculated by extrapolating gradients as shown in **Figure 59d**. The melting event is no longer present in the second scan, confirming the complete melting of the sample at 450 °C. These results confirm the thermal stability of MIL-53 above the melting temperature of ZIF-62.

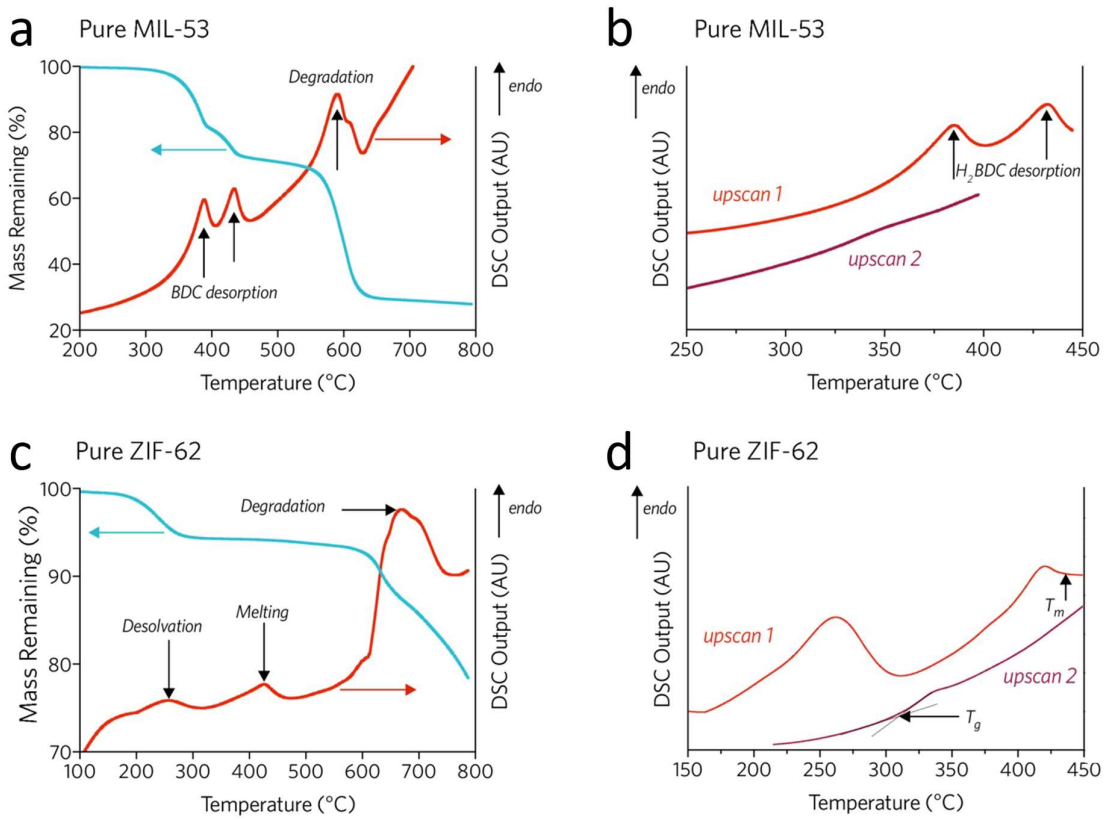

Figure 59: Thermogravimetric and calorimetric confirmation of ZIF-62 and MIL-53. *a. SDT of pure MIL-53, b. DSC of MIL-53, c. SDT of ZIF-62, and d. DSC of ZIF-62.*

4.2.2 Fabrication of a MOF CGC

A fabrication process for the MOF CGC was developed for the formation of the MOF CGC (**Figure 60**). In this process, the melting MOF component must successfully suffuse the crystalline material as extensively as possible to produce a well dispersed, rigid product. Given the reported high viscosity of MOF glasses ($\eta = 10^5$ Pa s for a ZIF-62 melt),[57] the fabrication process of the MOF CGC must account for this by optimising the steps to allow for the maximum liquid flow whilst

retaining the structural integrity of the non-melting component. Here, this is done by reducing each component's particle size by ball-milling the two components together. By doing so, the flow of the liquid MOF is improved, resulting in better dispersion of the MIL-53 within the resultant glass matrix. An interesting experiment to determine the change in particle size of the components would be to perform STEM-EDS analysis of the ball-milled, crystalline mixture to understand the extent of the particle size reduction and whether the particle size of both materials reduces equally.

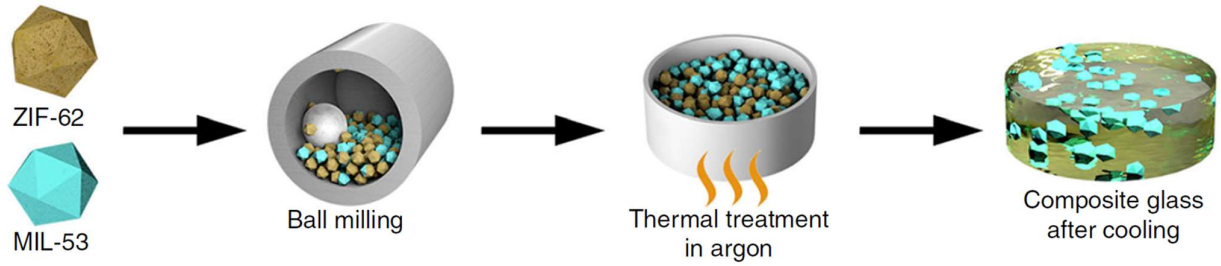

Figure 60: Procedure for the formation of a MOF crystal–glass composite. *A composite is formed here through the mixing of the crystal powders and melting the glass-forming MOF.*

Framework activation was not performed before ball-milling in this case since the presence of solvent within MOFs has been observed to stabilise against shear-induced collapse.[273] In one study, ZIF-8 was completely amorphised by ball-milling for only 10 minutes; however, upon the incorporation of ethanol or butanol within the pores of the framework, ZIF-8 could be ball milled for longer than 20 minutes, reducing the crystallinity of the framework by only *ca*. 50%.[273] Subsequently, this MOF CGC was heated to 450 °C and isothermally held for 10 minutes to melt the MOF glass completely to allow for glass flow before being cooled to room temperature. This heating was performed under an argon atmosphere to protect against oxidative decomposition.

A sample of 25 wt% MIL-53-as and 75 wt% ZIF-62 were ball-milled together (30 Hz, 5 min) to homogenise the mixture and reduce particle size. No significant change in crystalline structure was observed due to the ball-milling (**Figure 61a**). The mixtures of MIL-53 and ZIF-62 after ball milling are referred to as (MIL-53)(ZIF-62)(X/Y), where X and Y are mass percentages of each component. For example, a 25 wt% sample of crystalline MIL-53 and 75 wt% crystalline ZIF-62 sample is referred to as (MIL-53)(ZIF-62)(25/75). This sample of (MIL-53)(ZIF-62)(25/75) was then heated in flowing Ar to 450 °C, *i.e.*, above the melting temperature of ZIF-62, but below that of the thermal decomposition temperature of MIL-53. The samples were held at 450 °C for 10 min and then cooled back to room temperature under Ar protection over a period of approximately 90 min. In keeping with prior terminology on blended ZIFs, the resultant CGCs obtained upon cooling are referred to as $(\text{MIL-53})_X(a_g\text{ZIF-62})_Y$.[170]

SDT measurements were then collected on the sample of (MIL-53)(ZIF-62)(25/75), heating to 450 °C, allowing to cool to room temperature, and reheating to 450 °C again (**Figure 61b**). The first TGA trace of (MIL-53)(ZIF-62)(25/75) had a two-stage weight loss, consistent with the desorption of H_2BDC from MIL-53. The accompanying DSC indicated a broad endotherm at the expected melting temperature of ZIF-62, which is expected given the overlapping proximity in temperature ranges of both ZIF-62 melting and MIL-53 desorption phenomena. The DSC trace of the formed

$(MIL\text{-}53)_{0.25}(a_gZIF\text{-}62)_{0.75}$ CGC demonstrated a glass transition, T_g, of ~310 °C, and the melted samples, when cooled under Ar protection, displayed significant morphological changes due to vitrification.

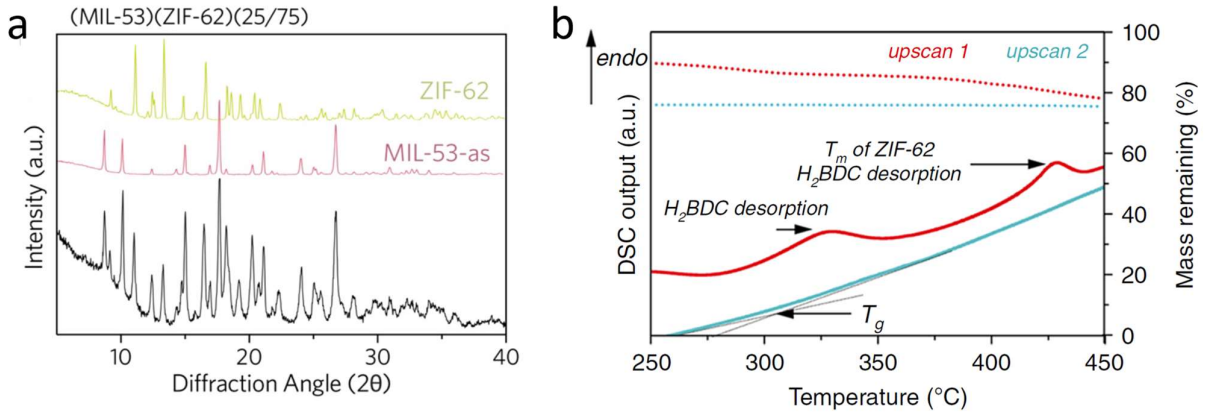

Figure 61: PXRD pattern and SDT measurements of (MIL-53)(ZIF-62)(25/75). *a. Confirmation of crystallinity of the mixtures through the retention of Bragg diffraction of each component in the mixture, and b. SDT of (MIL-53)(ZIF-62)(25/75).*

Optically transparent glasses could be obtained by clamping the crystalline powder mix between two glass slides during heating (**Figure 62a**). Notably, similar colouration is observed between the glass (**Figure 62b**) and the MOF CGC (**Figure 62c**). Scanning electron microscopy (SEM) performed on $(MIL\text{-}53)_{0.25}(a_gZIF\text{-}62)_{0.75}$ (**Figure 62d**) suggested good interfacial compatibility for the two different phases within the glass composite and evidenced the flowing of the liquid ZIF-62.

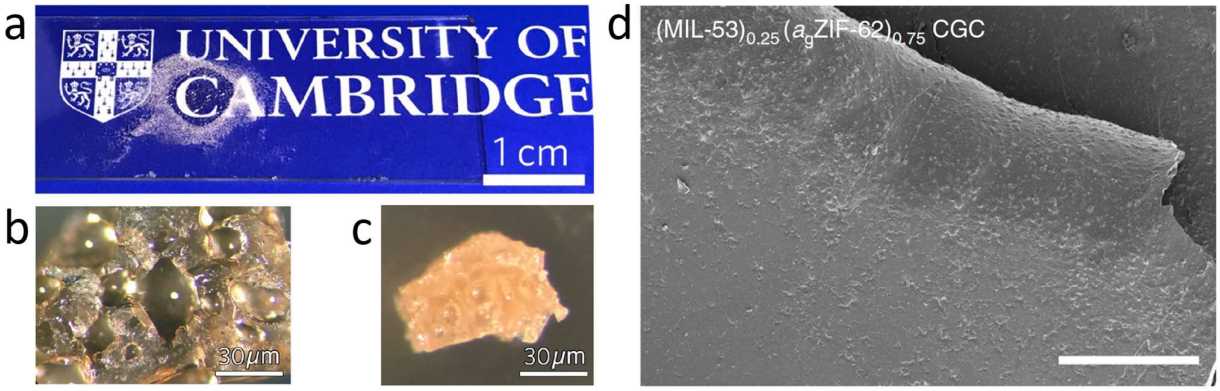

Figure 62: Macrostructural analysis of $(MIL\text{-}53)_{0.25}(a_gZIF\text{-}62)_{0.75}$. *a. Optical image of $(MIL\text{-}53)_{0.25}(a_gZIF\text{-}62)_{0.75}$, prepared by clamping the crystal mixture between two glass slides during heating. Optical microscopic images of b. a_gZIF-62, and c. $(MIL\text{-}53)_{0.25}(a_gZIF\text{-}62)_{0.75}$. d. SEM image of $(MIL\text{-}53)_{0.25}(a_gZIF\text{-}62)_{0.75}$; scale bar is 200 μm.*

4.2.3 Suspension of MIL-53-lp at Room Temperature

The PXRD pattern of $(MIL\text{-}53)_{0.25}(a_gZIF\text{-}62)_{0.75}$ CGC indicated that only the open-pore MIL-53-lp was present, *i.e.*, that rehydration and transition to close-pore MIL-53-np, does not occur. Later measurement would reveal that the MIL-53-lp remains even after 1-year storage at ambient conditions (**Figure 63a**). The absence of the MIL-53-lp to MIL-53-np transition, even when exposed to air at ambient conditions, provides a distinct advantage for the use of MOF CGCs.

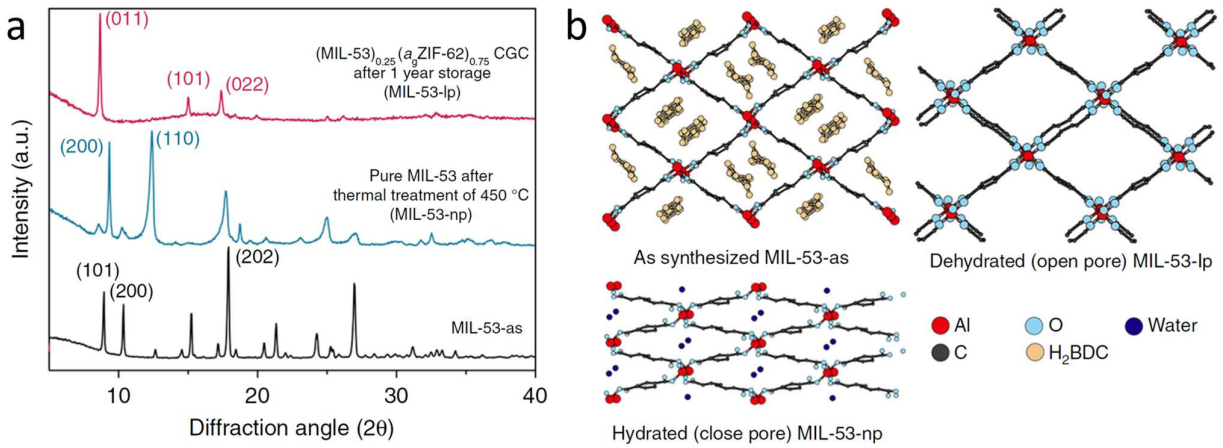

Figure 63: Entrapment of the metastable MIL-53-lp phase within the MOF CGC from MIL-53-as. *a. Stabilisation of MIL-53-lp in CGC; an XRD pattern of the MIL-53-as, MIL-53 crystal after thermal treatment (MIL-53-np) and CGC after 1 year storage. All measurements were conducted at ambient conditions. b. Illustration of the different MIL-53 crystal structures.*

MIL-53 crystallises in a "wine rack" structure (*Pnma*, *a* = 17.129(2) Å, *b* = 6.628(1) Å, *c* = 12.182(1) Å, α = β = γ = 90°) with large internal pores held open by excess solvent and unreacted ligand in the as-synthesised state ("MIL-53-as").[121] The removal or replacement of these guest molecules can cause the pore structure to undergo significant volume contraction or expansion, leading to phase transformations at different temperatures (**Figure 63b**). When the pore occupying species are expelled, typically by heating, an open-pore structure (*Imma*, *a* = 6.608(1) Å, *b* = 16.675(3) Å, *c* = 12.813(2) Å, α = β = γ = 90°) is formed with a greater internal void volume that is referred to as "MIL-53-lp" (large pore). The spontaneous uptake of water into the large-pore phase, typically upon cooling, causes the pores to contract to produce a narrow-pore structure (*Cc*, *a* = 19.513(2) Å, *b* = 7.612(1) Å, *c* = 6.576(1) Å, α = γ = 90°, β = 104.24(1)°) that is referred to as "MIL-53-np" (narrow pore).[121] Reversible transitions between MIL-53-np and MIL-53-lp are known as "breathing".

Notably, the MIL-53-as and MIL-53-lp phases are structurally similar and show only a small difference in their PXRD patterns. Therefore, it is crucial to confirm whether this phenomenon occurs for the MIL-53-np or whether it is caused by the excess ligand trapped within the pores of MIL-53-as. This was tested by activating a sample of MIL-53-as (330 °C for 3 days) to form the MIL-53-np phase (**Figure 64**) before preparing a 25 wt% MOF CGC using the same methods as with MIL-53-as. The resultant sample was analysed using PXRD and also found to retain the high-temperature MIL-53-lp phase (**Figure 64**). The sample of MIL-53-np must therefore expand to the MIL-53-lp phase before being trapped in this phase upon vitrification of the glass. The transition to the MIL-53-lp phase must also be the case for MIL-53-as since the DSC trace of (MIL-53)(a_gZIF-62)(25/75) evidences the desorption of excess H_2BDC adsorbed to MIL-53 (**Figure 61b**). As shown for MIL-53-np, the cooling of the melt from this stage must trap the MIL-53-lp phase within the glass in a process unaffected by excess H_2BDC.

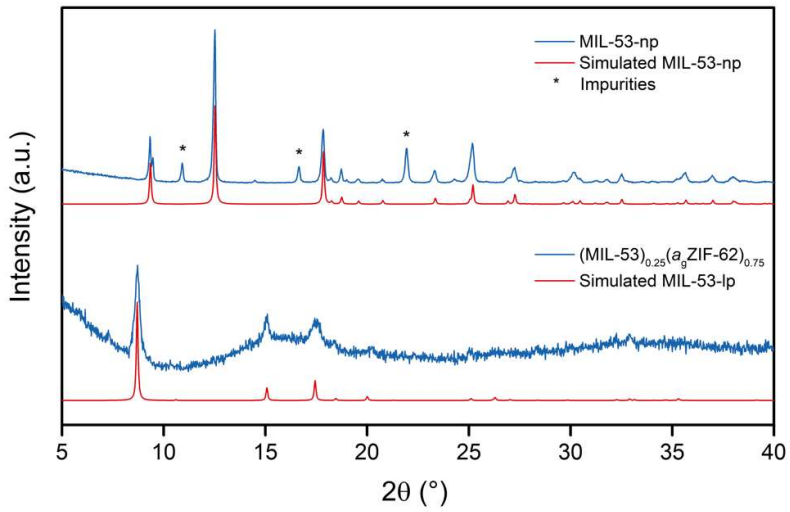

Figure 64: Confirmation of MIL-53-lp retention from MIL-53-np starting phase. *Experimental PXRD patterns (blue) of pure MIL-53-np (top) and the CGC (bottom). The simulated patterns (red) demonstrates the retention of the MIL-53-lp phase in quenched CGCs. Impurities marked with "*".*

4.2.4 Phase Behaviour of MIL-53

To confirm the reported phase change behaviour of MIL-53-as[121] in the synthesis of $(MIL\text{-}53)_{0.25}(a_gZIF\text{-}62)_{0.75}$, *in situ* synchrotron VT-PXRD was performed on a sample of (MIL-53)(ZIF-62)(25/75). Additionally, the melting and structural collapse of ZIF-62 was also investigated using this method. In these experiments, Bragg diffraction from ZIF-62 became weaker after the removal of adsorbed solvent and disappeared completely, as expected, above the T_m of 435 °C. Furthermore, the emergence of diffuse scattering, particularly evident at q = ~0.9–1.3 $Å^{-1}$ at this temperature, indicated melting, consistent with prior literature (**Figure 65a,b**).[65] As in the experiment performed on pure ZIF-62, Bragg diffraction from ZIF-62 ceased at 435 °C for the (MIL-53)(ZIF-62)(25/75) sample, although an abrupt change at *ca.* 160 °C is observed in the diffraction patterns (**Figure 65**). This change is indicative of a transition between the initial MIL-53-as and the final MIL-53-lp phase, where both phases coexist for a further *ca.* 260 °C. For example, above *ca.* 160 °C, the MIL-53-lp (011) Bragg peak at 0.62–0.65 $Å^{-1}$ grows in intensity, accompanied by a reduction in the intensity of the MIL-53-as (101) Bragg peak at 0.61–0.62 $Å^{-1}$.[274] Peaks from both phases remain until 420 °C when only Bragg peaks arising from MIL-53-lp are observed. This broad transition is ascribed to the constant heating rate used and the need to perform the experiment in a sealed capillary under Ar.

Unit cell parameters for the MIL-53 and ZIF-62 components were refined by fitting each diffraction pattern using Pawley refinements across the temperature range (**Figure 66**). A large increase in cell volume for MIL-53-lp was noted above 350 °C, *i.e.*, above the temperature at which H_2BDC is desorbed from the pores. The area of the rhombic pores was also calculated, using the distances between the four Al ions surrounding this opening (**Figure 66a–d**) which are uniquely determined by the unit cell parameters. Notably, the high-temperature cell parameters (and hence pore opening area) are broadly unchanged upon cooling the sample to room temperature and confirm that the MIL-53-lp phase pores do

not close upon cooling and atmospheric water sorption (**Figure 66e**). Meanwhile, during the thermal treatment process, the glass-forming phase (ZIF-62) in (MIL-53/ZIF-62)(25/75) behaves similarly to that of pure ZIF-62 (**Figure 66f**).

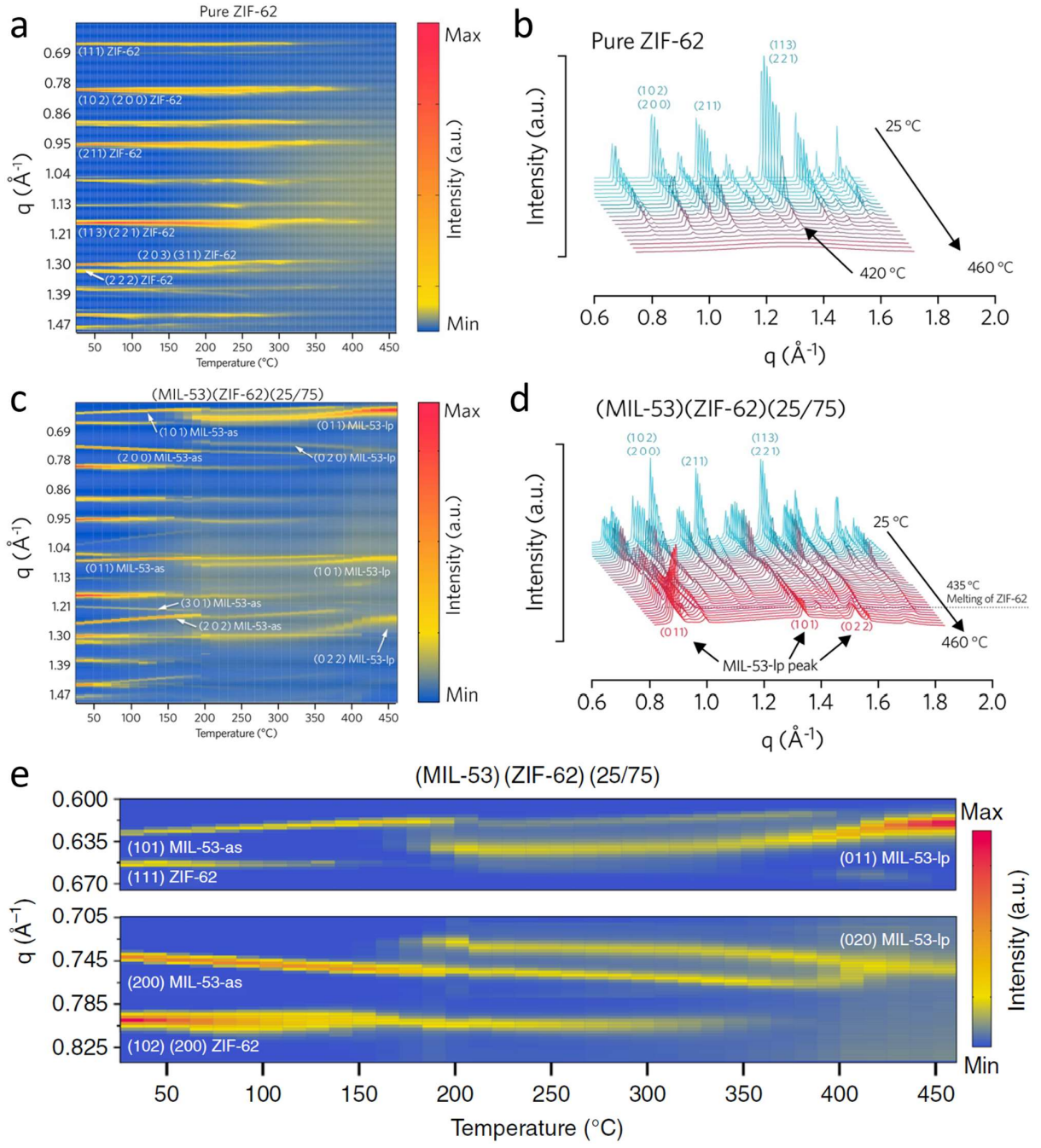

Figure 65: In-situ synchrotron PXRD profile during the thermal treatment process of (MIL-53)(ZIF-62)(25/75) (10 °C/min). *a–b. Contour plot and overlay of the variable temperature PXRD profile of pure ZIF-62 with hkl indices marked, c–d. Contour plot and overlay of the variable temperature PXRD profile of (MIL-53)(ZIF-62)(25/75) with hkl indices marked for ZIF-62 (blue) and MIL-53 (red). e. a Contour plots of in situ synchrotron powder diffraction data measured during the thermal treatment process of (MIL-53)(ZIF-62)(25/75) (10 °C min^{-1}). The Bragg peak hkl indices are marked for ZIF-62, MIL-53-as and MIL-53-lp.*

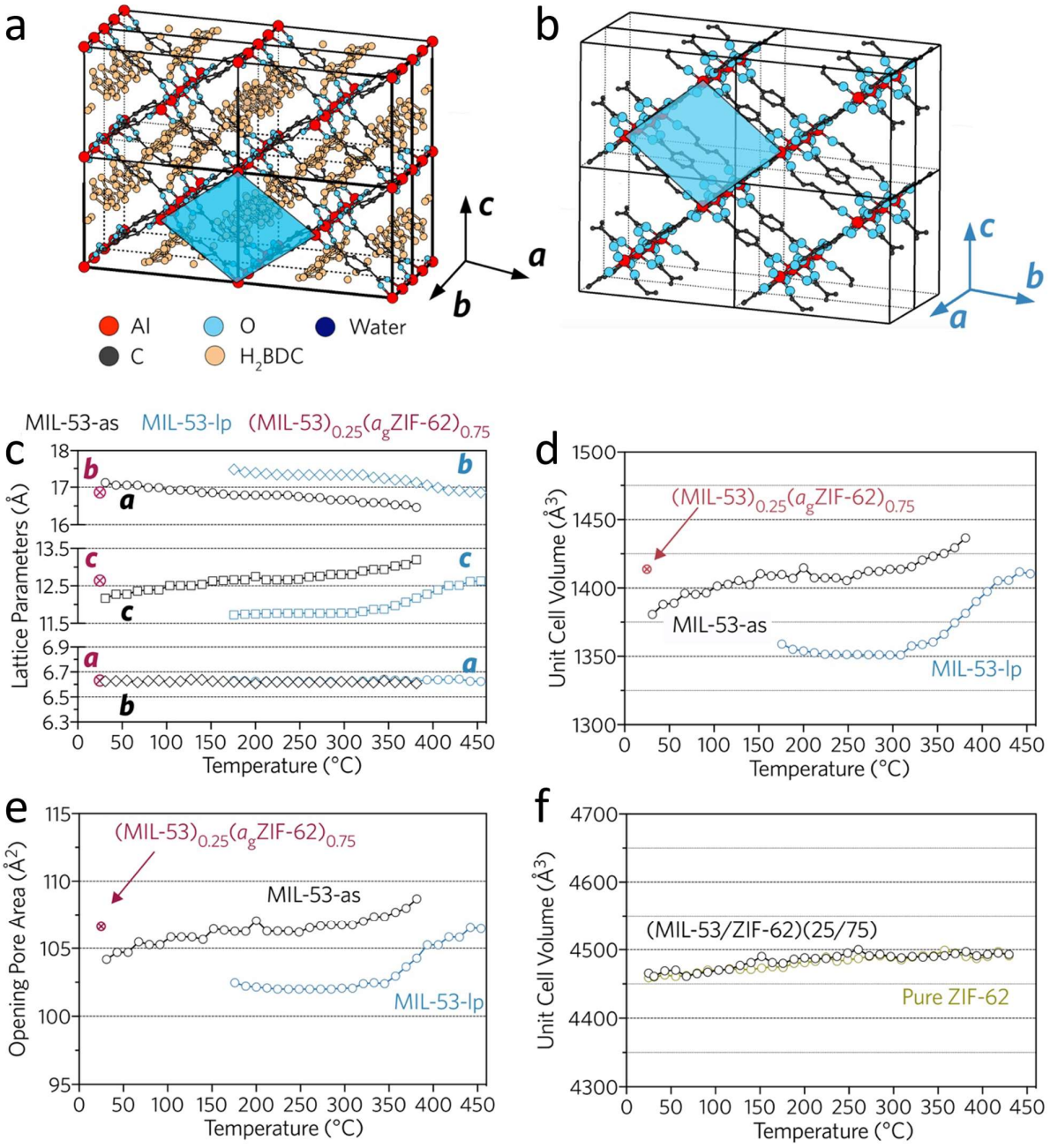

Figure 66: Phase transition of MIL-53 and melting of ZIF-62 during the $(MIL\text{-}53)_{0.25}(a_gZIF\text{-}62)_{0.75}$ CGC fabrication process. *a–b. Schematic diagram of the MIL-53-as and MIL-53-lp unit cell structure. Atom size is not to scale. c. Change of the lattice parameters and d. unit cell volume of MIL-53-as (black) and MIL-53-lp (blue) during the phase transition process. e. Change of the opening pore area during the phase transition process. The opening pore area is indicated in the scheme a and b with blue colour. The ex-situ XRD patterns from samples at room temperature are highlighted in the figure (c-e) with red marks. f. Change of the unit cell volume of ZIF-62 phase during the thermal treatment process for both pure ZIF-62 and (MIL-53)(ZIF-62)(25/75). All values were fitted from the in-situ synchrotron powder diffraction and ex-situ powder XRD patterns using the published cif files.*

4.2.5 Component Distribution

Electron microscopy was used to investigate the crystal–glass microstructure in $(MIL\text{-}53)_{0.25}(a_gZIF\text{-}62)_{0.75}$. STEM electron energy loss spectroscopy (STEM-EELS) measurements demonstrated characteristic signatures corroborating the co-location of carboxylate and imidazolate ligands in the respective MIL-53 and ZIF-62 glass domains (**Figure 67**).[275] STEM-EDS was also used to map the elemental distribution of the metal centres, demonstrating a mixture of the two separated phases in $(MIL\text{-}53)_{0.25}(a_gZIF\text{-}62)_{0.75}$.

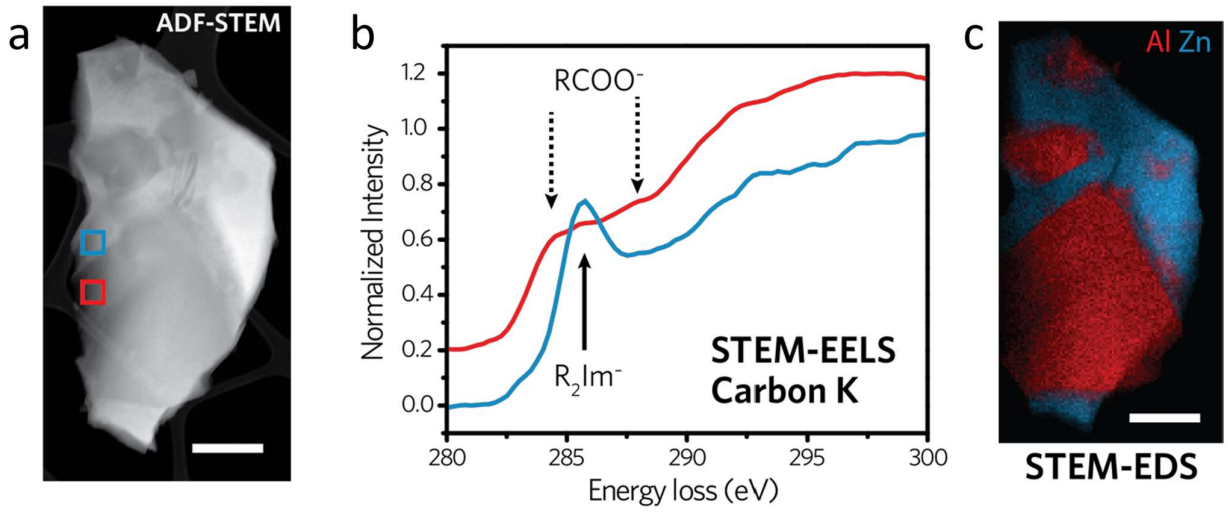

Figure 67: Observation of ligand chemistry by STEM-EELS of the $(MIL\text{-}53)_{0.25}(a_gZIF\text{-}62)_{0.75}$ CGC (thermal treatment at 450 °C for 10 min). *a. Annular dark-field (ADF) STEM image with selected areas marked by colour-coded squares. b. STEM-EELS spectra at the carbon energy K ionisation edge corresponding to the two selected areas in panel a. c. Corresponding STEM-EDS map of the Al and Zn elemental distribution. Scale bars are 400 nm.*

EELS signals in the range of 284–290 eV are indicative of the carbon bonding environment due to the appearance of sharp peaks associated with chemically sensitive π* states above the Fermi energy. The carbon spectrum corresponding to the Al-rich phase (red) exhibits two low-intensity π* features at approximately 284 eV and 288 eV (marked with dashed arrows). In contrast, the carbon spectrum corresponding to the Zn-rich phase (blue) exhibits a single sharp π* peak at approximately 285.5 eV. The energy axis was scaled relative to the carbon *K* edge features for amorphous carbon (in the lacey carbon support film), with a π* at 284.5 eV. The sharp π* peak at 285.5 eV is characteristic of carbon K edge features observed in ZIF-62 and matches previous reports on the imidazole ligand.[275] The lower intensity peaks at 284 and 288 eV are consistent with reports of X-ray adsorption near-edge spectroscopy (XANES) for carboxylic acid moieties.[276]

STEM-EDS was also used to map the elemental distribution of the metal centres, demonstrating a mixture of the two separated phases in the $(MIL\text{-}53)_{0.25}(a_gZIF\text{-}62)_{0.75}$ CGC. Two-dimensional STEM-EDS mapping indicated near homogeneous mixing of the two phases (**Figure 68a**), though the distribution in three-dimensional space remained unknown. STEM-EDS tomography was used to reconstruct a complete shard of $(MIL\text{-}53)_{0.25}(a_gZIF\text{-}62)_{0.75}$ CGC (**Figure 68b**). This revealed MIL-53 particles of between 30 and 300 nm in size, evenly embedded within the ZIF-62 glass substrate. The degree of surface-

facing MIL-53 phase in the reconstructed particles may indicate an increased preference for fracturing at MIL-53/ZIF-62 interfaces.

SED has recently emerged as an effective way to obtain nanoscale structural insight from beam sensitive materials.[277] Here, the number of Bragg diffraction discs found in the diffraction pattern recorded at each probe position was plotted to reveal the location of crystalline phases, as shown in **Figure 68c**. These crystallinity maps demonstrated close contact between crystalline and non-crystalline regions within the composites. Comparison with compositional maps obtained *via* STEM-EDS mapping of the same particles, showing the distribution of the metal centres, confirm that the crystalline regions correspond to the metal-centres expected for the MIL-53 CGC material. However, whilst the tomograph would appear to detail no separation between the crystalline and glass components, the resolution of the data (1 pixel) corresponds to a *ca*. 5 nm distance. Component separation greater than 5 nm is, however, absent in this sample.

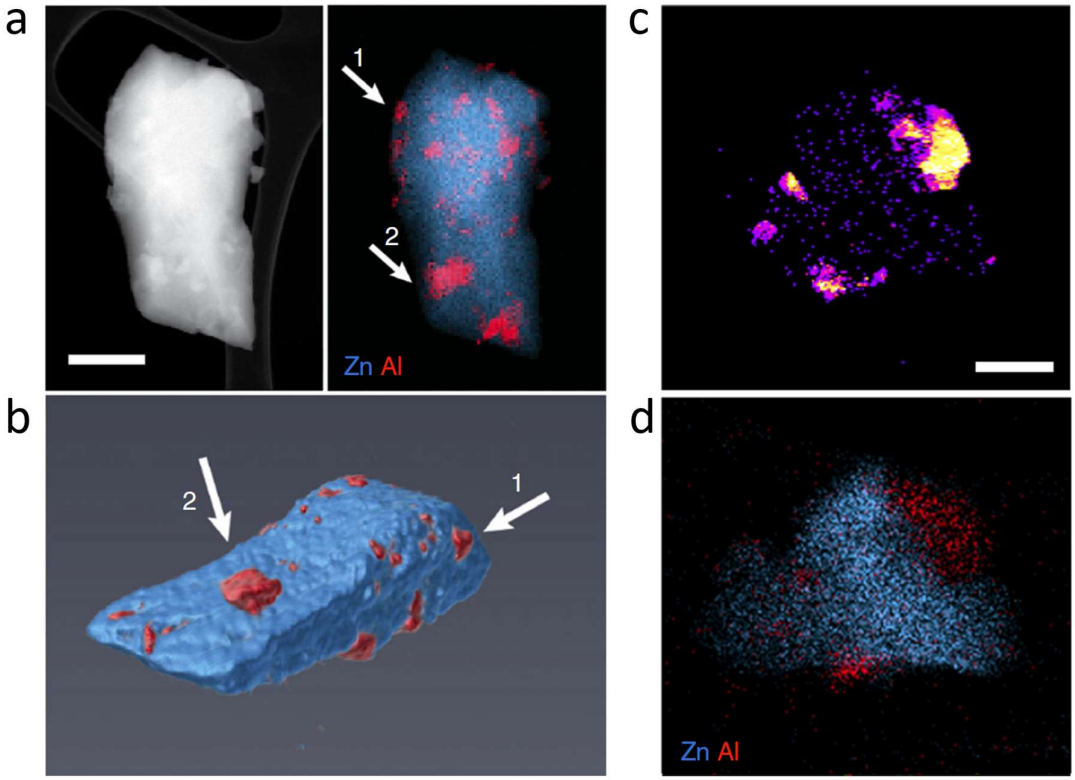

Figure 68: STEM-EDS and SED mapping of (MIL-53)$_{0.25}$(a$_g$ZIF-62)$_{0.75}$. *a. STEM-EDS mapping of (MIL-53)$_{0.25}$(a$_g$ZIF-62)$_{0.75}$, b. corresponding three-dimensional tomography from the STEM-EDS mapping. c. SED mapping of another shard of (MIL-53)$_{0.25}$(a$_g$ZIF-62)$_{0.75}$ and d. the corresponding STEM-EDS mapping of the sample in c. Scale bar is 200 nm.*

Particle sizes of MIL-53 were isolated in the 3D tomograph of the (MIL-53)$_{0.25}$(a_gZIF-62)$_{0.75}$ shard in **Figure 68b**. These regions of crystalline MIL-53 were then processed to produce a particle volume distribution of MIL-53 within the composite (**Figure 69a**). Whilst informative for absolute mass calculations, a spherical equivalent is more useful for particle size comparison. Therefore, a size distribution of equivalent spherical particle radii was calculated (**Figure 69b**). Notably, this data is filtered to exclude regions smaller than 2×2×2 pixels for accuracy. As such, data for particles smaller than the reported values cannot be accurately represented here.

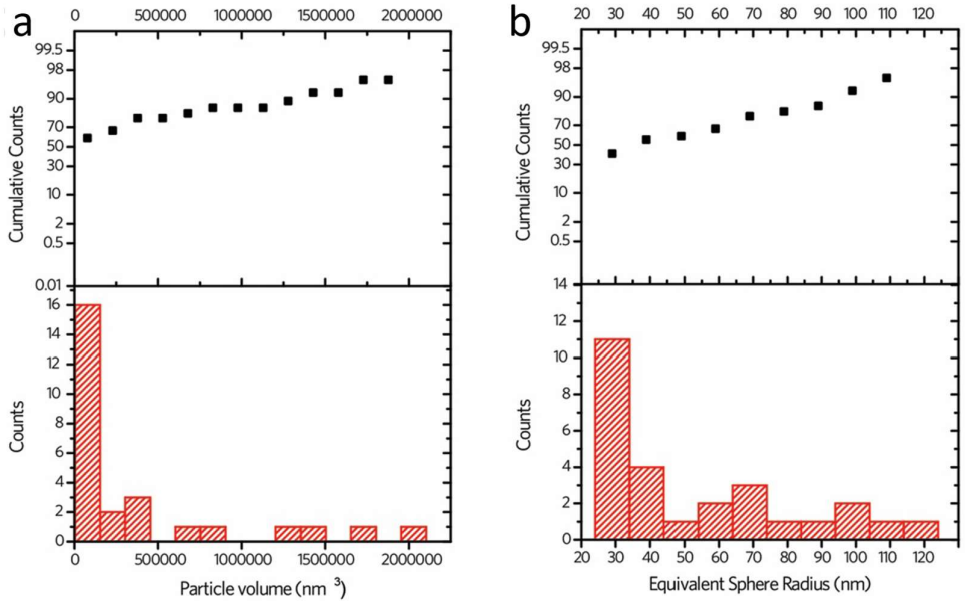

Figure 69: Calculated crystalline particle size from 3D tomography. *a. MIL-53 crystal particle volume distribution profile within* $(MIL\text{-}53)_{0.25}(a_gZIF\text{-}62)_{0.75}$*, and b. MIL-53 crystal particle size distribution profile within the composite.*

Broadly, the particle sizes of MIL-53 are smaller than the equivalent of 200 nm diameter spheres. These particle sizes contrast with those observed in SEM images of MIL-53-as (**Figure 58b**), which display widths of *ca.* 1000–4000 nm. Such reduction can be attributed to the ball-milling step of the composite fabrication. It is, however, evident from **Figure 68c** and **Figure 68a** that the particle size of MIL-53 is poorly controlled. This considerably limits the accuracy of the data shown in **Figure 69** since only a single sample was used, and there is a noticeable difference in particle size between the two samples. A much larger sample size would be required for more reliable results, though this may be too resource-demanding to perform in practice.

4.2.6 Atomic Structure and Domain Analysis

To collect structural information, total scattering data were collected for samples of (MIL-53)(ZIF-62)(25/75) and $(MIL\text{-}53)_{0.25}(a_gZIF\text{-}62)_{0.75}$ (**Figure 70a**). The total scattering data, $S(Q)$, of the crystalline mixture exhibits sharp Bragg reflections originating from both the MIL-53 and ZIF-62 components. Upon composite fabrication, peaks are significantly broadened; however, the pattern retains its general shape but leaving identifiable MIL-53 reflections (**Figure 70a**).

Total scattering data were subsequently processed using GudrunX software (**Section 3.1.4.2**) to produce the PDFs of these samples (**Figure 70b**). Short-range order (1–8 Å) peaks are retained in the $(MIL\text{-}53)_{0.25}(a_gZIF\text{-}62)_{0.75}$ sample, where atom-to-atom correlations from both the crystalline ZIF-62 and MIL-53-lp structures can be identified. Namely, peaks corresponding to Al–O, and Al–Al bond distances were visible in this PDF at *ca.* 5 and 7.5 Å originating from MIL-53, Zn–Zn (*ca.* 6 Å), and Zn–N (*ca*. 4 Å) originating from a_gZIF-62 are easily distinguishable. As expected, the PDFs of the composite retain the longer-range oscillations due to Al–Al correlations in MIL-53 exceeding 8 Å. As with samples of pure ZIF-62, longer-range correlations are no longer observable in the $S(Q)$. These samples are, by weight, heavily dominated by ZIF-62

containing heavily scattering Zn metal ions; correlations from MIL-53, whose Al centres weakly scatter in comparison, appear much weaker. These data provide evidence that the ZIF-62 behaves similarly in the composite material as in the pure state.

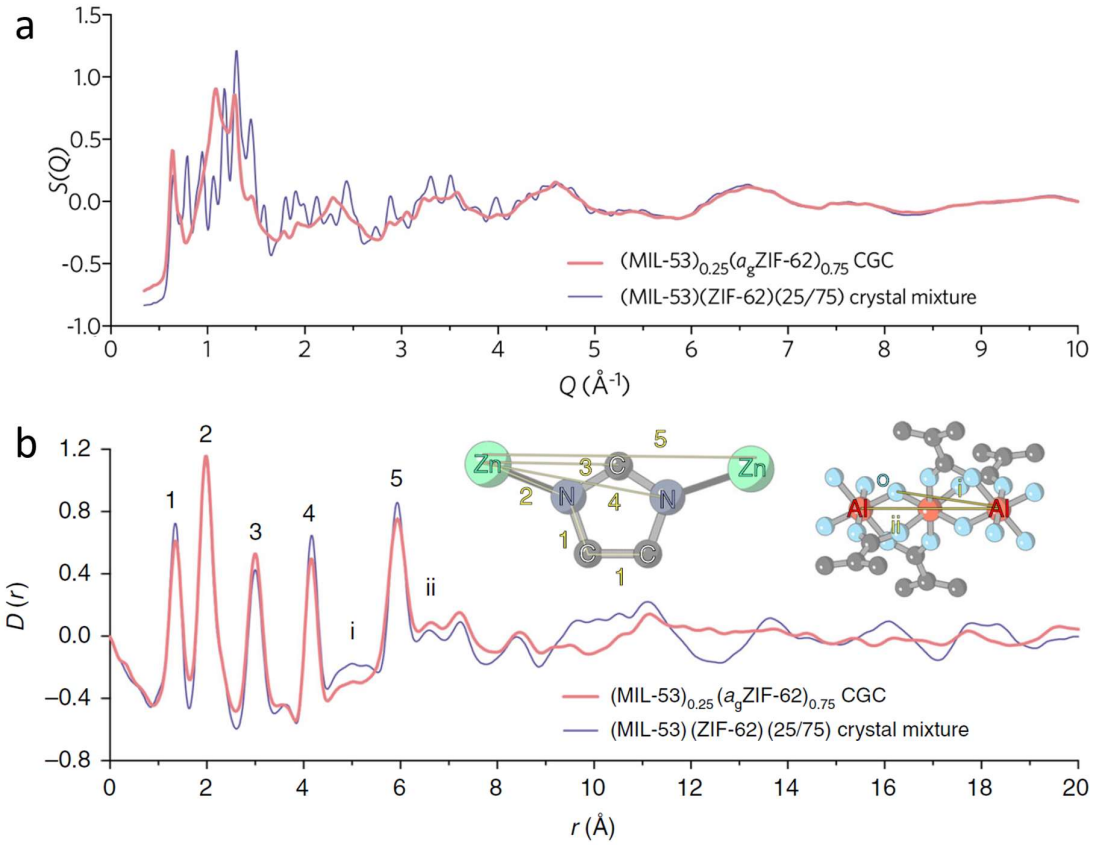

Figure 70: Comparison of total X-ray scattering data of (MIL-53)(ZIF-62)(25/75) and (MIL-53)$_{0.25}$(a$_g$ZIF-62)$_{0.75}$. *a. Structure factor, S(Q), comparison of (MIL-53)(ZIF-62)(25/75) and (MIL-53)$_{0.25}$(a$_g$ZIF-62)$_{0.75}$. b. Pair distribution function (PDF) D(r) calculated* via *Fourier transform of the X-ray total scattering structure factor S(Q) for the crystal mixtures and CGC. The inset shows the scheme for PDF peak assignment.*

Whilst PDF measurements provide valuable information on the structure of the material, nuclear magnetic resonance (NMR) was implemented to probe the proton polarisation transfer to investigate interfacial distances dynamically. To confirm the homogeneous distribution of MIL-53 particles within the a_gZIF-62 matrix (as shown by STEM), ^{1}H and ^{13}C magic angle spinning (MAS) solid-state NMR spectroscopic measurements were performed on samples of both (MIL-53)(ZIF-62)(25/75) and (MIL-53)$_{0.25}$(a_gZIF-62)$_{0.75}$ (**Figure 71**).

Peaks arising from bIm and Im, from ZIF-62, and BDC, from MIL-53, are present before and after vitrification in the solid-state ^{13}C MAS NMR with little change. The structural similarity of MIL-53-as and MIL-53-lp is apparent in the similar chemical environments observed for each structure. Peaks assigned to the bIm and Im linkers in ZIF-62 and the peaks of the BDC linker in MIL-53 are broadly similar for both samples in both ^{13}C and ^{1}H NMR spectra. The most notable differences in the recorded spectra for the crystalline mixture and the composite appear in the ^{1}H spectra. The peak

corresponding to the bridging Al–OH–Al species within the MIL-53 in the composite shifts downfield and a shoulder on the broad peak associated with the bIm and Im species at *ca*. 6.5 ppm appears in the composite. The former observation is likely a result of the desorption of excess linker from the pores of the MIL-53 framework. Additionally, this shift corroborates the observed change in MIL-53 structure from the MIL-53-as in the mixture. However, the extra peak could be from a number of sources. Firstly the reduction in particle size of the MIL-53 vastly increases the proportion of terminating, protonated linkers at the particle surface and may be a product of this. Secondly, in the fabrication of the composite, excess material is expelled. This compositional change may alter the peak resolution and induce the emergence of a peak otherwise merged with other similar environments.

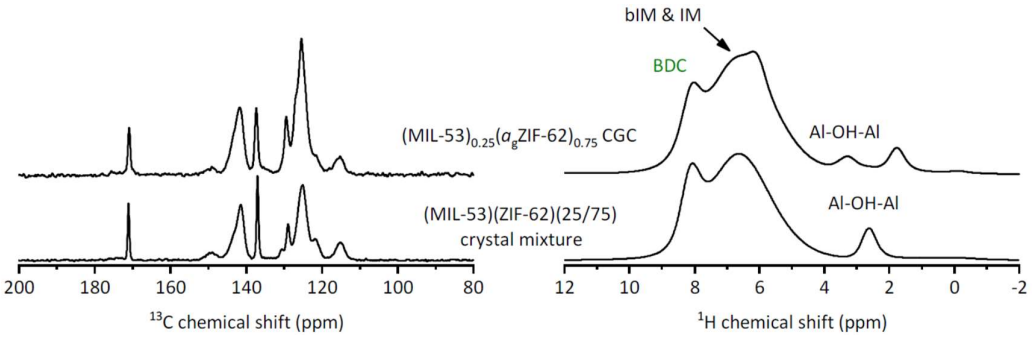

Figure 71: Chemical environments of (MIL-53)(ZIF-62)(25/75) and (MIL-53)$_{0.25}$(a$_g$ZIF-62)$_{0.75}$. *^{13}C MAS NMR, and ^{1}H MAS NMR analysis for (MIL-53)(ZIF-62)(25/75) crystal mixture (lower spectra) and (MIL-53)$_{0.25}$(a$_g$ZIF-62)$_{0.75}$ CGC (upper spectra).*

Since 1D MAS NMR did not show the emergence of clear signals that may be ascribed to the chemical bonding of the two-component material, 2D NMR techniques were employed to screen for component interactions. Spin-diffusion NMR spectroscopy makes use of the differential rates of proton polarisation transfer between species on the same, or separate, organic linkers. 2D back-to-back (BABA) spectra were recorded for (MIL-53)$_{0.25}$(a$_g$ZIF-62)$_{0.75}$ (**Figure 72a**) and spin diffusion was recorded at intervals of 1, 10, 100, and 1000 ms (**Figure 72b**). Vertical dashed lines indicate the traces of the 2D spectra, which were analyzed to determine spin-diffusion curves and obtain information about the rate and extent of polarisation transfer between the OH protons of MIL-53 to both BDC protons of MIL-53 and imidazolate protons of ZIF-62. The 2D spectra also show that species resonating at 1.7 ppm are within MIL-53 or on its surface.

Analysis of two series of spin diffusion NMR spectra of (MIL-53)(ZIF-62)(25/75) crystal mixture and (MIL-53)$_{0.25}$(a_gZIF-62)$_{0.75}$ (**Figure 72c,d**) shows a significant difference between the two samples. Within the figure, blue lines represent the slices through the spectra measured at a spin-diffusion mixing time of 1 ms, red lines correspond to mixing time of 1000 ms, and grey lines correspond to mixing times of 2, 5, 10, 20, 50, 100, 200 and 500 ms. In both samples, a peak at *ca*. 8 ppm is due to protons on BDC linkers, and a peak at *ca.* 3 ppm is due to protons of the bridging OH groups of the inorganic chains of MIL-53. A single, broad proton peak from ZIF-62 appears at *ca.* 6.8 ppm. Whereas in the crystal mixture, no proton polarisation transfer between MIL-53 and ZIF-62 is detected, transfer of polarisation between the OH protons of MIL-53 and the imidazolate-based protons of a_gZIF-62 is observed in the CGC.

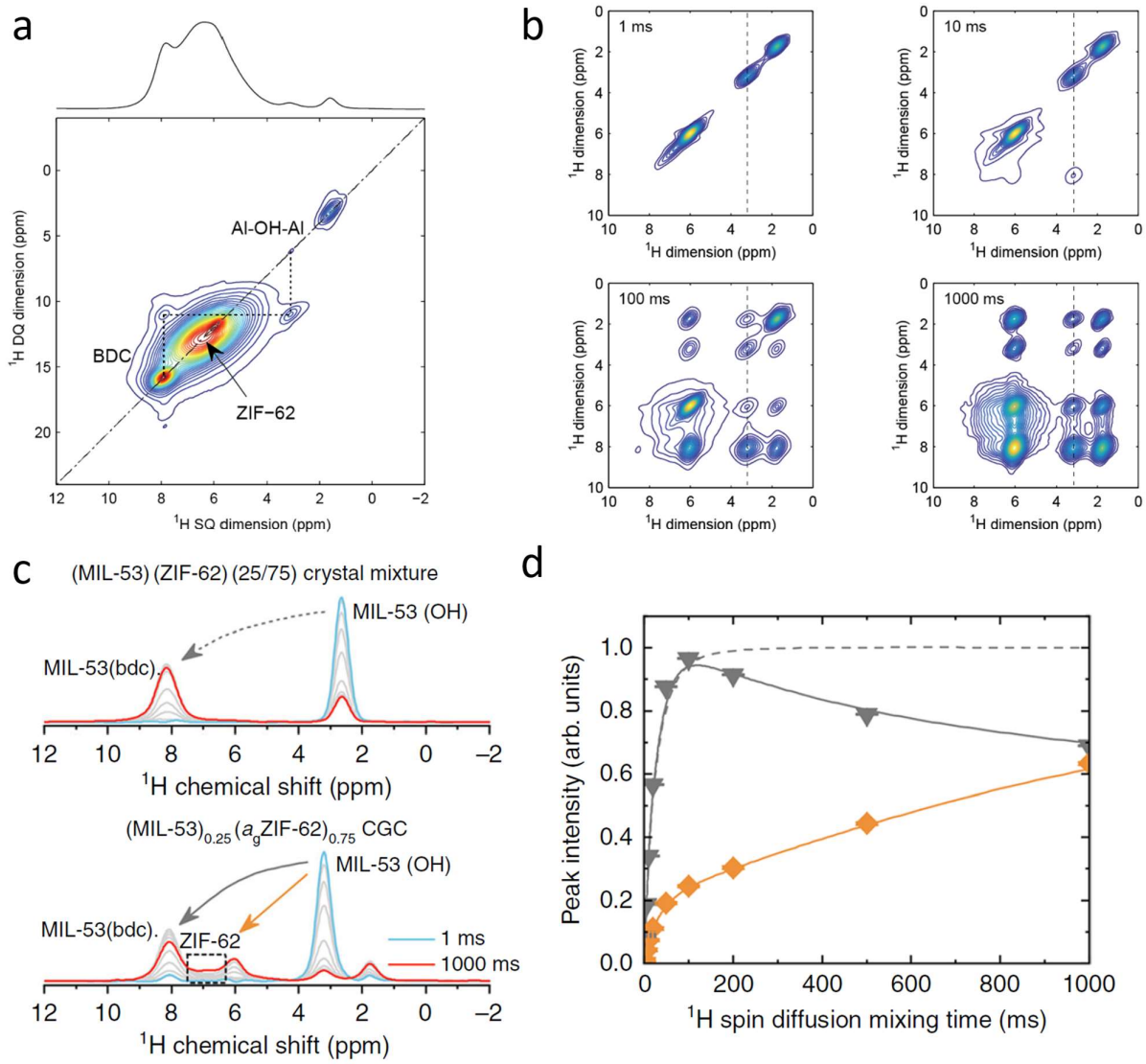

Figure 72: Proximities among different species within (MIL-53)$_{0.25}$(a_gZIF-62)$_{0.75}$ CGC as inspected by proton-proton dipolar-recoupled NMR experiments. *a. Two-dimensional ^{1}H-^{1}H back-to-back (BABA) spectrum, facilitating the assignment of the BDC and OH signals of MIL-53, and of the imidazolate signal of ZIF-62. b. 2D ^{1}H-detected T2-filtered proton-spin-diffusion spectra of the CGC sample recorded with different mixing times.* c. *Slices along the indirectly detected dimension through the 2D ^{1}H spin-diffusion NMR spectra. Slices were taken at a chemical shift of about 3 ppm, and show how polarisation transfer between the OH groups of MIL-53 and all other protons of the samples proceeds.* d. *Spin-diffusion curves obtained by extracting integrated intensities of selected peaks within the slices through the 2D ^{1}H spin-diffusion NMR spectra. The dashed grey line describes proton polarisation transfer between OH groups and BDC linkers of the crystal mixture, grey triangles and solid line describe polarisation transfer between OH groups and BDC linkers of MIL-53 within the CGC, and orange diamond signs and solid line describe polarisation transfer between the OH groups of MIL-53 and imidazolate linkers of ZIF-62 within the CGC.*

The fast polarisation transfer (steep curve) for short mixing times is indicative of the close contacts between MIL-53 and ZIF-62 domains in the CGC (**Figure 72d**). The fact that the curve shown does not reach a plateau, and is still rising at mixing times as long as 1 s, suggests that the OH groups in MIL-53 crystals and imidazolate linkers in a_gZIF-62, are present within

distinct domains. If they were present within the same framework, the polarisation–transfer curve would resemble the one that describes transfer between the OH groups and BDC linkers of MIL-53, which reaches a plateau at about 200 ms.

4.2.7 Density and Mechanical Properties

One benefit of the CGC is their processability, which will enable the material to be shaped for different applications. The density and mechanical properties can provide important information on whether these materials will withstand industrial conditions.[173] The densities of the crystalline mixture and of the CGC were thus measured with gas pycnometry. The density of the CGC was higher than the corresponding initial crystal powder mixture, from 1.62 ± 0.03 to 1.78 ± 0.08 g/cm^3 for (MIL-53)(ZIF-62)(25/75) crystal and (MIL-53)$_{0.25}$(a_gZIF-62)$_{0.75}$, respectively.

The mechanical properties of the glass composite were probed by nanoindentation on surfaces polished to 0.25 µm coarseness. The Young's modulus (E) increase for (MIL-53)$_{0.25}$(a_gZIF-62)$_{0.75}$ (E ≈ 7.7 GPa) compared with the pure a_gZIF-62 counterpart (E ≈ 5.8 GPa), correlates well with their densities, as well as the larger (obtained through quantum chemistry calculations) elastic moduli of MIL-53 (E = 25 GPa).[131] This observation suggests the glass composite has a similar resistance to irreversible plastic deformation as the pure glass.

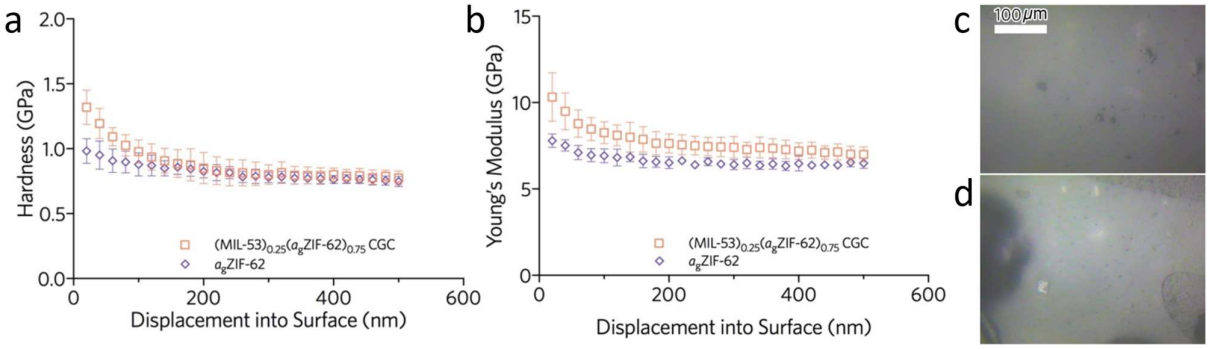

Figure 73: Nanoindentation to determine the mechanical properties of (MIL-53)$_{0.25}$(a_gZIF-62)$_{0.75}$ and a_gZIF-62*. a. variance of hardness with depth, b. variance of elastic modulus with depth, and optical images of indentations for c. a_gZIF-62, and d. (MIL-53)$_{0.25}$(a_gZIF-62)$_{0.75}$.*

4.2.8 MOF CGC Porosity

A range of gas adsorption isotherm experiments was performed on the MIL-53 CGC samples to determine the effect of encapsulation on gas adsorption behaviours. a_gZIF-62 has been previously demonstrated to possess accessible, permanent porosity toward both hydrogen (H_2) and carbon dioxide (CO_2),[55] with uptake capacities of 0.40 mmol/g at 77 K and 0.90 mmol/g at 273 K, respectively (**Figure 74**). Measurements were repeated here, and, as expected, the ZIF-62 glass is porous to small gas molecules (with H_2 of 2.9 Å kinetic diameter uptake of 0.62 mmol/g at 1 bar and 77 K, **Figure 74b**).

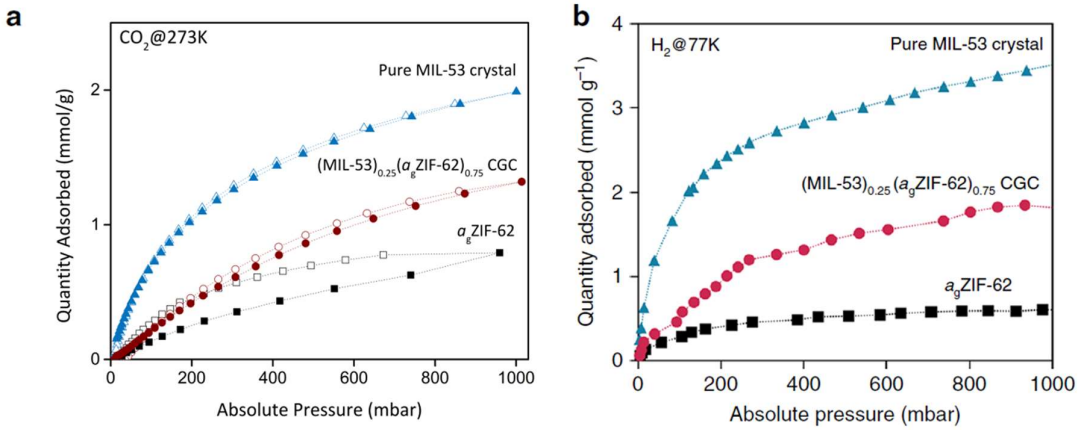

Figure 74: CO_2 and H_2 gas sorption isotherms of a sample of $(MIL\text{-}53)_{0.25}(a_gZIF\text{-}62)_{0.75}$. *a. CO_2 adsorption (solid) / desorption (open) profiles at 273 K. b H_2 adsorption profiles at 77 K.*

The incorporation of crystalline MIL-53 improves the H_2 uptake of a_gZIF-62 to *ca.* 1.9 mmol/g at 1 bar. This can be attributed to the high measured gas adsorption capacity of pure MIL-53 (open pore structure) at 3.55 mmol/g, which aligns with the reported values.[278,279] In comparison, N_2 adsorption isotherms at 77 K of the a_gZIF-62 and the MOF CGC shows very little adsorption relative to that of crystalline MIL-53 (**Figure 75**) in accordance with previous literature on gas sorption experiments performed on a_gZIF-62.[55]

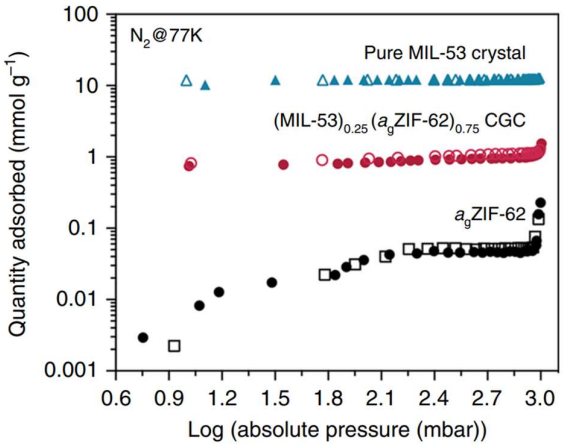

Figure 75: N_2 gas sorption isotherms of a sample of $(MIL\text{-}53)_{0.25}(a_gZIF\text{-}62)_{0.75}$. *$N_2$ adsorption(solid)/desorption(open) profiles at 77 K.*

Ar (3.4 Å kinetic diameter); adsorption experiments were performed at 87 K and demonstrate similar inaccessibility of the glass component to large analyte molecules. Though the slow diffusion kinetics (as evident in the isotherm hysteresis) severely limits precision, pore size distributions gained from Ar isotherms on (MIL-53)(ZIF-62)(25/75) and $(MIL\text{-}53)_{0.25}(a_gZIF\text{-}62)_{0.75}$ CGC demonstrate pores at 5–6 Å for both crystalline mixture and CGC (**Figure 76**), in addition to one at *ca.* 11 Å for the CGC. Using an analyte gas with a slightly smaller critical diameter, CO_2 (3.3 Å kinetic diameter), it

is found that the gas adsorption capacity of $(MIL\text{-}53)_{0.25}(a_gZIF\text{-}62)_{0.75}$ CGC approaches the capacity of a sample of pure MIL-53 at the same condition (273 K, 1 bar, **Figure 74a**).

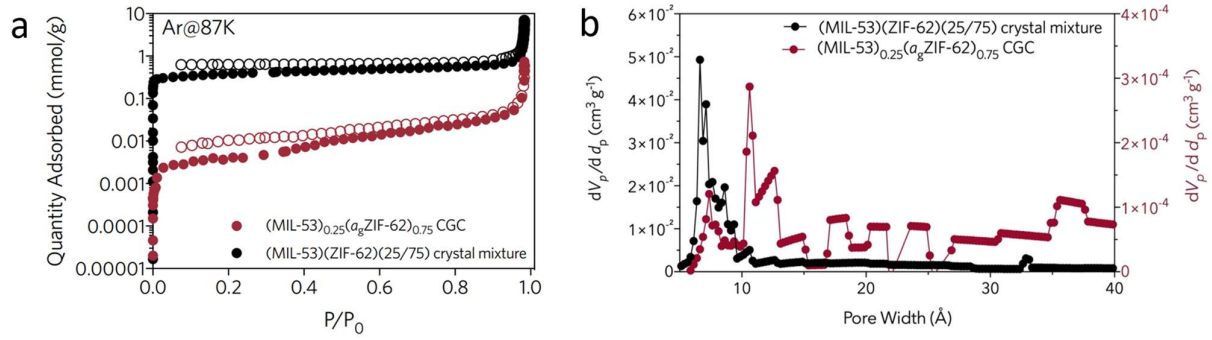

Figure 76: Pore size distribution of $(MIL\text{-}53)_{0.25}(a_gZIF\text{-}62)_{0.75}$ and (MIL-53)(ZIF-62)(25/75) from Ar adsorption. *a. Ar adsorption(solid)/desorption(open) profile, recorded at 87 K. b. pore size distribution for the crystal mixture (black) and CGC (red) obtained from Ar adsorption branch. The distributions were calculated using the Horwath-Kawazoe method* via *the Saito-Foley approach.*

High-pressure CO_2 adsorption experiments were performed on both (MIL-53)(ZIF-62)(25/75) and $(MIL\text{-}53)_{0.25}(a_gZIF\text{-}62)_{0.75}$. The CGC demonstrated an improvement of *ca.* 30% in CO_2 adsorptive capacity at 303 K and 50 bar (**Figure 77a**). This phenomenon can be explained by considering the breathing behaviour of MIL-53. Below pressures of 3 bar, the adsorption of CO_2 results in weak dipolar or quadrupolar host-guest interactions. This interaction causes the unit cell to contract to a narrow pore structure with a relatively low adsorption capacity of ca. 2.5 mmol/g.[280] At higher pressures above 10 bar, the pores of the framework are re-opened, increasing the CO_2 adsorption capacity to 8–9 mmol/g.[281]

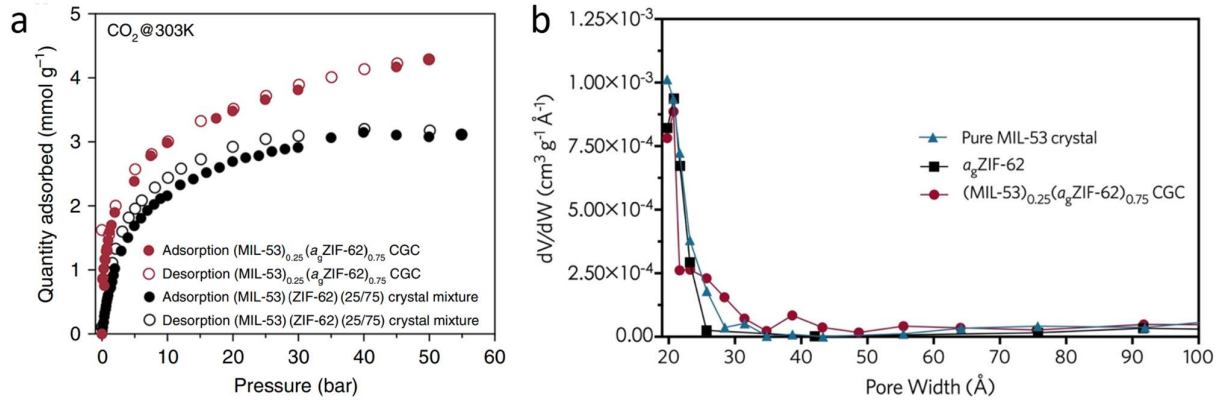

Figure 77: High-pressure CO_2 gas sorption isotherms and N_2 pore size distribution. *a. High-pressure CO_2 adsorption (solid)/desorption (open) isotherms of the crystalline mixture (black) and CGCs (red) performed at 303 K, and b. N_2 (77 K) pore size distributions, calculated using the Barrett, Joyner, and Halenda method.*[282]

In comparison, the stabilisation of open-pore MIL-53 within the glass composite readily allows a high CO_2 adsorption quantity even at low-pressure conditions (up to 1 bar)—although the narrow pore phase has a higher affinity for CO_2, as can be seen in the very low-pressure region (<100 mbar). Based on the composition of the CGC, the estimated CO_2

adsorption is 2.71 mmol/g, which is lower than the experimental results. This suggests that the excess CO_2 uptake observed here may be partially ascribed to a small number of mesopores within CGC, arising from the interface between crystal and glass components (**Figure 77b**). The BJH method was utilised here since the Kelvin equation holds for the interfacial macropores that may be predictably induced in the synthesis of a composite. However, DFT-based models such as the Saito-Foley approach are likely to provide more accurate results due to the ability to fit pore-condensation hysteresis.[283]

Water adsorption experiments were also performed on both (MIL-53)(ZIF-62)(25/75) and $(MIL\text{-}53)_{0.25}(a_gZIF\text{-}62)_{0.75}$ CGC (**Figure 78**). An abrupt uptake at 60% relative humidity is noted for both samples during the first cycle, whilst subsequent cycles showed a better cyclability and higher amount adsorbed for the $(MIL\text{-}53)_{0.25}(a_gZIF\text{-}62)_{0.75}$. The uptake of H_2O here implies that the stabilisation of MIL-53-lp does not arise because it is excluded from entering the composite CGC material. Instead, the glass phase may not be "soft" enough to accommodate a large-scale change of the crystal phase structure while the interfacial contact between the two phases is maintained.

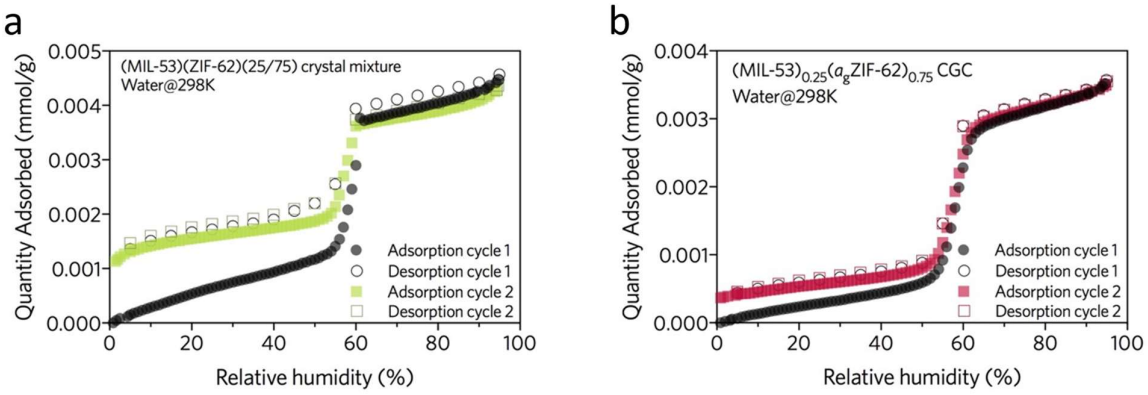

Figure 78: **The effect of water adsorption on the phase of MIL-53 in *(MIL-53)(ZIF-62)(25/75) and $(MIL\text{-}53)_{0.25}(a_gZIF\text{-}62)_{0.75}$.*** *Water adsorption (solid)/desorption (open) isotherms of the a. crystal mixture and b. CGCs, performed at 298 K.*

4.3 Conclusions

Composite formation has been used to exert control over the chemical functionality and physical properties of materials such as molecular crystals.[284] Here, this approach has been adapted to metal–organic frameworks; this is a prototypical example of a MOF CGC formed by embedding a MIL-53 within a MOF glass matrix. The structural integrity of both the crystalline and glass components of the materials has been demonstrated for samples both before and after vitrification. In this first example of a metal–organic framework crystal–glass composite, ZIF-62 was selected as the glass-former due to its relatively low T_m. A MOF with a T_d greater than the T_m of ZIF-62, MIL-53, was successfully encapsulated within the glass without decomposition. The high-temperature, large-pore phase of MIL-53 was suspended in the glass at room temperature in this material. This phenomenon was explored using water adsorption experiments, showing that this MIL-53-lp phase is retained in the glass even when exposed to water.

In this material, two separated phases are in close proximity and well mixed at a nanoscale. The resolution of STEM tomography precludes the determination of crystal–glass bonding but does indicate that the components are not separated by larger than *ca*. 5 nm. NMR measurements support these findings as chemical bonding could not be observed, but polarisation transfer times corroborate proximal components within the composite.

It may be possible that a glass matrix support may hinder temperature-dependent structural rearrangements in other MOFs. In addition, this family of composite materials may also facilitate the assembly of discrete MOF crystal particles into thermally and mechanically stable devices with various shapes, such as adsorption column or molecular separation membranes. This may open routes to further functional MOF CGCs and take advantage of many recent reports of MOF and coordination polymer glass formation.[72,159,285,286]

Due to the retention of the MIL-53-lp phase, a significant improvement of CO_2 gas adsorption was measured using only a 25 wt% sample. However, this is a relatively safe loading of MIL-53 into the matrix, and the glass material did not show signs of over-saturation, such as crumbling. The loading limit within this glass matrix is currently unknown, and the exploitation of the MIL-53-lp retention in the glass may provide a route to even higher CO_2 adsorption capacities through higher loading composites.

Chapter 5 Determination of Matrix Loading Capacity

Following the successful synthesis of a metal–organic framework crystal–glass composite, the maximum loading capacity of the glass matrix is investigated to capitalise on the enhanced gas sorption properties—aided by the open-pore retention phenomenon observed in the MIL-53 MOF CGC. An upper limit of MIL-53 loading within a_gZIF-62 is identified between 60–70 wt% as determined by Cu and synchrotron source X-ray data. This work is published in the following manuscripts:

[1] Ashling C. W., Johnstone, D. N., Widmer R. N., Hou J., Collins S. M., Sapnik A. F., Bumstead A. M., Midgley P. A., Chater P. A., Keen D. A., and Bennett T. D., **Synthesis and Properties of a Compositional Series of MIL-53(Al) Metal–Organic Framework Crystal–glass Composites**, *J. Am. Chem. Soc.* 2019, **141**, 15641–15648.

In this publication, the total scattering data was recorded by myself, with the aid of A. F. Sapnik, and A. M. Bumstead at Diamond Light Source, beamline I15-1, and processed by myself with the aid of D. A. Keen. PXRD measurements were recorded by myself and NMR measurements were recorded at the University of Cambridge Department of Chemistry and analysed by myself. STEM images were recorded and analysed by D. N. Johnstone and S. M. Collins. R. N. Widmer and I performed X-ray diffraction refinements. Finally, the manuscript was written by myself and T. D. Bennett, with the aid of all authors.

[2] Collins S. M., Kepaptsoglou D. M., Hou J., Ashling C. W., Radtke G., Bennett T. D., Midgley P. A., Ramasse Q. M., **Functional Group Mapping by Electron Beam Vibrational Spectroscopy from Nanoscale Volumes**, *Nano Lett.* 2020, **20** (2), 1272–1279

In this publication, I synthesised the composite material and provided FT-IR analysis of the isolated components, mixtures, and composite materials in addition to helping write the manuscript.

5.1 Synthesis of a Series of MIL-53 MOF CGCs

In the optimisation of a novel composite material, it is essential to understand the limits to the production of the material. One of the most important of such considerations is the loading limit to which the matrix can effectively be utilised. Fortunately, the retention of MIL-53-lp within the composite presents a unique opportunity for this loading limit. It is expected that on increasing MIL-53 concentration, any crystalline material in the end composite that has not been encapsulated will activate through to the MIL-53-np phase.

Samples of $(MIL\text{-}53)_x(a_gZIF\text{-}62)_{1-x}$, where x = 0.25, and also $0.3 \leqslant \times \leqslant 0.9$ in 0.1 increments, were synthesised by ball milling appropriate masses of crystalline ZIF-62 and MIL-53-as, pressing the resultant intimately mixed powder in a 13-mm-diameter dye at 0.74 GPa, heating to 450 °C for 15 min, and quenching to room temperature. The materials produced were opaque, cream-coloured monoliths, which became brown with increasing concentrations of MIL-53, ascribed to a small amount of thermal decomposition of the MIL-53 component. Neither parent material can be identified from SEM images, and the relatively smooth surfaces of the bulk material provide evidence of appreciable flow in the ZIF-62 liquid state (**Figure 79**).

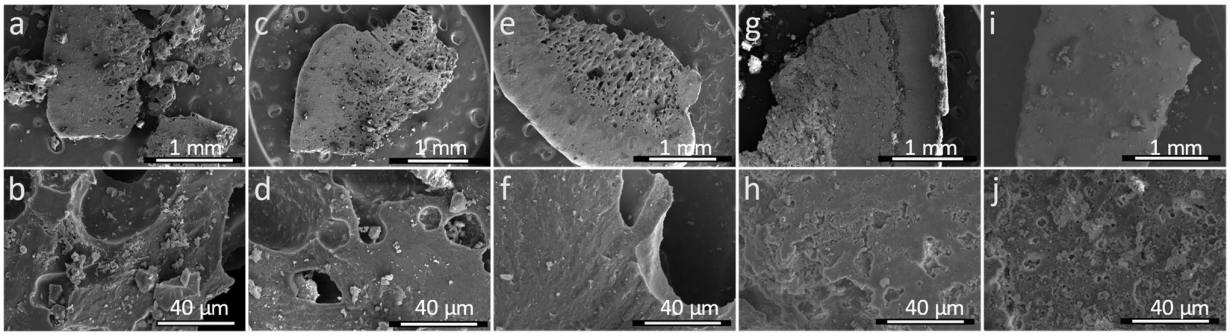

Figure 79: Scanning electron microscopy images of CGCs with different loadings of MIL-53. *a–b.* $(MIL\text{-}53)_{0.3}(a_gZIF\text{-}62)_{0.7}$, c–d. $(MIL\text{-}53)_{0.4}(a_gZIF\text{-}62)_{0.6}$, e–f. $(MIL\text{-}53)_{0.5}(a_gZIF\text{-}62)_{0.5}$, *g–h.* $(MIL\text{-}53)_{0.7}(a_gZIF\text{-}62)_{0.3}$, i–j. $(MIL\text{-}53)_{0.8}(a_gZIF\text{-}62)_{0.2}$.

5.1.1 Composite Series Composition

For component analysis, the composite series were studied by nuclear magnetic resonance spectroscopy (NMR). This was performed by first dissolving the frameworks in an acidic deuterated medium of 3:1 d^6-dimethyl sulfoxide with deuterated hydrochloric acid mixture and sonicating to ensure dissolution. Such dissolution breaks the framework into its corresponding protonated ligands (**Figure 80**).

All assignable signals are shown between 10–7.25 ppm. Each of these signals can be seen to vary proportionally with its concentration within the sample. Explicitly, the single signal arising from BDC (due to chemical equivalence), c, at 7.95 ppm can be seen to rise whilst peaks corresponding to protons in ZIF-62, a–b and d–f, all decrease with increasing MIL-53 loading. It is also of note that the integral ratio of peaks a and b, (corresponding to molecules of benzimidazole and

imidazole, respectively) remain constant at 1:~7. This ratio corresponds to formulae of ~[Zn(Im)$_{1.75}$(bIm)$_{0.25}$], consistent with prior literature.[65]

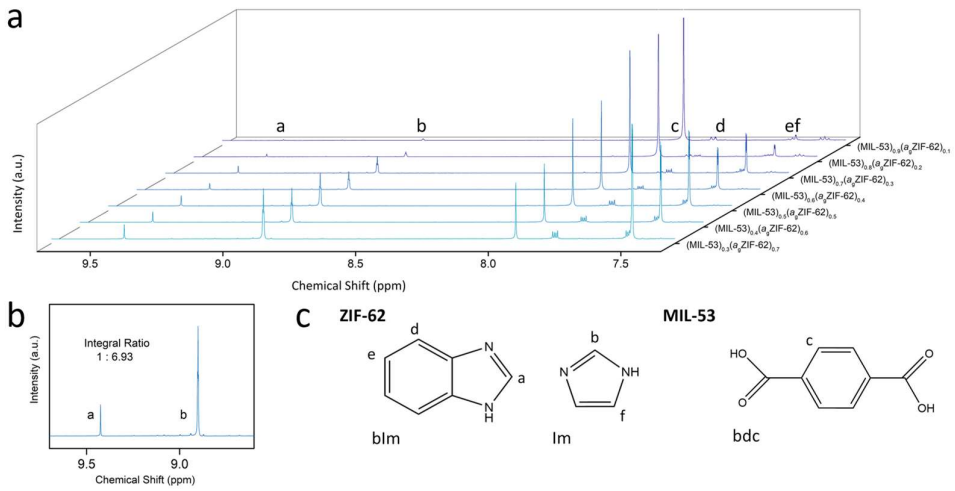

Figure 80: Ligand ratio calculation for a compositional series of (MIL-53)$_x$(a$_g$ZIF-62)$_{1-x}$. *a. ^{1}H NMR spectra of the (MIL-53)$_x$(a$_g$ZIF-62)$_{1-x}$ MOF CGC series using a 2.5:1 ratio of deuterated dimethyl sulfoxide and hydrochloric acid solvents. b. Peak integral ratios of (MIL-53)$_{0.25}$(agZIF-62)$_{0.75}$. c. Ligands within the frameworks. Peaks in the NMR spectra (a) are assigned (a–f) to protons in the ligands as indicated in c.*

The previous sets of analyses have not so far been able to determine whether the synthesis of the composite has generated any additional bonds. Each sample was probed using infra-red radiation to screen for any new chemical interactions (**Figure 81**).

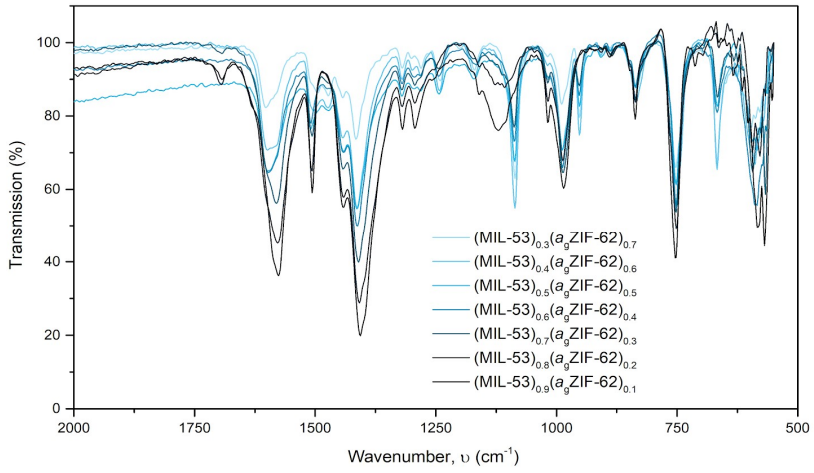

Figure 81: Transmission FTIR of the (MIL-53)$_x$(agZIF-62)$_{1-x}$ composite series. *Overlay of the Fourier transformed infrared (FTIR) spectra of the (MIL-53)$_x$(a$_g$ZIF-62)$_{1-x}$ series.*

Surface interactions of the two components would be at a maximum at the maximum loading capacity, sequentially increasing up to this point from lower loadings, and decreasing after this point. Any interactions from these materials

must, therefore, scale with the interfacial surface areas, and as such, modes of bond vibrations would be at a maximum at the maximum loading capacity of the composite. However, so too would vibrational modes arising from MIL-53-lp which increase in intensity due to greater content but subsequently decrease after the maximum loading due to conversion through to the MIL-53-np phase. Samples of MIL-53-np, MIL-53-as and a_gZIF-62 are accompanied to search for new bond vibrations.

What is observed in this sequence are the weakening IR bands associated with a_gZIF-62 (700, 950, and 1100 cm^{-1}) accompanied by the strengthening bands of MIL-53-lp (750, 1000, 1300, 1350, 1400, 1470, and 1600 cm^{-1}) and a broad, weak band correlating to increasing content of MIL-53-np (1125 cm^{-1}). The frequencies of these transitions are consistent with prior studies delineating the bond vibration and stretching mode differences between MIL-53-lp and MIL-53-np.[287]

5.1.2 MIL-53 Phase Identification and Matrix Loading Capacity

Laboratory PXRD measurements (Cu K_α radiation, λ = 1.5418 Å) were carried out on the compositional series of finely ground $(MIL\text{-}53)_x(a_gZIF\text{-}62)_{1-x}$ (**Figure 82**). The diffraction pattern for $(MIL\text{-}53)_{0.3}(a_gZIF\text{-}62)_{0.7}$ contained several peaks ascribed to the MIL-53-lp phase, of which the (101), (011), and (202) reflections were most prominent. No reflections were observed which could be ascribed to the MIL-53-np phase. However, upon the increasing concentration of MIL-53 within the composite to 70 wt%, peaks ascribed to the (200) and (110) reflections of MIL-53-np phase emerged and increased in relative intensity thereafter.

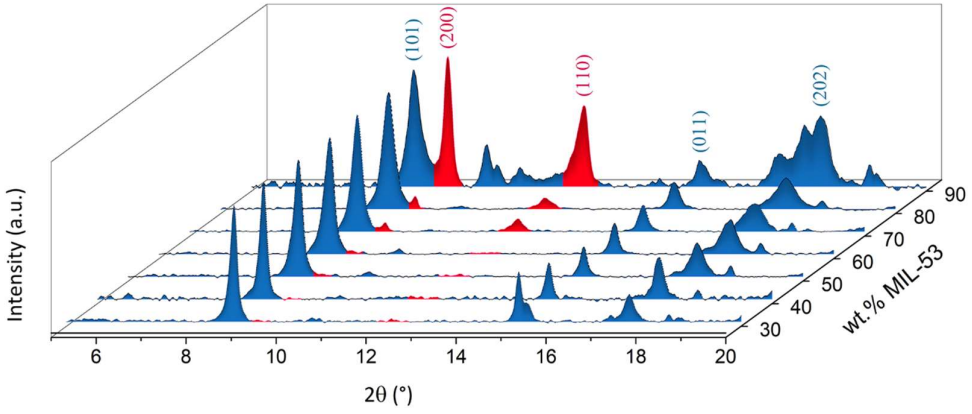

***Figure 82: Laboratory powder X-ray diffraction patterns of the $(MIL\text{-}53)_x(a_gZIF\text{-}62)_{1-x}$ composite series**, highlighting the MIL-53-np Bragg reflections in red. Background subtracted for clarity and normalised to the (101) peak of MIL-53-lp (blue).*

Subsequently, room-temperature X-ray total scattering data were collected for samples of the $(MIL\text{-}53)_x(a_gZIF\text{-}62)_{1-x}$ series (and the corresponding crystalline mixtures of the same proportions) using synchrotron radiation (λ = 0.161669 Å), shown in *Q* space (a function of 2θ, $|Q| = \frac{4\pi}{\lambda} Sin\left(\frac{2\theta}{2}\right)$). These data display a rise of a peak emerging at 1.3 $Å^{-1}$ for sample compositions of 70 wt% MIL-53 and above (**Figure 83**). This peak corresponds to the formation of the MIL-53-np phase and agrees with laboratory PXRD measurements. For greater phase determination accuracy, Rietveld refinement was performed on the synchrotron-source total scattering data using MIL-53-lp and MIL-53-np crystallographic information

files (**Figure 83**). The threshold for MIL-53-lp stabilisation, using the materials processing described here, was therefore identified as between 60 and 70 wt% MIL-53. Higher incorporations led to the emergence of MIL-53-np.

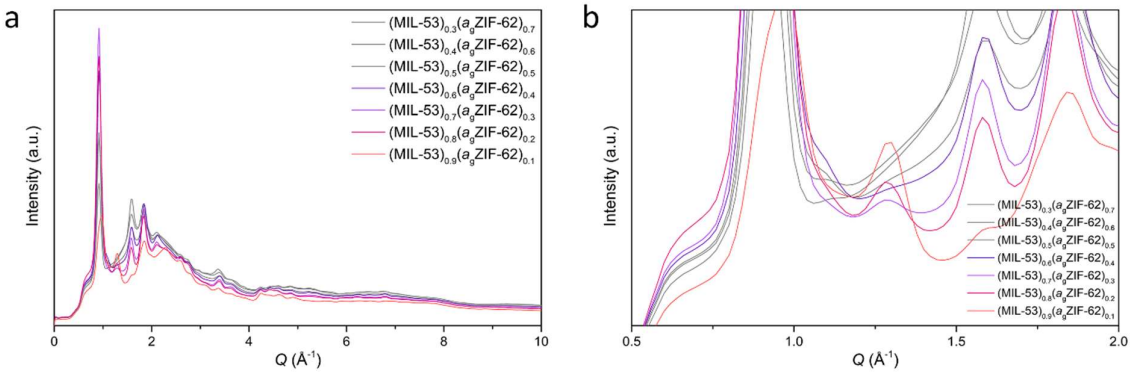

Figure 83: Emergence of MIL-53-np Bragg diffraction peaks in recorded total-scattering data. *a. Synchrotron recorded total scattering data (Q space range 0–10 Å^{-1}), and b. synchrotron recorded total scattering data (Q space range 0.5–2.0 Å^{-1}).*

These data were analysed using TOPAS (academic) V6 software. Pseudo-Voigt peak shapes were globally refined as a single set of parameters for all scan files. A ninth-order Chebychev polynomial background, a Gaussian background accounting for the diffuse scattering from the ZIF-62 glass, scale factors, unit cell parameters of the MIL-53 structures, eighth-order spherical harmonics, and preferred orientation corrections were refined individually for all scans. With no signs of MIL-53-np, samples of (MIL-53)$_{0.3}$(a_gZIF-62)$_{0.7}$ to (MIL-53)$_{0.6}$(a_gZIF-62)$_{0.4}$ were refined using only the MIL-53-lp hkl phase. Samples of ≥ 70 wt% MIL-53-as were refined using MIL-53-np and MIL-53-lp hkl phases to determine phase contributions to the PXRD patterns. Since a Pawley refinement is unable to provide quantitative phase determination, these PXRD patterns were analysed with a basic Rietveld refinement strategy. Whilst atomic coordinates were entered, for simplicity, they were not refined to each pattern (**Appendix Figures A1–7**).

Table 7: (MIL-53)$_x$(a_gZIF-62)$_{1-x}$ unit cell refinements. *Crystallographic data determined from Rietveld analyses of total scattering data of the (MIL-53)$_x$(a_gZIF-62)$_{1-x}$ X-ray diffraction series.*

	MIL-53-lp				MIL-53-np				
Sample	a (Å)	b (Å)	c (Å)	Quantity (%)	a (Å)	b (Å)	c (Å)	B (°)	Quantity (%)
MIL-53-lp*	6.608(1)	16.675(3)	12.813(2)						
MIL-53-np*					19.513(2)	7.612(1)	6.576(1)	104.241(1)	
(MIL-53)$_{0.3}$(a_gZIF-62)$_{0.7}$	6.59(1)	16.9(1)	12.65(5)	100					0
(MIL-53)$_{0.4}$(a_gZIF-62)$_{0.6}$	6.61(2)	16.7(2)	12.71(9)	100					0
(MIL-53)$_{0.5}$(a_gZIF-62)$_{0.5}$	6.64(2)	17.0(1)	12.46(6)	100					0
(MIL-53)$_{0.6}$(a_gZIF-62)$_{0.4}$	6.64(2)	17.0(1)	12.44(4)	100					0
(MIL-53)$_{0.7}$(a_gZIF-62)$_{0.3}$	6.64(2)	16.9(3)	12.55(13)	60(5)	19.22(10)	7.80(4)	6.82(5)	107.5(6)	40(5)
(MIL-53)$_{0.8}$(a_gZIF-62)$_{0.2}$	6.63(2)	16.8(3)	12.63(11)	55(5)	19.37(11)	7.73(3)	6.91(4)	106.2(4)	45(5)
(MIL-53)$_{0.9}$(a_gZIF-62)$_{0.1}$	7.02(6)	16.5(1)	12.74(8)	30(5)	19.37(7)	7.83(2)	6.84(4)	105.8(5)	70(5)

* Published data by Loiseau *et al.*

5.1.3 Crystal–Glass Composite Microstructure

Scanning transmission electron microscopy (STEM) was used to investigate the microstructure in the $(MIL\text{-}53)_x(a_gZIF\text{-}62)_{1-x}$ CGCs (**Figure 84**, **Appendix Figures A8–9**). Scanning electron diffraction (SED) was used to map the number of Bragg diffraction peaks measured in the diffraction pattern recorded at each probe position, as the electron probe was scanned across the sample, to reveal the location of the crystalline phases in MOF CGCs, as shown in part c) of each figure. These crystallinity maps demonstrate close contact between crystalline and noncrystalline regions within the MOF CGCs across the composition range. Comparison with compositional maps showing the distribution of metal centres, obtained *via* STEM X-ray energy-dispersive spectroscopy (STEM-EDS) mapping of the same particles and shown in part a) of each figure, confirms that the crystalline regions correspond to those which are rich in Al metal centres, as expected for MIL-53.

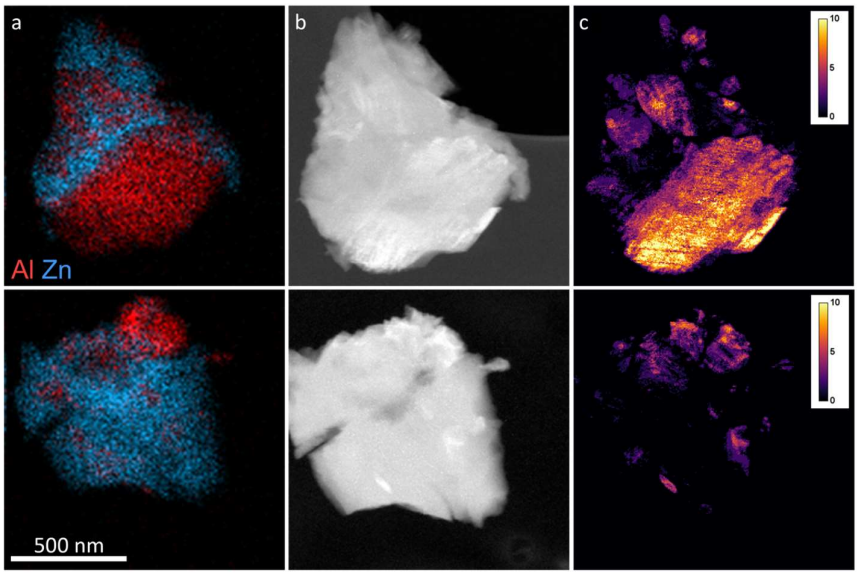

Figure 84: Scanning transmission electron microscopy of MOF CGC particles of $(MIL\text{-}53)_{0.6}(a_gZIF\text{-}62)_{0.4}$. *a. Compositional maps of Al (red) and Zn (blue) metal centres from STEM-EDS mapping. b. Annular dark-field images. c. Crystallinity maps showing the number of Bragg peaks as a function of probe position in SED data. The colour intensity scale for the crystallinity maps showing the number of Bragg scattering peaks identified at each probe position in the scanned field of view is presented for reference. Bragg peaks are recorded only from crystalline material, and the number of peaks recorded at each position depends on the local crystal orientation. The scale is identical for all images.*

Samples of 60, 70, and 90 wt% were specifically chosen to isolate areas of large and narrow-pore MIL-53 for a better understanding of the MIL-53-lp phase stabilisation phenomenon. Regions showing scattering from the (200) or (110) of the MIL-53-np phase could not be identified in any of the samples. Likely, this is due to the ultra-high vacuum conditions required to record the data, which induces the phase shift to MIL-53-lp.[120]

With microstructural analysis, we move to an atomic scale analysis of the materials using PDF analysis. Data of the samples were recorded on the I15-1 beamline at Diamond Light Source, UK (λ = 0.161669 Å, EE20038-1, see **Section 3.1.4.2**). Structure factors, *S*(*Q*), of the composite series were obtained from processing the total scattering data of the composite series and the corresponding crystalline mixtures, (MIL-53)(ZIF-62)(X/Y), where *X* and *Y* represent the respective weight percentages of each component.

The structure factors of the crystalline components as expected show Bragg scattering from both phases, and those peaks corresponding to ZIF-62 are replaced with a diffuse scattering in the composite series. Appropriate corrections of these data were performed with GudrunX software and the data were Fourier transformed to obtain the corresponding PDFs (**Figure 85**). The intensity of the peaks in the PDF of the (MIL-53)(ZIF-62)(X/Y) series varies proportionally between the two end-members (MIL-53-as and ZIF-62) as a function of the relative proportions of each end member. The PDFs of the composite series do not display the same ideal conformity between the two end-members (MIL-53-as and a_gZIF-62). This is likely due to (i) mixtures of MIL-53-lp and MIL-53-np phases present, (ii) possible interactions at the interfaces between the crystal and glass, and (iii) slight difference between MIL-53-as and MIL-53-lp as the proper end member for the series (**Figure 85**).

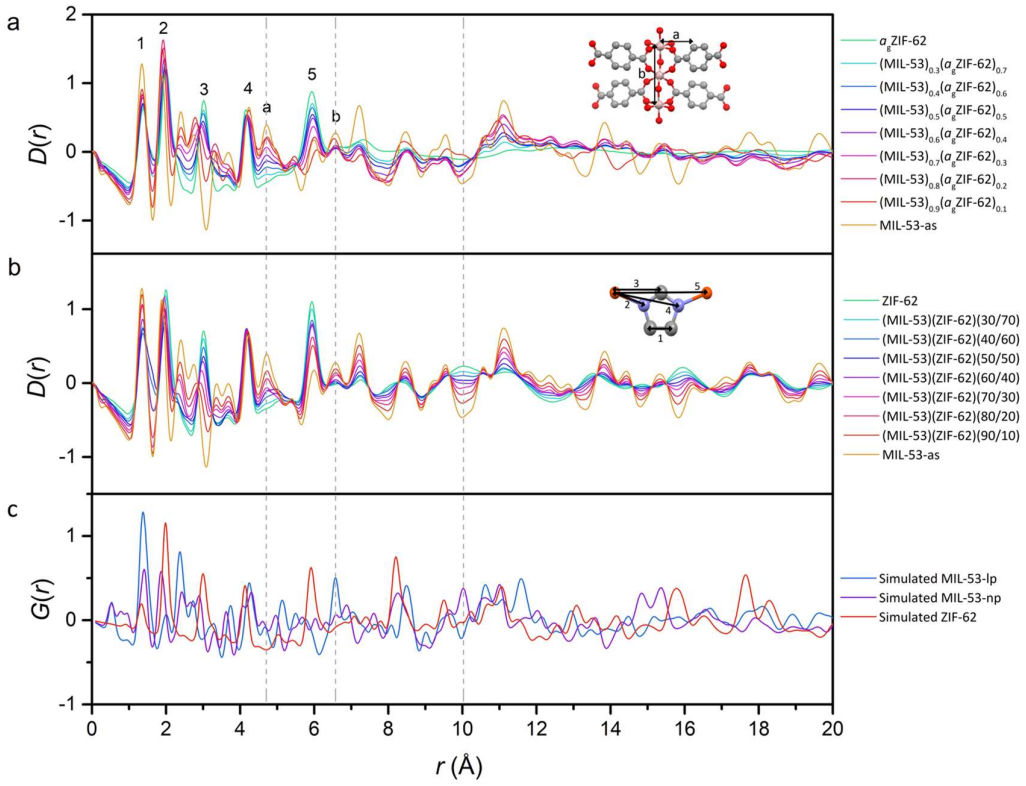

Figure 85: PDF series of the crystalline and composite series with predicted atomic correlations. *a. Overlay PDFs of the (MIL-53)$_x$(a_gZIF-62)$_{1-x}$ series with a_gZIF-62 and MIL-53-as for comparison. (Inset) MIL-53-lp (Al, pink; O, red; C, grey) with correlation assignments. b. Overlay PDFs of the crystalline mixtures of the (MIL-53)(ZIF-62)(X/Y) series with MIL-53 and ZIF-62. (Inset) ZIF-62 (Zn, red; N, blue; C, grey) with correlation assignments. c. Simulated PDFs of MIL-53-lp, MIL-53-np, and ZIF-62 using PDFGUI software. Sub-1 Å data are due to the way the solvent occupancies were modelled in the published crystallographic information files used.*

A comparison of the PDFs of (MIL-53)(ZIF-62)(X/Y) and $(MIL\text{-}53)_x(a_gZIF\text{-}62)_{1-x}$ shows that correlations ascribed to the short-range order of ZIF-62 are retained after vitrification (**Figure 85** peaks 1-5). These peaks may be assigned to C–C (1.38 Å, 1), Zn–N (1.98 Å, 2), Zn–C (3.02 Å, 3), Zn–N (4.18 Å, 4), and Zn–Zn (5.96 Å, 5) interatomic distances, confirmed by simulated PDF (**Figure 86**). In the composites, correlations above 6 Å ascribed to ZIF-62 tend to zero due to the loss of long-range order. Interatomic distances associated with MIL-53 may be identified in both series (**Figure 85** peaks a&b)—these peaks are assigned to Al–C (4.71 Å, a), and Al–Al (6.57 Å, b) interatomic distances—though they are noticeably less intense due to weaker scattering of Al compared to Zn, confirmed by simulated PDF (**Figure 86**). In the composite series, all correlations past the short-range order of ZIF-62 (~8 Å) originate from crystalline MIL-53. Predicted PDF patterns for ZIF-62, MIL-53-as, MIL-53-np, and MIL-53-lp with their corresponding metal–metal and metal–(N or O) are provided in **Figure 85**.

The PDF of $(MIL\text{-}53)_{0.9}(a_gZIF\text{-}62)_{0.1}$ contains correlations at 10, 13.1, and 14.8 Å, which qualitatively agree with peak positions in a predicted PDF for MIL-53-np (**Figure 86c**). These are absent in the experimental PDF of MIL-53-as. The identification of the MIL-53-np phase within the $(MIL\text{-}53)_{0.9}(a_gZIF\text{-}62)_{0.1}$ agrees with PXRD data collected. We note that the PDFs of $(MIL\text{-}53)_{0.8}(a_gZIF\text{-}62)_{0.2}$ and $(MIL\text{-}53)_{0.7}(a_gZIF\text{-}62)_{0.3}$ do not display readily distinguishable MIL-53-np PDF correlations belonging to MIL-53-np. This may imply that an insufficient concentration of the MIL-53-np phase is present in these samples to give rise to such correlations, especially considering that the peak at 10 Å corresponds to a minimum in the PDFs from MIL-53-lp and MIL-53-as.

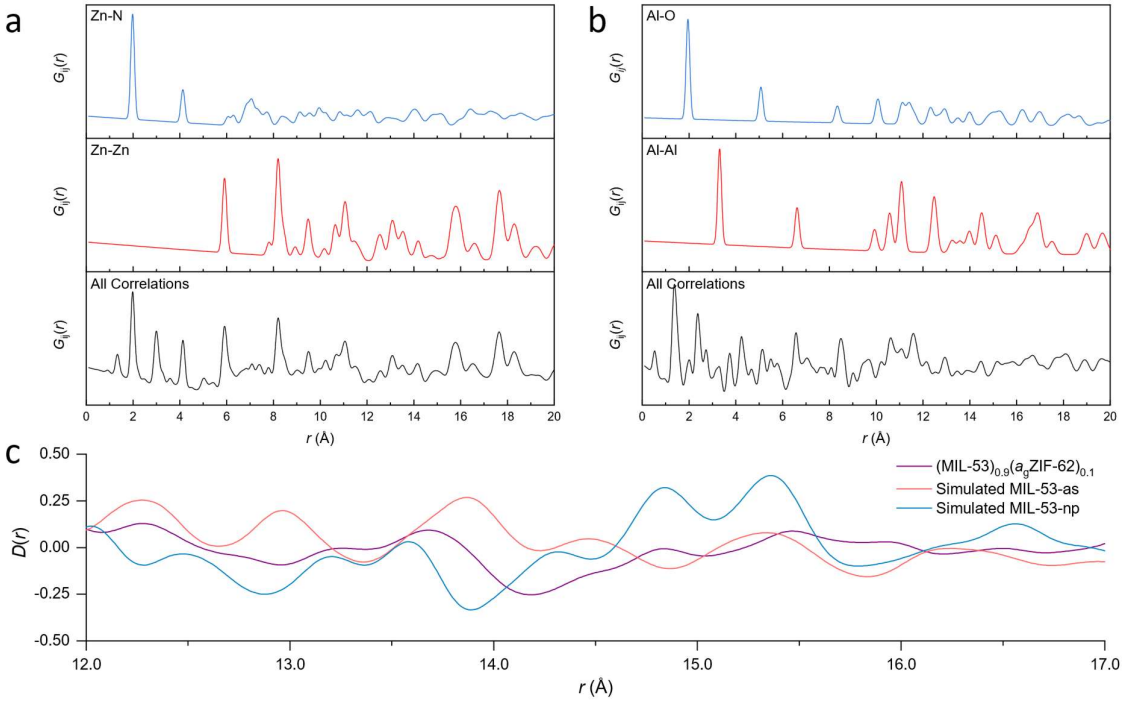

Figure 86: Simulated total and partial PDFs of ZIF-62 and MIL-53-lp. *a. Simulated G(r) data for zinc-nitrogen, zinc-zinc, and all correlations in ZIF-62. b. Simulated G(r) data for zinc-nitrogen, zinc-zinc, and all correlations in MIL-53-lp. c. Comparison of* $(MIL\text{-}53)_{0.9}(a_gZIF\text{-}62)_{0.1}$ *with PDFs of MIL-53-as and MIL-53-np simulated using their respective crystalline structures in PDFGUI.*

5.1.4 Maximum CO_2 Uptake

A sample of $(MIL\text{-}53)_{0.25}(a_gZIF\text{-}62)_{0.75}$ was previously observed to possess a CO_2 gas uptake of 66% that of a pure sample of MIL-53-np. Given that (i) MIL-53-lp is the main contributor to the adsorption capacity, and (ii) the phase of MIL-53 remains unaltered to loadings of $\leqslant$ 60 wt%, the adsorption capacities are expected to increase across those composites displaying only the MIL-53-lp phase. However, changes in adsorption trends are expected on moving to compositions above 60 wt%, *i.e.* the emergence of the MIL-53-np phase. The relationship between MIL-53 loading and gas uptake properties was probed using CO_2 gas adsorption isotherms for the full compositional series of MOF CGCs (**Figure 87**).

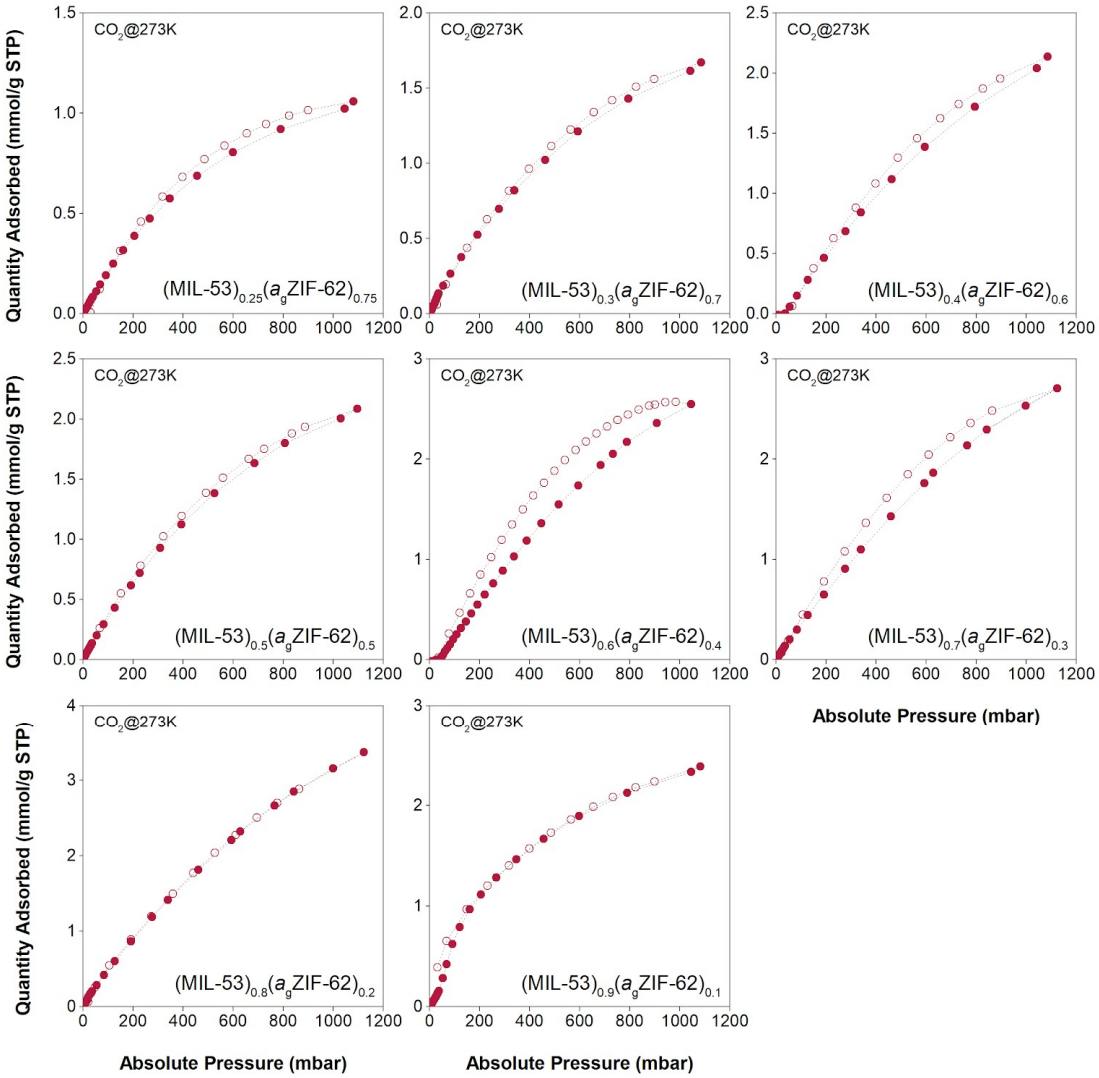

Figure 87: CO_2 gas adsorption for the composition series of $(MIL\text{-}53)_x(a_gZIF\text{-}62)_{1-x}$. *In these isotherms adsorption and desorption points are marked by solid and open points, respectively, and measured at 273 K.*

A small degree of hysteresis is observed for most samples but most prominent for those of $(MIL\text{-}53)_{0.6}(a_gZIF\text{-}62)_{0.4}$ and $(MIL\text{-}53)_{0.7}(a_gZIF\text{-}62)_{0.3}$. Hysteresis in the composite samples is likely due to the reduced diffusion kinetics caused by the glass component. It would be expected that the degree of hysteresis, given the same equilibration time across the samples, to correlate with the percentage of glass within the samples. This is not the case in these samples and likely indicates some degree of experimental error.

As an indication of reproducibility, three CO_2 isotherms of a sample of $(MIL\text{-}53)_{0.25}(a_gZIF\text{-}62)_{0.75}$ taken at various points in this thesis were contrasted against one another (**Appendix Figure A10**). These samples are part of three separate batches, produced by myself and Dr Jingwei Hou, and analysed using two separate instruments. It is clear that there is some error in the equilibration or calibration of the experiments. From these experiments, the value at 1013 mbar (the highest point on the lowest recorded isotherm) is averaged with the centre of the hysteresis loop at 1013 mbar for the other two isotherms. The error in this value is then recorded as the largest difference in the value from the average. Since experiments were not repeated for the other samples within the series, the error in these values is taken as the full range of recorded values for the sample of $(MIL\text{-}53)_{0.25}(a_gZIF\text{-}62)_{0.75}$ to indicate a reasonable error.

For the samples of $(MIL\text{-}53)_{0.25}(a_gZIF\text{-}62)_{0.75}$ – $(MIL\text{-}53)_{0.6}(a_gZIF\text{-}62)_{0.4}$, the total CO_2 quantity adsorbed increases in a broadly linear fashion, from 1.06 to 2.55 mmol/g, following the increasing concentration of MIL-53 in these samples, which is all present in the MIL-53-lp phase (**Figure 88**). A direct comparison of the gas sorption capacity of pure MIL-53-lp is not possible because the phase is unstable under the (room temperature) conditions used for gas adsorption measurement of these composites. Furthermore, any high-temperature study on MIL-53-lp provides a poor comparison given the temperature dependence of gas adsorption.

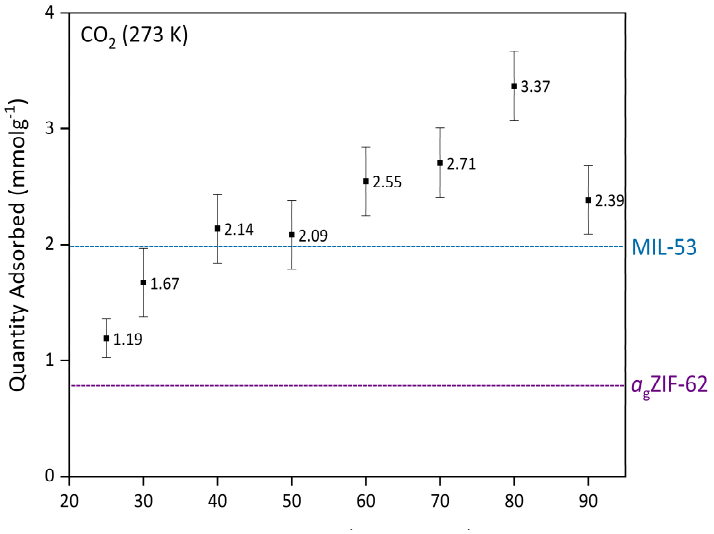

Figure 88: Quantity adsorbed from gas adsorption isotherms for the $(MIL\text{-}53)_x(a_gZIF\text{-}62)_{1-x}$ series at 1 bar using CO_2 gas at 273 K. *The quantities adsorbed for samples of activated MIL-53 (MIL-53-np, 1.99 mmol/g) and a_gZIF-62 (0.79 mmol/g) are displayed by blue and purple lines, respectively.*

$(MIL\text{-}53)_{0.7}(a_gZIF\text{-}62)_{0.3}$ and $(MIL\text{-}53)_{0.8}(a_gZIF\text{-}62)_{0.2}$ also display successively higher CO_2 adsorption. These two samples possess comparable amounts of MIL-53-lp, though the greater proportion of MIL-53 compared to a_gZIF-62 in the latter sample renders its total CO_2 uptake higher. A significant decline in capacity is observed for $(MIL\text{-}53)_{0.9}(a_gZIF\text{-}62)_{0.1}$ as this material primarily comprises the MIL-53-np phase. Pure samples of MIL-53-np and a_gZIF-62 were previously shown to display CO_2 adsorption capacities of 1.99 and 0.79 mmol/g, respectively (at 273 K at 1 bar pressure). Furthermore, the sorption capacity of MIL-53-as is expected to be far lower than that of MIL-53-np due to the pore occupying species. Hence, compared with the room temperature stable forms of the pure MIL-53 (*i.e.* MIL-53-np and MIL-53-as), the composite has the greatest CO_2 capacity under ambient conditions. As before, mesopores are expected in all of the composites, which may enhance CO_2 uptake capacity.

5.2 Conclusions

In this chapter, a compositional series of $(MIL\text{-}53)_x(a_gZIF\text{-}62)_{1-x}$ crystal–glass composites have been synthesised. Sample composition was confirmed by NMR, which displayed relevant linker peak integrals varying in proportion to their relative contributions. The crystalline phase contribution of MIL-53 was determined by Rietveld refinement of X-ray diffraction studies, concluding that for MIL-53 loadings up to 60 wt%, the only phase observed at room temperature is the metastable MIL-53-lp.

Beyond this limit, a percentage of the excluded MIL-53-lp phase proceeds to form MIL-53-np upon cooling. This demonstrates a maximum total loading capacity of between 60 and 70 wt % MIL-53 within a_gZIF-62 in this case. Gas adsorption measurements demonstrate that the maximum effective gas adsorption capacity of the $(MIL\text{-}53)_x(a_gZIF\text{-}62)_{1-x}$ series is around 80 wt %. Here, the MOF CGC displays a CO_2 adsorption capacity that far exceeds the value of pure MIL-53-np; a sample of just 30-40 wt % loading of MIL-53 is expected to adsorb a similar quantity of CO_2 to a sample of pure MIL-53-np. These results show that relatively high loading capacities of crystalline MOFs within a MOF glass can be achieved and provide a first look at the interesting physical properties which may arise as a result.

This investigation into the loading limit of a MOF CGC system may open multiple avenues for potential future research. One such avenue may be the advancement of processing methods, leading to larger incorporations of the active MOF component. However, the breadth of applicable gases for these MOF CGC systems remains undefined for these systems.

Chapter 6 Exploring Alternative Crystalline MOF Systems

Predominantly, this work has discussed examples of MOF CGCs that have been successfully fabricated using MIL-53. In this chapter, the thermal stabilities of various other non-melting potential MOF candidates are studied, searching for those with decomposition temperatures above 450 °C. This chapter details efforts to synthesise a variety of MOF CGCs to uncover interesting potential properties. Thermogravimetric analysis of various materials was carried out to screen for obvious framework decomposition before 450 °C. Whilst many samples appeared to show mass loss events in regions where activation was expected, many MIL compounds were shown to undergo multiple-step framework decomposition. Two MOFs displayed definite thermal stability to the CGC synthesis conditions: MIL-118, $Al_2O_2(C_{10}O_8H_2)$, and UL-MOF-1, Li_2(2,6-ndc) (2,6-ndc, 2,6-naphthalenedicarboxylate). MOF-CCGs were subsequently synthesised using these two materials, and the gas sorption properties of these materials were investigated. This work is published in the following manuscript:

[1] Ashling C. W., Macreadie L. K., Southern T. J. F., Zhang Y., McHugh L. N., Evans R., Kaskel S., Telfer S. G., and Bennett T. D., **Guest size limitation in metal–organic framework crystal–glass composites**, *J. Mat. Chem. A.* 2021, **9**, 8386–8393.

Towards this publication, synthesis of MOFs, PXRD, PXRD refinements, TGA, and MOF CGC syntheses were all performed by myself. S. Kaskel provided samples of DUT-6 and DUT-8. T. J. F. Southern aided in the collection and processing of SEM data. L. K. Macreadie and S. G. Telfer aided in the collection and analysis of gas sorption data. Y. Zhang synthesised and melted a sample of ZIF-62 for gas sorption experiments. The manuscript was written by myself and T. D. Bennett with input from all authors.

6.1 Material Selection

The extension of this approach to crystalline MOFs, other than the previously described system using MIL-53, is dependent upon their structural integrity at the temperatures required for the fabrication of the MOF CGC (*e.g.* T_m, ZIF-62 = 437 °C).[65] This is further complicated by the lack of thermal stability data using standardised atmospheric conditions and heating rates, and furthermore by the lack of data on stability when held isothermally at elevated temperatures.[117]

In turn, the lack of additional MOF CGC chemistries limits any further conclusions on the gas sorption and separation behaviour of these materials, which is confined to N_2 and CO_2 adsorption on MIL-53 based samples only. Such considerations motivated us to provide further examples of MOF CGCs from different crystalline chemistries and architectures and evaluate their gas adsorption behaviour.

Table 8: Reported thermal stabilities of crystalline MOF component candidates.

MOF	Composition	Decomposition temperature, T_d (°C)	Heating Rate (°C/min)	Ref.
CUmof-9	$Yb_2(2,6\text{-ndc})_3(H_2O)\cdot(H_2O)_2$	550[a]	5	288
DUT-6	$Zn_4O(2,6\text{-ndc})(btb)_{4/3}(def)_{16}(H_2O)_{9/2}$	~400	5	289
DUT-8	$Ni_2(2,6\text{-ndc})_2(dabco)$	~400	5	290
MIL-68	V(OH)(BDC)	~500	10	261
MIL-118	$Al_2(OH)_2(C_{10}O_8H_2)$	~450	1	191
MIL-120	$Al_4(OH)_8(C_{10}O_8H_2)$	~480	1	262
MIL-126(Sc)	$Sc_3O(H_2O)_2(bpdc)_3X$ (X = OH or Cl)	~500	10	263
UL-MOF-1	$Li_2(2,6\text{-ndc})$	610[a]	10	192

2,6-ndc = naphthalene-2,6-dicarboxylate
BDC = benzene-1,4-dicarboxylate
bpdc = biphenyl-4,4′-dicarboxylate
btb = benzene-1,3,5-tribenzoate
def = *N,N*-diethylformamide
dabco = 1,4-diazabicyclo[2.2.2]octane

[a] Experiment performed under an inert atmosphere

Several MOF candidates for the crystalline filler were selected according to their reported thermogravimetric analyses (TGA) indicating the required stability to 450 °C (**Figure 89**) and were synthesised using the published procedures (see **Section 3.2.1**), except for DUT-6 and DUT-8—S. Kaskel kindly provided activated samples of these. An elevated low angle baseline is also observed in these samples—which is more pronounced in those with less intense peaks e.g. MIL-68 and MIL-126—due to instrumental error.

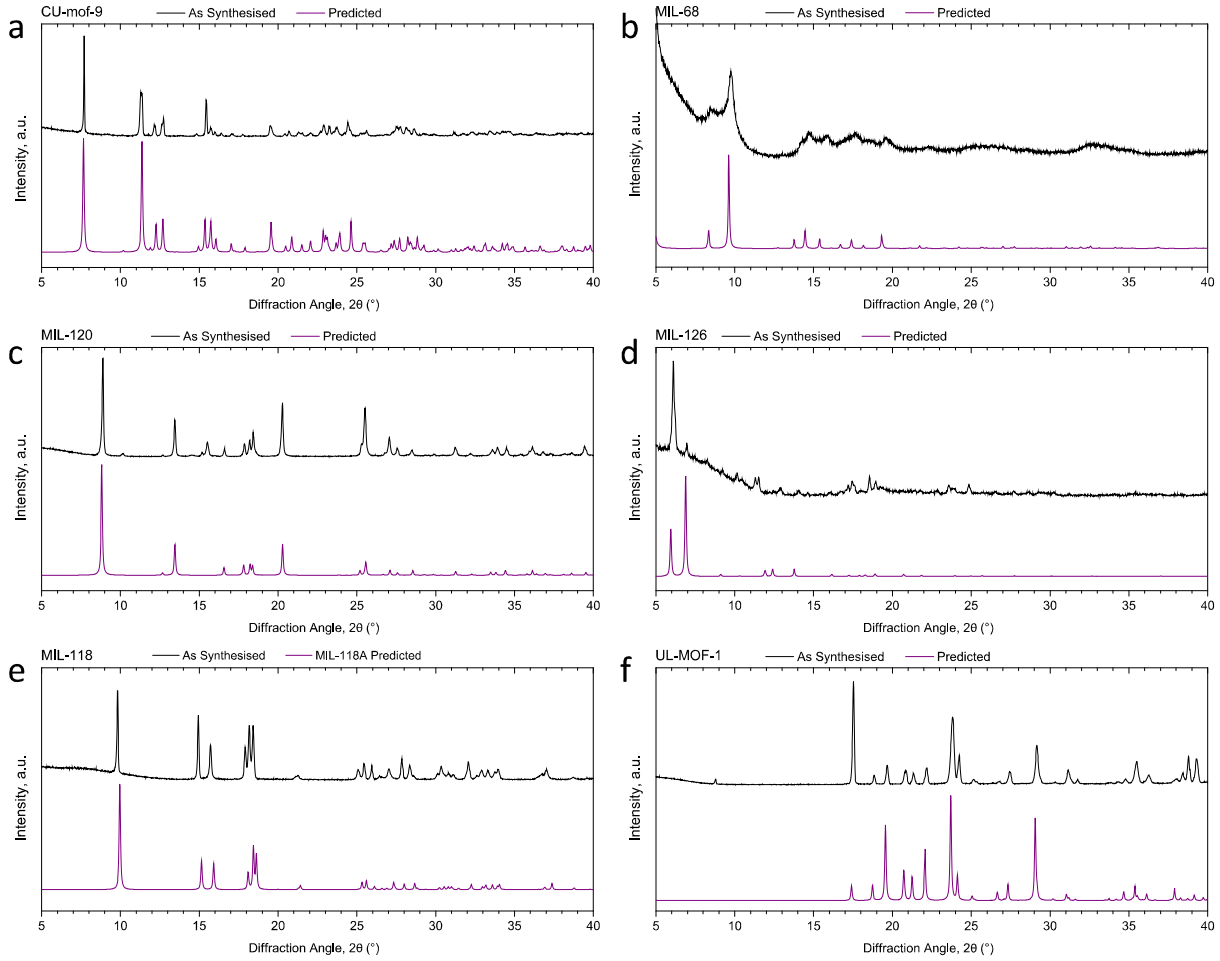

Figure 89: Synthesis of a range of MOF materials. *PXRD patterns of the as-synthesised and predicted patterns of a. CU-mof-9, b. MIL-68, c. MIL-120, d. MIL-126, e. MIL-118, and f. UL-MOF-1.*

Each of these frameworks shows a similar diffraction profile to the predicted pattern. Notably, (i) the synthesised MIL-68 sample displayed weak Bragg diffraction peaks; however, this is consistent with the reported pattern.[261] (ii) the synthesised MIL-126 sample displays the greatest similarity in the position of the two reflections at 6° and 7° 2θ and little similarity elsewhere. However, this may be due to the measurement of a non-activated sample. (iii) predictably, MIL-118 is synthesised in its as-synthesised "MIL-118A" phase.

Each of the eight frameworks selected was analysed using TGA conducted at a standard heating rate of 10 °C/min under inert nitrogen (N_2) to confirm thermal stability (**Figure 90a**). The onset of thermal decomposition, T_d, below 450 °C was only observed for samples of DUT-6 and DUT-8. However, the T_ds of these two materials were greater than the reported values due to the faster heating rate used in our evaluation compared to those employed in the literature. As mass loss had already begun to occur at 450 °C, and given the need for isothermal heat treatment at this temperature for CGC fabrication, this precluded further study of these specific materials (**Figure 90b,c**).

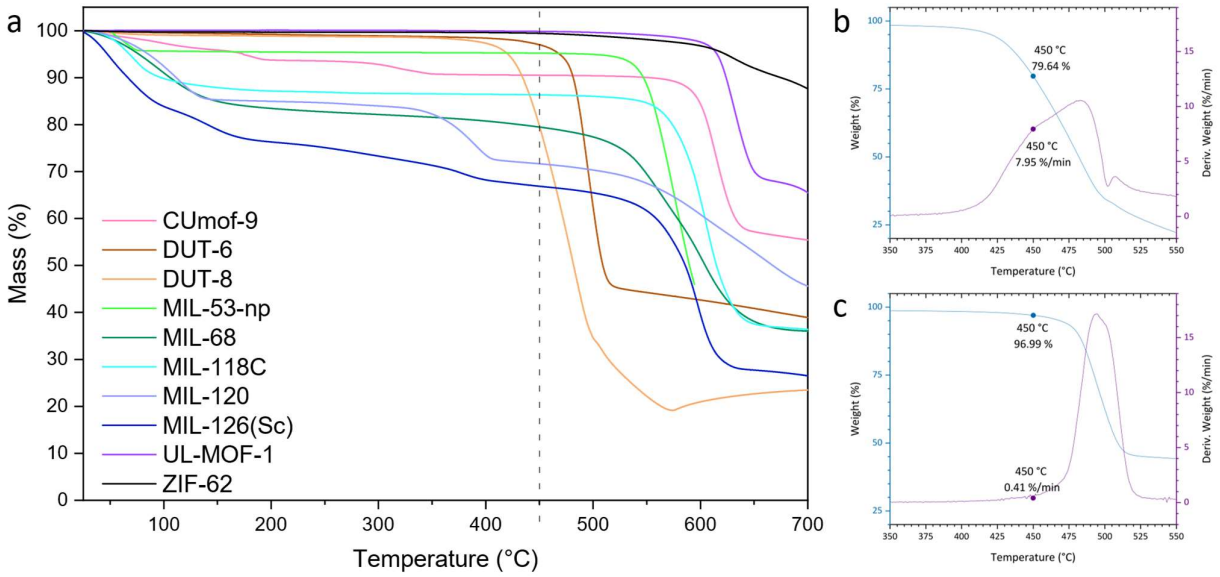

Figure 90: Thermogravimetric analysis of a series of MOF CGC filler candidates. *a. Thermogravimetric analysis, performed at 10 °C/min under nitrogen gas on the MOFs listed in* ***Table 8****, and Thermogravimetric analysis of b. DUT-8, and c. DUT-6, displaying the normalised mass loss and the first differential of the normalised mass with respect to time. This experiment was performed at a heating rate of 10 °C/min under a nitrogen protective atmosphere.*

To provide a more accurate evaluation of thermal stability, the remaining MOFs were heated to 450 °C for 1 min, under N_2, and allowed to cool to room temperature *in situ*. Ambient temperature powder X-ray diffraction (PXRD) data were then recorded (**Figure 91**). This relatively simple experiment highlighted the importance of performing thermal analysis of MOFs using an appropriate set of conditions, chosen according to the individual processing or application requirements. For example, Bragg peaks intensities in the PXRD pattern for MIL-68 (**Figure 91b**) were reduced to near negligible levels, alongside a significant reduction in intensities, or changes in the patterns, for MIL-120 and MIL-126(Sc) (**Figure 91c,d**). This is consistent with the thermal analysis performed by Volkringer *et al.*, confirming that the first step in decomposition for MIL-120 is due to ligand degradation.[262] An unreported recrystallisation of CUmof-9 was also observed (**Figure 91a**), though the high-temperature phase was not identified. MIL-68, MIL-120, MIL-126, and CUmof-9 were, therefore, not studied further.

The PXRD patterns of the three remaining samples: MIL-118, UL-MOF-1, and MIL-53-np, displayed Bragg peaks in good agreement with their room temperature structures after heating to 450 °C (**Figure 91e,f**, **Figure 92**). UL-MOF-1 has been reported to display exceptional thermal stability (T_d = 610 °C); the structure consists of alternating two-dimensional antifluorite type lithium oxide layers connected by 2,6-ndc struts (**Figure 92c**).[192] No flexible behaviour has been reported for this material. Conversely, MIL-118, $Al_2(OH)_2(C_{10}O_8H_2)$ ($C_{10}O_8H_2^{4-}$ - benzene-1,2,4,5-tetracarboxylate), exhibits a water-driven reversible structural transition, analogous to that of MIL-53.[191]

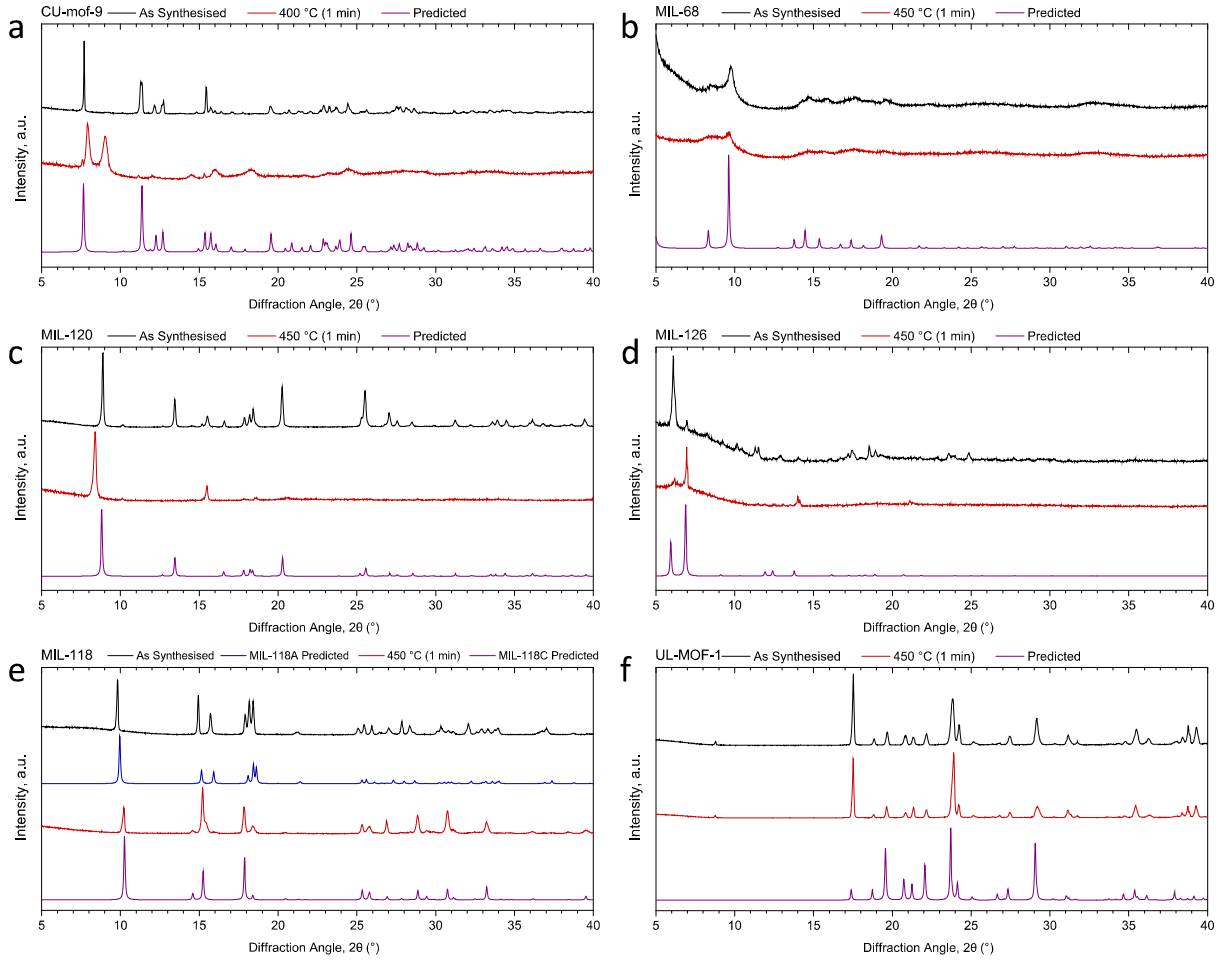

Figure 91: Thermal treatment of a selection of MOF fillers to determine crystal stability. *Powder X-ray diffraction patterns of a. CUmof-9, b. MIL-68, c. MIL-120, d. MIL-126, e. MIL-118, and f. UL-MOF-1 before and after heat treatment, including the simulated patterns for each structure for comparison.*

MIL-118 is typically synthesised with excess ligand in the pores of the framework and is named MIL-118A (*C2/c*). Upon heating MIL-118A, this excess ligand is removed, resulting in the open-pore framework, MIL-118B (*Pbam*), which is stable at high temperatures. Upon cooling, the framework adsorbs water to form the room temperature stable phase, MIL-118C (*Pnam*). The transition causes a shift from the rectangular 1-D tunnels in MIL-118B to lozenge-shaped channels, with water molecules occupying the pores in MIL-118C. Temperature-induced breathing is observed between the MIL-118C and MIL-118B phases. (**Figure 92a,b**).

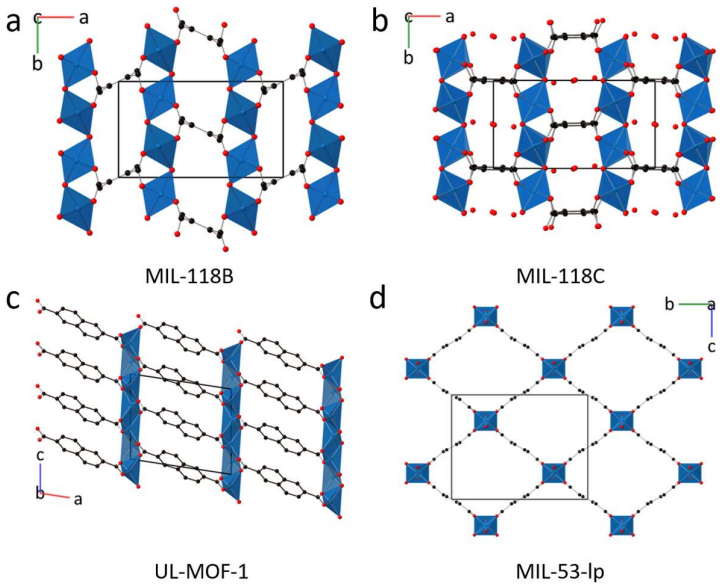

Figure 92: Crystal structures of suitable crystalline MOFs for MOF CGC fabrication. *Representations of a. MIL-118B, b. MIL-118C, c. UL-MOF-1, d. MIL-53-lp where; carbon – black, oxygen – red and M–O nodes replaced by blue polyhedra. Hydrogen atoms have been omitted for clarity. The unit cell is indicated by a black box with an overlay of crystallographic axes.*

6.2 Successful Synthesis of Further MOF CGCs

MOF CGCs containing 50 wt% crystalline UL-MOF-1 and MIL-118 were synthesised using the method outlined previously for a CGC containing MIL-53. Ambient temperature PXRD data were recorded for the three MOF CGCs. As expected, Bragg peaks present in the crystalline sample of UL-MOF-1 were also present in $(\text{UL-MOF-1})_{0.5}(a_g\text{ZIF-62})_{0.5}$. PXRD data for $(\text{MIL-53})_{0.25}(a_g\text{ZIF-62})_{0.75}$ demonstrated the presence of the open-pore MIL-53 phase, per previous results.[251,17] Interestingly, the PXRD data for $(\text{MIL-118})_{0.5}(a_g\text{ZIF-62})_{0.5}$ indicated little change in lattice parameters from the synthesised MIL-118 sample, which remained in the low-temperature MIL-118C (*Pnam*) phase (**Figure 93**, **Table 9**). This shows that, unlike the MIL-53 in $(\text{MIL-53})_{0.25}(a_g\text{ZIF-62})_{0.75}$, the MIL-118 encapsulated within the glass does not retain the high-temperature MIL-118B (*Pbam*) phase (**Figure 93a**).

In **Chapter 4**, the ingress of water was shown not to drive a transition from MIL-53-lp back to MIL-53-np in a room temperature MOF CGC.[16] It was, therefore, suggested that the stabilisation of MIL-53-lp does not arise because it is excluded from entering the composite CGC material. Instead, the polymeric phase is not soft enough to accommodate a large-scale change of the crystal phase structure, while the interfacial contact between the two phases is maintained.[16] Here, it is perhaps the case that either (i) interfacial contact between MIL-118 and the glass is less than that of MIL-53 and the glass, or (ii) that the volume changes upon the transition from MIL-118B to MIL-118C can be accommodated by the glass phase.

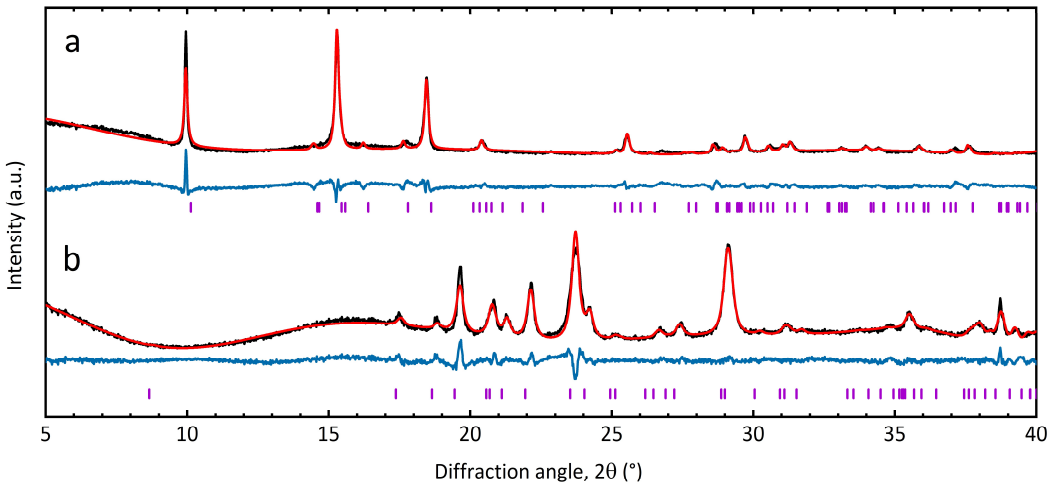

Figure 93: Crystallinity of (MIL-118)$_{0.5}$(a_gZIF-62)$_{0.5}$, and (UL-MOF-1)$_{0.5}$(a_gZIF-62)$_{0.5}$. *PXRD data of a. (MIL-118)$_{0.5}$(a_gZIF-62)$_{0.5}$, and b. (UL-MOF-1)$_{0.5}$(a_gZIF-62)$_{0.5}$. Recorded data in black, Pawley refinements in red, difference patterns in blue, and hkl indices in purple underneath the respective patterns.*

Table 9: Comparison of pure and composited MOF unit cells. *Lattice parameters from published crystallographic files and the corresponding lattice parameters of the crystalline material as determined by Pawley refinements.*[191,192]

Sample	**Lattice parameters**				
	a (Å)	*b* (Å)	*c* (Å)	β (°)	Rwp
MIL-118C	12.132	6.619	17.227	90	-
(MIL-118)$_{0.5}$(a_gZIF-62)$_{0.5}$	12.127	6.431	17.459	90	11.152
UL-MOF-1	10.302	5.345	8.662	98.659	-
(UL-MOF-1)$_{0.5}$(a_gZIF-62)$_{0.5}$	10.316	5.373	8.727	98.547	7.677

Scanning electron microscopy (SEM) images of MIL-53-np, MIL-118, and UL-MOF-1 display micrometre-sized crystals (**Figure 94**). Samples of MIL-118 and MIL-53 display reasonable size and shape uniformity in comparison to UL-MOF-1, which comprises a range of morphologies from 10 µm cubic structures to 200 µm sheets (**Figure 94e,f**). This occurs despite (i) X-ray diffraction phase purity which matches the reported crystallographic information, and (ii) a single thermal decomposition event at the reported temperature.

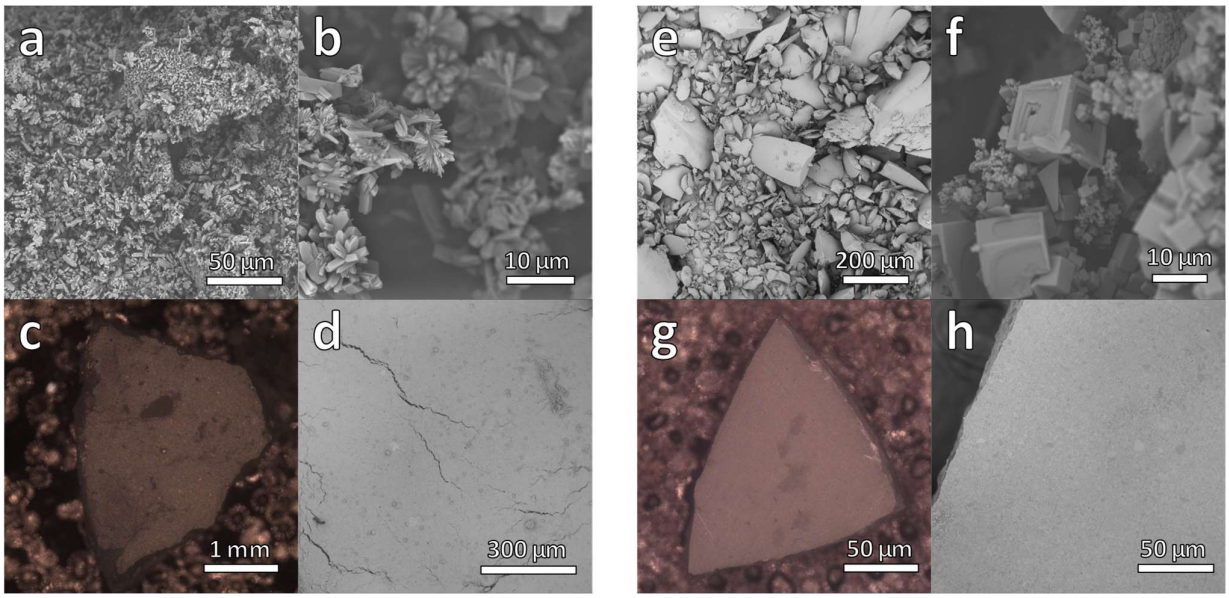

***Figure 94**: SEM and optical images of MIL-118, UL-MOF-1, and their respective MOF CGCs .* *SEM images of a–b. MIL-118C, c–d. $(MIL\text{-}118)_{0.5}(a_gZIF\text{-}62)_{0.5}$, e–f. UL-MOF-1, and g–h. $(UL\text{-}MOF\text{-}1)_{0.5}(a_gZIF\text{-}62)_{0.5}$.*

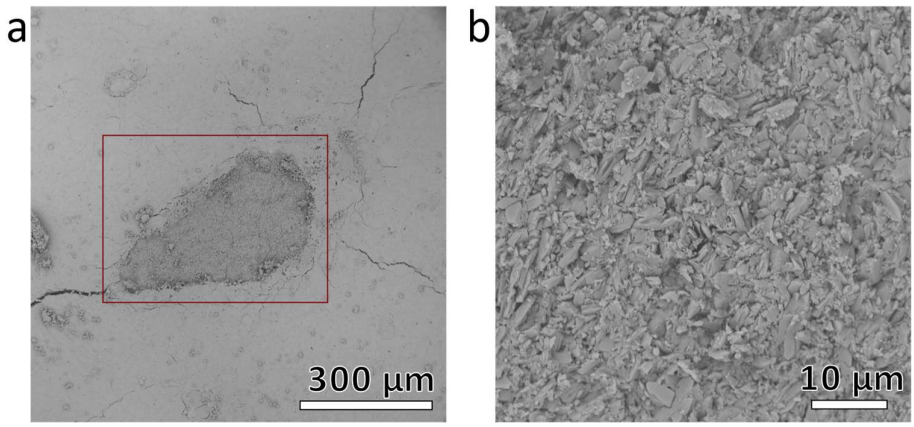

***Figure 95**: Structural investigations of $(MIL\text{-}118)_{0.5}(a_gZIF\text{-}62)_{0.5}$.* *Scanning electron microscopy images of a shard of $(MIL\text{-}118)_{0.5}(a_gZIF\text{-}62)_{0.5}$. An enhanced view of the surface defect in a. highlighted in red is shown in b.*

The MOF CGCs formed in each case demonstrated self-supporting, contiguous, bulk morphologies. SEM performed upon deliberately fractured pieces of these materials did not contain distinguishable remnants of the respective parent crystalline phases at the surface of the composite (**Figure 94**). Their self-supporting nature, coupled with the smooth surface of the MOF CGCs, provides evidence that the liquid ZIF-62 permeated through the pellet. However, a region of coarse material matching the morphology of MIL-118 was observed at a macroscale surface defect in the sample of $(MIL\text{-}118)_{0.5}(a_gZIF\text{-}62)_{0.5}$ (**Figure 95**).

6.3 Gas Uptake Behaviour

Prior work on MOF CGCs has investigated only the gas uptake behaviour of a series of $(MIL\text{-}53)_x(a_gZIF\text{-}62)_{1-x}$ CGCs with carbon dioxide (CO_2) and nitrogen (N_2).[16,17] A range of analyte gases was employed here to investigate the factors underpinning gas uptake in MOF CGCs. Gas sorption isotherms were performed predominantly at 273 K, with further experiments performed for some gases at 77 K and 293 K. For full experimental methodology, see **Section 3.1.9.2**.

6.3.1 Gas Sorption Properties of a_gZIF-62

A sample of pure a_gZIF-62 was prepared (see **Section 3.2.1**) and observed to exhibit porosity towards H_2 (1.05 mmol/g at 77 K, and 0.18 mmol/g at 273K) and CO_2 (0.95 mmol/g at 273 K) (**Figure 96**), both significantly lower than crystalline ZIF-62 which adsorbs ~6.03 mmol/g H_2 at 77 K and ~1.79 mmol/g CO_2 at 273 K.[55] These results are in accordance with previous studies which demonstrate porosity in ZIF-glass materials.[73]

Methane (CH_4) adsorption for a_gZIF-62 was observed in this work at 0.21 mmol/g at 273 K (**Figure 96b**), in agreement with the reported measurement of 0.18 mmol/g and representing a decrease from the reported value of 1.21 mmol/g in the crystalline ZIF-62.[258] Hysteresis is observed in the a_gZIF-62 isotherms as a result of the diffusion limitations through the amorphous structure, increasing in magnitude with the kinetic diameter of the adsorbent, also consistent with prior work.[58,72] This is especially evident in the propene isotherm, with the uptake amount appearing to diminish in the region 70–100 kPa. This is an artefact of slow diffusion kinetics. The recorded adsorption/desorption points are not at equilibrium and are imperfectly estimated in the higher-pressure region.

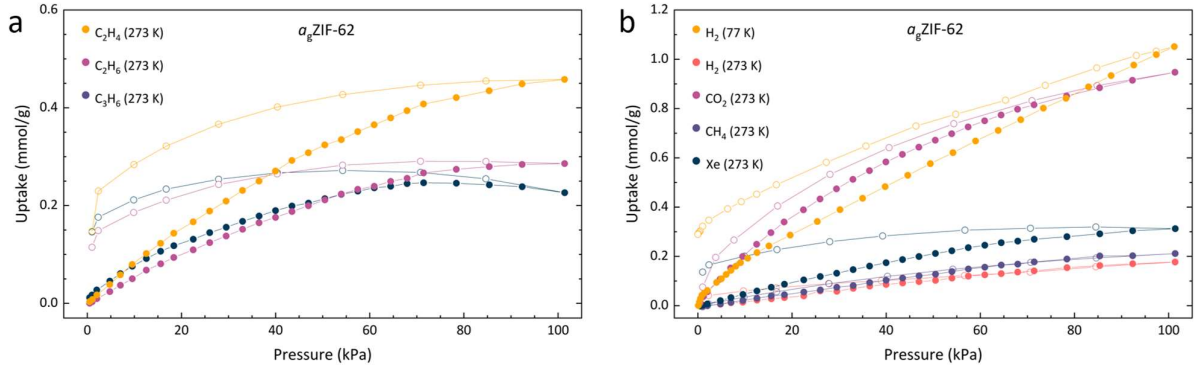

Figure 96: Gas adsorption isotherms of a_gZIF-62. *Solid and open circles of the same colour indicate adsorption and desorption, respectively.*

Remarkably, in addition to the reported selectivity towards propane (C_3H_8) and propene (C_3H_6) by a_gZIF-62 by Frentzel-Beyme *et al.*,[58] some selectivity towards ethene (C_2H_4) over ethane (C_2H_6) is observed here with uptakes of 0.46 and 0.29 mmol/g, respectively (**Figure 96**). Industrially, the separation of small hydrocarbons is currently performed using cryogenic high-pressure distillation processes and accounts for a large portion of global energy expenditure. Membrane-

based separation of these materials is reportedly tenfold less energy-intensive making development in this area both environmentally and economically desirable.[115]

6.3.2 Gas Sorption Behaviour of MOF CGCs

To understand how incorporation within a_gZIF-62 affects the gas sorption properties of the crystalline MOF, the results for the pure crystalline material are compared to that of the MOF CGC. Samples of MIL-118C and $(MIL\text{-}118)_{0.5}(a_gZIF\text{-}62)_{0.5}$ display identical trends in their adsorption isotherms of H_2, CH_4, and CO_2, indicating no significant change in the chemical environment of MIL-118 upon inclusion in the MOF CGC (**Figure 97a,b**). Since MIL-118C displays porosity to H_2 at 77 K, the negligible uptake of H_2 at 273 K is ascribed to temperature effects. However, the generally poor uptake capacity of MIL-118C is consistent with a dense atomic arrangement, in accordance with the published crystallographic information.[191]

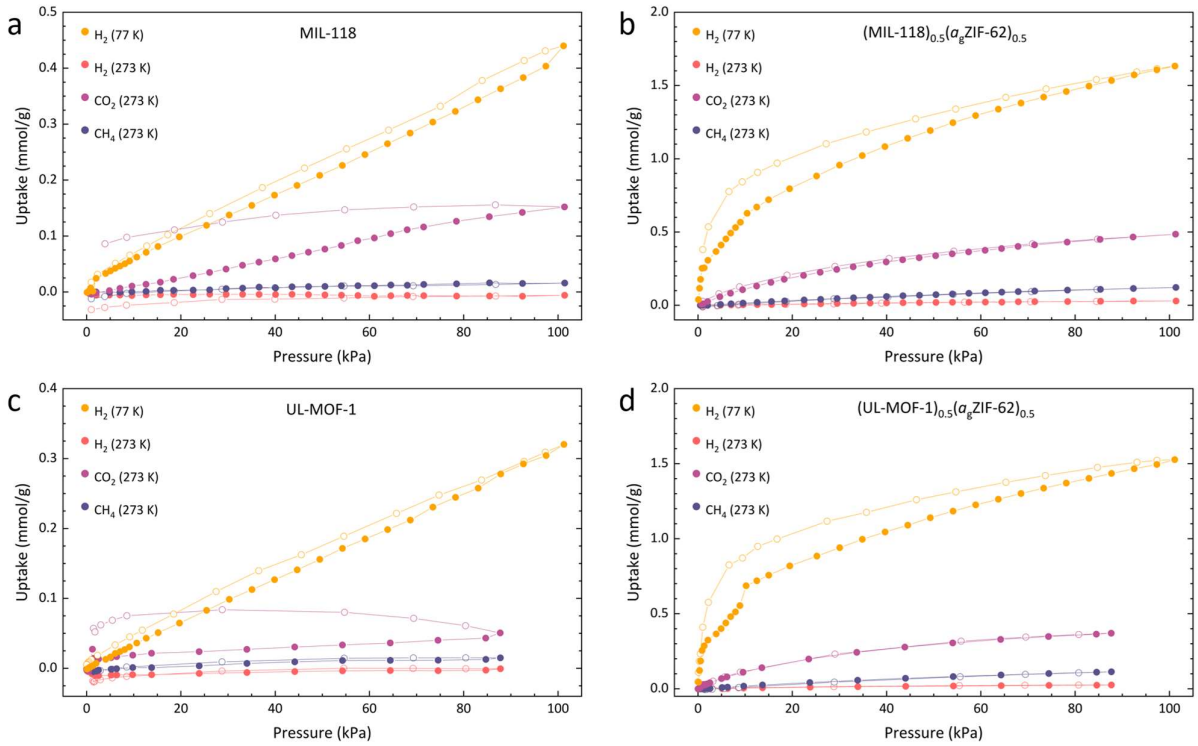

Figure 97: Differences in gas adsorption isotherm trends between the pure crystalline and composite samples. *Gas adsorption isotherms of samples of a. MIL-118C, b. $(MIL\text{-}118)_{0.5}(a_gZIF\text{-}62)_{0.5}$, c. UL-MOF-1and d. $(UL\text{-}MOF\text{-}1)_{0.5}(a_gZIF\text{-}62)_{0.5}$. Solid and open circles of the same colour indicate the adsorption and desorption, respectively.*

The adsorption of gases at 273 K by the 50 wt% composite material, $(MIL\text{-}118)_{0.5}(a_gZIF\text{-}62)_{0.5}$, is broadly comparable to a linear combination of the parent materials (**Table 10**). This, however, is not the case for H_2 adsorption at 77 K. Here, the recorded composite uptake is greater than either of its parent components and more than double the weighted average of the parent materials; this may suggest the presence of macroporous interfacial regions.

Identical experiments were performed on UL-MOF-1 and (UL-MOF-1)$_{0.5}$(a_gZIF-62)$_{0.5}$, and again, the generally poor adsorption to UL-MOF-1 is consistent with a dense structure (**Figure 97c,d**). The same thermal effects observed in the MIL-118 H_2 isotherms at 77K and 273 K were also observed for UL-MOF-1. The gas uptakes displayed by (UL-MOF-1)$_{0.5}$(a_gZIF-62)$_{0.5}$ are broadly consistent with a linear combination of parent UL-MOF-1 and a_gZIF-62 materials (**Table 10**). Interestingly, the 77 K H_2 sorption isotherm for (UL-MOF-1)$_{0.5}$(a_gZIF-62)$_{0.5}$ also exhibits a twofold increase in gas uptake over the weighted average of its parent materials.

***Table 10**: **Measured and predicted MOF CGC gas uptake.** Predicted and experimentally measured gas uptake of MOF crystal–glass composites based on the combination of their parent materials. Experimental temperatures of 273 K unless otherwise stated.*

Sample/gas	Crystalline MOF (mmol/g)	a_gZIF-62 (mmol/g)	Weighted Average (mmol/g)	Measured MOF CGC (mmol/g)
MIL-118				
Methane	0.016	0.212	0.114	0.122
Carbon Dioxide	0.152	0.947	0.550	0.485
Hydrogen (77 K)	0.440	1.051	0.746	1.632
UL-MOF-1				
Methane	0.015	0.212	0.113	0.113
Carbon Dioxide	0.051	0.947	0.499	0.370
Hydrogen (77 K)	0.320	1.051	0.686	1.527

The prediction of gas uptake through the weighted average of its components calculated here assume that the quantity of gas adsorbed in the MOF CGCs is due to the combined individual contributions from the two composited materials, where their adsorption is identical to the isolated components. It is important to note, however, that the hysteresis observed in the CO_2 isotherms for both a_gZIF-62 and the isolated crystalline MOFs is no longer present in the respective MOF CGCs. This suggests that the MOF CGC reaches equilibrium more rapidly than its isolated components, indicating that there may be new pathways for the gas to diffuse in the MOF CGC.

6.3.3 Further Investigation of MIL-53 MOF CGC Gas Sorption

A CO_2 adsorption isotherm was also recorded at 273 K for the pure crystalline sample of MIL-53-np and is consistent with previously reported data (2.25 mmol/g (recorded), and 2.13 mmol/g (reported) (273 K), **Figure 98a,b**).[122] As expected, MIL-53-np displays a significantly higher uptake of C_3H_6 than C_2H_4, C_2H_6, or xenon (Xe), reaching 3.47 mmol/g (273 K). The observation of two-step isotherms when using larger hydrocarbons is consistent with pore-opening behaviour where MIL-53-np expands to the MIL-53-lp phase, as comprehensively illustrated in the literature.[121]

Consistent with prior work, the MOF CGC exhibits appreciable porosity. However, due to fixation of the MIL-53-lp phase within the (MIL-53)$_{0.25}$(a_gZIF-62)$_{0.75}$ composite, the pore opening behaviour of pure phase MIL-53 is no longer observed, and all recorded isotherms of (MIL-53)$_{0.25}$(a_gZIF-62)$_{0.75}$ display Langmuir-type behaviour, often with hysteresis in the desorption branch. The CO_2 sorption of a sample of (MIL-53)$_{0.25}$(a_gZIF-62)$_{0.75}$ displayed similar CO_2 uptake behaviour to that recorded previously (1.33 mmol/g (recorded), and 1.14 mmol/g (reported)).[122] The sample of

(MIL-53)$_{0.25}$(a_gZIF-62)$_{0.75}$ also displayed poor adsorption of both N_2 and CH_4 (<0.13 and <0.36 mmol/g at 273 K, respectively), since neither component of the CGC strongly adsorbs these gases (**Figure 98c**).

Since this sample, unlike (MIL-118)$_{0.5}$(a_gZIF-62)$_{0.5}$ and (UL-MOF-1)$_{0.5}$(a_gZIF-62)$_{0.5}$, demonstrates a permeable crystalline component, further gas sorption experiments using larger gases were performed (**Figure 98d**). A considerable difference between the uptake of C_2H_4 and C_2H_6 is observed in a sample of (MIL-53)$_{0.25}$(a_gZIF-62)$_{0.75}$, which is typical of the a_gZIF-62 component but is not observed in MIL-53. This result evidences the contribution of the adsorption properties of a_gZIF-62 to the overall composite characteristics.

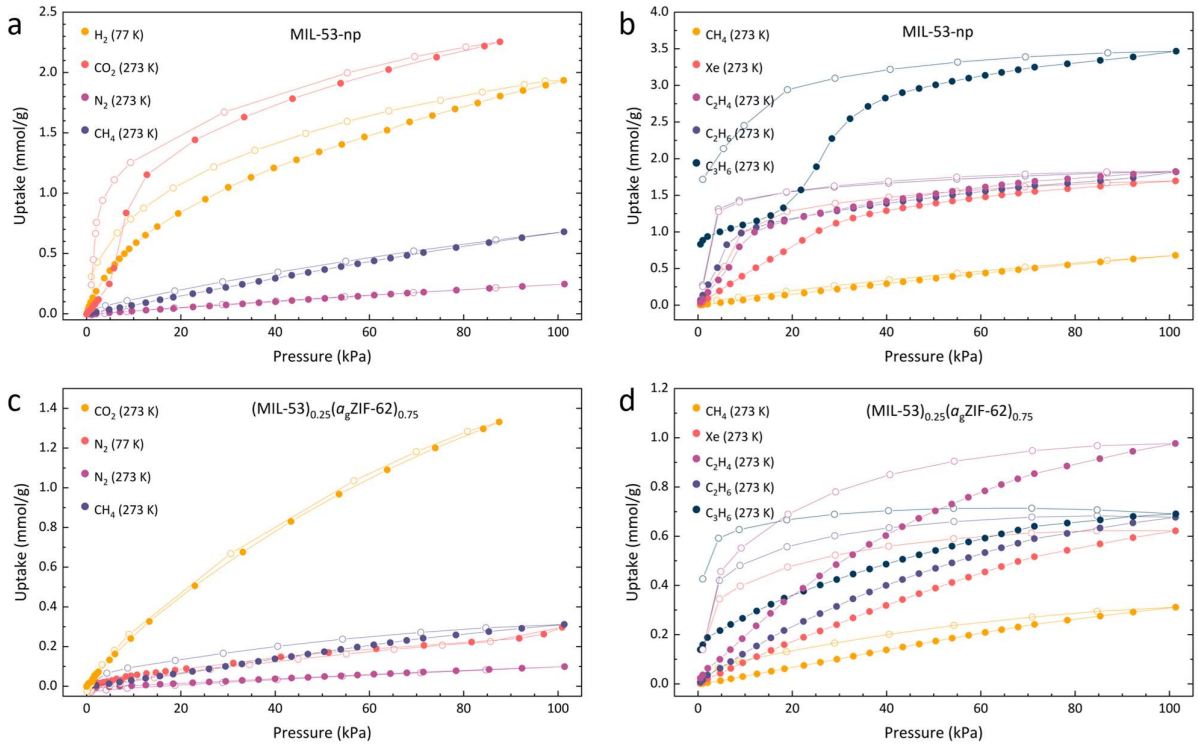

***Figure 98**: **Differences in gas adsorption isotherm trends between MIL-53-np and (MIL-53)$_{0.25}$(a_gZIF-62)$_{0.75}$.** Gas adsorption isotherms of a–b. MIL-53-np, and c–d. (MIL-53)$_{0.25}$(a_gZIF-62)$_{0.75}$. Solid and open circles of the same colour indicate the adsorption and desorption, respectively.*

Of the gases employed, the most striking result was that of C_3H_6, where the composite adsorbs far less than the combination of the parent materials. A weighted average C_3H_6 adsorption of MIL-53 (3.47 mmol/g) and a_gZIF-62 (0.23 mmol/g) for a 25 wt% MIL-53 mixture would be 1.04 mmol/g, where an uptake of only 0.69 mmol/g is observed for the composite. However, the adsorption isotherm for C_3H_6 to (MIL-53)$_{0.25}$(a_gZIF-62)$_{0.75}$ shows an increase in uptake on desorption, strongly indicating that the system had not reached equilibrium. This is likely due to poor diffusion of C_3H_6 through the a_gZIF-62 matrix as a result of the comparatively large kinetic diameter of the gas. Though the MIL-53 component in the composite would be the dominant contributor to the gas uptake, adsorption to this component is greatly hindered whilst encapsulated within a matrix that is poorly permeable to the analyte gas.

6.4 Conclusions

Thermal analysis of a selection of crystalline MOFs revealed that two MOFs: UL-MOF-1, and MIL-118, are suitable for inclusion with a MOF glass (a_gZIF-62) matrix. Despite reported TGA evidence to the contrary, several other crystalline MOFs were observed to undergo partial or complete collapse at the processing temperatures required for composite formation. This highlights the necessity of detailed thermal characterisation and the avoidance of an over-reliance on constant-rate TGA experiments.[19]

It is clear from this research that to expand the scope of MOF CGCs to include frameworks with more diverse properties, new synthetic pathways must be explored. Two of such avenues may lie in (i) the utilisation of coordination polymers or MOFs with lower melting temperatures or (ii) exchanging the crystalline glass-forming MOF for a premade glass MOF. In doing so, the temperatures required for the fabrication of the MOF CGC may be reduced as the glass transition temperature (T_g) occurs at a lower temperature than the melting temperature (T_m) used here.[161–163,291]

The adsorption behaviour of the resultant two new MOF CGCs is dominated by contributions from the a_gZIF-62 matrix, which prevents the diffusion of molecules with a kinetic diameter larger than that of C_3H_6. The development of more permeable a_gMOFs may aid in the expansion of MOF CGC applicability. Alternatively, work on overcoming percolation thresholds in MOF CGCs would mean guest diffusion is primarily controlled by the crystalline MOF component. This would allow further control of interactions leading to multifunctional materials with the ability to act as both molecular sieves and separators.

Chapter 7 Thermomechanical Properties of MOF CGCs

Though progress has been made on expanding the scope of possible MOF CGC materials through the use of novel fabrication methods, there remains little information regarding the effect of encapsulation on the physical properties of the crystalline MOF.[39,251] Unusual physical behaviour has been observed in the $(MIL\text{-}53)_x(a_gZIF\text{-}62)_{1-x}$ system, where the metastable open-pore MIL-53-lp phase is retained at room temperature; this phenomenon has been exploited to create MOF CGCs with significantly higher CO_2 sorption capabilities.[122] In contrast, whilst MIL-118 is also a "breathing" framework like MIL-53, the open-pore MIL-118B phase is not stabilised in the composite, and the low-temperature MIL-118C phase is observed in the MOF CGC. The behavioural divergence of the crystalline components in these two systems demonstrates that the nature of the fabricated MOF CGCs is more complex than that of a non-interacting system.

In this chapter, the thermal expansion behaviour of three MOF CGCs, incorporating two flexible (MIL-53(Al) and MIL-118) and one rigid (UL-MOF-1) MOF within a_gZIF-62 matrices, is investigated. Specifically, variable-temperature powder X-ray diffraction data and thermomechanical analysis show the suppression of thermal expansivity in each of these three crystalline MOFs when suspended within a ZIF-62 glass matrix. In particular, for the two flexible frameworks, MIL-53(Al) and MIL-118, the average volumetric thermal expansion (α_v) were found to be near-zero in the crystal–glass composite. This work is published in the following manuscript:

[1] Ashling C. W., Lampronti G. I., Southern T. J. F., Evans R. C., and Bennett T. D., **Thermal Expansion of Metal–Organic Framework Crystal–Glass Composites**, *ChemRxiv*, 2021, DOI: 10.26434/chemrxiv.14597670.v1

Experiments performed in this manuscript were carried out by myself with the aid of G. I. Lampronti (for recording VT-PXRD data, and Rietveld refinements) and T. J. F. Southern (for aid with statistical analysis). Analysis of the data and the preparation of the manuscript were carried out by myself and T. D. Bennett with input from all authors.

7.1 Variable Temperature Powder X-ray Diffraction (VT-PXRD)

Variable temperature PXRD (VT-PXRD) was carried out to study the unit cell expansion of the three crystalline samples and their respective MOF CGCs. Samples of MIL-53-np, **(**MIL-53)$_{0.25}$(a_gZIF-62)$_{0.75}$, MIL-118, (MIL-118)$_{0.5}$(a_gZIF-62)$_{0.5}$, UL-MOF-1, and (UL-MOF-1)$_{0.5}$(a_gZIF-62)$_{0.5}$ were doped with a silicon standard (approximately 10% by volume), flattened onto a sample holder, and placed under vacuum (8.5 ×10^{-3} mbar). The sample displacement was then corrected using a silicon internal standard (Si, see **Section 3.1.2.1.1**). Each experiment began by heating the sample to 30 °C and equilibrating for 5 minutes before recording the initial PXRD pattern. Data were subsequently collected at 20 °C intervals to 310 °C, allowing for thermal equilibration before each collection (**Figure 99**). These images are contour plots of the PXRD patterns, which display a birds-eye view of the full VT-PXRD series, coloured by the peak intensity.

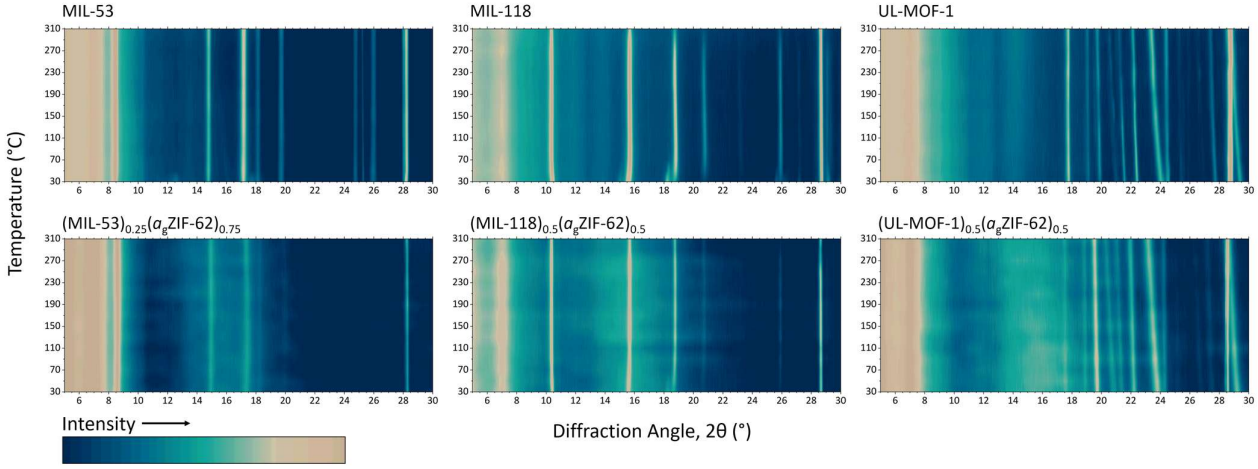

***Figure 99: Contour maps of variable temperature powder X-ray diffraction data**. a. MIL-53, b. (MIL-53)$_{0.25}$(a_gZIF-62)$_{0.75}$ c. MIL-118, d. (MIL-118)$_{0.5}$(a_gZIF-62)$_{0.5}$, e. UL-MOF-1, f. (UL-MOF-1)$_{0.5}$(a_gZIF-62)$_{0.5}$. Intensity scale bar below, of which units are arbitrary.*

Unit cell parameters of the crystalline materials were then extracted using Rietveld refinement of the VT-PXRD data (**Figures 100–105**, see **Section 3.1.3.1**). In these refinements, the added silicon is used to determine sample displacement accurately before refining the crystalline MOF component in the PXRD patterns. Diffuse scattering of the glass is accounted for by including a broad Gaussian peak with the background in the refinements. In the case of MIL-53 and MIL-118, refinements were begun once the conversion to the high-temperature phase had completed.

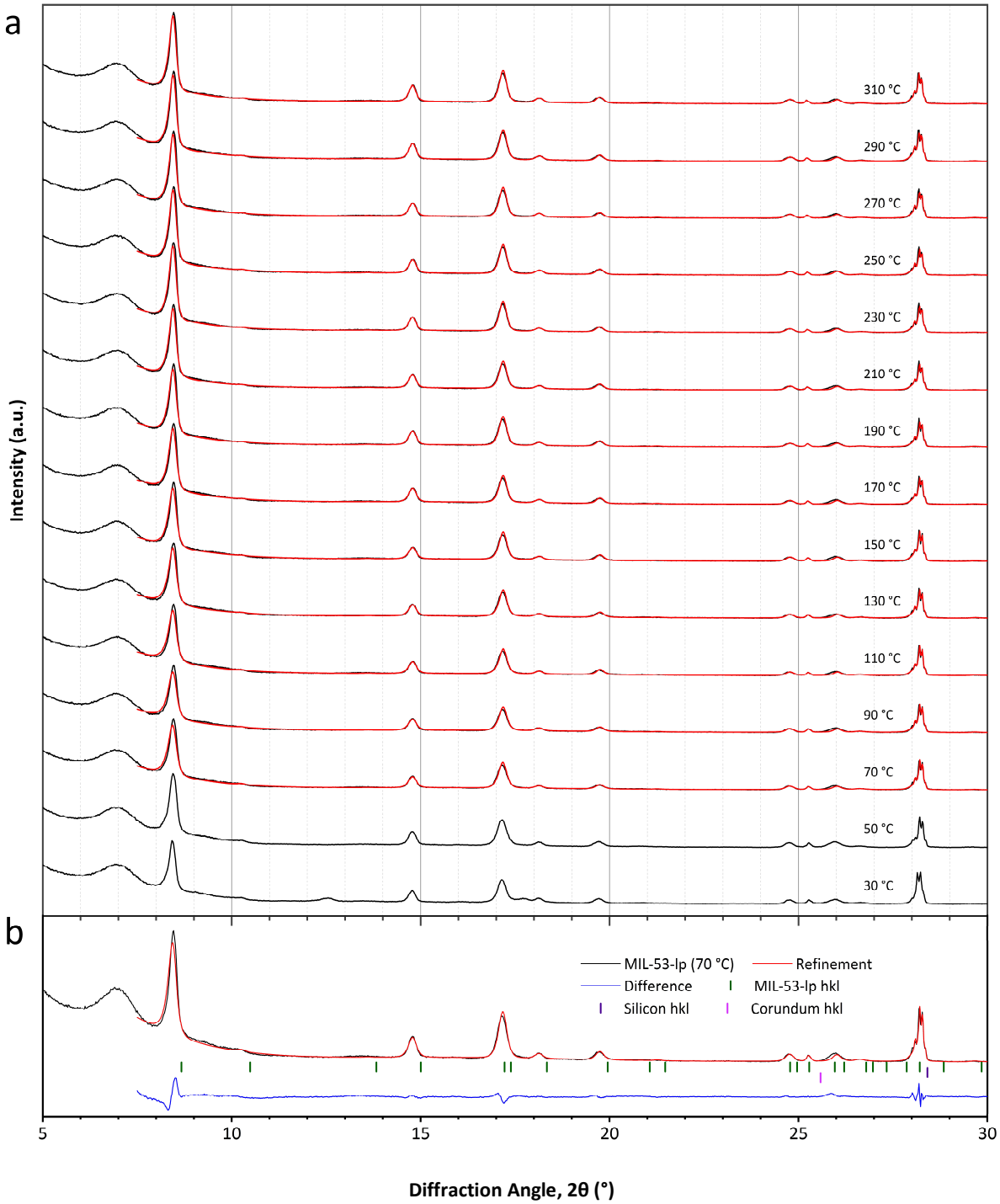

Figure 100: Expansion of MIL-53-lp mapped by refinement of VT-PXRD data. *a. Variable temperature powder X-ray diffraction patterns of MIL-53-lp. Black – experimental data, red - refinement, and b. Initial refinement of MIL-53-lp at 70 °C with peak marks for all phases.*

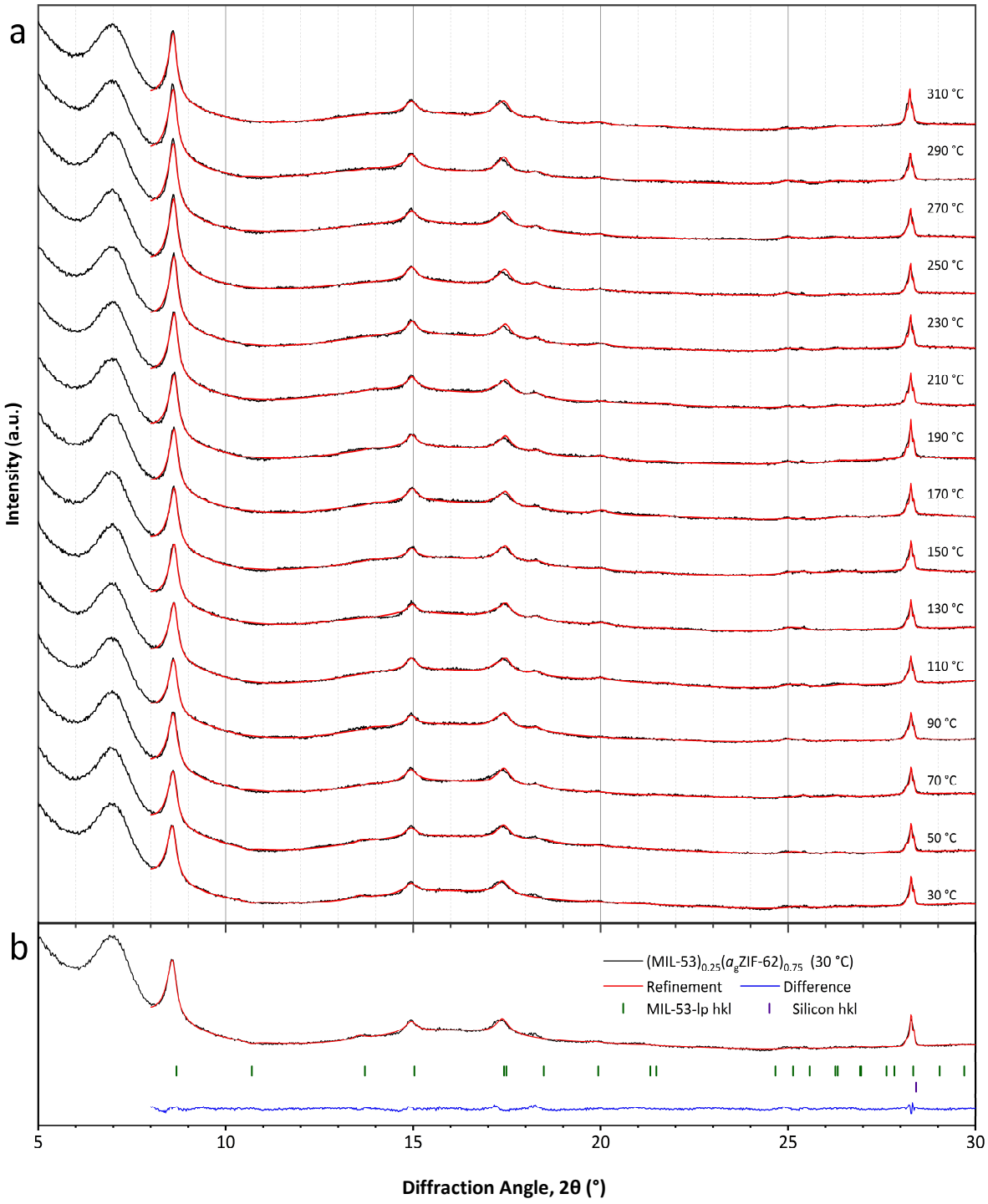

***Figure 101*: Expansion of $(MIL\text{-}53)_{0.25}(a_gZIF\text{-}62)_{0.75}$ mapped by refinement of VT-PXRD data.** *a. Variable temperature powder X-ray diffraction patterns of $(MIL\text{-}53)_{0.25}(a_gZIF\text{-}62)_{0.75}$. Black – experimental data, red – refinement, and b. Initial refinement of $(MIL\text{-}53)_{0.25}(a_gZIF\text{-}62)_{0.75}$ with peak marks for all phases.*

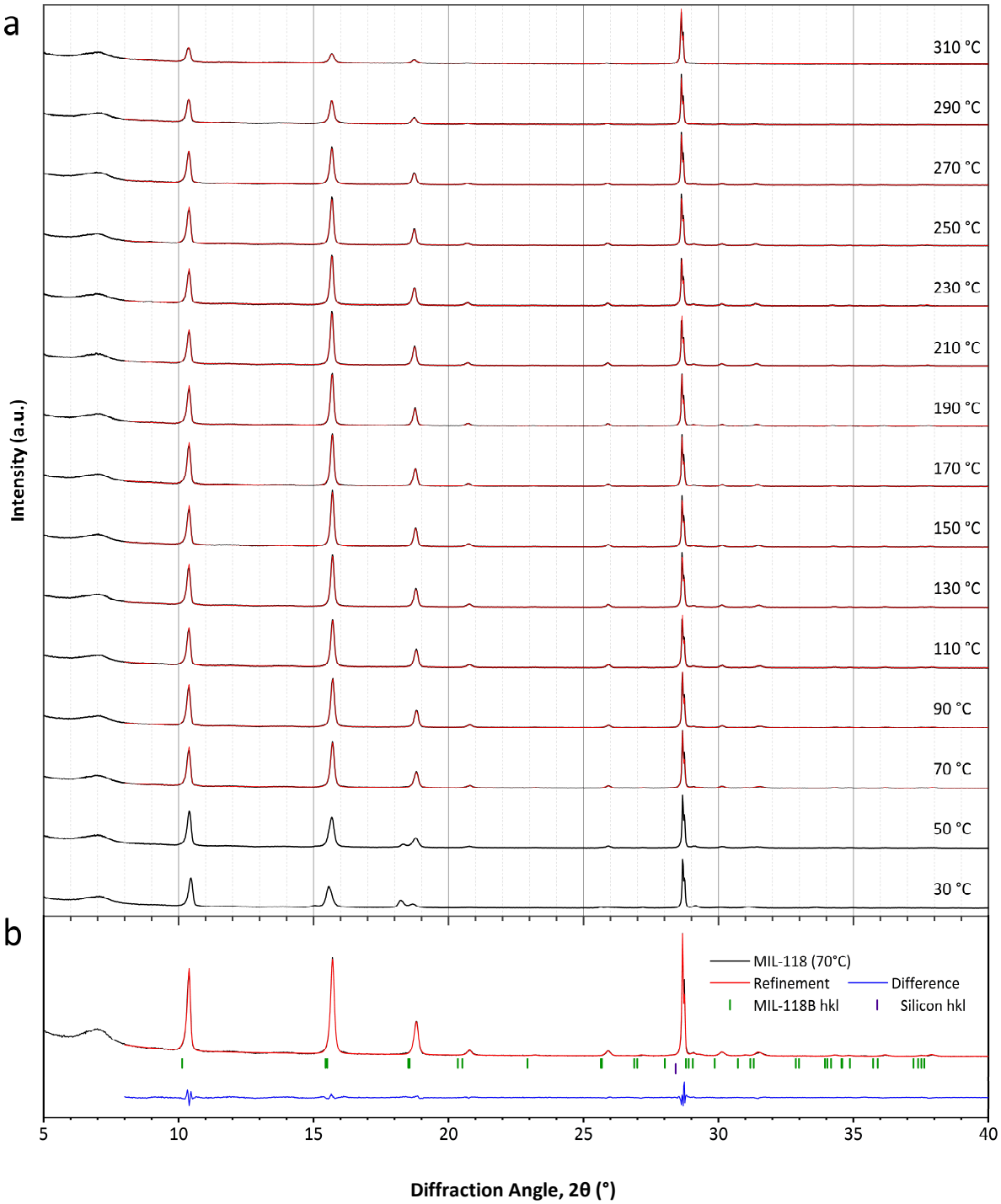

***Figure 102*: Expansion of MIL-118B mapped by refinement of VT-PXRD data.** *a. Variable temperature powder X-ray diffraction patterns of MIL-118. Black – experimental data, red - refinement., and b. Initial refinement of MIL-118B with peak marks for all phases.*

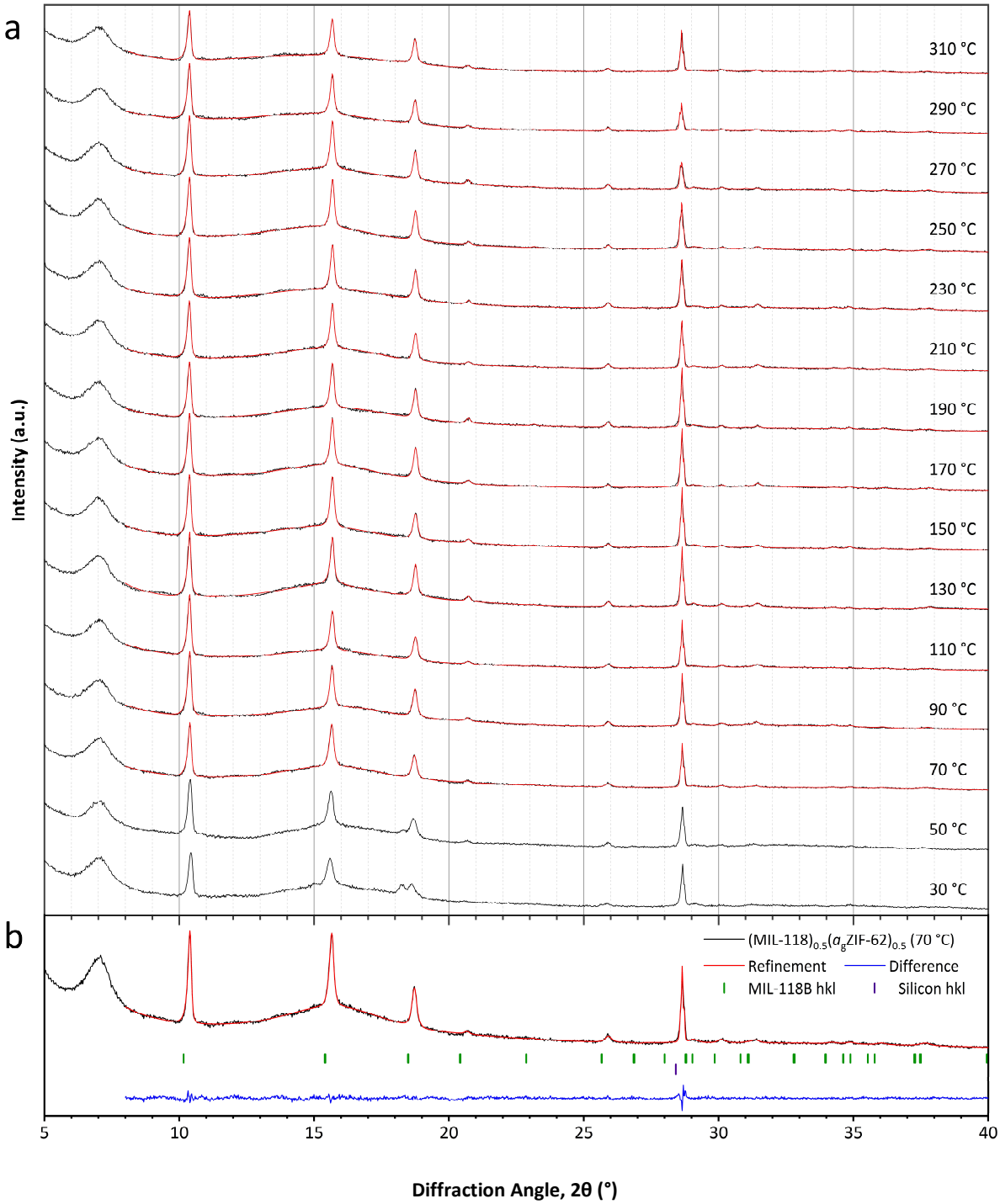

***Figure 103*: Expansion of $(MIL\text{-}118)_{0.5}(a_gZIF\text{-}62)_{0.5}$ mapped by refinement of VT-PXRD data.** *a. Variable temperature powder X-ray diffraction patterns of $(MIL\text{-}118)_{0.5}(a_gZIF\text{-}62)_{0.5}$. Black – experimental data, red - refinement, and b. Initial refinement of $(MIL\text{-}118)_{0.5}(a_gZIF\text{-}62)_{0.5}$ with peak marks for all phases.*

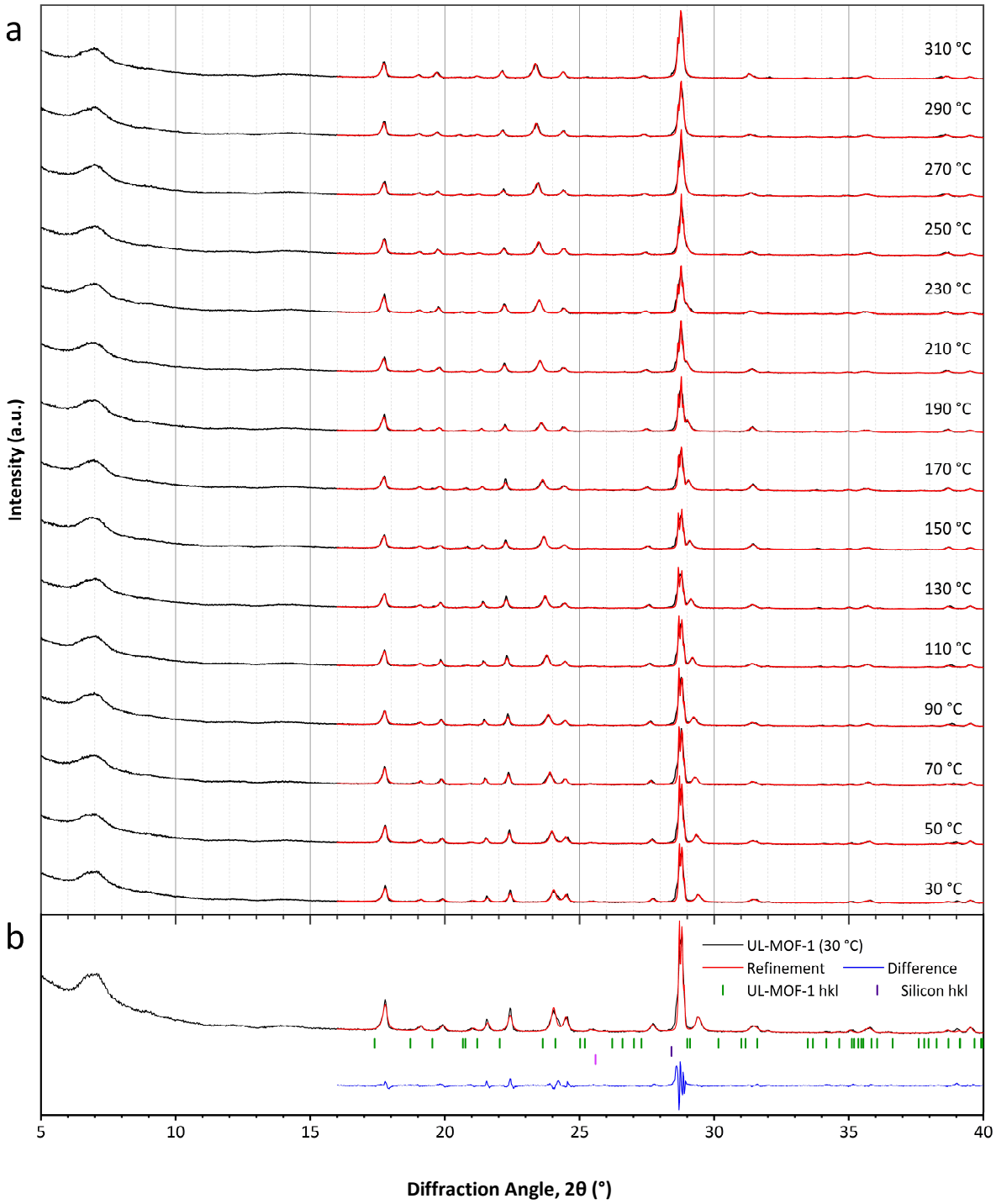

***Figure 104**: **Expansion of UL-MOF-1 mapped by refinement of VT-PXRD data.** a. Variable temperature powder X-ray diffraction patterns of UL-MOF-1. Black – experimental data, red - refinement, and b. Initial refinement of UL-MOF-1 with peak marks for all phases.*

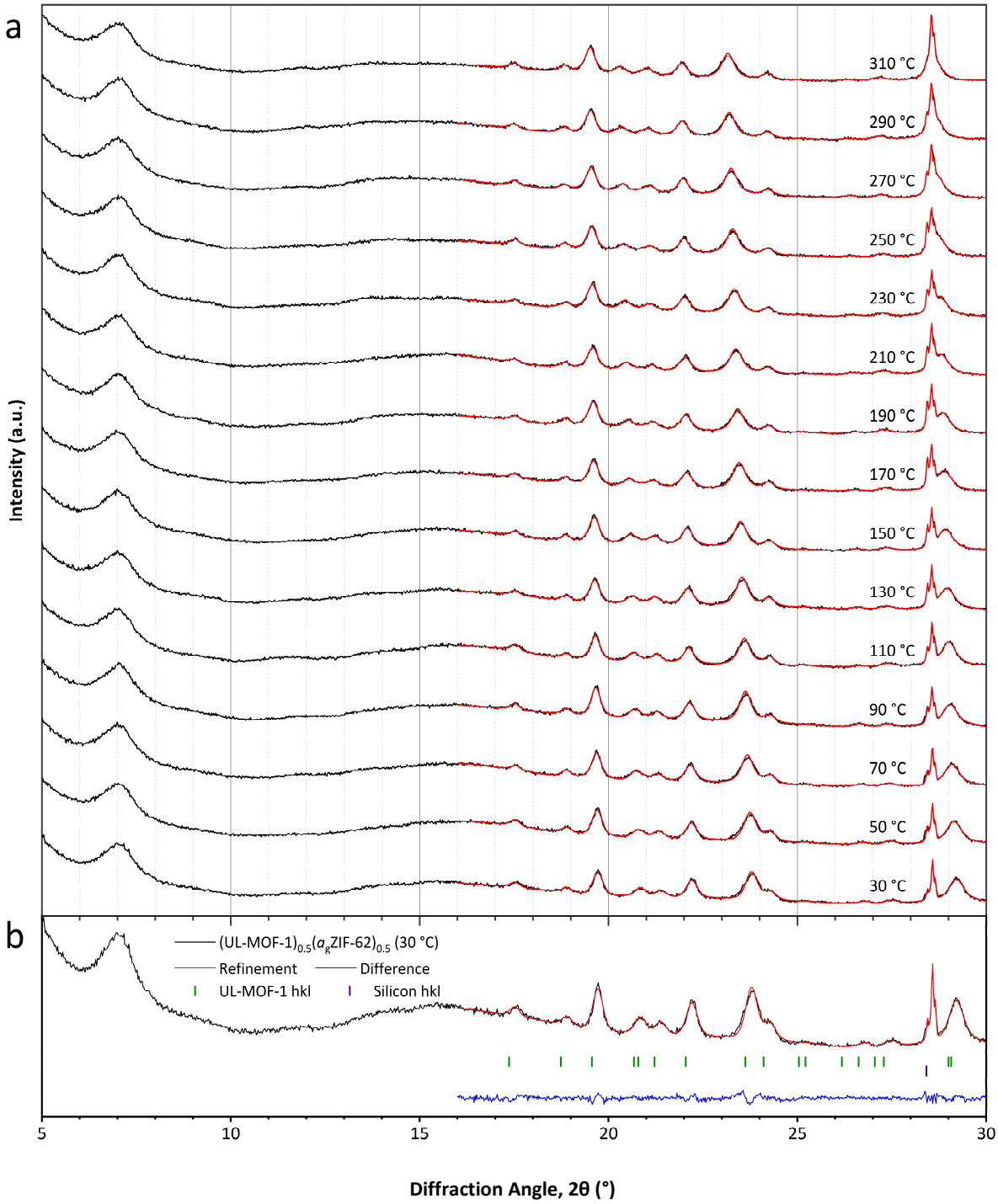

***Figure 105**: **Expansion of (UL-MOF-1)$_{0.5}$(a_gZIF-62)$_{0.5}$ mapped by refinement of VT-PXRD data.** a. Variable temperature powder X-ray diffraction patterns of (UL-MOF-1)$_{0.5}$(a_gZIF-62)$_{0.5}$. Black – experimental data, red - refinement, and b. Initial refinement of (UL-MOF-1)$_{0.5}$(a_gZIF-62)$_{0.5}$ with peak marks for all phases.*

The full results of these refinements are tabulated in **Appendix Tables A1–6** and plotted in **Figure 106**, which describe the temperature dependence of the unit cell volumes for each of the refined unit cells within and without the MOF glass. The expansivity of each system may be compared through the calculation of the coefficient of thermal expansion in each system.

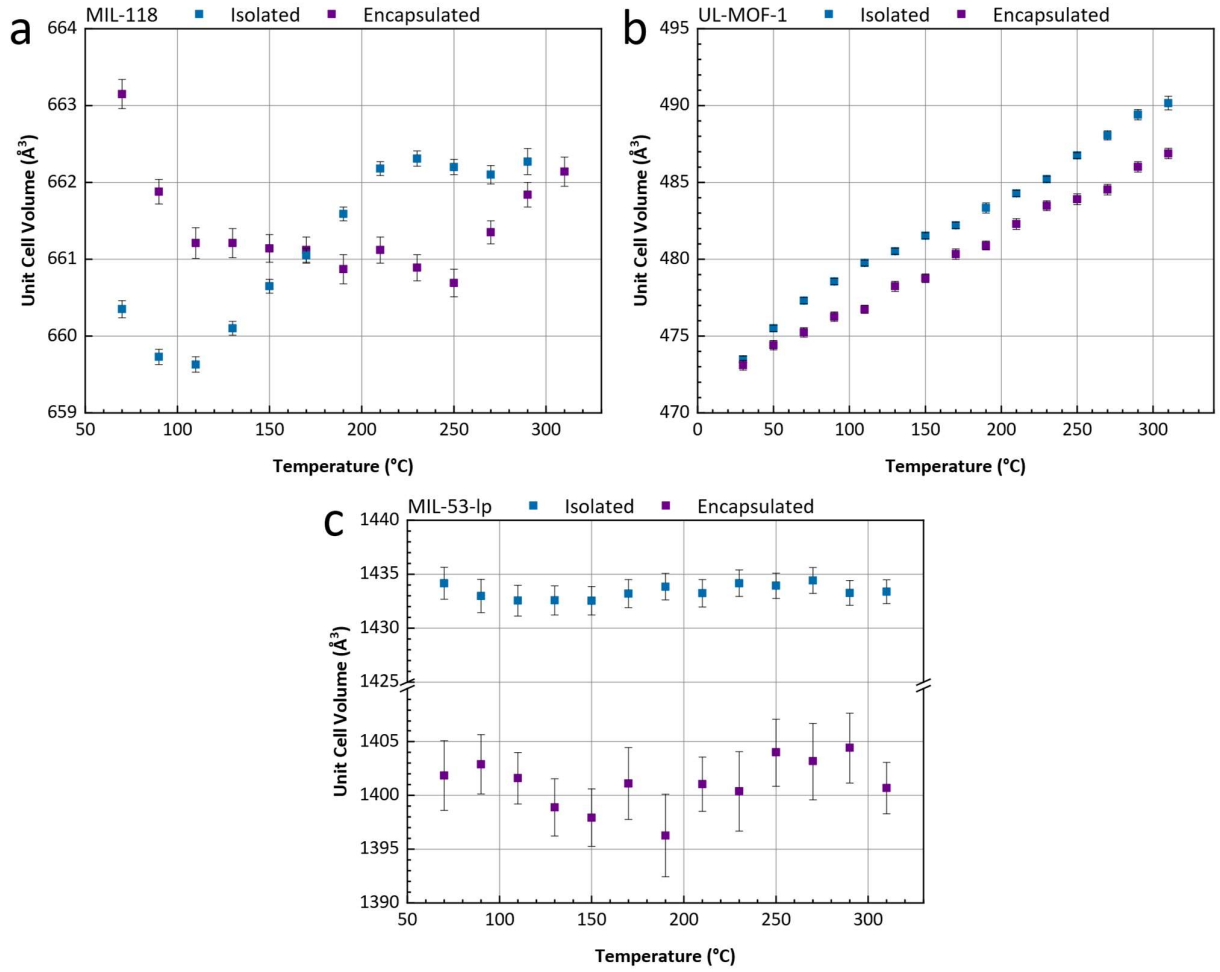

***Figure 106*: Comparison of the crystalline MOF expansion within and without the composite.** *Refined unit cell volumes of the isolated MOFs and crystal–glass composites of a. MIL-118, b. UL-MOF-1, and c. MIL-53-lp. Estimated standard deviations are shown as error bars.*

7.1.1 Calculation of The Coefficient of Thermal Expansion

The assumptions made for the calculation of CTE made in **Section 3.1.2** are valid for all crystalline MOFs measured here. The volumetric and linear CTEs for the isolated MOFs and crystalline MOFs within the MOF CGCs were calculated over the temperature ranges stated, where linear relationships are observed (**Table 11**). Three distinct regions of unit cell volume change for the crystalline MIL-118 sample are evident in **Figure 106a**. The initial decrease in unit cell volume to 110 °C may be attributed to the contraction of the structure upon conversion from MIL-118C to MIL-118B as water is

expelled from the framework. Evidence of this conversion is apparent from the change in PXRD pattern as shown in **Figure 99**, and **Figure 102**, most notably the peak at *ca.* 18° 2θ. On completion of the transformation to MIL-118B, the structure expands uniformly between 110–230 °C where the first region of α_v is calculated ($35.6 \times 10^{-6}\,K^{-1}$, taken at 110 °C).

Table 11: Volumetric and linear coefficients of unit cell thermal expansion. *Errors given as the average standard deviation reported to 5 SF in crystallographic notation.*

Sample	Temperature Range (°C)	Volumetric	Linear		
		α_v* ($10^{-6}K^{-1}$)	α_a* ($10^{-6}K^{-1}$)	α_b* ($10^{-6}K^{-1}$)	α_c* ($10^{-6}K^{-1}$)
MIL-118B	110–230	35.572(5)	51.795(6)	–3.1281(2)	–12.982(1)
	230–290	–1.6609(3)	–8.8327(8)	–3.8524(2)	10.795(1)
$(MIL\text{-}118)_{0.5}(a_gZIF\text{-}62)_{0.5}$	110–250	–4.9963(15)	–2.9865(7)	–4.0969(7)	2.0710(2)
	250–310	36.628(10)	30.507(6)	4.8333(7)	1.1480(1)
UL-MOF-1	30–310	117.84(5)	0.84381(20)	18.300(5)	90.226(22)
$(UL\text{-}MOF\text{-}1)_{0.5}(a_gZIF\text{-}62)_{0.5}$	30–310	103.22(7)	–3.3784(19)	16.398(3)	80.862(24)
MIL-53-lp	70–310	2.2259(23)	1.9377(6)	–6.3306(54)	6.6444(34)
$(MIL\text{-}53)_{0.25}(a_gZIF\text{-}62)_{0.75}$	70–310	5.3364(123)	–4.1684(26)	6.9688(133)	2.5676(29)

*Single value using the lowest temperature of the specified temperature range.

The expansion over this range is dominated by extension along the *a* axis ($\alpha_a = 51.8 \times 10^{-6}\,K^{-1}$) which details the distance between Al–O columns connected by ortho-substituted carboxylates around the benzene-1,2,4,5-tetracarboxylate linkers. Above 230 °C, negligible change in the unit cell volume is observed ($\alpha_v = -1.66 \times 10^{-6}\,K^{-1}$, taken at 230 °C), possibly demonstrating a maximum unit cell volume—and by extension, pore size—under the experimental conditions. Decomposition of the sample is evident from the peak intensity reduction toward the end of the experiment (**Figure 102**); data at 310 °C is therefore omitted from the calculations.

The unit cell expansion of MIL-118 within $(MIL\text{-}118)_{0.5}(a_gZIF\text{-}62)_{0.5}$ is also observed to undergo three distinct regions of change. The first region is analogous to the isolated material, where unit cell contraction occurs during the conversion to the MIL-118B phase, ending at 110 °C. After 110 °C, the thermal behaviour of the encapsulated MIL-118B diverges from the isolated sample; rather than steadily expanding, a slight decrease in the unit cell volume is observed from 110–250 °C ($\alpha_v = -5.00 \times 10^{-6}K^{-1}$, taken at 110 °C). At 250 °C, MIL-118B begins expanding at a similar rate ($\alpha_v = 36.6 \times 10^{-6}K^{-1}$, taken at 250 °C) to the expanding region of the isolated crystalline material. The temperature at which MIL-118B begins to expand within a_gZIF-62 is broadly comparable to the softening point of a_gZIF-62, as demonstrated in the thermomechanical analysis in **Figure 108**. This thermal behaviour may be caused by the suppression of MIL-118 expansion by the rigid glass matrix, which permits the material to expand as it softens.

The "rigid" UL-MOF-1 framework was observed to expand linearly across the 30–310 °C temperature range in this experiment *via* a single mode of expansion (**Figure 106b**). A single value of the volumetric CTE (α_v) of UL-MOF-1 from 30–310 °C was therefore calculated to be $118 \times 10^{-6}\,K^{-1}$ which is dominated by expansion along the *b* and *c* axes ($18.3 \times 10^{-6}\,K^{-1}$ and $90.2 \times 10^{-6}\,K^{-1}$ respectively). Connectivity along the *bc* plane aligns with the planes of the Li-O sheets that make up UL-MOF-1. Li–Li distances in this plane must, therefore, increase as the area expands. The expansivity along the *a* axis is

almost negligible (1×10^{-6} K^{-1}), which describes the distance between nearest lithium atoms on adjacent Li–O sheets and is limited by the length of the connecting 2,6-ndc linkers. These results are in accordance with a study carried out on a sodium analogue of UL-MOF-1, which details a decrease in the unit cell β angle and an increase in the volumetric and *b* parameters.[292]

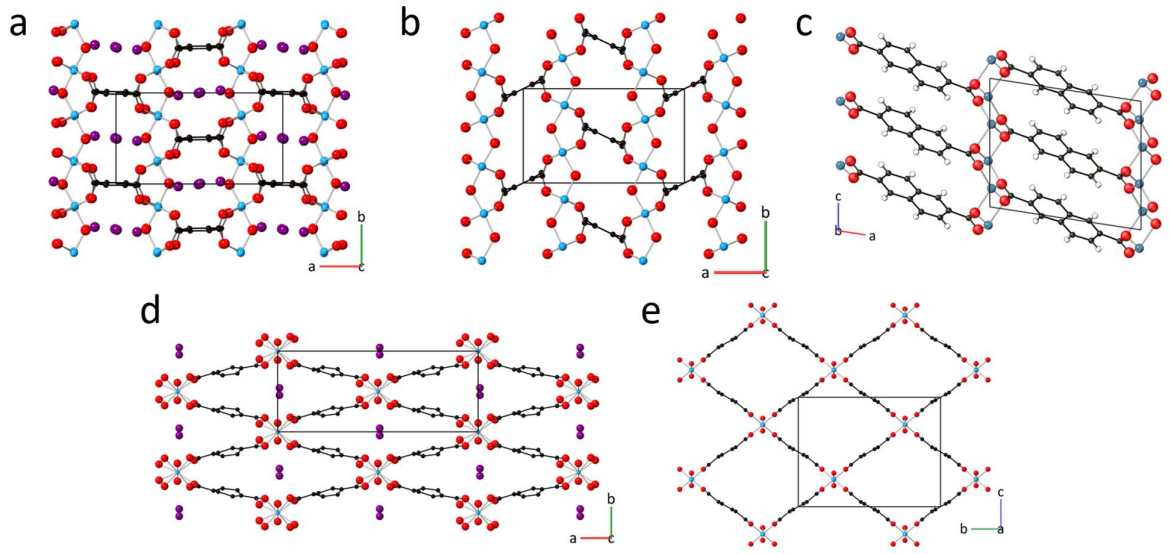

Figure 107: Crystal structures and their reversible transitions of the crystalline components of MOF CGCs synthesised. *a. MIL-118C, b. MIL-118B, c. UL-MOF-1, d. MIL-53-np, and e. MIL-53-lp. (Metal, blue; O, red; C, black; H, white in UL-MOF-1 and omitted for clarity in others). Unit cells represented by black boxes.*

The expansion mode of UL-MOF-1 within $(UL\text{-}MOF\text{-}1)_{0.5}(a_gZIF\text{-}62)_{0.5}$ is identical to the isolated crystalline material; however, α_v over the same temperature range was reduced by 12.4%, to 103×10^{-6} K^{-1} in the glass. It is apparent that expansion suppression by the a_gZIF-62 matrices is present even for MOF CGC systems containing "rigid" crystalline MOFs.

A sample of MIL-53-np was prepared through the calcination of MIL-53-as (See **Section 3.2.1**). Upon reducing atmospheric pressure in the experimental setup, MIL-53-np underwent an expansion to the MIL-53-lp phase, according to previous studies.[293] Incomplete conversion at this stage was evidenced by the presence of small Bragg peaks corresponding to MIL-53-np present in the PXRD pattern recorded at 30 °C but were no longer present by 70 °C. Refinement of the patterns from 70–310 °C indicated no change within the error. The near-zero net thermal expansion of MIL-53-lp over this range is broadly consistent with the <0.3% volumetric expansion of MIL-53-lp observed in a previous study, where no pressure reduction was applied.[294] This expansivity behaviour is also observed for a sample of $(MIL\text{-}53)_{0.25}(a_gZIF\text{-}62)_{0.75,}$ which was present in the MIL-53-lp phase as a result of the fabrication method (**Figure 106c**).

7.1.2 Rationale for Phase Behaviour Divergence

Previous gas sorption isotherms demonstrated that the retention of MIL-53-lp in the MOF CGC is not a result of the a_gZIF-62 hydrophobicity, suppressing the water-driven narrowing of the pores.[251] Whilst linker penetration into the pores

of the crystalline MOF remains a possibility for the retention of MIL-53-lp in the composite, this work supports an alternative explanation for the disparity in behaviour between MIL-53 and MIL-118.

The melting and glass transition temperatures of ZIF-62 are far greater than those required to convert MIL-53 or MIL-118 to their respective high-temperature phases. Therefore, in the process of forming a MOF CGC, ZIF-62 melts and subsequently flows. At this temperature, MIL-53 and MIL-118 are present in their high-temperature phases. The relatively high vitrification temperature of ZIF-62 (T_g > 293 °C) means that when the glass is formed, the high-temperature phases of MIL-53 and MIL-118 are still present. This, therefore, excludes the possibility that the difference in behaviour is simply due to the temperature of transitions.

Therefore, an explanation based upon the volume of expansion may explain why MIL-118 reverts to the low-temperature phase where MIL-53 does not. The transition from the high- to low- temperature phases of both MIL-53 and MIL-118 is accompanied by considerable volumetric change. However, it has been shown here that significant expansion of these crystalline materials is hindered within the glass phase. The expansion of each axis for both MIL-53 and MIL-118 is calculated in **Table 12**. In the case of MIL-53, the *x* and *y* axes are equal to the distance between Al atoms corresponding to the width and height of the diamond-shaped pores. The *z* axis is equal to the Al–Al distance across the Al–O–Al bonds along the Al–O columns. For MIL-118, the *x* and *y* axes are the distances between Al–O columns, and the *z* axis is the distance between Al–Al atoms within the Al–O columns.

***Table 12**: Volumetric changes of MIL-53 and MIL-118 from their high- to low-temperature phases.*

	MIL-53			**MIL-118**		
Axis	MIL-53-lp (Å)	MIL-53-np (Å)	Change (%)	MIL-118B (Å)	MIL-118C (Å)	Change (%)
x	16.675	19.513	17.02	8.722	8.614	–1.23
y	12.813	7.612	–40.59	5.666	6.067	7.08
z	3.304	3.288	0.48	3.312	3.208	–3.14

A possibility for why MIL-53 remains in the MIL-53-lp phase is due to the substantial uniaxial expansion (17.02 %) upon cooling to the MIL-53-np phase. Whilst a perpendicular 40.59 % contraction is also observed in the narrowing of the MIL-53 pores, the glass which has solidified around the MIL-53-lp phase may not be able to accommodate the expansion. However, in the case of MIL-118, the largest uniaxial expansion towards the MIL-118C phase is only 7.08 %. This difference in uniaxial expansion upon transition to the low-temperature phase may be the cause of the resultant phase behaviour divergence in the MOF CGCs. Thus, the presence of MIL-53-lp at room temperature in the MOF CGC may be a result of physical obstruction by the denser MOF glass matrix.

7.2 Bulk Thermomechanical Measurements and CTE Comparison

Complementary to the study of the crystalline MOFs within the composite, the thermal expansion of the bulk composites was recorded using thermomechanical analysis (TMA). This method involves the application of a very small force (0.05 N in this case) to the surface of a material and measures the change in material length upon heating. Such an analysis provides a one-dimensional change in length, *L*, over the temperature, *T*; quantifying the change, $\Delta L/\Delta T$ provides a length

variant of the CTE, α_L. Samples of a_gZIF-62, (MIL-53)$_{0.25}$(a_gZIF-62)$_{0.75}$, (MIL-118)$_{0.5}$(a_gZIF-62)$_{0.5}$, and (UL-MOF-1)$_{0.5}$(a_gZIF-62)$_{0.5}$ were thus probed using TMA. Experimental data are recorded in absolute length, so for meaningful comparison of material expansivity, data reported here are in percentage dimension change to account for differences in initial length (**Figure 108**).

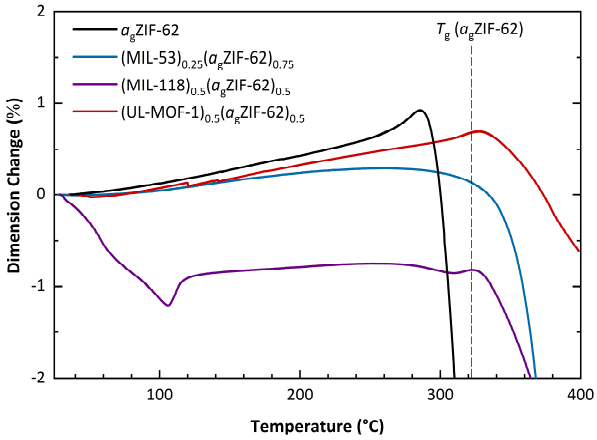

Figure 108: Bulk expansivity of the glass and MOF CGCs. *Thermomechanical Analysis (TMA) of (MIL-53)$_{0.25}$(a_gZIF-62)$_{0.75}$, (MIL-118)$_{0.5}$(a_gZIF-62)$_{0.5}$, and (UL-MOF-1)$_{0.5}$(a_gZIF-62)$_{0.5}$. Including a guideline for the largest reported T_g of a_gZIF-62.*[15]

A pure sample of a_gZIF-62 is observed to exhibit the largest thermal expansivity (α_L = 32.11 × 10^{-6} K^{-1}) of the measured materials, following previously reported data (35 × 10^{-6}K^{-1}).[295] Predictably, the sample of (UL-MOF-1)$_{0.5}$(a_gZIF-62)$_{0.5}$ with the largest volumetric expansion also exhibits the largest thermal expansion of the measured composites (α_L = 27.59 × 10^{-6} K^{-1}, 143–306 °C). A smaller expansion of (MIL-53)$_{0.25}$(a_gZIF-62)$_{0.75}$ (α_L = 14.22 × 10^{-6} K^{-1}, 111–177 °C) is likely due to the very small expansion of the MIL-53-lp phase inside the composite and a larger contributing volume of ZIF-62 compared to that in (UL-MOF-1)$_{0.5}$(a_gZIF-62)$_{0.5}$. The initial sharp decrease in length in the (MIL-118)$_{0.5}$(a_gZIF-62)$_{0.5}$ is ascribed to the temperature-induced phase change of MIL-118 from MIL-118C to MIL-118B as observed in VT-PXRD. After this phase change, a small thermal expansion (α_L = 8.79 × 10^{-6} K^{-1}, 128–270 °C) is observed, arising from the combination of the negative thermal expansion from composited MIL-188B and the positive thermal expansion of a_gZIF-62.

The density of each metal–organic framework (a_gZIF-62 = ~1.57 gcm^{-3}, MIL-118B = 1.696 gcm^{-3}, UL-MOF-1 = 1.606 gcm^{-3}, and MIL-53-lp = 0.9797 gcm^{-3})[65,121,191,192] is accounted for by assuming that the contribution of each material is equivalent to its vol%. An "isotropic" value of 1-dimensional expansivity, calculated by the average over the three mutually perpendicular coordinate axes (as determined by VT-PXRD), may represent the crystalline MOF contribution to the 1-D bulk expansivity. Averaging these isotropic values with the measured value of a_gZIF-62, weighted by their volume contributions, provides a predicted expansivity of a non-interacting system.

The calculated value of (UL-MOF-1)$_{0.5}$(a_gZIF-62)$_{0.5}$ using data from the encapsulated UL-MOF-1 is nearer to the measured value than using the isolated crystalline UL-MOF-1 data. Samples of (MIL-53)$_{0.25}$(a_gZIF-62)$_{0.75}$ and (MIL-118)$_{0.5}$(a_gZIF-62)$_{0.5}$, however, show an appreciable reduction in expansivity compared to the calculated values. Whilst crystalline expansion values are reliably calculated from VT-PXRD refinements, these calculations assume that no substantial preferred

crystalline orientation is induced during the synthesis of the MOF CGCs. The range of α_L value boundaries under extreme orientation conditions are hence calculated by substituting the averaged, "isotropic" CTE value for the minimum and maximum linear CTE values of each crystalline material within the composite (**Table 13**).

***Table 13**: Calculated and measured 1-D expansion of the MOF CGCs studied herein.*

Sample	Weighted Combination of Isolated MOF Components (10^{-6} K^{-1})	Weighted Combination of Components within the MOF CGC (10^{-6} K^{-1})	Aligned Crystalline Orientation		Measured (10^{-6} K^{-1})
			Minimum Value (10^{-6} K^{-1})	Maximum Value (10^{-6} K^{-1})	
a_gZIF-62	--	--	--	--	32.11
(MIL-53)$_{0.25}$(a_gZIF-62)$_{0.75}$	21.18	21.54	19.47	23.35	14.22
(MIL-118)$_{0.5}$(a_gZIF-62)$_{0.5}$	22.37	15.87	14.70	17.67	8.79
(UL-MOF-1)$_{0.5}$(a_gZIF-62)$_{0.5}$	36.19	33.44	16.65	60.84	27.59

The range of possible (UL-MOF-1)$_{0.5}$(a_gZIF-62)$_{0.5}$ CTE values is relatively vast. However, the predicted and measured values remain broadly comparable, signifying no great degree of preferred orientation. In contrast, for the composites with "flexible" crystalline MOFs, (MIL-53)$_{0.25}$(a_gZIF-62)$_{0.75}$ and (MIL-118)$_{0.5}$(a_gZIF-62)$_{0.5}$, the near-zero CTE values along each crystallographic axis acutely narrow the range of values in extreme conditions. Notably, for these samples, the measured data remains considerably out of the predicted range. While preferential orientation may affect the measured data, it does not fully account for the disparity in predicted and measured values, even accounting for the minimum expansivity of the flexible crystalline MOF. Two further compounding factors may be (i) a discrepancy between the expansion of a_gZIF-62 in the pure and composite samples and (ii) macrostructural features, such as interfacial void spaces, that cause deviation in recorded values. If the former is true, a reduction in expansivity of a_gZIF-62 may indicate interacting behaviour between the a_gZIF-62 and the composited crystalline MOF.

7.3 Mechanical Properties of MOF CGCs

To further probe the behaviour of the MOF CGC systems, the Young's moduli of each sample was extracted using nanoindentation. In the grinding stage of sample preparation, samples of (MIL-53)$_{0.5}$(a_gZIF-62)$_{0.5}$ and (UL-MOF-1)$_{0.5}$(a_gZIF-62)$_{0.5}$ repeatedly crumbled, and a flat sample surface could not be achieved. Lower loadings of each MOF CGC (25 wt%) were synthesised using the same fabrication procedure, and samples were successfully prepared for nanoindentation.

Indentation values were obtained for each sample over a series of 40 indents, typically in an array, processed to remove anomalous experiments, and averaged to provide values of *E* for each sample (**Figure 109**). Young's modulus values for (MIL-53)$_{0.25}$(a_gZIF-62)$_{0.75}$ are slightly lower than previously recorded (6.7 GPa compared to 7.7 GPa in **Section 4.2.7**) but represents a small change compared to the significant variation in reported values for a_gZIF-62 discussed in **Section 2.4.2**.

Notably, whilst the incorporation of MIL-53 within the glass MOF has little effect on the recorded elastic modulus of the sample, incorporation of UL-MOF-1 or MIL-118 induce a significant increase in stiffness (*E* = 8.3 GPa and 9.3 GPa for the respective MOF CGCs). Furthermore, the incorporation of higher loadings of MIL-118 further stiffens the composite (*E* = 13.1 GPa for (MIL-118)$_{0.5}$(a_gZIF-62)$_{0.5}$); however, this is accompanied by a decrease in measurement uniformity, observable in the broader standard deviation error. This change in the samples' physical properties on the variation of

material incorporation may serve as a method to further tune the composite to bespoke requirements. Further investigation is required to determine the extent to which these properties may be tuned.

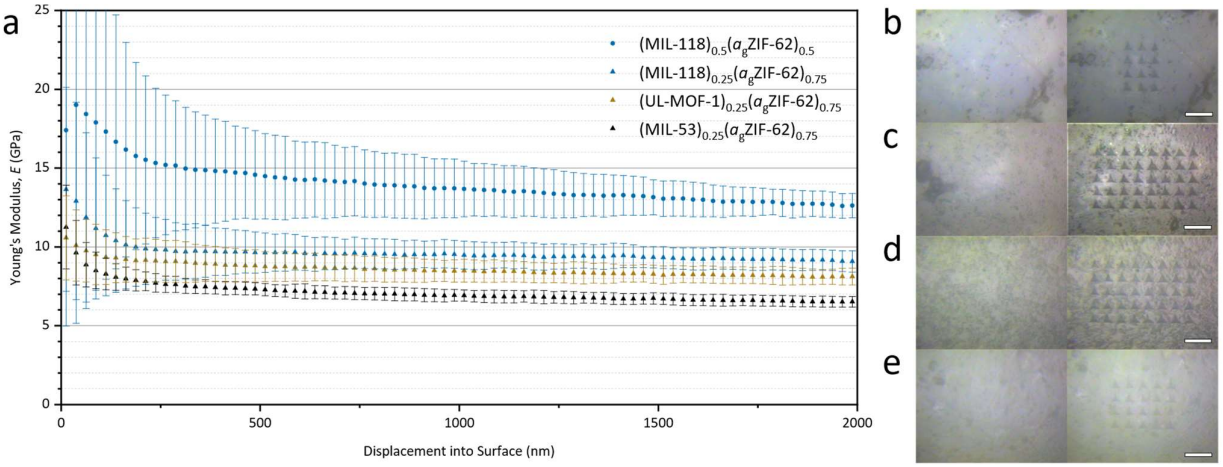

***Figure 109: Mechanical properties of MOF CGCs**. a. Displacement dependence of Young's moduli measured for samples of $(MIL\text{-}53)_{0.25}(a_gZIF\text{-}62)_{0.75}$, $(MIL\text{-}118)_{0.25}(a_gZIF\text{-}62)_{0.5}$, $(MIL\text{-}118)_{0.5}(a_gZIF\text{-}62)_{0.5}$, and $(UL\text{-}MOF\text{-}1)_{0.5}(a_gZIF\text{-}62)_{0.5}$. Pre- and post-indentation optical images of b. $(MIL\text{-}53)_{0.25}(a_gZIF\text{-}62)_{0.75}$, c. $(MIL\text{-}118)_{0.25}(a_gZIF\text{-}62)_{0.75}$, d. $(MIL\text{-}118)_{0.5}(a_gZIF\text{-}62)_{0.5}$, and e. $(UL\text{-}MOF\text{-}1)_{0.25}(a_gZIF\text{-}62)_{0.75}$. Scale bar is 30 µm.*

7.4 Conclusions

In this work, the effect on the unit cell expansion of three crystalline MOFs, when suspended within an a_gZIF-62 matrix, was analyzed using refinements of VT-PXRD data. Bulk expansivity measurements were then recorded for a_gZIF-62 and all three MOF CGCs using TMA. Having determined the expansivity of the encapsulated crystalline materials and an isolated sample of a_gZIF-62, the one-dimensional bulk expansivity of the MOF CGCs was approximated using a weighted average of the component materials. Comparison of these values with recorded data for the MOF CGCs was performed to validate the approximation and speculate on possible MOF-a_gMOF interactions.

When encapsulated within a_gZIF-62, the unit cell volume thermal expansivity of UL-MOF-1 behaves similarly to the pure crystalline material but is reduced by 12.4%. In contrast, samples of $(MIL\text{-}53)_{0.25}(a_gZIF\text{-}62)_{0.75}$ and $(MIL\text{-}118)_{0.5}(a_gZIF\text{-}62)_{0.5}$ display near-zero volumetric thermal expansion of the crystalline MOFs. As a result, the aperture size of these flexible frameworks remains relatively stable within a_gZIF-62 compared to their isolated crystalline materials. The fixture of these apertures may be key to the reliability of host-guest interactions for systems utilising MIL-53 or MIL-118 over the measured temperature ranges.

The experiments herein support an argument that the degree of expansion of the flexible crystalline component upon returning to the low-temperature phase determines whether the high-temperature phase is present in the room-temperature composite. Therefore, it is proposed that metastable high-temperature phases of flexible systems with significant uniaxial expansion on cooling may be retained within a MOF CGC.

Furthermore, bulk expansivity approximations using a combination of VT-PXRD and TMA data were shown to greatly overestimate values for samples of (MIL-53)$_{0.25}$(α_gZIF-62)$_{0.75}$ and (MIL-118)$_{0.5}$(α_gZIF-62)$_{0.5}$, which may be a result of MOF-α_gMOF interactions. The development of bulk property predictions presents an opportunity to produce zero thermal expansion MOF CGCs by offsetting the expansivity of the glass through the incorporation of MOFs with negative thermal expansivities.[123] Such materials may be useful for applications such as glass-deposited electronics and settings in which large temperature swings may be expected.

Chapter 8 Conclusions and Further Work

8.1 Conclusions

8.1.1 A Novel Family of Materials

A novel family of composite materials comprising a crystalline MOF within a MOF glass matrix has been developed in this work. These materials are most similar to the family of mixed-matrix membranes (MMMs), which embed crystalline MOFs within the bulk of a polymer. However, some critical differences between the two materials are (i) the higher T_g of MOF glasses compared to polymers permits broader operating temperatures, (ii) the greater stiffnesses of MOF glasses permits applications requiring enhanced structural rigidity, and (iii) the components are more structurally and chemical similar. This first example of a MOF composite formed from a crystalline MOF embedded in a MOF glass matrix represents a significant step in new materials discovery for the field.

Initial work on MOF CGCs, detailed in **Chapter 4**, describes the design of the material where ranges of temporally available glass-forming hybrid materials are considered, in combination with a selection of crystalline MOFs. In this section, the compatibility of the two materials is discussed regarding their melting and decomposition temperatures. The subsequent synthesis and characterisation of the first successful MOF CGC is performed using an a_gZIF-62 glass matrix supporting MIL-53 within the glass. The physical characteristics of this MOF CGC are then studied using a variety of analytic techniques. Subsequently, the scope of studied systems is broadened in **Chapter 6**, where further MOF CGCs with alternative crystalline MOF components, MIL-118, and UL-MOF-1, are successfully fabricated.

8.1.2 Crystalline Component Studies

In the characterisation of the MIL-53 MOF CGC, PXRD analysis presented the retention of the high-temperature stable, large-pore MIL-53-lp phase at room temperature within the MOF CGC. This phenomenon was studied using synchrotron-source variable temperature powder diffraction data to track the MOF crystallinity on heating, displaying a clear conversion of the MIL-53-as to the MIL-53-lp phase. The dispersion of the crystalline MOF within the CGC was revealed using STEM techniques. Well-dispersed ~100 nm regions of crystalline, aluminium dense sections, corresponding to regions with characteristic carboxylate profiles were observed. These areas may be confidently ascribed to clusters of crystalline MIL-53 within the glass. This same dispersivity was also observed with subsequent MOF CGCs fromed from MIL-118 and UL-MOF-1.

The phenomenon of MIL-53-lp retention within the glass was assumed to be caused by chemical bonding at the crystal–glass interface. To probe this, the proximity of the two components were analysed using a variety of solid-state, COSY, and spin diffusion NMR. Assignable peaks of each component—including protonated BDC, assigned as surface ligands—were observed, and polarisation transfer between the hydroxy groups of MIL-53 and the imidazolate linkers of a_gZIF-62 was revealed. Though bonding could not be verified using this technique, this displayed clear evidence of component proximity in the MOF CGC.

8.1.3 Bulk Material Studies

One of the more unique properties of the MIL-53 MOF CGC, related to the suspension of the MIL-53-lp phase, is its enhanced gas sorption properties. In **Chapter 4**, it was revealed that a 25 wt% MOF CGC exhibited greater CO_2 adsorption capacity than the combination of its parent materials. This phenomenon was then exploited in **Chapter 5** by synthesising a series of composites varying the concentration of crystalline material. A maximum capacity of the glass was thus determined through the emergence of MIL-53-np peaks in the diffraction patterns between 60–70 wt%. However, though the CO_2 uptake capacity increased with the concentration of MIL-53-lp present, an 80 wt% composite containing some MIL-53-np displayed the largest CO_2 uptake at 3.37 mmol/g (compared to the respective CO_2 capacities of crystalline MIL-53-np and a_gZIF-62 of 1.99 mmol/g and 0.79 mmol/g). Notably, some of the gas uptake may be ascribed to the induction of mesopores within the structure, likely at the interfaces.

Due to the tortuous diffusion of gases through a glass, the permeability of this component is likely the limiting factor for MOF CGC applications. The gas uptake capabilities of the glass and the MOF CGCs were studied further in **Chapter 6** using a variety of analyte gases. Whilst MIL-118 and UL-MOF-1 were determined to be too dense to significantly uptake even hydrogen, MIL-53 is porous to a range of analyte gases. In this MIL-53 CGC sample, the selective uptake of ethene over ethane, typical of a_gZIF-62, was preserved in the composite; secondly, significant hysteresis is observed in the propene adsorption isotherm. Since propene is reversibly adsorbed by a sample of MIL-53-np—and furthermore induced clear MIL-53-np to MIL-53-lp phase transition—this indicates an upper limit of kinetic diameter analyte gases that may permeate through the MOF glass.

Furthermore, in **Chapter 7** the thermal expansion of the MOF CGCs and of the isolated crystalline material was probed using TMA and refinement of VT-PXRD data, respectively. In these experiments, the change in expansion mode of the crystalline material when encapsulated within the glass matrix is revealed. Interestingly, no significant expansion is observed in either of the two flexible MOFs, MIL-53 and MIL-118, and the expansivity of UL-MOF-1 is reduced. These reductions in all measured MOF expansivities are ascribed to resistance from the surrounding dense glass matrix. Combining this information with water adsorption experiments in **Chapter 4** provides a rationale for the divergence in phase behaviour of MIL-53 and MIL-118 within the MOF CGCs. Since the T_g of a_gZIF-62 is greater than the high- to low-temperature phase transition of either framework, and the glass resists the expansion of the composited MOF, large uniaxial changes may be prevented by the vitrified glass.

8.1.4 Outlook of Current MOF CGCs

The results of this work indicate that encapsulating crystalline MOFs within a porous MOF glass matrix may be a suitable method to aggregate MOF powders into bulk processable materials. In these materials, large quantities of MOF may be loaded within the glass, though the calculation of accurate volume fractions may be more informative and translatable to other systems than weight fraction reports. These MOF CGCs using a_gZIF-62 may be applied to gas storage/separation systems with critical diameters of gases up to that of propene (4.678 Å)[296] and used at temperatures up to the T_s (softening temperature) of the host matrix. Furthermore, there lies potential to retain additional metastable MOFs at room temperature by obstructing transitions that occur with large expansion elements such as MIL-53. The prediction of resultant CTE values may overestimate in these cases, which is not yet fully explored; however, for "rigid" MOFs, rough estimates for the bulk expansivity of the MOF CGC may be predicted using the volume fraction weighted expansion values of the component materials.

8.2 Further Work

8.2.1 Component Compatibility

To better understand these materials and their full potential, further studies must be performed to extract information regarding the component interfaces. This would provide critical information concerning both the process by which the liquid MOF suffuses through the sample and how the crystalline MOF rests within the glass matrix. This knowledge would provide essential information such as whether the crystalline material rests within pockets of the glass, whether the glass is chemically bonded to the filler material, and whether pendant linkers of the glass penetrate within the pores of the MOF. Such information may provide clearer answers to uncertainties discussed herein. Furthermore, this would be informative to determine macrostructural properties such as crack propagation or antenna effects for luminescent MOFs. One method to possibly probe such information is through applying non-negative matrix factorisation (NMF) to PDF data recorded on the composites and parent materials. This method extracts interface PDF (iPDF) of the composites through the weighted subtraction of parent material PDF data. The resultant data may provide information regarding the atomic configuration at the composite interfaces.[297]

8.2.2 Alternative MOF Components

The balance between the melting of the glass former and the thermal stability of the crystalline MOF components has been discussed in this work, and the selection criteria have been laid out clearly. However, alternative MOF systems may exist, or become available through research into more thermally stable MOFs, for incorporation within further MOF CGCs. The potential range of these materials is vast and may permit the application of MOFs to systems incompatible with microcrystalline powders.

To improve the gas separation properties of the MOF CGCs the incorporation of alternative porous MOFs with complementary gas separation properties to the host matrix may work synergistically to separate mixtures—rather than

decrease the volumetric performance of the crystalline MOF as with inert binders. Notably, this work has only considered the synthesis of MOF CGCs with a single MOF filler as proof-of-concept and for simplicity of analysis. However, the incorporation of more than one filler material may provide multi-functional materials. For example, it may be possible to incorporate two catalytically active MOFs working in tandem, or incorporating two sensing MOFs for multi-functionality. Alternatively, the filler material may act as a property modulator; for example, the expansivity of the glass may be reduced through the incorporation of a negative thermal expansion material. In this case, a MOF CGC may be synthesised with zero thermal expansion properties. Further materials may be subsequently incorporated to enhance, for example, the optical properties, electrical/proton conductivity, mechanical properties or porosity of the composite.

8.2.3 Development of the Glass Matrix

To further expand the range of possible MOF CGCs and their applications from the perspective of the MOF glass component, the physical and thermodynamic properties of the glass must be considered. The greatest limiting factor to the synthesis of MOF CGCs is the high processing temperatures required to melt the glass-forming MOF. The generality of this family of materials would benefit greatly from reduced processing temperatures; this may be achieved through two means. The first of which requires the development of MOF glasses with lower melting temperatures. Investigation into the reduction of melting temperatures and glass transitions has been the focus of much scientific interest in the hybrid glass field and may yield MOFs with significantly lower transitions. However, such materials would face lower operating temperatures as the glass transition is also likely to decrease.

The second method involves the exploitation of the glass transition to produce MOF CGCs at a lower temperature. However, the viscosity of the liquid is directly proportional to the applied temperature, meaning that the glass will be much more viscous at these lower temperatures. Despite this, successful MOF CGCs have already been produced by this method, broadening the range of incorporable MOFs.[295]

Regarding the physical properties of the glass, among the most significant developments for these materials would be enhancing the glass' porosity. In doing so, the glass may accommodate gases with larger kinetic diameters, thereby expanding the utility of these materials. Perhaps incorporating bulkier linkers that occupy larger spaces—hindering the optimal packing of the components—may open the structure to incorporate larger analyte gases. Furthermore, the rapid quenching of a sample may entrap the molecular structure in a lower density state, potentially increasing permeability. Furthermore, the development of these materials on a bulk scale would provide informative measurements using the traditional tensile testing equipment to determine some of the macrostructural properties of the material accurately.

8.2.4 Development of Processing Techniques

Though the processing of the MOF CGCs developed here has been successful for this proof-of-concept work, they would benefit from optimisation studies to enhance particular properties of the product or enhance the suitability of the fabrication process. In the current process, materials are subject to ball-milling and pelletisation, both of which induce large stresses/strains. However, the ball-milling of the crystalline component may be avoided by mixing the components

after the particle size reduction of the glass former; however, the crystalline component must be at the desired particle size. The mixing of the two components may then be performed by using a mixing rotor on the powders or a fluid suspension—evaporating the solvent thereafter. The pelletisation step may also be avoided if low enough temperatures are applied since longer heating times would lead to better flow of the liquid MOF.

Lastly, the shaping of the end product is essential for industrially use, which is one of the key benefits of using a liquid-state component. Bespoke shapes or morphologies may be produced using the techniques described here in combination with a mould for the starting materials. Alternatively, heating above the T_g of the glass but below the T_d of the filler MOF may also allow the assimilation and shaping of standard-sized MOF CGC pellets.

8.3 Final Word

The generality of the novel materials detailed herein provides a promisingly vast scope for potential MOF CGCs, especially upon reduction of necessary MOF liquefaction temperatures. This inaugural work on MOF CGCs will hopefully serve to guide the development of further MOF CGCs and other supported crystalline MOF aggregates. However, further research is required to probe the fundamental properties of these materials more thoroughly. It is possible that these materials, given their porosity and preferential adsorption, may be used in zero thermal expansion, gas storage, gas separation, or membrane applications, and it will be exciting to see how this field develops.

Bibliography

(1) Farha, O. K.; Eryazici, I.; Jeong, N. C.; Hauser, B. G.; Wilmer, C. E.; Sarjeant, A. A.; Snurr, R. Q.; Nguyen, S. T.; Yazaydin, A. Ö.; Hupp, J. T. Metal−Organic Framework Materials with Ultrahigh Surface Areas: Is the Sky the Limit? *J. Am. Chem. Soc.* **2012**, *134*, 15016–15021. https://doi.org/10.1021/ja3055639.

(2) Rouquerol, F.; Rouquerol, J.; Sing, K. S. W.; Llewellyn, P.; Maurin, G. Adsorption by Powders and Porous Solids Principles, Methodology and Applications. In *Adsorption by Powders and Porous Solids Principles, Methodology and Applications*; Elsevier, 2014; p 8.

(3) Bojdys, M. J.; Briggs, M. E.; Jones, J. T. A.; Adams, D. J.; Chong, S. Y.; Schmidtmann, M.; Cooper, A. I. Supramolecular Engineering of Intrinsic and Extrinsic Porosity in Covalent Organic Cages. *J. Am. Chem. Soc.* **2011**, *133*, 16566–16571. https://doi.org/10.1021/ja2056374.

(4) Image of a Sea Sponge https://www.restorationhardware.com/catalog/product/product.jsp?productId=prod1850003 (accessed Jun 3, 2020).

(5) Image of Cork http://viemagazine.com/article/cork-is-popping-out-of-wine-bottles-and-into-your-home/ (accessed Jun 3, 2020).

(6) SEM Image of a Bone Sample https://www.pinterest.co.uk/pin/275775177151848606/ (accessed Jun 3, 2020).

(7) Diagram of Soil Particles https://wmap.blogs.delaware.gov/2019/03/11/wetlands-function-like-sponges/ (accessed Jun 3, 2020).

(8) Image of Zeolite Stones with Overlaid Structural Diagram http://www.pratley.com/operating-divisions/pratley-zeolite (accessed Jun 3, 2020).

(9) Inglezakis, V. J.; Zorpas, A. A. Chapter 1. In *Handbook of Natural Zeolites*; Bentham Science Publishers, 2012; pp 3–10.

(10) Ghobarkar, H.; Schäf, O.; Guth, U. Zeolites — from Kitchen to Space. *Prog. Solid State Chem.* **1999**, *27*, 29–73. https://doi.org/10.1016/S0079-6786(00)00002-9.

(11) Wragg, D. S.; Morris, R. E.; Burton, A. W. Pure Silica Zeolite-Type Frameworks: A Structural Analysis. *Chem. Mater.* **2008**, *20* (4), 1561–1570. https://doi.org/10.1021/cm071824j.

(12) Davis, M. E.; Lobo, R. F. Zeolite and Molecular Sieve Synthesis. *Chem. Mater.* **1992**, *4*, 756–768. https://doi.org/10.1021/cm00022a005.

(13) Holm, M. S.; Taarning, E.; Egeblad, K.; Christensen, C. H. Catalysis with Hierarchical Zeolites. *Catal. Today* **2011**, *168*, 3–16. https://doi.org/10.1016/j.cattod.2011.01.007.

(14) Barua, S.; Yoo, J.-W.; Kolhar, P.; Wakankar, A.; Gokarn, Y. R.; Mitragotri, S. Particle Shape Enhances Specificity of Antibody-Displaying Nanoparticles. *Proc. Natl. Acad. Sci. U. S. A.* **2013**, *110* (9), 3270–3275. https://doi.org/10.1073/pnas.1216893110.

(15) McKinlay, A. C.; Morris, R. E.; Horcajada, P.; Férey, G.; Gref, R.; Couvreur, P.; Serre, C. BioMOFs: Metal–Organic Frameworks for Biological and Medical Applications. *Angew. Chemie - Int. Ed.* **2010**, *49*, 6260–6266. https://doi.org/10.1002/anie.201000048.

(16) Cai, H.; Huang, Y.-L.; Li, D. Biological Metal–Organic Frameworks: Structures, Host–Guest Chemistry and Bio-Applications. *Coord. Chem. Rev.* **2019**, *378*, 207–221. https://doi.org/10.1016/j.ccr.2017.12.003.

(17) Mehmood, A.; Ghafar, H.; Yaqoob, S.; Gohar, U. F.; Ahmad, B. Mesoporous Silica Nanoparticles: A Review. *J. Dev. Drugs* **2017**, *6* (2), 1–14. https://doi.org/10.4172/2329-6631.1000174.

(18) Wan, Y.; Zhao, D. On the Controllable Soft-Templating Approach to Mesoporous Silicates. *Chem. Rev.* **2007**, *107* (7), 2821–

2860. https://doi.org/10.1021/cr068020s.

(19) Sing, K. S. W. Section 1.3 Physisorption by Porous Carbons. In *Adsorption by Carbons: Novel Carbon Adsorbents*; Tascón, J. M. D., Ed.; Elsevier Science & Technology, 2008; p 7.

(20) Cui, W.-R.; Zhang, C.-R.; Jiang, W.; Li, F.-F.; Liang, R.-P.; Liu, J.; Qiu, J.-D. Regenerable and Stable sp^2 Carbon-Conjugated Covalent Organic Frameworks for Selective Detection and Extraction of Uranium. *Nat. Commun.* **2020**, *11*, 436. https://doi.org/10.1038/s41467-020-14289-x.

(21) Spitler, E. L.; Dichtel, W. R. Lewis Acid-Catalysed Formation of Two-Dimensional Phthalocyanine Covalent Organic Frameworks. *Nat. Chem.* **2010**, *2*, 672–677. https://doi.org/10.1038/nchem.695.

(22) Smith, B. J.; Dichtel, W. R. Mechanistic Studies of Two-Dimensional Covalent Organic Frameworks Rapidly Polymerized from Initially Homogenous Conditions. *J. Am. Chem. Soc.* **2014**, *136*, 8783–8789. https://doi.org/10.1021/ja5037868.

(23) Calik, M.; Sick, T.; Dogru, M.; Döblinger, M.; Datz, S.; Budde, H.; Hartschuh, A.; Auras, F.; Bein, T. From Highly Crystalline to Outer Surface-Functionalized Covalent Organic Frameworks—A Modulation Approach. *J. Am. Chem. Soc.* **2016**, *138*, 1234–1239. https://doi.org/10.1021/jacs.5b10708.

(24) Côte, A. P.; Benin, A. I.; Ockwig, N. W.; O'Keeffe, M.; Matzger, A. J.; Yaghi, O. M. Porous, Crystalline, Covalent Organic Frameworks. *Science* **2005**, *310*, 1166–1170. https://doi.org/10.1126/science.1120411.

(25) Uribe-Romo, F. J.; Hunt, J. R.; Furukawa, H.; Klöck, C.; O'Keeffe, M.; Yaghi, O. M. A Crystalline Imine-Linked 3-D Porous Covalent Organic Framework. *J. Am. Chem. Soc.* **2009**, *131*, 4570–4571. https://doi.org/10.1021/ja8096256.

(26) Wan, S.; Gándara, F.; Asano, A.; Furukawa, H.; Saeki, A.; Dey, S. K.; Liao, L.; Ambrogio, M. W.; Botros, Y. Y.; Duan, X.; Seki, S.; Stoddart, J. F.; Yaghi, O. M. Covalent Organic Frameworks with High Charge Carrier Mobility. *Chem. Mater.* **2011**, *23*, 4094–4097. https://doi.org/10.1021/cm201140r.

(27) Kandambeth, S.; Mallick, A.; Lukose, B.; Mane, M. V.; Heine, T.; Banerjee, R. Construction of Crystalline 2D Covalent Organic Frameworks with Remarkable Chemical (Acid/Base) Stability *via* a Combined Reversible and Irreversible Route. *J. Am. Chem. Soc.* **2012**, *134*, 19524–19527. https://doi.org/10.1021/ja308278w.

(28) Ascherl, L.; Sick, T.; Margraf, J. T.; Lapidus, S. H.; Calik, M.; Hettstedt, C.; Karaghiosoff, K.; Döblinger, M.; Clark, T.; Chapman, K. W.; Auras, F.; Bein, T. Molecular Docking Sites Designed for the Generation of Highly Crystalline Covalent Organic Frameworks. *Nat. Chem.* **2016**, *8*, 310–316. https://doi.org/10.1038/nchem.2444.

(29) Uribe-Romo, F. J.; Doonan, C. J.; Furukawa, H.; Oisaki, K.; Yaghi, O. M. Crystalline Covalent Organic Frameworks with Hydrazone Linkages. *J. Am. Chem. Soc.* **2011**, *133*, 11478–11481. https://doi.org/10.1021/ja204728y.

(30) Stegbauer, L.; Schwinghammer, K.; Lotsch, B. V. A Hydrazone-Based Covalent Organic Framework for Photocatalytic Hydrogen Production. *Chem. Sci.* **2014**, *5*, 2789–2793. https://doi.org/10.1039/c4sc00016a.

(31) Ascherl, L.; Evans, E. W.; Hennemann, M.; Di Nuzzo, D.; Hufnagel, A. G.; Beetz, M.; Friend, R. H.; Clark, T.; Bein, T.; Auras, F. Solvatochromic Covalent Organic Frameworks. *Nat. Commun.* **2018**, *9*, 3802. https://doi.org/10.1038/s41467-018-06161-w.

(32) Gui, B.; Lin, G.; Ding, H.; Gao, C.; Mal, A.; Wang, C. Three-Dimensional Covalent Organic Frameworks: From Topology Design to Applications. *Acc. Chem. Res.* **2020**, *53*, 2225–2234. https://doi.org/10.1021/acs.accounts.0c00357.

(33) Tozawa, T.; Jones, J. T. A.; Swamy, S. I.; Jiang, S.; Adams, D. J.; Shakespeare, S.; Clowes, R.; Bradshaw, D.; Hasell, T.; Chong, S. Y.; Tang, C.; Thompson, S.; Parker, J.; Trewin, A.; Bacsa, J.; Slawin, A. M. Z.; Steiner, A.; Cooper, A. I. Porous Organic Cages. *Nat. Mater.* **2009**, *8*, 973–978. https://doi.org/10.1038/nmat2545.

(34) Mitra, T.; Jelfs, K. E.; Schmidtmann, M.; Ahmed, A.; Chong, S. Y.; Adams, D. J.; Cooper, A. I. Molecular Shape Sorting Using Molecular Organic Cages. *Nat. Chem.* **2013**, *5*, 276–281. https://doi.org/10.1038/nchem.1550.

(35) Chen, L.; Reiss, P. S.; Chong, S. Y.; Holden, D.; Jelfs, K. E.; Hasell, T.; Little, M. A.; Kewley, A.; Briggs, M. E.; Stephenson, A.; Thomas, K. M.; Armstrong, J. A.; Bell, J.; Busto, J.; Noel, R.; Liu, J.; Strachan, D. M.; Thallapally, P. K.; Cooper, A. I. Separation

of Rare Gases and Chiral Molecules by Selective Binding in Porous Organic Cages. *Nat. Mater.* **2014**, *13*, 954–960. https://doi.org/10.1038/nmat4035.

(36) Jung, M.; Kim, H.; Baek, K.; Kim, K. Synthetic Ion Channel Based on Metal–Organic Polyhedra. *Angew. Chemie - Int. Ed.* **2008**, *47*, 5755–5757. https://doi.org/10.1002/anie.200802240.

(37) Furukawa, H.; Cordova, K. E.; O'Keeffe, M.; Yaghi, O. M. The Chemistry and Applications of Metal-Organic Frameworks. *Science* **2013**, *341*, 974–986. https://doi.org/10.1126/science.1230444.

(38) Tranchemontagne, D. J.; Mendoza-Cortés, J. L.; O'Keeffe, M.; Yaghi, O. M. Secondary Building Units, Nets and Bonding in the Chemistry of Metal–Organic Frameworks. *Chem. Soc. Rev.* **2009**, *38*, 1257–1283. https://doi.org/10.1039/b817735j.

(39) Moghadam, P. Z.; Li, A.; Liu, X.-W.; Bueno-Perez, R.; Wang, S.-D.; Wiggin, S. B.; Wood, P. A.; Fairen-Jimenez, D. Targeted Classification of Metal–Organic Frameworks in the Cambridge Structural Database (CSD). *Chem. Sci.* **2020**, *11*, 8373–8387. https://doi.org/10.1039/d0sc01297a.

(40) Rosi, N. L.; Eckert, J.; Eddaoudi, M.; Vodak, D. T.; Kim, J.; O'Keeffe, M.; Yaghi, O. M. Hydrogen Storage in Microporous Metal-Organic Frameworks. *Science* **2003**, *300*, 1127–1129. https://doi.org/10.1126/science.1083440.

(41) Huang, B. L.; Ni, Z.; Millward, A.; McGaughey, A. J. H.; Uher, C.; Kaviany, M.; Yaghi, O. Thermal Conductivity of a Metal-Organic Framework (MOF-5): Part II. Measurement. *Int. J. Heat Mass Transf.* **2007**, *50*, 405–411. https://doi.org/10.1016/j.ijheatmasstransfer.2006.10.001.

(42) Kaye, S. S.; Dailly, A.; Yaghi, O. M.; Long, J. R. Impact of Preparation and Handling on the Hydrogen Storage Properties of Zn_4O(1,4-Benzenedicarboxylate)$_3$ (MOF-5). *J. Am. Chem. Soc.* **2007**, *129*, 14176–14177. https://doi.org/10.1021/ja076877g.

(43) Zhu, Q.-L.; Xu, Q. Metal–Organic Framework Composites. *Chem. Soc. Rev.* **2014**, *43* (16), 5648–5512. https://doi.org/10.1039/c3cs60472a.

(44) Gkaniatsou, E.; Sicard, C.; Ricoux, R.; Mahy, J.-P.; Steunou, N.; Serre, C. Metal–Organic Frameworks: A Novel Host Platform for Enzymatic Catalysis and Detection. *Mater. Horizons* **2017**, *4*, 55–63. https://doi.org/10.1039/c6mh00312e.

(45) Guo, C.; Guo, J.; Zhang, Y.; Wang, D.; Zhang, L.; Guo, Y.; Ma, W.; Wang, J. Synthesis of Core–Shell ZIF-67@Co-MOF-74 Catalyst with Controllable Shell Thickness and Enhanced Photocatalytic Activity for Visible Light- Driven Water Oxidation. *CrystEngComm* **2018**, *20*, 7659–7665. https://doi.org/10.1039/c8ce01266k.

(46) Wiktor, C.; Meledina, M.; Turner, S.; Lebedev, O. I.; Fischer, R. A. Transmission Electron Microscopy on Metal–Organic Frameworks – a Review. *J. Mater. Chem. A* **2017**, *5*, 14969–14989. https://doi.org/10.1039/c7ta00194k.

(47) Pastore, V. J.; Cook, T. R.; Rzayev, J. Polymer−MOF Hybrid Composites with High Porosity and Stability through Surface-Selective Ligand Exchange. *Chem. Mater.* **2018**, *30*, 8639–8649. https://doi.org/10.1021/acs.chemmater.8b03881.

(48) Küsgens, P.; Zgaverdea, A.; Fritz, H.-G.; Siegle, S.; Kaskel, S. Metal-Organic Frameworks in Monolithic Structures. *J. Am. Ceram. Soc.* **2010**, *93* (9), 2476–2479. https://doi.org/10.1111/j.1551-2916.2010.03824.x.

(49) Notman, N. MOFs Find a Use. *Chemistry World*. 2017.

(50) Faust, T. MOFs Move to Market. *Nat. Chem.* **2016**, *8*, 990–991. https://doi.org/10.1038/nchem.2656.

(51) Cairns, A. B.; Goodwin, A. L. Structural Disorder in Molecular Framework Materials. *Chem. Soc. Rev.* **2013**, *42*, 4881–4893. https://doi.org/10.1039/c3cs35524a.

(52) Bennett, T. D.; Cheetham, A. K. Amorphous Metal−Organic Frameworks. *Acc. Chem. Res.* **2014**, *47*, 1555–1562. https://doi.org/10.1021/ar5000314.

(53) Bennett, T. D.; Horike, S. Liquid, Glass and Amorphous Solid States of Coordination Polymers and Metal–Organic Frameworks. *Nat. Rev. Mater.* **2018**, *3*, 431–440. https://doi.org/10.1038/s41578-018-0054-3.

(54) Bennett, T. D.; Cao, S.; Tan, J. C.; Keen, D. A.; Bithell, E. G.; Beldon, P. J.; Friscic, T.; Cheetham, A. K. Facile Mechanosynthesis of Amorphous Zeolitic Imidazolate Frameworks. *J. Am. Chem. Soc.* **2011**, *133*, 14546–14549.

https://doi.org/10.1021/ja206082s.

(55) Widmer, R. N.; Lampronti, G. I.; Anzellini, S.; Gaillac, R.; Farsang, S.; Zhou, C.; Belenguer, A. M.; Wilson, C. W.; Palmer, H.; Kleppe, A. K.; Wharmby, M. T.; Yu, X.; Cohen, S. M.; Telfer, S. G.; Redfern, S. A. T.; Coudert, F.-X.; MacLeod, S. G.; Bennett, T. D. Pressure Promoted Low-Temperature Melting of Metal–Organic Frameworks. *Nat. Mater.* **2019**, *18*, 370–376. https://doi.org/10.1038/s41563-019-0317-4.

(56) Sanchez-Sanchez, M.; de Asua, I.; Ruano, D.; Diaz, K. Direct Synthesis, Structural Features, and Enhanced Catalytic Activity of the Basolite F300-like Semiamorphous Fe-BTC Framework. *Cryst. Growth Des.* **2015**, *15*, 4498–4506. https://doi.org/10.1021/acs.cgd.5b00755.

(57) Qiao, A.; Bennett, T. D.; Tao, H.; Krajnc, A.; Mali, G.; Doherty, C. M.; Thornton, A. W.; Mauro, J. C.; Greaves, G. N.; Yue, Y. A Metal-Organic Framework with Ultrahigh Glass-Forming Ability. *Sci. Adv.* **2018**, *4*, eaao6827. https://doi.org/10.1126/sciadv.aao6827.

(58) Frentzel-Beyme, L.; Kloß, M.; Kolodzeiski, P.; Pallach, R.; Henke, S. Meltable Mixed-Linker Zeolitic Imidazolate Frameworks and Their Microporous Glasses: From Melting Point Engineering to Selective Hydrocarbon Sorption. *J. Am. Chem. Soc.* **2019**, *141*, 12362–12371. https://doi.org/10.1021/jacs.9b05558.

(59) Bennett, T. D.; Goodwin, A. L.; Dove, M. T.; Keen, D. A.; Tucker, M. G.; Barney, E. R.; Soper, A. K.; Bithell, E. G.; Tan, J.-C.; Cheetham, A. K. Structure and Properties of an Amorphous Metal-Organic Framework. *Phys. Rev. Lett.* **2010**, *104* (11), 115503. https://doi.org/10.1103/PhysRevLett.104.115503.

(60) Gaillac, R.; Pullumbi, P.; Bennett, T. D.; Coudert, F.-X. Structure of Metal−Organic Framework Glasses by *Ab Initio* Molecular Dynamics. *Chem. Mater.* **2020**, *32*, 8004–8011. https://doi.org/10.1021/acs.chemmater.0c02950.

(61) Orellana-Tavra, C.; Baxter, E. F.; Tian, T.; Bennett, T. D.; Slater, N. K. H.; Cheetham, A. K.; Fairen-Jimenez, D. Amorphous Metal–Organic Frameworks for Drug Delivery. *Chem. Commun.* **2015**, *51*, 13878–13881. https://doi.org/10.1039/c5cc05237h.

(62) Debenedetti, P. G.; Stillinger, F. H. Supercooled Liquids and the Glass Transition. *Nature* **2001**, *410*, 259–267. https://doi.org/10.1038/35065704.

(63) Gibbs, J. H.; DiMarzio, E. A. Nature of the Glass Transition and the Glassy State. *J. Chem. Phys.* **1958**, *28*, 373–383. https://doi.org/10.1063/1.1744141.

(64) Atomistic Configuration of Crystalline and Amorphous SiO_2 https://www.e-education.psu.edu/matse81/node/2154 (accessed May 10, 2021).

(65) Bennett, T. D.; Yue, Y.; Li, P.; Qiao, A.; Tao, H.; Greaves, N. G.; Richards, T.; Lampronti, G. I.; Redfern, S. A. T.; Blanc, F.; Farha, O. K.; Hupp, J. T.; Cheetham, A. K.; Keen, D. A. Melt-Quenched Glasses of Metal−Organic Frameworks. *J. Am. Chem. Soc.* **2016**, *138*, 3484–3492. https://doi.org/10.1021/jacs.5b13220.

(66) Moghadam, P. Z.; Li, A.; Wiggin, S. B.; Tao, A.; Maloney, A. G. P.; Wood, P. A.; Ward, S. C.; Fairen-Jimenez, D. Development of a Cambridge Structural Database Subset: A Collection of Metal−Organic Frameworks for Past, Present, and Future. *Chem. Mater.* **2017**, *29*, 2618–2625. https://doi.org/10.1021/acs.chemmater.7b00441.

(67) Bumstead, A. M.; Ríos Gómez, M. L.; Thorne, M. F.; Sapnik, A. F.; Longley, L.; Tuffnell, J. M.; Keeble, D. S.; Keen, D. A.; Bennett, T. D. Investigating the Melting Behaviour of Polymorphic Zeolitic Imidazolate Frameworks. *CrystEngComm* **2020**, *22*, 3627–3637. https://doi.org/10.1039/d0ce00408a.

(68) Gaillac, R.; Pullumbi, P.; Beyer, K. A.; Chapman, K. W.; Keen, D. A.; Bennett, T. D.; Coudert, F.-X. Liquid Metal–Organic Frameworks. *Nat. Mater.* **2017**, *16*, 1149–1155. https://doi.org/10.1038/nmat4998.

(69) Horike, S.; Nagarkar, S. S.; Ogawa, T.; Kitagawa, S. A New Dimension for Coordination Polymers and Metal–Organic Frameworks: Towards Functional Glasses and Liquids. *Angew. Chemie Int. Ed.* **2020**, *59*, 2–15.

https://doi.org/10.1002/anie.201911384.

(70) Bennett, T. D.; Tan, J.-C.; Yue, Y.; Baxter, E.; Ducati, C.; Terrill, N. J.; Yeung, H. H.-M.; Zhou, Z.; Chen, W.; Henke, S.; Cheetham, A. K.; Greaves, G. N. Hybrid Glasses from Strong and Fragile Metal-Organic Framework Liquids. *Nat. Commun.* **2015**, *6*, 8079. https://doi.org/10.1038/ncomms9079.

(71) Qiao, A.; Tao, H.; Carson, M. P.; Aldrich, S. W.; Thirion, L. M.; Bennett, T. D.; Mauro, J. C.; Yue, Y. Optical Properties of a Melt-Quenched Metal–Organic Framework Glass. *Opt. Lett.* **2019**, *44* (7), 1623–1625. https://doi.org/10.1364/ol.44.001623.

(72) Frentzel-Beyme, L.; Kloß, M.; Pallach, R.; Salamon, S.; Moldenhauer, H.; Landers, J.; Wende, H.; Debus, J.; Henke, S. Porous Purple Glass – a Cobalt Imidazolate Glass with Accessible Porosity from a Meltable Cobalt Imidazolate Framework. *J. Mater. Chem. A* **2019**, *7*, 985–990. https://doi.org/10.1039/c8ta08016j.

(73) Zhou, C.; Longley, L.; Krajnc, A.; Smales, G. J.; Qiao, A.; Erucar, I.; Doherty, C. M.; Thornton, A. W.; Hill, A. J.; Ashling, C. W.; Qazvini, O. T.; Lee, S. J.; Chater, P. A.; Terrill, N. J.; Smith, A. J.; Yue, Y.; Mali, G.; Keen, D. A.; Telfer, S. G.; Bennett, T. D. Metal-Organic Framework Glasses with Permanent Accessible Porosity. *Nat. Commun.* **2018**, *9*, 5042. https://doi.org/10.1038/s41467-018-07532-z.

(74) Thornton, A. W.; Jelfs, K. E.; Konstas, K.; Doherty, C. M.; Hill, A. J.; Cheetham, A. K.; Bennett, T. D. Porosity in Metal–Organic Framework Glasses. *Chem. Commun.* **2016**, *52* (19), 3750–3753. https://doi.org/10.1039/C5CC10072K.

(75) Li, S.; Limbach, R.; Longley, L.; Shirzadi, A. A.; Walmsley, J. C.; Johnstone, D. N.; Midgley, P. A.; Wondraczek, L.; Bennett, T. D. Mechanical Properties and Processing Techniques of Bulk Metal−Organic Framework Glasses. *J. Am. Chem. Soc.* **2019**, *141*, 1027–1034. https://doi.org/10.1021/jacs.8b11357.

(76) Stepniewska, M.; Januchta, K.; Zhou, C.; Qiao, A.; Smedskjaer, M. M.; Yue, Y. Observation of Indentation-Induced Shear Bands in a Metal−organic Framework Glass. *Proc. Natl. Acad. Sci. U. S. A.* **2020**, *117* (19), 10149–10154. https://doi.org/10.1073/pnas.2000916117.

(77) Cook, T. R.; Zheng, Y.-R.; Stang, P. J. Metal-Organic Frameworks and Self-Assembled Supramolecular Coordination Complexes: Comparing and Contrasting the Design, Synthesis and Functionality of Metal-Organic Materials. *Chem. Rev.* **2013**, *113* (1), 734–777. https://doi.org/10.1021/cr3002824.

(78) Deng, H.; Grunder, S.; Cordova, K. E.; Valente, C.; Furukawa, H.; Hmadeh, M.; Gandara, F.; Whalley, A. C.; Liu, Z.; Asahina, S.; Kazumori, H.; O'Keeffe, M.; Terasaki, O.; Stoddart, J. F.; Yaghi, O. M. Large-Pore Apertures in a Series of Metal-Organic Frameworks. *Science* **2012**, *336* (6084), 1018–1023. https://doi.org/10.1126/science.1220131.

(79) Bosch, M.; Zhang, M.; Zhou, H.-C. Increasing the Stability of Metal-Organic Frameworks. *Adv. Chem.* **2014**, 1–8. https://doi.org/10.1155/2014/182327.

(80) Takacs, L. The Historical Development of Mechanochemistry. *Chem. Soc. Rev.* **2013**, *42*, 7649–7659. https://doi.org/10.1039/c2cs35442j.

(81) James, S. L.; Adams, C. J.; Bolm, C.; Braga, D.; Collier, P.; Friščić, T.; Grepioni, F.; Harris, K. D. M.; Hyett, G.; Jones, W.; Krebs, A.; Mack, J.; Maini, L.; Orpen, A. G.; Parkin, I. P.; Shearouse, W. C.; Steed, J. W.; Waddell, D. C. Mechanochemistry: Opportunities for New and Cleaner Synthesis. *Chem. Soc. Rev.* **2012**, *41*, 413–447. https://doi.org/10.1039/c1cs15171a.

(82) Burmeister, C. F.; Kwade, A. Process Engineering with Planetary Ball Mills. *Chem. Soc. Rev.* **2013**, *42*, 7660–7667. https://doi.org/10.1039/c3cs35455e.

(83) Crawford, D.; Casaban, J.; Haydon, R.; Giri, N.; McNally, T.; James, S. L. Synthesis by Extrusion: Continuous, Large-Scale Preparation of MOFs Using Little or No Solvent. *Chem. Sci.* **2015**, *6*, 1645–1649. https://doi.org/10.1039/c4sc03217a.

(84) Halasz, I.; Kimber, S. A. J.; Beldon, P. J.; Belenguer, A. M.; Adams, F.; Honkimäki, V.; Nightingale, R. C.; Dinnebier, R. E.; Friščić, T. *In Situ* and Real-Time Monitoring of Mechanochemical Milling Reactions Using Synchrotron X-Ray Diffraction. *Nat. Protoc.* **2013**, *8* (9), 1718–1729. https://doi.org/10.1038/nprot.2013.100.

(85) Surati, M. A.; Jauhari, S.; Desai, K. R. A Brief Review: Microwave Assisted Organic Reaction. *Arch. Appl. Sci. Res.* **2012**, *4* (1), 645–661.

(86) Klinowski, J.; Almeida Paz, F. A.; Silva, P.; Rocha, J. Microwave-Assisted Synthesis of Metal–Organic Frameworks. *Dalt. Trans.* **2011**, *40*, 321–330. https://doi.org/10.1039/c0dt00708k.

(87) Dahl, J. A.; Maddux, B. L. S.; Hutchison, J. E. Toward Greener Nanosynthesis. *Chem. Rev.* **2007**, *107*, 2228–2269. https://doi.org/10.1021/cr050943k.

(88) Friščić, T.; Halasz, I.; Beldon, P. J.; Belenguer, A. M.; Adams, F.; Kimber, S. A. J.; Honkimäki, V.; Dinnebier, R. E. Real-Time and *in Situ* Monitoring of Mechanochemical Milling Reactions. *Nat. Chem.* **2013**, *5*, 66–73. https://doi.org/10.1038/nchem.1505.

(89) Carlucci, L.; Ciani, G.; Proserpio, D. M. Polycatenation, Polythreading and Polyknotting in Coordination Network Chemistry. *Coord. Chem. Rev.* **2003**, *246*, 247–289. https://doi.org/10.1016/S0010-8545(03)00126-7.

(90) Shekhah, O.; Wang, H.; Paradinas, M.; Ocal, C.; Schüpbach, B.; Terfort, A.; Zacher, D.; Fischer, R. A.; Wöll, C. Controlling Interpenetration in Metal–Organic Frameworks by Liquid-Phase Epitaxy. *Nat. Mater.* **2009**, *8*, 481–484. https://doi.org/10.1038/nmat2445.

(91) Rowsell, J. L. C.; Yaghi, O. M. Metal-Organic Frameworks: A New Class of Porous Materials. *Microporous Mesoporous Mater.* **2004**, *73*, 3–14. https://doi.org/10.1016/j.micromeso.2004.03.034.

(92) Chen, B.; Wang, X.; Zhang, Q.; Xi, X.; Cai, J.; Qi, H.; Shi, S.; Wang, J.; Yuan, D.; Fang, M. Synthesis and Characterization of the Interpenetrated MOF-5. *J. Mater. Chem.* **2010**, *20*, 3758–3767. https://doi.org/10.1039/b922528e.

(93) Ma, S.; Sun, D.; Ambrogio, M.; Fillinger, J. A.; Parkin, S.; Zhou, H.-C. Framework-Catenation Isomerism in Metal-Organic Frameworks and Its Impact on Hydrogen Uptake. *J. Am. Chem. Soc.* **2007**, *129*, 1858–1859. https://doi.org/10.1021/ja067435s.

(94) Ferguson, A.; Liu, L.; Tapperwijn, S. J.; Perl, D.; Coudert, F.-X.; Van Cleuvenbergen, S.; Verbiest, T.; van der Veen, M. A.; Telfer, S. G. Controlled Partial Interpenetration in Metal–Organic Frameworks. *Nat. Chem.* **2016**, *8*, 250–257. https://doi.org/10.1038/nchem.2430.

(95) Mondloch, J. E.; Karagiaridi, O.; Farha, O. K.; Hupp, J. T. Activation of Metal–Organic Framework Materials. *CrystEngComm* **2013**, *15*, 9258–9264. https://doi.org/10.1039/c3ce41232f.

(96) Bordiga, S.; Regli, L.; Bonino, F.; Groppo, E.; Lamberti, C.; Xiao, B.; Wheatley, P. S.; Morris, R. E.; Zecchina, A. Adsorption Properties of HKUST-1 toward Hydrogen and Other Small Molecules Monitored by IR. *Phys. Chem. Chem. Phys.* **2007**, *9*, 2676–2685. https://doi.org/10.1039/b703643d.

(97) Banerjee, R.; Phan, A.; Wang, B.; Knobler, C.; Furukawa, H.; O'Keefe, M.; Yaghi, O. M. High-Throughput Synthesis of Zeolitic Imidazolate Frameworks and Application to CO_2 Capture. *Science* **2008**, *319*, 939–944. https://doi.org/10.1126/science.1152516.

(98) Chen, B.; Yang, Z.; Zhu, Y.; Xia, Y. Zeolitic Imidazolate Framework Materials: Recent Progress in Synthesis and Applications. *J. Mater. Chem. A* **2014**, *2*, 16811–16831. https://doi.org/10.1039/c4ta02984d.

(99) Bux, H.; Chmelik, C.; Krishna, R.; Caro, J. Ethene/Ethane Separation by the MOF Membrane ZIF-8: Molecular Correlation of Permeation, Adsorption, Diffusion. *J. Memb. Sci.* **2011**, *369*, 284–289. https://doi.org/10.1016/j.memsci.2010.12.001.

(100) McCarthy, M. C.; Varela-Guerrero, V.; Barnett, G. V.; Jeong, H.-K. Synthesis of Zeolitic Imidazolate Framework Films and Membranes with Controlled Microstructures. *Langmuir* **2010**, *26* (18), 14636–14641. https://doi.org/10.1021/la102409e.

(101) Jiang, H.; Liu, B.; Akita, T.; Haruta, M.; Sakurai, H.; Qiang, X. Au@ZIF-8: CO Oxidation over Gold Nanoparticles Deposited to Metal–Organic Framework. *J. Am. Chem. Soc.* **2009**, *131*, 11302–11303. https://doi.org/10.1021/ja9047653.

(102) Lu, G.; Hupp, J. T. Metal–Organic Frameworks as Sensors: A ZIF-8 Based Fabry–Pérot Device as a Selective Sensor for Chemical Vapors and Gases. *J. Am. Chem. Soc.* **2010**, *132*, 7832–7833. https://doi.org/10.1021/ja101415b.

(103) Vasconcelos, I. B.; da Silva, T. G.; Militão, G. C. G.; Soares, T. A.; Rodrigues, N. M.; Rodrigues, M. O.; da Costa Jr., N. B.; Freire, R. O.; Junior, S. A. Cytotoxicity and Slow Release of the Anti-Cancer Drug Doxorubicin from ZIF-8. *RSC Adv.* **2012**, *2*, 9437–9442. https://doi.org/10.1039/c2ra21087h.

(104) Park, K. S.; Ni, Z.; Côté, A. P.; Choi, J. Y.; Huang, R.; Uribe-Romo, F. J.; Chae, H. K.; O'Keeffe, M.; Yaghi, O. M. Exceptional Chemical and Thermal Stability of Zeolitic Imidazolate Frameworks. *Proc. Natl. Acad. Sci. U. S. A.* **2006**, *103* (27), 10186–10191. https://doi.org/10.1073/pnas.0602439103.

(105) Amrouche, H.; Creton, B.; Siperstein, F.; Nieto-Draghi, C. Prediction of Thermodynamic Properties of Adsorbed Gases in Zeolitic Imidazolate Frameworks. *RSC Adv.* **2012**, *2*, 6028–6035. https://doi.org/10.1039/c2ra00025c.

(106) US DoE. *Target Explanation Document: Onboard Hydrogen Storage for Light-Duty Fuel Cell Vehicles*; 2017.

(107) Shearer, G. C.; Chavan, S.; Bordiga, S.; Svelle, S.; Olsbye, U.; Lillerud, K. P. Defect Engineering: Tuning the Porosity and Composition of the Metal−Organic Framework UiO-66 *via* Modulated Synthesis. *Chem. Mater.* **2016**, *28*, 3749–3761. https://doi.org/10.1021/acs.chemmater.6b00602.

(108) Sapnik, A. F.; Johnstone, D. N.; Collins, S. M.; Divitini, G.; Bumstead, A. M.; Ashling, C. W.; Chater, P. A.; Keeble, D. S.; Johnson, T.; Keen, D. A.; Bennett, T. D. Stepwise Collapse of a Giant Pore Metal–Organic Framework. *Dalt. Trans.* **2021**, *50*, 5011–5022. https://doi.org/10.1039/d1dt00881a.

(109) García-Holley, P.; Schweitzer, B.; Islamoglu, T.; Liu, Y.; Lin, L.; Rodriguez, S.; Weston, M. H.; Hupp, J. T.; Gómez-Gualdrón, D. A.; Yildirim, T.; Farha, O. K. Benchmark Study of Hydrogen Storage in Metal−Organic Frameworks under Temperature and Pressure Swing Conditions. *ACS Energy Lett.* **2018**, *3*, 748–754. https://doi.org/10.1021/acsenergylett.8b00154.

(110) Wilmer, C. E.; Farha, O. K.; Yildirim, T.; Eryazici, I.; Krungleviciute, V.; Sarjeant, A. A.; Snurr, R. Q.; Hupp, J. T. Gram-Scale, High-Yield Synthesis of a Robust Metal–Organic Framework for Storing Methane and Other Gases. *Energy Environ. Sci.* **2013**, *6*, 1158–1163. https://doi.org/10.1039/c3ee24506c.

(111) Liu, G.; Chernikova, V.; Liu, Y.; Zhang, K.; Belmabkhout, Y.; Shekhah, O.; Zhang, C.; Yi, S.; Eddaoudi, M.; Koros, W. J. Mixed Matrix Formulations with MOF Molecular Sieving for Key Energy-Intensive Separations. *Nat. Mater.* **2018**, *17*, 283–289. https://doi.org/10.1038/s41563-017-0013-1.

(112) Adatoz, E.; Avci, A. K.; Keskin, S. Opportunities and Challenges of MOF-Based Membranes in Gas Separations. *Sep. Purif. Technol.* **2015**, *152*, 207–237. https://doi.org/10.1016/j.seppur.2015.08.020.

(113) Li, X.; Li, J.; Yang, B. Design and Control of the Cryogenic Distillation Process for Purification of Synthetic Natural Gas from Methanation of Coke Oven Gas. *Ind. Eng. Chem. Res.* **2014**, *53* (50), 19583–19593. https://doi.org/10.1021/ie5024063.

(114) Baker, R. W. Future Directions of Membrane Gas Separation Technology. *Ind. Eng. Chem. Res.* **2002**, *41*, 1393–1411. https://doi.org/10.1021/ie0108088.

(115) Sholl, D. S.; Lively, R. P. Seven Chemical Separations to Change the World. *Nature* **2016**, *532*, 435–437. https://doi.org/10.1038/532435a.

(116) Horike, S.; Shimomura, S.; Kitagawa, S. Soft Porous Crystals. *Nat. Chem.* **2009**, *1*, 695–704. https://doi.org/10.1038/nchem.444.

(117) Healy, C.; Patil, K. M.; Wilson, B. H.; Hermanspahn, L.; Harvey-Reid, N. C.; Howard, B. I.; Kleinjan, C.; Kolien, J.; Payet, F.; Telfer, S. G.; Kruger, P. E.; Bennett, T. D. The Thermal Stability of Metal-Organic Frameworks. *Coord. Chem. Rev.* **2020**, *419*, 213388. https://doi.org/10.1016/j.ccr.2020.213388.

(118) House of Representatives Committee on Science and Technology. *Investigation of the Challenger Accident*; 1986.

(119) Morse Potential Curve https://courses.lumenlearning.com/boundless-chemistry/chapter/bond-energy-and-enthalpy/ (accessed Dec 17, 2020).

(120) Neimark, A. V.; Coudert, F.-X.; Triguero, C.; Boutin, A.; Fuchs, A. H.; Beurroies, I.; Denoyel, R. Structural Transitions in MIL-53

(Cr): View from Outside and Inside. *Langmuir* **2011**, *27*, 4734–4741. https://doi.org/10.1021/la200094x.

(121) Loiseau, T.; Serre, C.; Huguenard, C.; Fink, G.; Taulelle, F.; Henry, M.; Bataille, T.; Férey, G. A Rationale for the Large Breathing of the Porous Aluminum Terephthalate (MIL-53) Upon Hydration. *Chem. Eur. J.* **2004**, *10*, 1373–1382. https://doi.org/10.1002/chem.200305413.

(122) Ashling, C. W.; Johnstone, D. N.; Widmer, R. N.; Hou, J.; Collins, S. M.; Sapnik, A. F.; Bumstead, A. M.; Midgley, P. A.; Chater, P. A.; Keen, D. A.; Bennett, T. D. Synthesis and Properties of a Compositional Series of MIL-53(Al) Metal−Organic Framework Crystal-Glass Composites. *J. Am. Chem. Soc.* **2019**, *141*, 15641–15648. https://doi.org/10.1021/jacs.9b07557.

(123) Cliffe, M. J.; Hill, J. A.; Murray, C. A.; Coudert, F.-X.; Goodwin, A. L. Defect-Dependent Colossal Negative Thermal Expansion in UiO-66(Hf) Metal–Organic Framework. *Phys. Chem. Chem. Phys.* **2015**, *17*, 11586–11592. https://doi.org/10.1039/c5cp01307k.

(124) Goodwin, A. L.; Calleja, M.; Conterio, M. J.; Dove, M. T.; Evans, J. S. O.; Keen, D. A.; Peters, L.; Tucker, M. G. Colossal Positive and Negative Thermal Expansion in the Framework Material $Ag_3[Co(CN)_6]$. *Science* **2008**, *319*, 794–797. https://doi.org/10.1126/science.1151442.

(125) Krishnan, R. S.; Srinivasan, R.; Devanarayanan, S. *Thermal Expansion of Crystals*, First Edit.; Pergamon Press Ltd., 1979.

(126) Felkins, K.; Leighly, H. P.; Jankovic, A. The Royal Mail Ship *Titanic*: Did a Metallurgical Failure Cause a Night to Remember? *JOM* **1998**, *50*, 12–18. https://doi.org/10.1007/s11837-998-0062-7.

(127) Hu, Y.; Kazemian, H.; Rohani, S.; Huang, Y.; Song, Y. *In Situ* High Pressure Study of ZIF-8 by FTIR Spectroscopy. *Chem. Commun.* **2011**, *47*, 12694–12696. https://doi.org/10.1039/c1cc15525c.

(128) Li, W.; Probert, M. R.; Kosa, M.; Bennett, T. D.; Thirumurugan, A.; Burwood, R. P.; Parinello, M.; Howard, J. A. K.; Cheetham, A. K. Negative Linear Compressibility of a Metal–Organic Framework. *J. Am. Chem. Soc.* **2012**, *134*, 11940–11943. https://doi.org/10.1021/ja305196u.

(129) Stress-Strain Graph https://www.servicethread.com/blog/what-is-youngs-modulus (accessed Feb 17, 2021).

(130) Compressive and Tensile Loads https://nigerianscholars.com/tutorials/friction-drag-elasticity/changes-in-length-tension-and-compression-elastic-modulus/ (accessed Jun 4, 2021).

(131) Ortiz, A. U.; Boutin, A.; Fuchs, A. H.; Coudert, F.-X. Anisotropic Elastic Properties of Flexible Metal-Organic Frameworks: How Soft Are Soft Porous Crystals? *Phys. Rev. Lett.* **2012**, *109* (19), 195502. https://doi.org/10.1103/PhysRevLett.109.195502.

(132) Tan, J. C.; Cheetham, A. K. Mechanical Properties of Hybrid Inorganic–Organic Framework Materials: Establishing Fundamental Structure–Property Relationships. *Chem. Soc. Rev.* **2011**, *40*, 1059–1080. https://doi.org/10.1039/c0cs00163e.

(133) Moghadam, P. Z.; Rogge, S. M. J.; Li, A.; Chow, C.-M.; Wieme, J.; Moharrami, N.; Aragones-Anglada, M.; Conduit, G.; Gomez-Gualdron, D. A.; Van Speybroeck, V.; Fairen-Jimenez, D. Structure-Mechanical Stability Relations of Metal-Organic Frameworks *via* Machine Learning. *Matter* **2019**, *1*, 219–234. https://doi.org/10.1016/j.matt.2019.03.002.

(134) Batten, S. R.; Champness, N. R.; Chen, X.-M.; Garcia-Martinez, J.; Kitagawa, S.; Öhrström, L.; O'Keeffe, M.; Suh, M. P.; Reedijk, J. Terminology of Metal–Organic Frameworks and Coordination Polymers (IUPAC Recommendations 2013). *Pure Appl. Chem.* **2013**, *85* (8), 1715–1724. https://doi.org/10.1351/PAC-REC-12-11-20.

(135) Chapman, K. W.; Halder, G. J.; Chupas, P. J. Pressure-Induced Amorphization and Porosity Modification in a Metal-Organic Framework. *J. Am. Chem. Soc.* **2009**, *131*, 17546–17547. https://doi.org/10.1021/ja908415z.

(136) Hu, Y. H.; Zhang, L. Amorphization of Metal-Organic Framework MOF-5 at Unusually Low Applied Pressure. *Phys. Rev. B.* **2010**, *81*, 174103. https://doi.org/10.1103/PhysRevB.81.174103.

(137) Masciocchi, N.; Ardizzoia, G. A.; LaMonica, G.; Maspero, A.; Galli, S.; Sironi, A. Metal Imidazolato Complexes: Synthesis, Characterization, and X-Ray Powder Diffraction Studies of Group 10 Coordination Polymers. *Inorg. Chem.* **2001**, *40*, 6983–6989. https://doi.org/10.1021/ic010585d.

(138) Masciocchi, N.; Bruni, S.; Cariati, E.; Cariati, F.; Galli, S.; Sironi, A. Extended Polymorphism in Copper(II) Imidazolate Polymers: A Spectroscopic and XRPD Structural Study. *Inorg. Chem.* **2001**, *40*, 5897–5905. https://doi.org/10.1021/ic010384+.

(139) Martí-Rujas, J.; Islam, N.; Hashizume, D.; Izumi, F.; Fujita, M.; Kawano, M. Dramatic Structural Rearrangements in Porous Coordination Networks. *J. Am. Chem. Soc.* **2011**, *133*, 5853–5860. https://doi.org/10.1021/ja109160a.

(140) Widmer, R. N.; Lampronti, G. I.; Casati, N.; Farsang, S.; Bennett, T. D.; Redfern, S. A. T. X-Ray Radiation-Induced Amorphization of Metal–Organic Frameworks. *Phys. Chem. Chem. Phys.* **2019**, *21*, 12389–12395. https://doi.org/10.1039/c9cp01463b.

(141) Tuffnell, J. M.; Ashling, C. W.; Hou, J.; Li, S.; Longley, L.; Ríos Gómez, M. L.; Bennett, T. D. Novel Metal-Organic Framework Materials: Blends, Liquids, Glasses and Crystal-Glass Composites. *Chem. Commun.* **2019**, *55* (60), 8705–8715. https://doi.org/10.1039/c9cc01468c.

(142) Bazer-Bachi, D.; Assié, L.; Lecocq, V.; Harbuzaru, B.; Falk, V. Towards Industrial Use of Metal-Organic Framework: Impact of Shaping on the MOF Properties. *Powder Technol.* **2014**, *255*, 52–59. https://doi.org/10.1016/j.powtec.2013.09.013.

(143) Cao, S.; Bennett, T. D.; Keen, D. A.; Goodwin, A. L.; Cheetham, A. K. Amorphization of the Prototypical Zeolitic Imidazolate Framework ZIF-8 by Ball-Milling. *Chem. Commun.* **2012**, *48*, 7805–7807. https://doi.org/10.1039/c2cc33773h.

(144) Katsenis, A. D.; Puškarić, A.; Štrukil, V.; Mottillo, C.; Julien, P. A.; Užarević, K.; Pham, M.-H.; Do, T.-O.; Kimber, S. A. J.; Lazić, P.; Magdysyuk, O.; Dinnebier, R. E.; Halasz, I.; Friščić, T. *In Situ* X-Ray Diffraction Monitoring of a Mechanochemical Reaction Reveals a Unique Topology Metal-Organic Framework. *Nat. Commun.* **2015**, *6*, 6662. https://doi.org/10.1038/ncomms7662.

(145) Ostwald, W. Z. Studien Über Die Bildung Und Umwandlung Fester Körper. *Zeitschrift Fur Phys. Chemie* **1897**, *22*, 289–330. https://doi.org/10.1515/zpch-1897-2233.

(146) Burley, J. C.; Duer, M. J.; Stein, R. S.; Vrcelj, R. M. Enforcing Ostwald's Rule of Stages: Isolation of Paracetamol Forms III and II. *Eur. J. Pharm. Sci.* **2007**, *31*, 271–276. https://doi.org/10.1016/j.ejps.2007.04.002.

(147) Ortiz, A. U.; Boutin, A.; Fuchs, A. H.; Coudert, F.-X. Investigating the Pressure-Induced Amorphization of Zeolitic Imidazolate Framework ZIF-8: Mechanical Instability Due to Shear Mode Softening. *J. Phys. Chem. Lett.* **2013**, *4*, 1861–1865. https://doi.org/10.1021/jz400880p.

(148) Bennett, T. D.; Saines, P. J.; Keen, D. A.; Tan, J.-C.; Cheetham, A. K. Ball-Milling-Induced Amorphization of Zeolitic Imidazolate Frameworks (ZIFs) for the Irreversible Trapping of Iodine. *Chem. Eur. J.* **2013**, *19*, 7049–7055. https://doi.org/10.1002/chem.201300216.

(149) Bennett, T. D.; Keen, D. A.; Tan, J.-C.; Barney, E. R.; Goodwin, A. L.; Cheetham, A. K. Thermal Amorphization of Zeolitic Imidazolate Frameworks. *Angew. Chemie* **2011**, *123*, 3123–3127. https://doi.org/10.1002/ange.201007303.

(150) Ryder, M. R.; Bennett, T. D.; Kelley, C. S.; Frogley, M. D.; Cinque, G.; Tan, J.-C. Tracking Thermal-Induced Amorphization of a Zeolitic Imidazolate Framework *via* Synchrotron in Situ Far-Infrared Spectroscopy. *Chem. Commun*. **2017**, *53*, 7041–7044. https://doi.org/10.1039/C7CC01985H.

(151) Hughes, J. T.; Bennett, T. D.; Cheetham, A. K.; Navrotsky, A. Thermochemistry of Zeolitic Imidazolate Frameworks of Varying Porosity. *J. Am. Chem. Soc.* **2013**, *135*, 598–601. https://doi.org/10.1021/ja311237m.

(152) Haines, J.; Levelut, C.; Isambert, A.; Hébert, P.; Kohara, S.; Keen, D. A.; Hammouda, T.; Andrault, D. Topologically Ordered Amorphous Silica Obtained from the Collapsed Siliceous Zeolite, Silicalite-1-F: A Step toward "Perfect" Glasses. *J. Am. Chem. Soc.* **2009**, *131*, 12333–12338. https://doi.org/10.1021/ja904054v.

(153) Greaves, G. N.; Sen, S. Inorganic Glasses, Glass-Forming Liquids and Amorphizing Solids. *Adv. Phys.* **2007**, *56* (1), 1–166. https://doi.org/10.1080/00018730601147426.

(154) Greaves, G. N.; Meneau, F.; Kargl, F.; Ward, D.; Holliman, P.; Albergamo, F. Zeolite Collapse and Polyamorphism. *J. Phys.*

Condens. Matter **2007**, *19*, 415102. https://doi.org/10.1088/0953-8984/19/41/415102.

(155) Lindemann, F. A. The Calculation of Molecular Vibration Frequencies. *Phys. Z.* **1910**, *11*, 609–612.

(156) Chakravarty, C.; Debenedetti, P. G.; Stillinger, F. H. Lindemann Measures for the Solid-Liquid Phase Transition. *J. Chem. Phys.* **2007**, *126*, 204508. https://doi.org/10.1063/1.2737054.

(157) Liu, M.; McGillicuddy, R. D.; Vuong, H.; Tao, S.; Slavney, A. H.; Gonzalez, M. I.; Billinge, S. J. L.; Mason, J. A. Network-Forming Liquids from Metal−Bis(Acetamide) Frameworks with Low Melting Temperatures. *J. Am. Chem. Soc.* **2021**, *143*, 2801–2811. https://doi.org/10.1021/jacs.0c11718.

(158) Horike, S.; Umeyama, D.; Inukai, M.; Itakura, T.; Kitagawa, S. Coordination-Network-Based Ionic Plastic Crystal for Anhydrous Proton Conductivity. *J. Am. Chem. Soc.* **2012**, *134*, 7612–7615. https://doi.org/10.1021/ja301875x.

(159) Umeyama, D.; Horike, S.; Inukai, M.; Itakura, T.; Kitagawa, S. Reversible Solid-to-Liquid Phase Transition of Coordination Polymer Crystals. *J. Am. Chem. Soc.* **2015**, *137*, 864–870. https://doi.org/10.1021/ja511019u.

(160) Spielberg, E. T.; Edengeiser, E.; Mallick, B.; Havenith, M.; Mudring, A.-V. (1-Butyl-4-Methyl-Pyridinium)[$Cu(SCN)_2$]: A Coordination Polymer and Ionic Liquid. *Chem. Eur. J.* **2014**, *20*, 5338–5345. https://doi.org/10.1002/chem.201302777.

(161) Nagarkar, S. S.; Kurasho, H.; Duong, N. T.; Nishiyama, Y.; Kitagawa, S.; Horike, S. Crystal Melting and Glass Formation in Copper Thiocyanate Based Coordination Polymers. *Chem. Commun.* **2019**, *55*, 5455–5458. https://doi.org/10.1039/c9cc02172h.

(162) Das, C.; Ogawa, T.; Horike, S. Stable Melt Formation of 2D Nitrile-Based Coordination Polymer and Hierarchical Crystal–Glass Structuring. *Chem. Commun.* **2020**, *56*, 8980–8983. https://doi.org/10.1039/d0cc03691a.

(163) Shaw, B. K.; Hughes, A. R.; Ducamp, M.; Moss, S.; Debnath, A.; Sapnik, A. F.; Thorne, M. F.; McHugh, L. N.; Pugliese, A.; Keeble, D. S.; Chater, P.; Bermudez-Garcia, J. M.; Moya, X.; Saha, S. K.; Keen, D. A.; Coudert, F.-X.; Blanc, F.; Bennett, T. D. Melting of Hybrid Organic–Inorganic Perovskites. *Nat. Chem.* **2021**, *13*, 778–785. https://doi.org/10.1038/s41557-021-00681-7.

(164) Castillo-Blas, C.; Moreno, J. M.; Romero-Muñiz, I.; Platero-Prats, A. E. Applications of Pair Distribution Function Analyses to the Emerging Field of *Non-Ideal* Metal–Organic Framework Materials. *Nanoscale* **2020**, *12*, 15577–15587. https://doi.org/10.1039/d0nr01673j.

(165) Bennett, T. D.; Todorova, T. K.; Baxter, E. F.; Reid, D. G.; Gervais, C.; Bueken, B.; Van de Voorde, B.; De Vos, D.; Keen, D. A.; Mellot-Draznieks, C. Connecting Defects and Amorphization in UiO-66 and MIL-140 Metal–Organic Frameworks: A Combined Experimental and Computational Study. *Phys. Chem. Chem. Phys.* **2016**, *18*, 2192–2201. https://doi.org/10.1039/c5cp06798g.

(166) Chapman, K. W.; Chupas, P. J.; Kepert, C. J. Selective Recovery of Dynamic Guest Structure in a Nanoporous Prussian Blue through *in Situ* X-Ray Diffraction: A Differential Pair Distribution Function Analysis. *J. Am. Chem. Soc.* **2005**, *127*, 11232–11233. https://doi.org/10.1021/ja053266k.

(167) Ali, M. A.; Liu, X.; Li, Y.; Ren, J.; Qiu, J. Nonlinear-Optical Response in Zeolitic Imidazolate Framework Glass. *Inorg. Chem.* **2020**, *59*, 8380–8386. https://doi.org/10.1021/acs.inorgchem.0c00806.

(168) Ali, M. A.; Ren, J.; Zhao, T.; Liu, X.; Hua, Y.; Yue, Y.; Qiu, J. Broad Mid-Infrared Luminescence in a Metal−Organic Framework Glass. *ACS Omega* **2019**, *4*, 12081–12087. https://doi.org/10.1021/acsomega.9b01559.

(169) To, T.; Sørensen, S. S.; Stepniewska, M.; Qiao, A.; Jensen, L. R.; Bauchy, M.; Yue, Y.; Smedskjaer, M. M. Fracture Toughness of a Metal–Organic Framework Glass. *Nat. Commun.* **2020**, *11*, 2593. https://doi.org/10.1038/s41467-020-16382-7.

(170) Longley, L.; Collins, S. M.; Zhou, C.; Smales, G. J.; Norman, S. E.; Brownbill, N. J.; Ashling, C. W.; Chater, P. A.; Tovey, R.; Schönlieb, C.-B.; Headen, T. F.; Terrill, N. J.; Yue, Y.; Smith, A. J.; Blanc, F.; Keen, D. A.; Midgley, P. A.; Bennett, T. D. Liquid Phase Blending of Metal-Organic Frameworks. *Nat. Commun.* **2018**, *9*, 2135. https://doi.org/10.1038/s41467-018-04553-6.

(171) Longley, L.; Calahoo, C.; Limbach, R.; Xia, Y.; Tuffnell, J. M.; Sapnik, A. F.; Thorne, M. F.; Keeble, D. S.; Keen, D. A.; Wondraczek, L.; Bennett, T. D. Metal-Organic Framework and Inorganic Glass Composites. *Nat. Commun.* **2020**, *11*, 5800. https://doi.org/10.1038/s41467-020-19598-9.

(172) Kermouche, G.; Loubet, J. L.; Bergheau, J. M. Extraction of Stress–Strain Curves of Elastic–Viscoplastic Solids Using Conical/Pyramidal Indentation Testing with Application to Polymers. *Mech. Mater.* **2008**, *40*, 271–283. https://doi.org/10.1016/j.mechmat.2007.08.003.

(173) Tian, T.; Zeng, Z.; Vulpe, D.; Casco, M. E.; Divitini, G.; Midgley, P. A.; Silvestre-Albero, J.; Tan, J.-C.; Moghadam, P. Z.; Fairen-Jimenez, D. A Sol–Gel Monolithic Metal–Organic Framework with Enhanced Methane Uptake. *Nat. Mater.* **2018**, *17*, 174–179. https://doi.org/10.1038/NMAT5050.

(174) Furukawa, S.; Reboul, J.; Diring, S.; Sumida, K.; Kitagawa, S. Structuring of Metal–Organic Frameworks at the Mesoscopic/Macroscopic Scale. *Chem. Soc. Rev.* **2014**, *43*, 5700–5734. https://doi.org/10.1039/C4CS00106K.

(175) Rubio-Martinez, M.; Avci-Camur, C.; Thornton, A. W.; Imaz, I.; Maspoch, D.; Hill, M. R. New Synthetic Routes towards MOF Production at Scale. *Chem. Soc. Rev.* **2017**, *46*, 3453–3480. https://doi.org/10.1039/c7cs00109f.

(176) Widmer, R. N.; Lampronti, G. I.; Kunz, B.; Battaglia, C.; Shepherd, J. H.; Redfern, S. A. T.; Bennett, T. D. Manufacturing Macroporous Monoliths of Microporous Metal–Organic Frameworks. *ACS Appl. Nano Mater.* **2018**, *1*, 497–500. https://doi.org/10.1021/acsanm.7b00335.

(177) Connolly, B. M.; Madden, D. G.; Wheatley, A. E. H.; Fairen-Jimenez, D. Shaping the Future of Fuel: Monolithic Metal−Organic Frameworks for High-Density Gas Storage. *J. Am. Chem. Soc.* **2020**, *142*, 8541–8549. https://doi.org/10.1021/jacs.0c00270.

(178) Yang, H.-C.; Hou, J.; Xu, Z.-K. Surface and Interface Engineering for Organic– Inorganic Composite Membranes. *J. Mater. Chem. A* **2016**, *4*, 9716–9729. https://doi.org/10.1039/c6ta02844f.

(179) Denny Jr., M. S.; Moreton, J. C.; Benz, L.; Cohen, S. M. Metal–Organic Frameworks for Membrane-Based Separations. *Nat. Rev. Mater.* **2016**, *1*, 16078. https://doi.org/10.1038/natrevmats.2016.78.

(180) Seoane, B.; Coronas, J.; Gascon, I.; Benavides, Miren Etxeberria Karvan, O.; Caro, J.; Freek, K.; Gascon, J. Metal–Organic Framework Based Mixed Matrix Membranes: A Solution for Highly Efficient CO_2 Capture? *Chem. Soc. Rev.* **2015**, *44*, 2421–2454. https://doi.org/10.1039/c4cs00437j.

(181) Samino, R.; Moreton, J. C.; Ramsahye, N. A.; Cohen, S. M.; Maurin, G. Understanding the Origins of Metal–Organic Framework/Polymer Compatibility. *Chem. Sci.* **2018**, *9*, 315–324. https://doi.org/10.1039/c7sc04152g.

(182) Sutrisna, P. D.; Hou, J.; Zulkifli, M. Y.; Li, H.; Zhang, Y.; Liang, W.; D'Alessandro, D. M.; Chen, V. Surface Functionalized UiO-66/Pebax-Based Ultrathin Composite Hollow Fiber Gas Separation Membranes. *J. Mater. Chem. A* **2018**, *6*, 918–931. https://doi.org/10.1039/c7ta07512j.

(183) Tominaka, S.; Hamoudi, H.; Suga, T.; Bennett, T. D.; Cairns, A. B.; Cheetham, A. K. Topochemical Conversion of a Dense Metal–Organic Framework from a Crystalline Insulator to an Amorphous Semiconductor. *Chem. Sci.* **2015**, *6*, 1465–1473. https://doi.org/10.1039/c4sc03295k.

(184) Wang, Y.; Jin, H.; Ma, Q.; Mo, K.; Mao, H.; Feldhoff, A.; Cao, X.; Li, Y.; Pan, F.; Jiang, Z. A MOF Glass Membrane for Gas Separation. *Angew. Chemie - Int. Ed.* **2020**, *59*, 4365–4369. https://doi.org/10.1002/anie.201915807.

(185) Bragg, W. H.; Bragg, W. L. The Reflection of X-Rays by Crystals. *R. Soc.* **1913**, *88* (605), 428–438. https://doi.org/https://doi.org/10.1098/rspa.1913.0040.

(186) Epp, J. X-Ray Diffraction (XRD) Techniques for Materials Characterization. In *Materials Characterization Using Nondestructive Evaluation (NDE) Methods*; Hübschen, G., Altpeter, I., Tschuncky, R., Herrmann, H.-G., Eds.; Woodhead Publishing, 2016; pp 81–124. https://doi.org/10.1016/B978-0-08-100040-3.00004-3.

(187) Patterson, A. L. The Scherrer Formula for X-Ray Particle Size Determination. *Phys. Rev.* **1939**, *56*, 978–982.

https://doi.org/10.1103/PhysRev.56.978.

(188) Coelho, A. *"Topas Academia v6" Coelho Software, Brisbane, Australia*; 2007.

(189) Coelho, A. A. TOPAS and TOPAS-Academic: An Optimization Program Integrating Computer Algebra and Crystallographic Objects Written in C++. *J. Appl. Crystallogr.* **2018**, *51*, 210–218. https://doi.org/10.1107/S1600576718000183.

(190) Yim, W. M.; Paff, R. J. Thermal Expansion of AlN, Sapphire, and Silicon. *J. Appl. Phys.* **1974**, *45*, 1456–1457. https://doi.org/10.1063/1.1663432.

(191) Volkringer, C.; Loiseau, T.; Guillou, N.; Férey, G.; Haouas, M.; Taulelle, F.; Audebrand, N.; Margiolaki, I.; Popov, D.; Burghammer, M.; Riekel, C. Structural Transitions and Flexibility during Dehydration−Rehydration Process in the MOF-Type Aluminum Pyromellitate $Al_2(OH)_2[C_{10}O_8H_2]$ (MIL-118). *Cryst. Growth Des.* **2009**, *9* (6), 2927–2936. https://doi.org/10.1021/cg900276g.

(192) Banerjee, D.; Kim, S. J.; Parise, J. B. Lithium Based Metal−Organic Framework with Exceptional Stability. *Cryst. Growth Des.* **2009**, *9* (5), 2500–2503. https://doi.org/10.1021/cg8014157.

(193) Billinge, S. J. L. Nanoscale Structural Order from the Atomic Pair Distribution Function (PDF): There's Plenty of Room in the Middle. *J. Solid State Chem.* **2008**, *181*, 1695–1700. https://doi.org/10.1016/j.jssc.2008.06.046.

(194) Egami, T.; Billinge, S. J. L. *Underneath the Bragg Peaks: Structural Analysis of Complex Materials*; Pergamon, Amsterdam: London, 2003.

(195) Petkov, V.; Billinge, S. J. L.; Shastri, S. D.; Himmel, B. Polyhedral Units and Network Connectivity in Calcium Aluminosilicate Glasses from High-Energy X-Ray Diffraction. *Phys. Rev. Lett.* **2000**, *85* (16), 3436–3439. https://doi.org/10.1103/PhysRevLett.85.3436.

(196) Hibble, S. J.; Fawcett, I. D.; Hannon, A. C. The True Structure and Metal-Metal-Bonded Framework of $LiMo^{III}O_2$ Determined from Total Neutron Scattering. *Inorg. Chem.* **1997**, *36* (9), 1749–1753. https://doi.org/10.1021/ic961325c.

(197) Soper, A. K.; Barney, E. R. Extracting the Pair Distribution Function from White-Beam X-Ray Total Scattering Data. *J. Appl. Crystallogr.* **2011**, *44*, 714–726. https://doi.org/10.1107/s0021889811021455.

(198) Experimental Setup at Diamond Light Source, U.K., I15-1 https://www.diamond.ac.uk/Instruments/Crystallography/I15-1.html (accessed Apr 16, 2021).

(199) Billinge, S. J. L. The Rise of the X-Ray Atomic Pair Distribution Function Method: A Series of Fortunate Events. *Phil. Trans. R. Soc. A* **2019**, *377*, 20180413. https://doi.org/10.1098/rsta.018.0413.

(200) Farrow, C. L.; Juhas, P.; Liu, J. W.; Bryndin, D.; Božin, E. S.; Bloch, J.; Proffen, T.; Billinge, S. J. L. PDFfit2 and PDFgui: Computer Programs for Studying Nanostructure in Crystals. *J. Phys. Condens. Matter* **2007**, *19*, 335219. https://doi.org/10.1088/0953-8984/19/33/335219.

(201) Soper, A. K. *GudrunN and GudrunX : Programs for Correcting Raw Neutron and X-Ray Diffraction Data to Differential Scattering Cross Section*; 2011.

(202) Khelifa, M.; Fierro, V.; Macutkevic, J.; Celzard, A. Nanoindentation of Flexible Graphite: Experimental versus Simulation Studies. *Adv. Mater. Sci.* **2018**, *3* (2), 1–11. https://doi.org/10.15761/ams.1000142.

(203) Oliver, W. C.; Pharr, G. M. Measurement of Hardness and Elastic Modulus by Instrumented Indentation: Advances in Understanding and Refinements to Methodology. *J. Mater. Res.* **2004**, *19* (1), 3–20. https://doi.org/10.1557/jmr.2004.19.1.3.

(204) Sneddon, I. N. The Relation between Load and Penetration in the Axisymmetric Boussinesq Problem for a Punch of Arbitrary Profile. *Int. J. Eng. Sci.* **1965**, *3*, 47–57. https://doi.org/10.1016/0020-7225(65)90019-4.

(205) Pharr, G. M.; Bolshakov, A. Understanding Nanoindentation Unloading Curves. *J. Mater. Res.* **2002**, *17* (10), 2660–2671. https://doi.org/10.1557/JMR.2002.0386.

(206) Hay, J. C.; Bolshakov, A.; Pharr, G. M. A Critical Examination of the Fundamental Relations Used in the Analysis of Nanoindentation Data. *J. Mater. Res.* **1999**, *14* (6), 2296–2305. https://doi.org/10.1016/j.matlet.2008.01.105.

(207) Abraham, R. J.; Fisher, J.; Loftus, P. *Introduction to NMR Spectroscopy*; Wiley, 1992.

(208) Alia, A.; Ganapathy, S.; de Groot, H. J. M. Magic Angle Spinning (MAS) NMR: A New Tool to Study the Spatial and Electronic Structure of Photosynthetic Complexes. *Photosynth. Res.* **2009**, *102*, 415–425. https://doi.org/10.1007/s11120-009-9478-3.

(209) Schledorn, M.; Malär, A. A.; Torosyan, A.; Penzel, S.; Klose, D.; Oss, A.; Org, M.-L.; Wang, S.; Lecoq, L.; Cadalbert, R.; Samoson, A.; Böckmann, A.; Meier, B. H. Protein NMR Spectroscopy at 150 KHz Magic-Angle Spinning Continues To Improve Resolution and Mass Sensitivity. *ChemBioChem* **2020**, *21*, 2540–2548. https://doi.org/10.1002/cbic.202000341.

(210) Scholz, I.; Hodgkinson, P.; Meier, B. H.; Ernst, M. Understanding Two-Pulse Phase-Modulated Decoupling in Solid-State NMR. *J. Chem. Phys.* **2009**, *130*, 114510. https://doi.org/10.1063/1.3086936.

(211) Bennett, A. E.; Rienstra, C. M.; Auger, M.; Lakshmi, K. V.; Griffin, R. G. Heteronuclear Decoupling in Rotating Solids. *J. Chem. Phys.* **1995**, *103* (16), 6951–6958. https://doi.org/10.1063/1.470372.

(212) Feike, M.; Demco, D. E.; Graf, R.; Gottwald, J.; Hafner, S.; Spiess, H. W. Broadband Multiple-Quantum NMR Spectroscopy. *J. Magn. Reson.* **1996**, *122* (2), 214–221. https://doi.org/10.1006/jmra.1996.0197.

(213) Krajnc, A.; Bueken, B.; De Vos, D.; Mali, G. Improved Resolution and Simplification of the Spin-Diffusion-Based NMR Method for the Structural Analysis of Mixed-Linker MOFs. *J. Magn. Reson.* **2017**, *279*, 22–28. https://doi.org/10.1016/j.jmr.2017.04.008.

(214) Chao, M.-Y.; Zhang, W.-H.; Lang, J.-P. Co_2 and Co_3 Mixed Cluster Secondary Building Unit Approach toward a Three-Dimensional Metal-Organic Framework with Permanent Porosity. *Molecules* **2018**, *23*, 755. https://doi.org/10.3390/molecules23040755.

(215) Lázaro, I. A. A Comprehensive Thermogravimetric Analysis Multifaceted Method for the Exact Determination of the Composition of Multifunctional Metal-Organic Framework Materials. *Eur. J. Inorg. Chem.* **2020**, 4284–4294. https://doi.org/10.1002/ejic.202000656.

(216) Gill, P.; Moghadam, T. T.; Ranjbar, B. Differential Scanning Calorimetry Techniques: Applications in Biology and Nanoscience. *J. Biomol Tech.* **2010**, *21*, 167–193.

(217) Zheng, Q.; Zhang, Y.; Montazerian, M.; Gulbiten, O.; Mauro, J. C.; Zanotto, E. D.; Yue, Y. Understanding Glass through Differential Scanning Calorimetry. *Chem. Rev.* **2019**, *119* (13), 7848–7939. https://doi.org/10.1021/acs.chemrev.8b00510.

(218) Example Thermogram https://faculty.uscupstate.edu/llever/Polymer Resources/DSC.htm (accessed Jun 4, 2021).

(219) Myers, A. L.; Prausnitz, J. M. Thermodynamics of Mixed-Gas Adsorption. *A. I. Ch. E.* **1965**, *11* (1), 121–127. https://doi.org/10.1002/aic.690110125.

(220) Nuhnen, A.; Janiak, C. A Practical Guide to Calculate the Isosteric Heat/Enthalpy of Adsorption *via* Adsorption Isotherms in Metal–Organic Frameworks, MOFs. *Dalt. Trans.* **2020**, *49*, 10295–10307. https://doi.org/10.1039/d0dt01784a.

(221) Brunauer, S. *The Adsorption of Gases and Vapors*; Oxford University Press, London, 1943.

(222) Sing, K. S. W.; Everett, D. H.; Haul, R. A. W.; Moscou, L.; Pierotti, R. A.; Rouquérol, J.; Siemieniewska, T. Reporting Physisorption Data For Gas/Solid Systems with Special Reference to the Determination of Surface Area and Porosity (Recommendations 1984). *Pure Appl. Chem.* **1985**, *57* (4), 603–619. https://doi.org/10.1351/pac198557040603.

(223) Gas Adsorption Isotherms https://gasadsorptiontech.wordpress.com/2016/01/08/adsorption-equilibrium/ (accessed May 15, 2021).

(224) Düren, T.; Millange, F.; Férey, G.; Walton, K. S.; Snurr, R. Q. Calculating Geometric Surface Areas as a Characterization Tool for Metal-Organic Frameworks. *J. Phys. Chem. C* **2007**, *111*, 15350–15356. https://doi.org/10.1021/jp074723h.

(225) Ambroz, F.; Macdonald, T. J.; Martis, V.; Parkin, I. P. Evaluation of the BET Theory for the Characterization of Meso and

Microporous MOFs. *Small Methods* **2018**, *2*, 1800173. https://doi.org/10.1002/smtd.201800173.

(226) Brunauer, S.; Emmett, P. H.; Teller, E. Adsorption of Gases in Multimolecular Layers. *J. Am. Chem. Soc.* **1938**, *60* (2), 309–319. https://doi.org/10.1021/ja01269a023.

(227) BET Particle Analysis http://particle.dk/methods-analytical-laboratory/surface-area-bet-2/ (accessed May 15, 2021).

(228) Webb, P. A.; Orr, C. *Analytical Methods in Fine Particle Technology*; Micromeritics Instrument Corp.: Norcross, Ga, 1997.

(229) Rouquerol, J.; Llewellyn, P.; Rouquerol, F. Is the Bet Equation Applicable to Microporous Adsorbents? In *Studies in Surface Science and Catalysis*; Llewellyn, P. L., Rodriquez-Reinoso, F., Rouqerol, J., Seaton, N., Eds.; 2007; pp 49–56. https://doi.org/10.1016/S0167-2991(07)80008-5.

(230) Haghighatju, F.; Rafsanjani, H. H.; Esmaeilzadeh, F. Estimation of the Dimension of Micropores and Mesopores in Single Walled Carbon Nanotubes Using the Method Horvath-Kawazoe, Saito and Foley and BJH Equations. *Micro Nano Lett.* **2017**, *12* (1), 1–5. https://doi.org/10.1049/mnl.2016.0306.

(231) Saito, A.; Foley, H. C. Curvature and Parametric Sensitivity in Models for Adsorption in Micropores. *AIChE J.* **1991**, *37* (3), 429–436. https://doi.org/10.1002/aic.690370312.

(232) Horváth, G.; Kawazoe, K. Method for the Calculation of Effective Pore Size Distribution in Molecular Sieve Carbon. *J. Chem. Eng. Japan* **1983**, *16* (6), 470–475. https://doi.org/10.1252/jcej.16.470.

(233) Vernon-Parry, K. D. Scanning Electron Microscopy: An Introduction. *III-Vs Rev.* **2000**, *13* (4), 40–44. https://doi.org/10.1016/S0961-1290(00)80006-X.

(234) Shah, F. A.; Ruscsák, K.; Palmquist, A. 50 Years of Scanning Electron Microscopy of Bone—a Comprehensive Overview of the Important Discoveries Made and Insights Gained into Bone Material Properties in Health, Disease, and Taphonomy. *Bone Res.* **2019**, *7*, 15. https://doi.org/10.1038/s41413-019-0053-z.

(235) Allen, L. J.; D'Alfonso, A. J.; Findlay, S. D.; LeBeau, J. M.; Lugg, N. R.; Stemmer, S. Elemental Mapping in Scanning Transmission Electron Microscopy. *J. Phys. Conf. Ser.* **2010**, *241*, 012061. https://doi.org/10.1088/1742-6596/241/1/012061.

(236) Eggeman, A. S. Scanning Transmission Electron Diffraction Methods. *Acta Cryst.* **2019**, *75*, 475–484. https://doi.org/10.1107/S2052520619006723.

(237) Williams, D. B.; Barry Carter, C. *Transmission Electron Microscopy - A Textbook for Materials Science*, Second Edi.; Springer US, 2009.

(238) Siegbahn, M. Relations between the *K* and *L* Series of the High-Frequency Spectra. *Nature* **1916**, *96*, 676. https://doi.org/10.1038/096676b0.

(239) Slater, T. J. A.; Janssen, A.; Camargo, P. H. C.; Burke, M. G.; Zaluzec, N. J.; Haigh, S. J. STEM-EDX Tomography of Bimetallic Nanoparticles: A Methodological Investigation. *Ultramicroscopy* **2016**, *162*, 61–73. https://doi.org/10.1016/j.ultramic.2015.10.007.

(240) Schematic of STEM Processing https://pyxem.github.io/pyxem-website/_images/sped_scheme.png (accessed May 11, 2021).

(241) Hydrogen Spectral Series https://en.wikipedia.org/wiki/Hydrogen_spectral_series#/media/File:Hydrogen_transitions.svg (accessed Jun 4, 2021).

(242) Egerton, R. F. Electron Energy-Loss Spectroscopy in the TEM. *Rep. Prog. Phys.* **2009**, *72*, 016502. https://doi.org/10.1088/0034-4885/72/1/016502.

(243) Nederlof, I.; van Genderen, E.; Li, Y.-W.; Abrahams, J. P. A Medipix Quantum Area Detector Allows Rotation Electron Diffraction Data Collection from Submicrometre Three-Dimensional Protein Crystals. *Acta Cryst.* **2013**, *69*, 1223–1230. https://doi.org/10.1107/S0907444913009700.

(244) Mir, J. A.; Clough, R.; MacInnes, R.; Gough, C.; Plackett, R.; Shipsey, I.; Sawada, H.; MacLaren, I.; Ballabriga, R.; Maneuski, D.;

O'Shea, V.; McGrouther, D.; Kirkland, A. I. Characterisation of the Medipix3 Detector for 60 and 80 KeV Electrons. *Ultramicroscopy* **2017**, *182*, 44–53. https://doi.org/10.1016/j.ultramic.2017.06.010.

(245) Peña, F. D. L. et al. Hyperspy: HyperSpy 1.0.1. 2016.

(246) Bredies, K.; Kunisch, K.; Pock, T. Total Generalized Variation. *SIAM J. Imaging Sci.* **2010**, *3* (3), 492–526. https://doi.org/10.1137/090769521.

(247) van Aarle, W.; Palenstijn, W. J.; De Beenhouwer, J.; Altantzis, T.; Bals, S.; Batenburg, K. J.; Sijbers, J. The ASTRA Toolbox: A Platform for Advanced Algorithm Development in Electron Tomography. *Ultramicroscopy* **2015**, *157*, 35–47. https://doi.org/10.1016/j.ultramic.2015.05.002.

(248) Chambolle, A.; Pock, T. A First-Order Primal-Dual Algorithm for Convex Problems with Applications to Imaging. *J. Math. Imaging Vis.* **2011**, *40*, 120–145. https://doi.org/10.1007/s10851-010-0251-1.

(249) Lever, T.; Haines, P.; Rouquerol, J.; Charsley, E. L.; Van Eckeren, P.; Burlett, D. J. ICTAC Nomenclature of Thermal Analysis (IUPAC Recommendations 2014). *Pure Appl. Chem.* **2014**, *86* (4), 545–553. https://doi.org/10.1515/pac-2012-0609.

(250) James, J. Chapter 7: Thermomechanical Analysis and Its Applications. In *Thermal and Rheological Measurement Techniques for Nanomaterials Characterization*; Elsevier, 2017; pp 159–172.

(251) Hou, J.; Ashling, C. W.; Collins, S. M.; Krajnc, A.; Zhou, C.; Longley, L.; Johnstone, D. N.; Chater, P. A.; Li, S.; Coulet, M.-V.; Llewellyn, P. L.; Coudert, F.-X.; Keen, D. A.; Midgley, P. A.; Mali, G.; Chen, V.; Bennett, T. D. Metal-Organic Framework Crystal-Glass Composites. *Nat. Commun.* **2019**, *10*, 2580. https://doi.org/10.1038/s41467-019-10470-z.

(252) Umeyama, D.; Funnell, N. P.; Cliffe, M. J.; Hill, J. A.; Goodwin, A. L.; Hijikata, Y.; Itakura, T.; Okubo, T.; Horike, S.; Kitagawa, S. Glass Formation *via* Structural Fragmentation of a 2D Coordination Network. *Chem. Commun.* **2015**, *51*, 12728–12731. https://doi.org/10.1039/c5cc04626b.

(253) Chen, W.; Horike, S.; Umeyama, D.; Ogiwara, N.; Itakura, T.; Tassel, C.; Goto, Y.; Kageyama, H.; Kitagawa, S. Glass Formation of a Coordination Polymer Crystal for Enhanced Proton Conductivity and Material Flexibility. *Angew. Chemie - Int. Ed.* **2016**, *55*, 5195–5200. https://doi.org/10.1002/anie.201600123.

(254) Ohara, Y.; Hinokimoto, A.; Chen, W.; Kitao, T.; Nishiyama, Y.; Hong, Y.; Kitagawa, S.; Horike, S. Formation of Coordination Polymer Glass by Mechanical Milling: Dependence on Metal Ions and Molecular Doping for H^+ Conductivity. *Chem. Commun.* **2018**, *54*, 6859–6862. https://doi.org/10.1039/c8cc02399a.

(255) Su, Y.-J.; Cui, Y.-L.; Wang, Y.; Lin, R.-B.; Zhang, W.-X.; Zhang, J.-P.; Chen, X.-M. Copper(I) 2-Isopropylimidazolate: Supramolecular Isomerism, Isomerization, and Luminescent Properties. *Cryst. Growth Des.* **2015**, *15*, 1735–1739. https://doi.org/10.1021/cg501737j.

(256) Inukai, M.; Nishiyama, Y.; Honjo, K.; Das, C.; Kitagawa, S.; Horike, S. Glass-Phase Coordination Polymer Displaying Proton Conductivity and Guest-Accessible Porosity. *Chem. Commun.* **2019**, *55*, 8528–8531. https://doi.org/10.1039/c9cc02744k.

(257) Saidi, K.; Kamoun, S.; Ayedi, H. F.; Arous, M. Crystal Structure, NMR Study, Dielectric Relaxation and AC Conductivity of a New Compound $[Cd_3(SCN)_2Br_6(C_2H_9N_2)_2]_n$. *J. Phys. Chem. Solids* **2013**, *74*, 1560–1569. https://doi.org/10.1016/j.jpcs.2013.05.024.

(258) Longley, L.; Collins, S. M.; Li, S.; Smales, G. J.; Erucar, I.; Qiao, A.; Hou, J.; Doherty, C. M.; Thornton, A. W.; Hill, A. J.; Yu, X.; Terrill, N. J.; Smith, A. J.; Cohen, S. M.; Midgley, P. A.; Keen, D. A.; Telfer, S. G.; Bennett, T. D. Flux Melting of Metal–Organic Frameworks. *Chem. Sci.* **2019**, *10*, 3592–3601. https://doi.org/10.1039/c8sc04044c.

(259) Biswas, S.; Ahnfeldt, T.; Stock, N. New Functionalized Flexible Al-MIL-53-X (X= -Cl, -Br, $-CH_3$, $-NO_2$, $-(OH)_2$) Solids: Syntheses, Characterization, Sorption, and Breathing Behavior. *Inorg. Chem.* **2011**, *50*, 9518–9526. https://doi.org/10.1021/ic201219g.

(260) Nguyen, L. T. L.; Nguyen, C. V.; Dang, G. H.; Le, K. K. A.; Phan, N. T. S. Towards Applications of Metal–Organic Frameworks in Catalysis: Friedel–Crafts Acylation Reaction over IRMOF-8 as an Efficient Heterogeneous Catalyst. *J. Mol. Catal. A Chem.*

2011, *349*, 28–35. https://doi.org/10.1016/J.MOLCATA.2011.08.011.

(261) Seoane, B.; Sebastián, V.; Téllez, C.; Coronas, J. Crystallization in THF: The Possibility of One-Pot Synthesis of Mixed Matrix Membranes Containing MOF MIL-68(Al). *CrystEngComm* **2013**, *15*, 9483–9490. https://doi.org/10.1039/c3ce40847g.

(262) Volkringer, C.; Loiseau, T.; Haouas, M.; Taulelle, F.; Popov, D.; Burghammer, M.; Riekel, C.; Zlotea, C.; Cuevas, F.; Latroche, M.; Phanon, D.; Knöfelv, C.; Llewellyn, P. L.; Férey, G. Occurrence of Uncommon Infinite Chains Consisting of Edge-Sharing Octahedra in a Porous Metal Organic Framework-Type Aluminum Pyromellitate $Al_4(OH)_8[C_{10}O_8H_2]$(MIL-120): Synthesis, Structure, and Gas Sorption Properties. *Chem. Mater.* **2009**, *21*, 5783–5791. https://doi.org/10.1021/cm9023106.

(263) Marshall, R. J.; Lennon, C. T.; Tao, A.; Senn, H. M.; Wilson, C.; Fairen-Jimenez, D.; Forgan, R. S. Controlling Interpenetration through Linker Conformation in the Modulated Synthesis of Sc Metal–Organic Frameworks. *J. Mater. Chem. A* **2018**, *6*, 1181–1187. https://doi.org/10.1039/c7ta09699b.

(264) Phan, N. T. S.; Le, K. K. A.; Phan, T. D. MOF-5 as an Efficient Heterogeneous Catalyst for Friedel–Crafts Alkylation Reactions. *Appl. Catal. A Gen.* **2010**, *382*, 246–253. https://doi.org/10.1016/j.apcata.2010.04.053.

(265) Yang, S.; Sun, J.; Ramirez-Cuesta, A. J.; Callear, S. K.; David, W. I. F.; Anderson, D. P.; Newby, R.; Blake, A. J.; Parker, J. E.; Tang, C. C.; Schröder, M. Selectivity and Direct Visualization of Carbon Dioxide and Sulfur Dioxide in a Decorated Porous Host. *Nat. Chem.* **2012**, *4*, 887–894. https://doi.org/10.1038/nchem.1457.

(266) Deria, P.; Bury, W.; Hupp, J. T.; Farha, O. K. Versatile Functionalization of the NU-1000 Platform by Solvent-Assisted Ligand Incorporation. *Chem. Commun.* **2014**, *50*, 1965–1968. https://doi.org/10.1039/c3cc48562e.

(267) Ikuno, T.; Zheng, J.; Vjunov, A.; Sanchez-Sanchez, M.; Ortuño, M. A.; Pahls, D. R.; Fulton, J. L.; Camaioni, D. M.; Li, Z.; Ray, D.; Mehdi, B. L.; Browning, N. D.; Farha, O. K.; Hupp, J. T.; Cramer, C. J.; Gagliardi, L.; Lercher, J. A. Methane Oxidation to Methanol Catalyzed by Cu-Oxo Clusters Stabilized in NU-1000 Metal−Organic Framework. *J. Am. Chem. Soc.* **2017**, *139*, 10294–10301. https://doi.org/10.1021/jacs.7b02936.

(268) Valenzano, L.; Civalleri, B.; Chavan, S.; Bordiga, S.; Nilsen, M. H.; Jakobsen, S.; Lillerud, K. P.; Lamberti, C. Disclosing the Complex Structure of UiO-66 Metal Organic Framework: A Synergic Combination of Experiment and Theory. *Chem. Mater.* **2011**, *23*, 1700–1718. https://doi.org/10.1021/cm1022882.

(269) Anjum, M. W.; Vermoortele, F.; Khan, A. L.; Bueken, B.; De Vos, D. E.; Vankelecom, I. F. J. Modulated UiO-66-Based Mixed-Matrix Membranes for CO_2 Separation. *ACS Appl. Mater. Interfaces* **2015**, *7*, 25193–25201. https://doi.org/10.1021/acsami.5b08964.

(270) Pan, Y.; Liu, Y.; Zeng, G.; Zhao, L.; Lai, Z. Rapid Synthesis of Zeolitic Imidazolate Framework-8 (ZIF-8) Nanocrystals in an Aqueous System. *Chem. Commun.* **2011**, *47*, 2071–2073. https://doi.org/10.1039/c0cc05002d.

(271) Wu, T.; Feng, X.; Elsaidi, S. K.; Thallapally, P. K.; Carreon, M. A. Zeolitic Imidazolate Framework-8 (ZIF-8) Membranes for Kr/Xe Separation. *Ind. Eng. Chem. Res.* **2017**, *56* (6), 1682–1686. https://doi.org/10.1021/acs.iecr.6b04868.

(272) Qian, X.; Yadian, B.; Wu, R.; Long, Y.; Zhou, K.; Zhu, B.; Huang, Y. Structure Stability of Metal-Organic Framework MIL-53 (Al) in Aqueous Solutions. *Int. J. Hydrogen Energy* **2013**, *38* (36), 16710–16715. https://doi.org/10.1016/j.ijhydene.2013.07.054.

(273) Bennett, T. D.; Sotelo, J.; Tan, J.-C.; Moggach, S. A. Mechanical Properties of Zeolitic Metal–Organic Frameworks: Mechanically Flexible Topologies and Stabilization against Structural Collapse. *CrystEngComm* **2015**, *17* (2), 286–289. https://doi.org/10.1039/c4ce02145b.

(274) Liu, Y.; Her, J.-H.; Dailly, A.; Ramirez-Cuesta, A. J.; Neumann, D. A.; Brown, C. M. Reversible Structural Transition in MIL-53 with Large Temperature Hysteresis. *J. Am. Chem. Soc.* **2008**, *130* (35), 11813–11818. https://doi.org/10.1021/ja803669w.

(275) Apen, E.; Hitchcock, A. P.; Gland, J. L. Experimental Studies of the Core Excitation of Imidazole, 4,5-Dicyanoimidazole, and s-Triazine. *J. Phys. Chem.* **1993**, *97* (26), 6859–6866. https://doi.org/10.1021/j100128a019.

(276) Urquhart, S. G.; Ade, H. Trends in the Carbonyl Core (C 1S, O 1S) $\rightarrow \pi^*_{c=o}$ Transition in the near-Edge X-Ray Absorption Fine

Structure Spectra of Organic Molecules. *J. Phys. Chem. B* **2002**, *106* (34), 8531–8538. https://doi.org/10.1021/jp0255379.

(277) Panova, O.; Chen, X. C.; Bustillo, K. C.; Ophus, C.; Bhatt, M. P.; Balsara, N.; Minor, A. M. Orientation Mapping of Semicrystalline Polymers Using Scanning Electron Nanobeam Diffraction. *Micron* **2016**, *88*, 30–36. https://doi.org/10.1016/j.micron.2016.05.008.

(278) Collins, D. J.; Zhou, H.-C. Hydrogen Storage in Metal–Organic Frameworks. *J. Mater. Chem.* **2007**, *17* (30), 3154–3160. https://doi.org/10.1039/b702858j.

(279) Kubo, M.; Shimojima, A.; Okubo, T. Effect of Lithium Doping into MIL-53(Al) through Thermal Decomposition of Anion Species on Hydrogen Adsorption. *J. Phys. Chem. C* **2012**, *116* (18), 10260–10265. https://doi.org/10.1021/jp211029y.

(280) Serre, C.; Bourrelly, S.; Vimont, A.; Ramsahye, N. A.; Maurin, G.; Llewellyn, P. L.; Daturi, M.; Filinchuk, Y.; Leynaud, O.; Barnes, P.; Férey, G. An Explanation for the Very Large Breathing Effect of a Metal–Organic Framework during CO_2 Adsorption. *Adv. Mater.* **2007**, *19* (17), 2246–2251. https://doi.org/10.1002/adma.200602645.

(281) Boutin, A.; Coudert, F.-X.; Springuel-Huet, M.-A.; Neimark, A. V.; Férey, G.; Fuchs, A. H. The Behavior of Flexible MIL-53(Al) upon CH_4 and CO_2 Adsorption. *J. Phys. Chem. C* **2010**, *114* (50), 22237–22244. https://doi.org/10.1021/jp108710h.

(282) Barrett, E. P.; Joyner, L. G.; Halenda, P. P. The Determination of Pore Volume and Area Distributions in Porous Substances. I. Computations from Nitrogen Isotherms. *J. Am. Chem. Soc.* **1951**, *73* (1), 373–380. https://doi.org/10.1021/ja01145a126.

(283) Thommes, M. Physical Adsorption Characterization of Nanoporous Materials. *Chemie-Ingenieur-Technik* **2010**, *82* (7), 1059–1073. https://doi.org/10.1002/cite.201000064.

(284) Adolf, C. R. R.; Ferlay, S.; Kyritsakas, N.; Hosseini, M. W. Welding Molecular Crystals. *J. Am. Chem. Soc.* **2015**, *137* (49), 15390–15393. https://doi.org/10.1021/jacs.5b10586.

(285) Kimata, H.; Mochida, T. Crystal Structures and Melting Behaviors of 2D and 3D Anionic Coordination Polymers Containing Organometallic Ionic Liquid Components. *Chem. – A Eur. J.* **2019**, *25* (43), 10111–10117. https://doi.org/10.1002/chem.201900979.

(286) Zhao, Y.; Lee, S.-Y.; Becknell, N.; Yaghi, O. M.; Angell, C. A. Nanoporous Transparent MOF Glasses with Accessible Internal Surface. *J. Am. Chem. Soc.* **2016**, *138* (34), 10818–10821. https://doi.org/10.1021/jacs.6b07078.

(287) Salazar, J. M.; Weber, G.; Simon, J. M.; Bezverkhyy, I.; Bellat, J. P. Characterization of Adsorbed Water in MIL-53(Al) by FTIR Spectroscopy and *Ab-Initio* Calculations. *J. Chem. Phys.* **2015**, *142*, 124702. https://doi.org/10.1063/1.4914903.

(288) Almeida Paz, F. A.; Klinowski, J. Hydrothermal Synthesis of a Novel Thermally Stable Three-Dimensional Ytterbium–Organic Framework. *Chem. Commun.* **2003**, *3* (13), 1484–1485. https://doi.org/10.1039/b302140h.

(289) Klein, N.; Senkovska, I.; Gedrich, K.; Stoeck, U.; Henschel, A.; Mueller, U.; Kaskel, S. A Mesoporous Metal-Organic Framework. *Angew. Chemie - Int. Ed.* **2009**, *48* (52), 9954–9957. https://doi.org/10.1002/anie.200904599.

(290) Klein, N.; Herzog, C.; Sabo, M.; Senkovska, I.; Getzschmann, J.; Paasch, S.; Lohe, M. R.; Brunner, E.; Kaskel, S. Monitoring Adsorption-Induced Switching by ^{129}Xe NMR Spectroscopy in a New Metal–Organic Framework $Ni_2(2,6\text{-ndc})_2(Dabco)$. *Phys. Chem. Chem. Phys.* **2010**, *12*, 11778–11784. https://doi.org/10.1039/c003835k.

(291) Bumstead, A. M.; Thorne, M. F.; Bennett, T. D. Identifying the Liquid and Glassy States of Coordination Polymers and Metal–Organic Frameworks. *Faraday Discuss.* **2021**, *225*, 210–225. https://doi.org/10.1039/d0fd00011f.

(292) Cabañero, J. M.; Pimenta, V.; Cannon, K. C.; Morris, R. E.; Armstrong, A. R. Sodium Naphthalene-2,6-Dicarboxylate: An Anode for Sodium Batteries. *ChemSusChem* **2019**, *12*, 4522–4528. https://doi.org/10.1002/cssc.201901626.

(293) Boutin, A.; Springuel-Huet, M.-A.; Nossov, A.; Gédéon, A.; Loiseau, T.; Volkringer, C.; Férey, G.; Coudert, F.-X.; Fuchs, A. H. Breathing Transitions in MIL-53(Al) Metal–Organic Framework Upon Xenon Adsorption. *Angew. Chemie - Int. Ed.* **2009**, *48*, 8314–8317. https://doi.org/10.1002/anie.200903153.

(294) Nanthamathee, C.; Ling, S.; Slater, B.; Attfield, M. P. Contradistinct Thermoresponsive Behavior of Isostructural MIL-53 Type

Metal−Organic Frameworks by Modifying the Framework Inorganic Anion. *Chem. Mater.* **2015**, *27*, 85–95. https://doi.org/10.1021/cm503311x.

(295) Li, S.; Yu, S.; Collins, S. M.; Johnstone, D. N.; Ashling, C. W.; Sapnik, A. F.; Chater, P. A.; Keeble, D. S.; McHugh, L. N.; Midgley, P. A.; Keen, D. A.; Bennett, T. D. A New Route to Porous Metal–Organic Framework Crystal–Glass Composites. *Chem. Sci.* **2020**, *11*, 9910–9918. https://doi.org/10.1039/d0sc04008h.

(296) Li, J.-R.; Kuppler, R. J.; Zhou, H.-C. Selective Gas Adsorption and Separation in Metal–Organic Frameworks. *Chem. Soc. Rev.* **2009**, *38*, 1477–1504. https://doi.org/10.1039/b802426j.

(297) Geddes, H. S.; Hutchinson, H. D.; Ha, A. R.; Funnell, N. P.; Goodwin, A. L. Extracting Interface Correlations from the Pair Distribution Function of Composite Materials. *ChemRxiv* **2021**.

(298) Billinge, S. J. L.; Dykhne, T.; Juhás, P.; Božin, E.; Taylor, R.; Florence, A. J.; Shankland, K. Characterisation of Amorphous and Nanocrystalline Molecular Materials by Total Scattering. *CrystEngComm* **2010**, *12*, 1366–1368. https://doi.org/10.1039/b915453a.

Appendix

8.4 Rietveld Refinements of X-ray Synchrotron Total Scattering Data

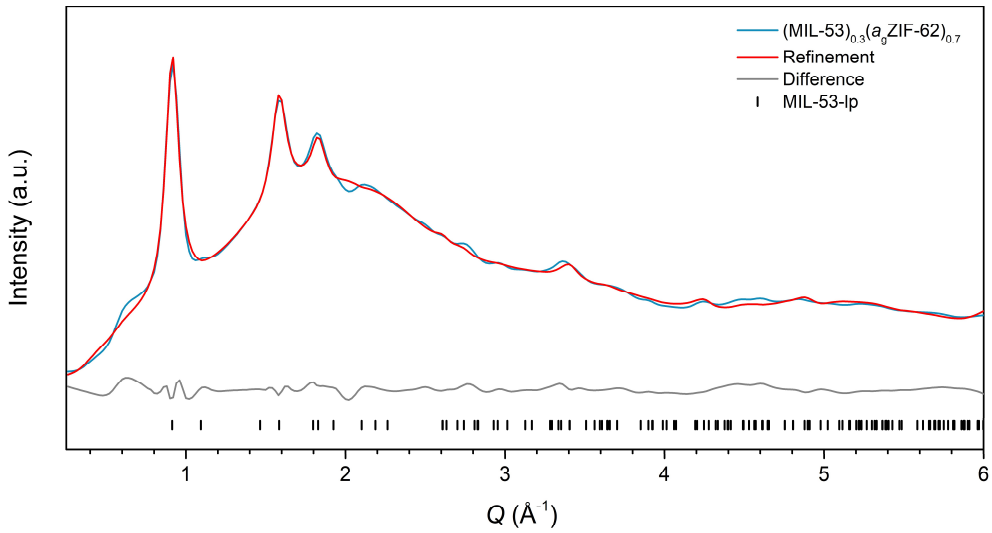

Figure A1: Rietveld refinement of (MIL-53)$_{0.3}$(a_gZIF-62)$_{0.7}$. *X-ray synchrotron total scattering data, Rietveld refinement, difference, and hkl tick marks for (MIL-53)$_{0.3}$(a_gZIF-62)$_{0.7}$.*

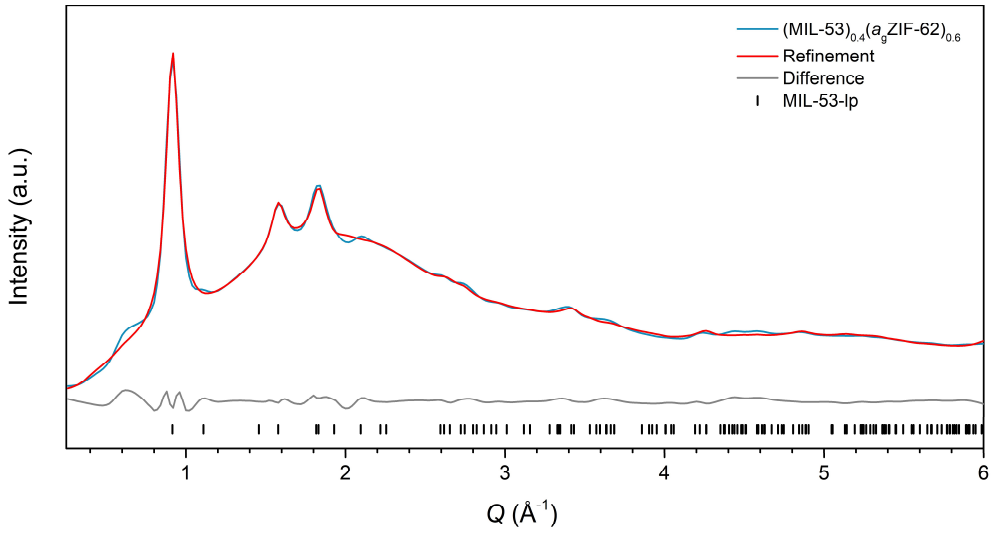

Figure A2: Rietveld refinement of (MIL-53)$_{0.4}$(a_gZIF-62)$_{0.6}$. *X-ray synchrotron total scattering data, Rietveld refinement, difference, and hkl tick marks for (MIL-53)$_{0.4}$(a_gZIF-62)$_{0.6}$.*

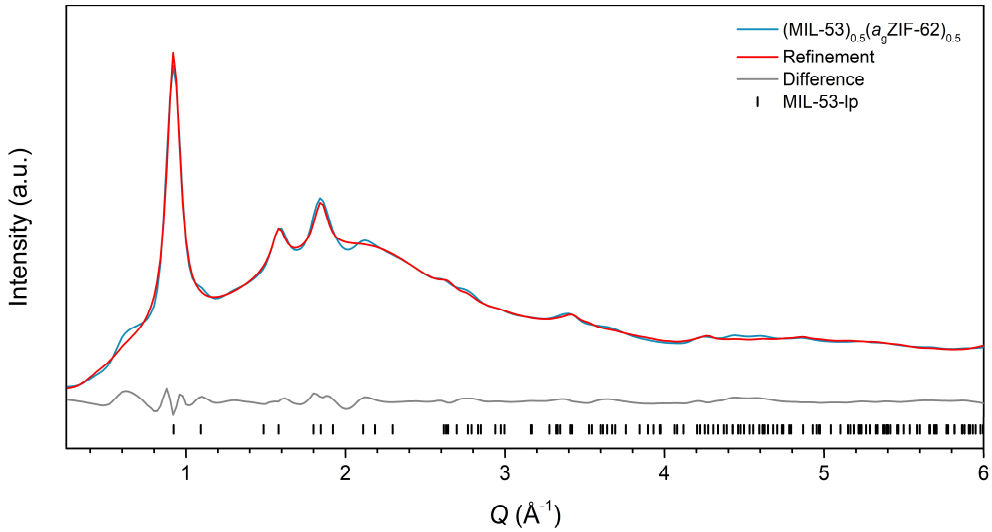

Figure A3: Rietveld refinement of $(MIL\text{-}53)_{0.5}(a_gZIF\text{-}62)_{0.5}$. *X-ray synchrotron total scattering data, Rietveld refinement, difference, and hkl tick marks for $(MIL\text{-}53)_{0.5}(a_gZIF\text{-}62)_{0.5}$.*

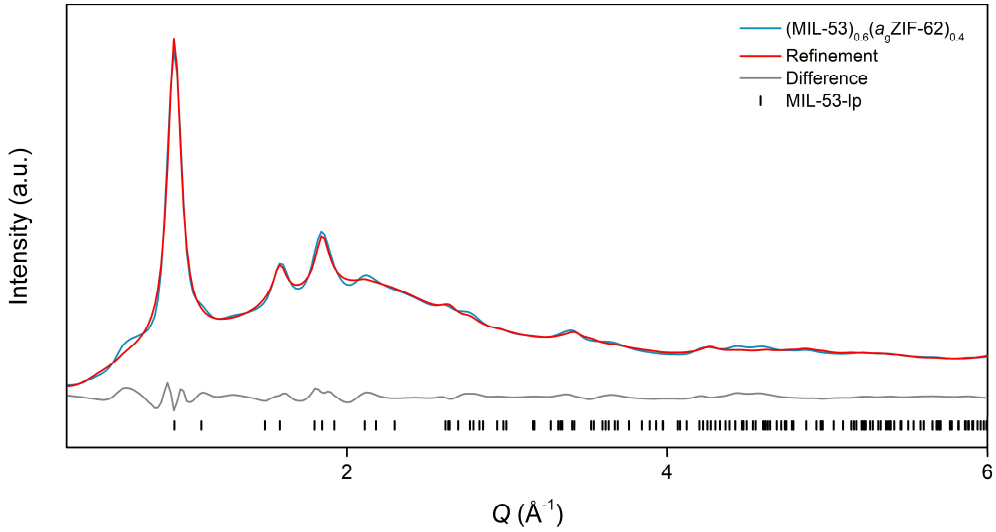

Figure A4: Rietveld refinement of $(MIL\text{-}53)_{0.6}(a_gZIF\text{-}62)_{0.4}$. *X-ray synchrotron total scattering data, Rietveld refinement, difference, and hkl tick marks for $(MIL\text{-}53)_{0.6}(a_gZIF\text{-}62)_{0.4}$.*

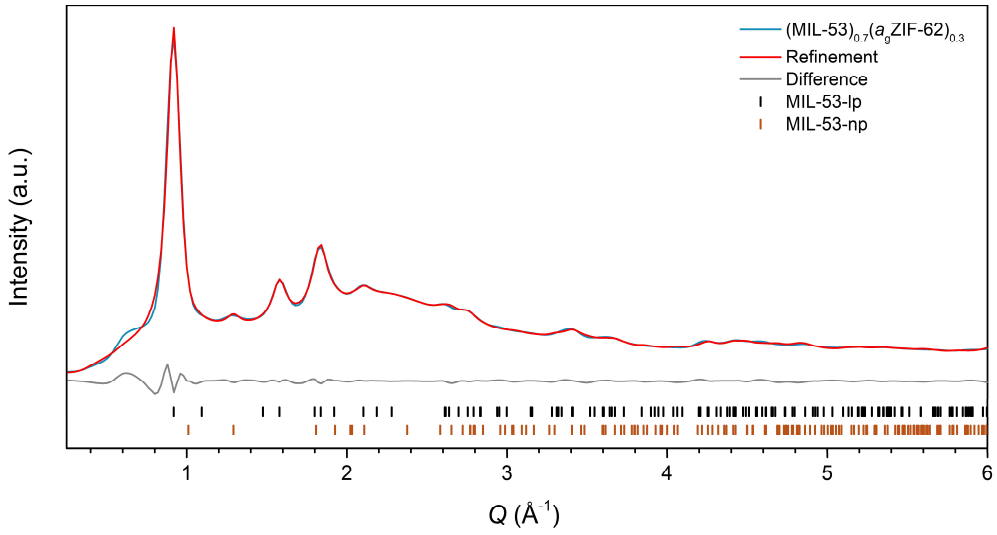

Figure A5: Rietveld refinement of $(MIL\text{-}53)_{0.7}(a_gZIF\text{-}62)_{0.3}$. *X-ray synchrotron total scattering data, Rietveld refinement, difference, and hkl tick marks for $(MIL\text{-}53)_{0.7}(a_gZIF\text{-}62)_{0.3}$.*

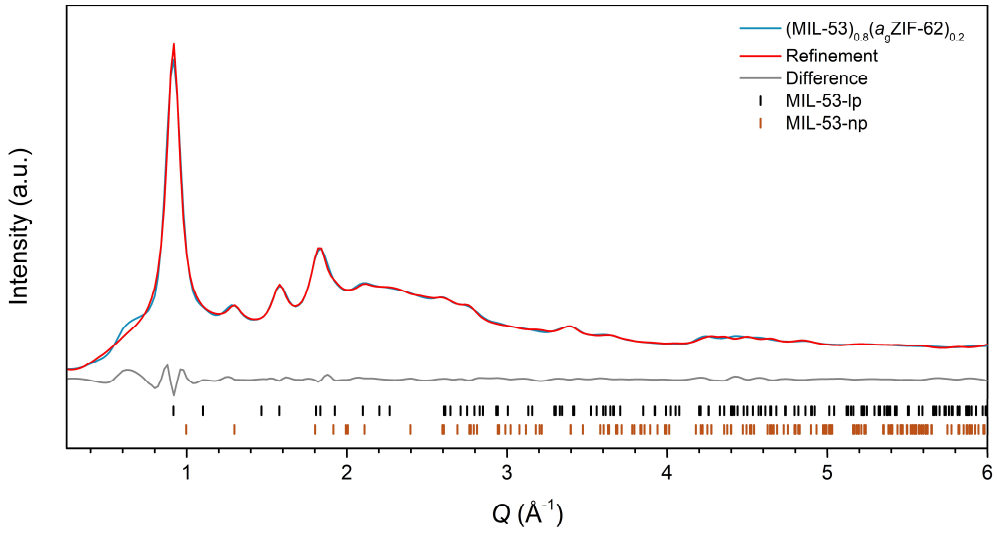

Figure A6: Rietveld refinement of $(MIL\text{-}53)_{0.8}(a_gZIF\text{-}62)_{0.2}$. *X-ray synchrotron total scattering data, Rietveld refinement, difference, and hkl tick marks for $(MIL\text{-}53)_{0.8}(a_gZIF\text{-}62)_{0.2}$.*

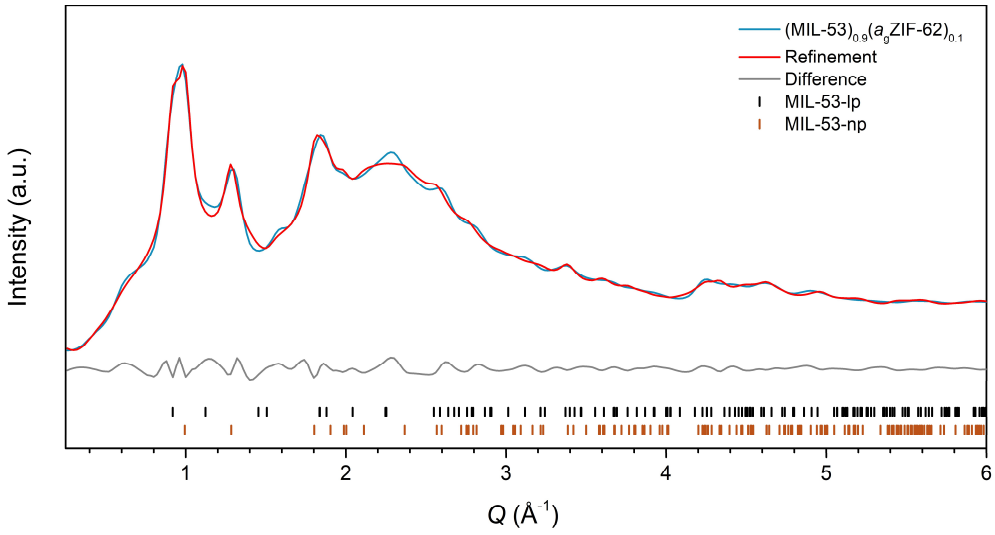

Figure A7: Rietveld refinement of $(MIL\text{-}53)_{0.9}(a_gZIF\text{-}62)_{0.1}$. *X-ray synchrotron total scattering data, Rietveld refinement, difference, and hkl tick marks for $(MIL\text{-}53)_{0.9}(a_gZIF\text{-}62)_{0.1}$.*

8.5 STEM-EDS Images of MIL-53 MOF CGCs

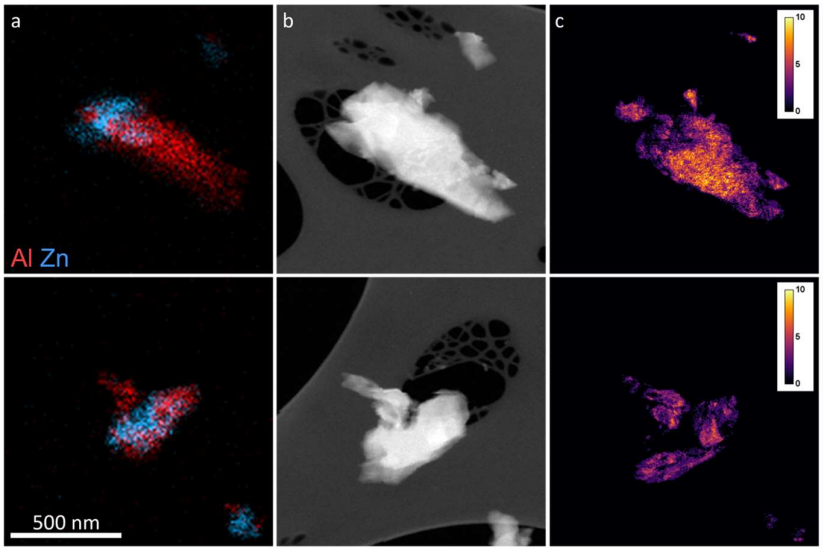

Figure A8: Scanning transmission electron microscopy of MOF CGC particles of $(MIL\text{-}53)_{0.7}(a_gZIF\text{-}62)_{0.3}$. *a. Compositional maps of Al (red) and Zn (blue) metal centres from STEM-EDS mapping. b. Annular dark-field images. c. Crystallinity maps. The scale is identical for all images.*

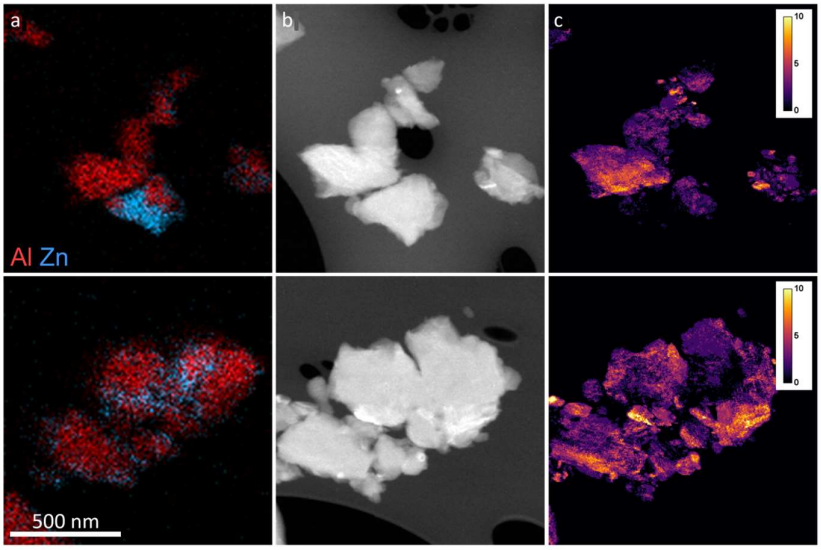

Figure A9: Scanning transmission electron microscopy of MOF CGC particles of (MIL-53)$_{0.9}$(a_gZIF-62)$_{0.1}$. *a. Compositional maps of Al (red) and Zn (blue) metal centres from STEM-EDS mapping. b. Annular dark-field images. c. Crystallinity maps. The scale is identical for all images.*

8.6 Comparison of MOF CGC Gas Sorption Isotherms

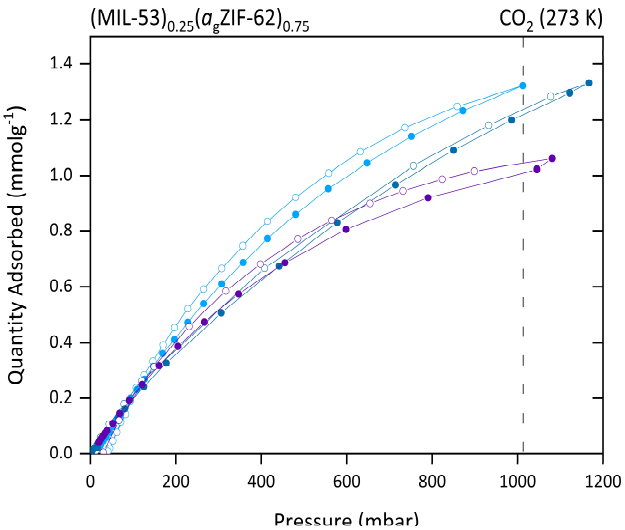

Figure A10: Testing the reproducibility of gas sorption isotherms of (MIL-53)$_{0.25}$(a_gZIF-62)$_{0.75}$. *Comparison of CO_2 isotherm experiments over three sample batches.*

8.7 VT-PXRD Rietveld Refinement Values

***Table A1**: Refinement values of the VT-PXRD of MIL-53-lp.*

T (°C)	rwp	χ^2	*a* (Å)	*a* st. dev.	*b* (Å)	*b* st. dev.	*c* (Å)	*c* st. dev.	Volume (Å^3)	Volume st. dev.
70	9.71	4.04	6.6494	0.0019	16.8596	0.0143	12.7927	0.0066	1434.15	1.48
90	10.07	4.11	6.6498	0.0019	16.8513	0.0150	12.7879	0.0069	1432.97	1.54
110	9.61	3.96	6.6485	0.0018	16.8548	0.0139	12.7840	0.0063	1432.55	1.43
130	9.46	3.90	6.6489	0.0017	16.8496	0.0130	12.7872	0.0060	1432.57	1.35
150	9.40	3.92	6.6490	0.0017	16.8386	0.0127	12.7952	0.0059	1432.54	1.32
170	9.38	3.86	6.6499	0.0016	16.8381	0.0126	12.7996	0.0059	1433.20	1.30
190	9.24	3.79	6.6510	0.0015	16.8337	0.0118	12.8065	0.0056	1433.84	1.23
210	9.28	3.78	6.6516	0.0016	16.8328	0.0122	12.8007	0.0058	1433.23	1.27
230	9.28	3.82	6.6524	0.0015	16.8406	0.0118	12.8015	0.0055	1434.16	1.23
250	8.97	3.69	6.6514	0.0015	16.8323	0.0112	12.8078	0.0053	1433.93	1.17
270	9.24	3.78	6.6519	0.0015	16.8450	0.0116	12.8014	0.0054	1434.41	1.20
290	9.14	3.81	6.6511	0.0014	16.8282	0.0110	12.8054	0.0052	1433.26	1.15
310	8.81	3.73	6.6512	0.0014	16.8295	0.0106	12.8055	0.0050	1433.38	1.10

***Table A2**: Refinement values of the VT-PXRD of $(MIL\text{-}53)_{0.25}(a_gZIF\text{-}62)_{0.75}$.*

T (°C)	rwp	χ^2	*a* (Å)	*a* st. dev.	*b* (Å)	*b* st. dev.	*c* (Å)	*c* st. dev.	Volume (Å^3)	Volume st. dev.
30	2.95	1.63	6.5848	0.0051	16.2963	0.0246	12.9001	0.0123	1384.29	2.70
50	2.91	1.60	6.6003	0.0046	16.4249	0.0264	12.7947	0.0128	1387.06	2.79
70	3.12	1.71	6.6236	0.0041	16.7346	0.0320	12.6471	0.0144	1401.85	3.24
90	2.98	1.63	6.6269	0.0046	16.8022	0.0270	12.5993	0.0113	1402.89	2.76
110	2.85	1.55	6.6281	0.0035	16.8297	0.0239	12.5649	0.0098	1401.60	2.39
130	3.02	1.65	6.6176	0.0043	16.8210	0.0262	12.5668	0.0110	1398.88	2.66
150	2.94	1.61	6.6212	0.0042	16.7489	0.0261	12.6057	0.0113	1397.93	2.67
170	3.16	1.74	6.6201	0.0041	16.8457	0.0342	12.5637	0.0137	1401.10	3.34
190	3.43	1.88	6.6183	0.0044	16.7338	0.0388	12.6074	0.0165	1396.27	3.83
210	2.98	1.66	6.6251	0.0035	16.8340	0.0254	12.5623	0.0104	1401.04	2.52
230	3.17	1.76	6.6193	0.0040	16.8359	0.0379	12.5660	0.0154	1400.38	3.69
250	3.05	1.68	6.6226	0.0034	16.8532	0.0323	12.5795	0.0134	1404.01	3.16
270	3.08	1.71	6.6192	0.0040	16.7919	0.0364	12.6243	0.0155	1403.18	3.60
290	3.21	1.78	6.6198	0.0037	16.8022	0.0332	12.6268	0.0143	1404.43	3.29
310	3.04	1.67	6.6160	0.0034	16.7874	0.0239	12.6114	0.0100	1400.68	2.39

***Table A3**: Refinement values of the VT-PXRD of MIL-118.*

T (°C)	rwp	χ^2	*a* (Å)	*a* st. dev.	*b* (Å)	*b* st. dev.	*c* (Å)	*c* st. dev.	Volume (Å^3)	Volume st. dev.
70	8.42	2.03	11.4201	0.0015	6.6282	0.0005	8.7238	0.0007	660.35	0.11
90	8.19	1.99	11.4128	0.0013	6.6248	0.0004	8.7258	0.0007	659.73	0.10
110	8.37	2.02	11.4220	0.0013	6.6221	0.0004	8.7210	0.0007	659.63	0.10
130	8.24	2.00	11.4321	0.0012	6.6222	0.0004	8.7193	0.0006	660.10	0.09
150	8.39	2.02	11.4492	0.0011	6.6211	0.0004	8.7149	0.0006	660.65	0.09
170	8.38	2.02	11.4584	0.0011	6.6207	0.0004	8.7137	0.0006	661.05	0.09
190	8.30	1.99	11.4695	0.0011	6.6212	0.0004	8.7117	0.0006	661.59	0.09
210	8.64	2.08	11.4835	0.0011	6.6207	0.0004	8.7096	0.0007	662.18	0.09
230	8.84	2.10	11.4914	0.0011	6.6192	0.0004	8.7074	0.0007	662.31	0.10
250	8.63	2.06	11.4925	0.0013	6.6175	0.0004	8.7073	0.0007	662.20	0.10
270	8.08	1.90	11.4860	0.0015	6.6175	0.0005	8.7108	0.0008	662.10	0.12
290	7.59	1.74	11.4868	0.0024	6.6175	0.0006	8.7125	0.0009	662.27	0.17
310	6.57	1.48	11.4776	0.0032	6.6135	0.0009	8.7087	0.0010	661.05	0.22

***Table A4**: Refinement values of the VT-PXRD of $(MIL\text{-}118)_{0.5}(a_gZIF\text{-}62)_{0.5}$.*

T (°C)	rwp	χ^2	*a* (Å)	*a* st. dev.	*b* (Å)	*b* st. dev.	*c* (Å)	*c* st. dev.	Volume (Å^3)	Volume st. dev.
70	4.03	1.33	11.5017	0.0025	6.6281	0.0010	8.6987	0.0010	663.15	0.19
90	4.17	1.42	11.4791	0.0018	6.6248	0.0010	8.7036	0.0009	661.88	0.16
110	4.17	1.36	11.4602	0.0026	6.6252	0.0012	8.7087	0.0009	661.21	0.20
130	4.75	1.65	11.4583	0.0023	6.6251	0.0011	8.7102	0.0011	661.21	0.19
150	4.16	1.43	11.4583	0.0024	6.6234	0.0009	8.7115	0.0009	661.14	0.18
170	4.09	1.42	11.4537	0.0021	6.6259	0.0010	8.7114	0.0010	661.12	0.17
190	4.23	1.45	11.4537	0.0025	6.6242	0.0009	8.7104	0.0010	660.87	0.19
210	3.80	1.28	11.4525	0.0022	6.6246	0.0009	8.7140	0.0008	661.12	0.17
230	4.18	1.43	11.4556	0.0021	6.6219	0.0010	8.7123	0.0010	660.89	0.17
250	4.21	1.44	11.4564	0.0023	6.6207	0.0009	8.7106	0.0010	660.69	0.18
270	4.02	1.38	11.4657	0.0019	6.6209	0.0008	8.7119	0.0010	661.35	0.15
290	4.08	1.30	11.4714	0.0020	6.6228	0.0008	8.7115	0.0009	661.84	0.16
310	4.57	1.44	11.4778	0.0024	6.6222	0.0010	8.7114	0.0011	662.14	0.19

***Table A5**: Refinement values of the VT-PXRD of UL-MOF-1.*

T (°C)	rwp	χ^2	*a* (Å)	*a* st. dev.	*b* (Å)	*b* st. dev.	*c* (Å)	*c* st. dev.	β (°)	β st. dev.	Volume (Å^3)	Volume st. dev.
30	15.63	2.87	10.3062	0.0025	5.3492	0.0016	8.6859	0.0021	98.5935	0.0006	473.48	0.22
50	15.12	2.81	10.3077	0.0025	5.3545	0.0015	8.7117	0.0020	98.5306	0.0006	475.50	0.21
70	16.06	2.98	10.3120	0.0026	5.3581	0.0016	8.7322	0.0019	98.3901	0.0006	477.31	0.21
90	14.26	2.60	10.3115	0.0027	5.3593	0.0015	8.7509	0.0018	98.2870	0.0006	478.55	0.21
110	13.69	2.50	10.3123	0.0024	5.3610	0.0013	8.7674	0.0017	98.1874	0.0006	479.76	0.19
130	13.71	2.48	10.3098	0.0026	5.3604	0.0014	8.7821	0.0018	98.0796	0.0006	480.52	0.20
150	13.01	2.32	10.3110	0.0024	5.3630	0.0015	8.7926	0.0018	97.9552	0.0006	481.53	0.20
170	13.53	2.43	10.3124	0.0026	5.3614	0.0015	8.8049	0.0020	97.8849	0.0006	482.21	0.21
190	13.43	2.41	10.3089	0.0048	5.3647	0.0022	8.8227	0.0027	97.8675	0.0010	483.34	0.33
210	12.73	2.31	10.3123	0.0025	5.3635	0.0014	8.8384	0.0023	97.8394	0.0006	484.28	0.21
230	12.46	2.27	10.3104	0.0022	5.3634	0.0013	8.8582	0.0023	97.8873	0.0006	485.21	0.20
250	11.59	2.10	10.3117	0.0021	5.3726	0.0013	8.8686	0.0021	97.8240	0.0006	486.75	0.19
270	12.18	2.23	10.3119	0.0034	5.3773	0.0019	8.8836	0.0031	97.7801	0.0008	488.06	0.29
290	11.54	2.11	10.3111	0.0040	5.3801	0.0022	8.9038	0.0035	97.7649	0.0010	489.41	0.34
310	11.56	2.19	10.3106	0.0052	5.3821	0.0029	8.9135	0.0046	97.7127	0.0013	490.16	0.44

***Table A6**: Refinement values of the VT-PXRD of (UL-MOF-1)$_{0.5}$(a_gZIF-62)$_{0.5}$.*

T (°C)	rwp	χ^2	*a* (Å)	*a* st. dev.	*b* (Å)	*b* st. dev.	*c* (Å)	*c* st. dev.	β (°)	β st. dev.	Volume (Å^3)	Volume st. dev.
30	4.16	1.50	10.3176	0.0058	5.3405	0.0011	8.6812	0.0026	98.4889	0.0009	473.10	0.32
50	4.29	1.57	10.3200	0.0055	5.3414	0.0011	8.7025	0.0026	98.5213	0.0009	474.41	0.31
70	3.94	1.41	10.3059	0.0057	5.3437	0.0011	8.7229	0.0023	98.3941	0.0009	475.24	0.31
90	4.09	1.51	10.3095	0.0055	5.3447	0.0011	8.7352	0.0025	98.3061	0.0009	476.27	0.31
110	3.98	1.45	10.3004	0.0048	5.3482	0.0011	8.7433	0.0021	98.1934	0.0008	476.74	0.27
130	4.10	1.45	10.3097	0.0059	5.3482	0.0011	8.7620	0.0026	98.1571	0.0010	478.24	0.33
150	3.56	1.28	10.3005	0.0052	5.3504	0.0010	8.7733	0.0021	98.0308	0.0008	478.77	0.28
170	3.92	1.39	10.3084	0.0062	5.3536	0.0011	8.7911	0.0027	98.0782	0.0010	480.34	0.34
190	3.68	1.27	10.3049	0.0052	5.3548	0.0010	8.7990	0.0023	97.9314	0.0008	480.89	0.29
210	3.85	1.32	10.3136	0.0063	5.3564	0.0011	8.8134	0.0028	97.8776	0.0010	482.29	0.35
230	3.79	1.30	10.3142	0.0057	5.3564	0.0011	8.8343	0.0026	97.8618	0.0009	483.48	0.32
250	4.26	1.47	10.2976	0.0059	5.3599	0.0012	8.8478	0.0031	97.7407	0.0010	483.90	0.35
270	4.01	1.40	10.3000	0.0061	5.3607	0.0011	8.8537	0.0027	97.6302	0.0010	484.53	0.34
290	4.08	1.39	10.3062	0.0058	5.3635	0.0012	8.8694	0.0032	97.5698	0.0010	486.01	0.34
310	3.99	1.38	10.3049	0.0056	5.3643	0.0011	8.8846	0.0032	97.5437	0.0010	486.88	0.34